JOHANNES GUTENBERG UNIVERSITÄT MAINZ

JG|U

Dissertation zur Erlangung des Grades
„Doktor der Naturwissenschaften“
am Fachbereich Physik, Mathematik und Informatik
der
Johannes Gutenberg-Universität

Digital Signal Processing for the Measurement of Particle Properties with the PANDA Electromagnetic Calorimeter

Ernst Johannes Oliver Noll

23. April 2020

Eidesstattliche Erklärung

Hiermit erkläre ich an Eides statt, dass ich meine Dissertation selbständig und ohne fremde Hilfe verfasst und keine anderen als die von mir angegebenen Quellen und Hilfsmittel zur Erstellung meiner Dissertation verwendet habe. Die Arbeit ist in vorliegender oder ähnlicher Form bei keiner anderen Prüfungsbehörde zur Erlangung eines Doktorgrades eingereicht worden.

Mainz, 23.4.2020
Ort, Datum

E. J. Oliver Noll

Abstract

In recent decades, the quantum field theory of strong interaction (QCD) has been impressively demonstrated in the area of high energies and momentum transfers. Nowadays, novel experiments allow for challenging the methods for the calculation of QCD also in the non-perturbative regime by the continuous improvement of measurement accuracy. $\bar{\text{P}}$ANDA at the upcoming FAIR accelerator facility is one of such experiments. At $\bar{\text{P}}$ANDA, antiprotons with momenta of up to 15 GeV/c will be annihilated at a fixed proton target under high luminosities. Among a variety of detector systems, $\bar{\text{P}}$ANDA stands out with its lead tungstate electromagnetic calorimeter (EMC), which is designed to have a wide dynamic range (10 MeV to 14.6 GeV) and a relative energy resolution of better than 2.5 % at 1 GeV. The development of the backward part of the $\bar{\text{P}}$ANDA EMC is the first scientific goal of this thesis. Since the development of the backward EMC has progressed so far, it is foreseen for an experiment within the FAIR Phase-0 research programme. It is proposed to measure the double-virtual electromagnetic transition form factor (TFF) of the pion in the Primakoff π^0 electroproduction at the Mainz Microtron facility (MAMI). The pion TFF is related via the hadronic light-by-light scattering to the $g_\mu - 2$ puzzle. Consequently, the second scientific goal of this thesis are preparatory studies for FAIR Phase-0.

The developments of this work resulted in a fully functional prototype calorimeter, which operated stably in numerous tests at MAMI. However, the focus of this work is digital signal processing (DSP) for the $\bar{\text{P}}$ANDA EMC. A specially developed software framework allowed for testing and optimising signal filtering algorithms and parameter extraction methods on realistically simulated signals. Thus, the algorithms are well-adapted to the time structure of the $\bar{\text{P}}$ANDA calorimeter preamplifier (APFEL) signals. Furthermore, the DSP methods were implemented on the Field Programmable Gate Arrays (FPGAs) of the $\bar{\text{P}}$ANDA digitisation board. The developed FPGA firmware provides a self-triggering readout for all calorimeter channels, an efficient implementation of a high order filter with a finite impulse response (FIR), noise hit suppression and pileup handling.

Together with the calorimeter prototype, the digital signal processing was tested at MAMI. Thanks to the use of the DSP methods, an energy detection threshold (single-crystal) of less than 2.5 MeV was achieved. This allowed for a measured relative energy resolution of 2.190(2) % at 1 GeV. Moreover, the non-linearity of the calorimeter is in the order of a few per mill. Due to the self-triggering concept of the FPGA firmware, measurements under high detector rates were possible. Thus, a dead time of 464(13) ns and a pileup probability of 4.53(12) % at 100 kHz was determined.

For the measurement of the pion TFF, a high flux of low energy electrons and photons is expected. Thus, test beams with the prototype were performed to determine the impact of the low energetic background on the measurement. By utilising both experiment data and simulations, an upper limit for the relative energy resolution (2.75(4) % to 6.57(2) % at 1 GeV) as a function of the luminosity (2.77 μb^{-1}/s to 55.34 μb^{-1}/s) was found. The study allows an estimation of the FAIR Phase-0 measuring time.

Zusammenfassung

In den letzten Jahrzehnten wurde die Quantenfeldtheorie der starken Wechselwirkung (QCD) eindrucksvoll im Bereich hoher Energien und Impulsüberträge belegt. Neuartige Experimente erlauben nun, durch immer größere Messgenauigkeiten im nichtperturbativen Bereich die Methoden zur Berechnung der QCD auch dort herauszufordern. $\bar{\text{P}}$ANDA an der zukünftigen FAIR Beschleunigeranlage ist eines dieser Experimente. Bei $\bar{\text{P}}$ANDA werden Antiprotonen mit Impulsen von bis zu 15 GeV/c an einem festen Protonentarget unter hoher Luminosität annihiliert. Ein wichtiges Detektorsystem ist dabei das Bleiwolframat elektromagnetische Kalorimeter (EMC), das einen dynamischen Bereich von 10 MeV bis 14.6 GeV und eine relative Energieauflösung von weniger als 2.5 % bei 1 GeV besitzt. Die Entwicklung des rückwärtigen Teiles eben dieses Kalorimeters ist das erste Forschungsziel dieser Arbeit. Da die Entwicklungsarbeiten soweit fortgeschritten sind, ist dises Kalorimeter für ein Experiment im Rahmen des FAIR Phase-0 Forschungsprogramms vorgesehen. Dabei ist eine Messung des doppel-virtuellen elektromagnetischen Übergangsformfaktors (TFF) des Pions mittels der Primakoff π^0 Elektroproduktion am Mainzer Mikrotron (MAMI) angestrebt. Der Pion TFF ist über die hadronische Licht-Licht-Streuung mit dem $g_\mu - 2$ Puzzle verbunden. Folglich sind vorbereitende Studien für dieses Experiment das zweite Forschungsziel dieser Dissertation. Die Entwicklungen dieser Arbeit mündeten in einem voll-funktionsfähigen Prototyp-Kalorimeter, das stabil in einer Vielzahl von Tests an MAMI operierte. Eine Schlüsselkomponente dafür und Schwerpunkt dieser Arbeit ist die Digitale Signalverarbeitung (DSP) für das $\bar{\text{P}}$ANDA Kalorimeter. Dafür wurde spezielle Software entwickelt, die es ermöglicht Filteralgorithmen und Parameter-Extraktionsmethoden mittels realistisch simulierter Signale zu testen und zu optimieren. Folglich sind die Algorithmen an die Zeitstruktur der $\bar{\text{P}}$ANDA EMC Vorverstärkersignale (APFEL) angepasst. Die optimierten Methoden wurden anschließend auf die Field Programmable Gate Arrays (FPGAs) der $\bar{\text{P}}$ANDA Digitalelektronik implementiert. Die FPGA Firmware bietet für alle Eingangskanäle eine selbstauslösende Auslese, eine effiziente Implementierung eines Filters hoher Ordnung mit endlicher Impulsantwort (FIR), eine Pile-Up Behandlung und eine Unterdrückung von Rauschereignissen.
Durch die erwähnten Methoden konnte zusammen mit dem Prototyp-Kalorimeter eine Energie-Detektionsschwelle von weniger als 2.5 MeV bei Tests an MAMI erzielt werden. Dadurch wurde eine gemessene relative Energieauflösung von 2.190(2) % bei 1 GeV möglich. Die Nicht-Linearität des Systems beträgt dabei wenige Promille. Durch das selbstauslösende Konzept der Auslese wurden Messungen unter hohen Raten möglich, womit die Totzeit des Kalorimeters zu 464(13) ns und die Pile-Up Wahrscheinlichkeit bei 100 kHz zu 4.53(12) % bestimmt wurden. Da für die Messung des Pion TFF ein hoher niederenergetischer Untergrund erwartet wird, wurde dieser mittels Streuexperimenten an MAMI bestimmt. Durch weiterführende Simulationen konnte eine obere Grenze der relativen Energieauflösung (2.75(4) % bis 6.57(2) % bei 1 GeV) in Abhängigkeit der Luminosität ($2.77\,\mu\text{b}^{-1}/\text{s}$ bis $55.34\,\mu\text{b}^{-1}/\text{s}$) bestimmt werden. Die Studie erlaubt eine bessere Abschätzung der benötigten Messzeit für FAIR Phase-0 in Mainz.

Acknowledgments

This part is omitted due to data protection regulations.

Outline of this Thesis

This work consists of seven main chapters. Each main chapter begins with a cover page that motivates the content of the chapter. However, in the following, the chapters are introduced by highlighting their interrelations.

- Chapter 1 gives an introduction to the future Facility for Ion Research (FAIR) at Darmstadt. After the consideration of the relevant accelerator structures for the antiproton beam, the discussion moves on to the $\bar{\text{P}}$ANDA (antiProton ANnihilation at DArmstadt) experiment, including its essential detector systems. Subsequently, the envisaged physics programme of $\bar{\text{P}}$ANDA is presented. Since the $\bar{\text{P}}$ANDA backward part of the ElectroMagnetic Calorimeter (EMC) was developed in this work, the importance of the EMC for the $\bar{\text{P}}$ANDA physics is emphasised at the end of the chapter.

- Chapter 2 presents the theoretical background for the measurement of the double-virtual electromagnetic transition form factor (TFF) of the pion at the Mainz Microtron facility (MAMI) using a version of the backward part of the $\bar{\text{P}}$ANDA EMC. Consequently, the relationship of the pion TFF via a dispersive approach to the hadronic light-by-light scattering is described. Furthermore, it is revealed how the measurement of the TFF contributes to the $g_\mu - 2$ puzzle. The chapter ends with a discussion about the experimental realisation.

- Chapter 3 deals with the development of the backward part of the $\bar{\text{P}}$ANDA EMC. After a general introduction of homogeneous electromagnetic calorimeters, the specific construction of the backward calorimeter with all its components and materials used is addressed. The discussion also includes the detector layout for $\bar{\text{P}}$ANDA and the detector layout for the pion TFF measurement. Finally, the calorimeter prototype is introduced, which is the central component for all laboratory tests and measurements with beam in this thesis.

- Chapter 4 begins with an introduction to nowadays digital electronics. Since Analogue to Digital Converters (ADCs) and Field-Programmable Gate Arrays (FPGAs) are vital devices in this work, they are explained in detail. Afterwards, the developed firmware for the $\bar{\text{P}}$ANDA EMC digitisation electronics is introduced. The chapter also covers the fundamental concepts of Digital Signal Processing (DSP). Furthermore, the implementation of a high order filter with a finite impulse response (FIR) via distributed arithmetic is addressed. Finally, the parameter extraction methods for EMC preamplifier signals are presented.

- Chapter 5 introduces the detector response simulation framework, which was developed to test and optimise the DSP methods presented in chapter 4. The discussion begins with the realistic signal generator, which can simulate both the EMC preamplifier pulse shape and the electronic signal noise. Subsequently,

simulations and measurements are compared to assess the accuracy of the simulation. Lastly, the simulation framework is used to optimise DSP parameters and to determine the performance of the parameter extraction.

- Chapter 6 reports the results of measurements with beam at MAMI with the prototype calorimeter. After the introduction of the MAMI facility, the experimental setup is explained. Subsequently, the data taking procedure is shown before the chapter moves on to the data analysis. Finally, the performance of both the prototype calorimeter and the DSP methods are addressed. The discussion includes the relative energy resolution, the linearity of the detector response, the pileup handling under high rates and the dead time of the system.

- Chapter 7 finalises the thesis with a feasibility study for the measurement of the pion TFF at MAMI using the prototype calorimeter in a test scattering experiment. After the discussion about the experimental setup at the MAMI A1 spectrometer hall and the objectives of the different measurements, the chapter focuses on the low energy background determination under small scattering angles. Subsequently, the extraction of the background energy distribution from the data is addressed. Afterwards, the implementation of the energy distribution into the detector response simulation framework (chapter 5) is shown. By utilising both the simulation framework and beam data from chapter 6, an upper limit of the relative energy resolution as a function of the luminosity for the pion TFF measurement is determined. The chapter ends with implications for the reachable luminosity and measuring time for the pion TFF determination.

Ultimately, in Chapter 8, all relevant results from this thesis are summarised. Furthermore, an outlook to future tasks is given.

Contents

1 The Study of Strong Interaction in Antiproton-Proton Annihilation Processes at FAIR

The picture shows a rendering of the upcoming Facility for Antiproton and Ion Research (FAIR) at Darmstadt. $\bar{P}$ANDA (antiProton ANnihilation at DArmstadt) is one of its experiments and designed to study the phenomena of the strong interaction. In this thesis, technology for the $\bar{P}$ANDA ElectroMagnetic Calorimeter (EMC) was developed. [FAI20]

The Standard Model (SM) of particle physics is very successful in describing all known particles and their interaction among each other [PSRZ14]. Nevertheless, the SM must be tested based on its predictions. In particular, the nature of hadronic matter, which is described by the strong force, will be examined by new high energy experiments. For instance, the SM predicts exotic matter states such as glueballs, hybrids and tetraquarks [Kop12]. Although some candidates were already discovered ([HG13], [Och13]), new experiments are required, which are optimised for the exotic matter search. Besides the extension of the particle zoo, there are fundamental questions, which need to be investigated by new experiments. The matter-antimatter asymmetry [Nay19] is both a condition for the existence of the universe itself and a mystery. The CP-violation, which is predicted by the SM, is not large enough to explain the asymmetry between matter and antimatter. The first evidence for CP-violation in the baryon sector was found at LHCb [A$^+$17] by the study of the decay of Λ_b^0 and its antimatter counterpart. However, new baryon antibaryon annihilation experiments could enhance the understanding of the matter-antimatter asymmetry. Furthermore, such experiments allow for the study of the nucleon structure. Such studies date back to the 1950s, where Hofstadter et al. [HM55] measured the proton form factor and M. N. Rosenbluth [Ros50] delivered the description. Nowadays, the nucleon form factors are extensively measured in the space-like momentum transfer regime ($q^2 < 0$) by electron-nucleon scattering experiments ([Ber13], [S$^+$13]). However, there is still a discrepancy between polarised data and un-polarised data, which is not yet well-understood [PPV07]. The situation for the time-like momentum transfer regime ($q^2 > 0$) is even more precarious. Only a few experiments were able to access this region by $e^+e^- \to \bar{p}p$ annihilation reactions. One unexpected outcome was an oscillation in the course of the effective proton form factor [L$^+$13a] [L$^+$13b] [A$^+$19] [A$^+$20], which requires further investigations.

The $\bar{P}$ANDA (antiProton ANnihilation at DArmstad) experiment at the upcoming Facility for Antiproton and Ion Research (FAIR) is designed to address the discussed topics and many others by the annihilation of antiprotons with protons. Within this thesis, technology for the electromagnetic calorimeter of $\bar{P}$ANDA was developed. In the following, the experiment and the main pillars of its physics programme will be presented. Subsequently, the contribution of this work will be placed in the context of the entire $\bar{P}$ANDA experiment.

1.1 The P̄ANDA Experiment at the FAIR Facility

The Facility for Antiproton and Ion Research (FAIR) is a large-scale research project which is currently under construction at the GSI Helmholtzzentrum für Schwerionenforschung in Darmstadt. FAIR has four main experiments:

1. NUclear STructure, Astrophysics and Reactions (NUSTAR).
2. Compressed Baryonic Matter (CBM).
3. Atomic, Plasma Physics and Applications (APPA).
4. antiProton ANnihilation at DArmstad (P̄ANDA).

The different experiments are supplied with protons, antiprotons or heavy ion beams by an arrangement of accelerator structures. In Figure 1.1 the key components of the facility are depicted. Accelerator structures, which are relevant for the P̄ANDA experiment will be addressed in the following.

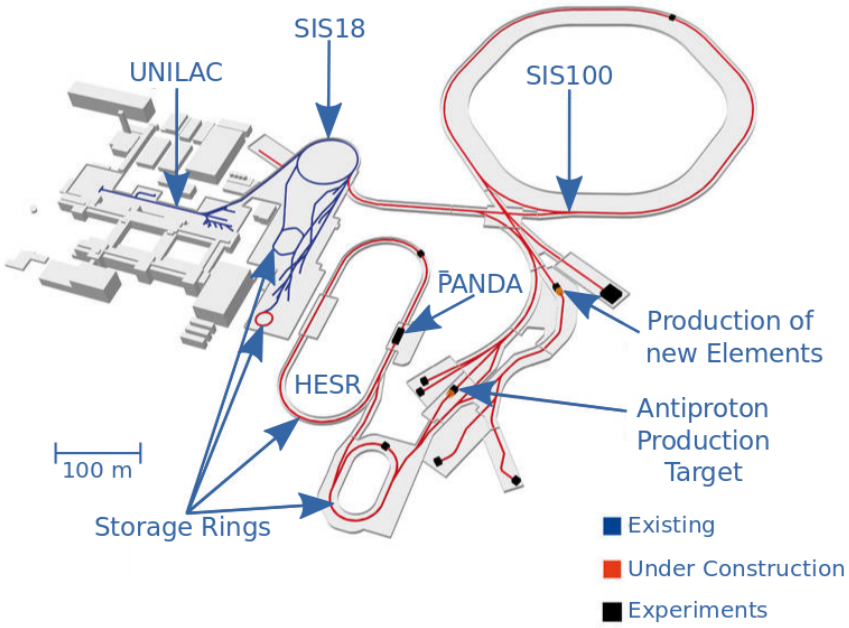

Figure 1.1: The Facility for Antiproton and Ion Research (FAIR) at the GSI Helmholtzzentrum für Schwerionenforschung in Darmstadt. The arrangement of accelerator structures supplies different experiments with proton, antiproton or heavy ion beams. At the center of the facility, the P̄ANDA experiment is located, which uses antiprotons in annihilation processes in order to study the strong force. [FAI20]

The primary beam is generated at the so-called Universal Linear Accelerator (UNILAC), which is capable of accelerating ions of any atomic mass. For the $\bar{\text{P}}$ANDA experiment, protons are accelerated and passed to two successive synchrotrons SIS18 and SIS100. Subsequently, the protons are hit on a production target, where besides other particles antiprotons are produced. The antiproton beam is then guided via a smaller storage ring into the final High Energy Storage Ring (HESR), at which the $\bar{\text{P}}$ANDA experiment is located. HESR offers an antiproton beam of momenta between 1.5 GeV/c and 15 GeV/c with a relative momentum spread of $\Delta p/p \sim 10^{-4}$. The targeted luminosity is $2 \times 10^{32}\,\text{cm}^{-2}\text{s}^{-1}$ [PAN19].

The $\bar{\text{P}}$ANDA detector, as depicted in Figure 1.2, uses a fixed proton target, realised by either a hydrogen gas jet or by dripping frozen hydrogen pellets [Kho11].

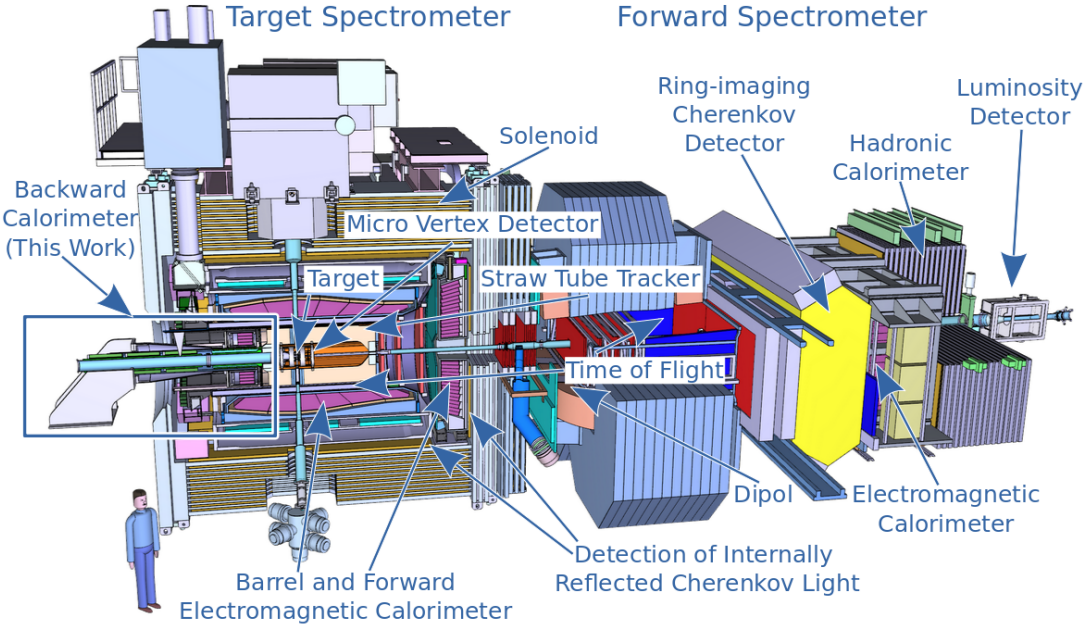

Figure 1.2: The $\bar{\text{P}}$ANDA detector is a typical "onion-shell" spectrometer. There is the target spectrometer, which surrounds the collision point with a Micro Vertex Detector (MVD), a Straw Tube Tracker (STT) and the ElectroMagnetic Calorimeter (EMC). The electromagnetic calorimeter is divided between the Forward EMC, the Barrel EMC and the Backward EMC. A solenoid magnet generates a 2 T axial magnetic field in order to measure momenta of charged particles with the STT. Further detector systems such as a muon detector, a Time of Flight (TOF) detector and a Cherenkov detector complete the target spectrometer. The forward spectrometer consists of detectors, which are capable of measuring properties of high momentum particles. The used technologies are similar to those, used in the target spectrometer. The development of the backward EMC is part of this work. A detailed description of the backward EMC can be found in Chapter 3. [PAN19]

Through the collision of the antiprotons with the target protons, it comes to annihilation and scattering events. However, most of the antiprotons continue circulating within the HESR. The process proceeds until the number of antiprotons falls below a specific limit, and the HESR needs to be refilled.

1.2 The $\bar{\text{P}}$ANDA Detector

The $\bar{\text{P}}$ANDA detector, as shown in Figure 1.2 can be divided into the target spectrometer, which surrounds the interaction point, and the forward spectrometer. In the following, the components of both systems are described.

1.2.1 The Target Spectrometer

The target spectrometer surrounds the annihilation point in an "onion-shell" manner. The Micro Vertex Detector (MVD) is the closest system to the target. The MVD is, in turn, surrounded by the Straw Tube Tracker (STT). A Time of Flight (TOF) detector encloses the STT and the backward part of the electromagnetic calorimeter. The TOF increases the particle identification redundancy of charged particles in combination with the DIRC (Detection of Internally Reflected Cherenkov Light) detector, which encloses the TOF.
The DIRC surrounds the barrel part of the electromagnetic calorimeter (EMC). The EMC is divided between the forward EMC, the barrel EMC and the backward EMC. The development of the backward EMC is part of this work. Thus, a detailed explanation of the $\bar{\text{P}}$ANDA EMC materials and techniques with an emphasis of their usage at the backward EMC are given in Chapter 3.
A superconducting solenoid magnet, which generates a 2 T axial magnetic field, encloses the EMC barrel. The magnetic field allows the measurement of charged particle momenta with the STT.
Finally, the flux-return yoke of the solenoid is used as an active muon range system. Therefore, mini-drift tubes are located between 13 layers of iron.

1.2.2 The Forward Spectrometer

The forward spectrometer is specialised in measuring properties of high momenta particles under small angles. The used technologies are similar to those, used in the target spectrometer. For instance, a dipole magnet bends the trajectory of charged particles. In combination with an STT, the momenta of these charged particles can be determined. A Ring Imaging Cherenkov (RICH) detector performs the particle identification similarly to the DIRC in the target spectrometer. Also here, a TOF detector contributes to the particle identification.
As well as the target spectrometer, the forward spectrometer has an electromagnetic calorimeter. Beyond that, the forward spectrometer has a hadronic calorimeter. Finally, a luminosity detector is placed downstream close to the beam pipe.

1.3 The Study of the Strong Interaction at $\bar{\text{P}}$ANDA

$\bar{\text{P}}$ANDA is set to become a versatile facility to study nuclear, hadron and particle physics with antiprotons as a hadronic probe. Thus, $\bar{\text{P}}$ANDA will become a unique tool to investigate the bound states and the dynamics in quantum chromodynamics (QCD). With antiproton momenta of up to 15 GeV/c, a centre of mass energy of up to 5.5 GeV can be achieved. As a result, both perturbative and non-perturbative aspects of QCD are accessible with $\bar{\text{P}}$ANDA. In Figure 1.3 a map of the different $\bar{\text{P}}$ANDA physics programme phases (P1, P2 and P3) is depicted. The illustration shows the strength of $\bar{\text{P}}$ANDA compared to competing experiments. The different programme aspects can be summarised in four research pillars, which are briefly discussed in the following. The description follows [L+09] and [PAN18].

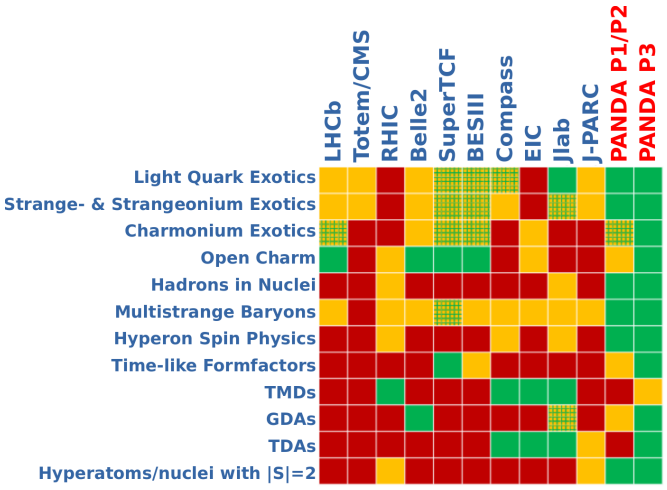

Figure 1.3: The map shows the $\bar{\text{P}}$ANDA research programme. The colors indicate the feasibility of an experiment. Whereby red indicates an impossibility of the measurement, yellow a limited outcome of the measurement, green/yellow a very good measurement and green an excellent measurement in plenty of channels and reactions.[PAN18]

1.3.1 Hadron Spectroscopy

Within the light-quark and gluon sector, it is planned to search for exotic states such as glueballs (ggg, gg), hybrids ($q\bar{q}g$) or tetraquark hadrons ($qq\bar{q}\bar{q}$) [KZ07]. Thanks to the antiproton probe at $\bar{\text{P}}$ANDA, all quantum states are accessible [Kop12]. Furthermore, the cross-sections for such states are higher compared to reactions with electromagnetic probes [PAN18]. The $\bar{\text{P}}$ANDA detector has to deal with final states of one or multiple $\phi, \omega, \eta, J/\psi$ as well as D and D_s mesons to reconstruct exotic states as mentioned above. Moreover, with a mass resolution of 50 keV/c^2, $\bar{\text{P}}$ANDA will complement the recently discovered charmonium-like XYZ-spectrum. For instance, states such as $X(3872)$, $Z_c(3900)$ and $Z_c(4020)$ will be accessible [GKPN19].

1.3.2 Hyperon Physics

The $p\bar{p}$-annihilation in the $\bar{\text{P}}$ANDA energy regime will give access to mesons and baryons with open-strange and charmness contribution. It is planned to exploit the pair production of baryons with $|S| = 1,2$ and 3 and $|C| = 1$ near the production

threshold [Tho12]. The analysis of the particle-antiparticle symmetry in the final states will give the possibility to test CP violations in baryon decays. Thus, $\bar{\text{P}}$ANDA will provide relevant information on the matter-antimatter asymmetry puzzle of the universe [Nay19].

1.3.3 Hadrons in Nuclei

$\bar{\text{P}}$ANDA envisages the determination of the antihyperon-nucleus potential [SLBSP15]. The potential is accessible by the associated production of hyperon pairs close to the production threshold. Furthermore, antiprotons can be used to implant hyperon pairs into a nucleus. The analysis of the decay products will improve the understanding of hyperon-hyperon interactions [Pap16]. In a later phase of $\bar{\text{P}}$ANDA, X-ray transitions of very heavy hyperons will be accessible. Thus, $\bar{\text{P}}$ANDA will complement the measurement at J-PARC with medium-heavy nuclei [FHH$^+$19]. Consequently, the contribution of hyperon interactions to the neutron skin can be studied.

1.3.4 Nucleon Structure Experiments

The measurement of the proton electromagnetic form factors in the time-like momentum transfer regime ($q^2 > 0$) in annihilation processes is a highlight of $\bar{\text{P}}$ANDA. Feasibility studies for the measurement of the process $\bar{p}p \to e^+e^-$ [S$^+$16] [Kha17] [BZD$^+$20] show that the proton form factors can be measured at $\bar{\text{P}}$ANDA with high precision. In comparison to the electron channel results, the muon channel $\bar{p}p \to \mu^+\mu^-$ provides lower precision of the measurement of the proton form factors due to the pion background contamination. However, muons in the final state have advantages compared to electrons since the contribution of final state photons lowers for higher lepton masses [VdWO13]. Thus, $\bar{\text{P}}$ANDA will be the first experiment, which uses muons in the final state to extract both the electric ($|G_E|$) and the magnetic ($|G_M|$) proton form factor. Besides the separate measurements of $|G_E|$ and $|G_M|$, an important parameter, which can be extracted even at low statistics experiments, is the proton effective form factor $|F_p|$. Feasibility studies [Zim18] revealed a statistical uncertainty for $|F_p|$ between 0.33 % for a momentum transfer of 5.1 GeV^2 and 1.39 % for a momentum transfer of 8.2 GeV^2. For the studied momentum interval, the systematic uncertainty is at a few percent for both electrons and muons in the final state.
The high accuracy of the $\bar{\text{P}}$ANDA $|F_p|$ measurement will contribute to the answer of at least two questions. Firstly, the experiments BaBar and BESIII determined $|F_p|$ in a continuous Q^2 range by using the processes $e^+e^- \to \bar{p}p$ [A$^+$20] and $e^+e^- \to \bar{p}p\gamma$ [L$^+$13a] [L$^+$13b] [A$^+$19]. They discovered a regular oscillation of $|F_p|$, which is currently subject of various theoretical studies. A more precise measurement of $|F_p|$ could help to find the origin of the oscillation. Secondly, $|F_p|$ should be identical if measured either with electrons or muons in the final state. Thus, $\bar{\text{P}}$ANDA can test the lepton universality.
Besides the measurement of the time-like proton form factor, it is envisaged to measure nucleon-to-meson transition distribution amplitudes (TDAs) by using hard exclusive

processes such as $\bar{p}p \to \gamma^*\pi^0 \to e^+e^-\pi^0$ [S$^+$15] and $\bar{p}p \to J/\psi\pi^0 \to e^+e^-\pi^0$ [S$^+$17]. Furthermore, generalised distribution amplitudes (GDAs) are accessible by the large angle production of neutral states such as $\gamma\gamma$ and $\pi^0\gamma$. Finally, a Drell-Yan programme is foreseen in order to access transverse momentum dependent (TMD) parton distribution functions by using the inclusive production of lepton pairs in $p\bar{p}$-annihilations [Des14].

1.4 Importance of the Electromagnetic Calorimeter for the $\bar{\text{P}}$ANDA Physics

In order to perform the planned $\bar{\text{P}}$ANDA physics programme, the interplay of the different detector systems is crucial. Within this interplay, the EMC has to take on various tasks. From these tasks, in turn, requirements on the calorimeter technology can be derived. In the following, the main functions of the EMC and the corresponding requirements are discussed.

1.4.1 Measurements at Wide Angular Ranges

The measurement of generalised distribution amplitudes (GDAs) has to be performed in a wide angular range since wide angular distribution gives more constraints on theoretical models. The electromagnetic calorimeter detects the neutral final states $\gamma\gamma$ and $\pi^0\gamma$ for the GDA measurement. Consequently, the $\bar{\text{P}}$ANDA Technical Design Report (TDR) demands broad angular acceptance of the calorimeter. The backward calorimeter, which was developed in this work, complements the detector acceptance for strongly backscattered events.

1.4.2 Background Suppression by Photodetection

The EMC is the only photon detector at $\bar{\text{P}}$ANDA. In particular, the detection of exotic matter states demands efficient photon detection. One example is the hybrid creation $\bar{p}p \to \eta_{c1}\eta$, which decays via an intermediate state into $J/\psi\gamma\pi^0\pi^0\eta$. This needs to be distinguished from the final states of background events such as $J/\psi\pi^0\pi^0\pi^0\eta$.
The pions decay most likely (98.8 % [N$^+$18]) into two photons, while the eta has different dominant decay modes (i.e. $\eta \to \gamma\gamma$ or $\eta \to 3 \cdot \pi^0$ and others see [N$^+$18]). Eventually, the signal events have a signature of an odd number of photons, while the background events have a signature of an even number of photons. The simple example shows the need for a sufficient photon detection of the calorimeter. Thus, the $\bar{\text{P}}$ANDA TDR requires a single-particle energy threshold of 10 MeV [TDR08].

1.4.3 Background Suppression by Electron Stopping

In contrast to hadrons, which only lose a fraction of their energy within the calorimeter, electrons are entirely stopped. In combination with the momentum determination of the straw tube tracker, a separation between electrons and hadrons can be performed.

Figure 1.4 shows the ratio between reconstructed particle energy and reconstructed particle momentum against the particle momentum. The ratio is one for electrons since the energy measurement equals the momentum measurement. In contrast to this, for hadrons the ratio differs from one.

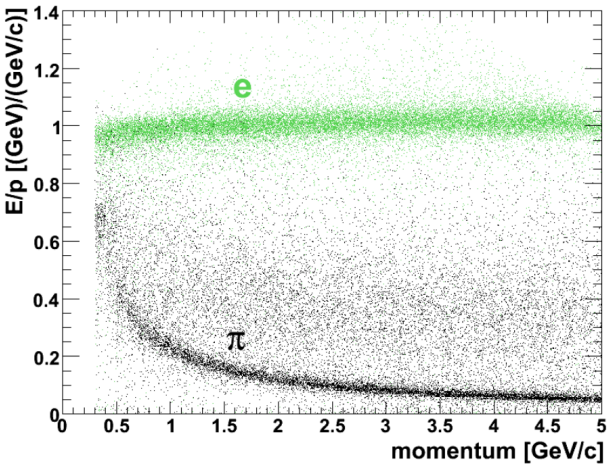

Figure 1.4: The plot shows a simulation for the ratio of reconstructed particle energy and momentum. Since electrons are stopped within the calorimeter, the energy measurement equals the momentum measurement. Thus the ratio is one for electrons. In contrast, hadrons are not stopped in the calorimeter. Thus, the ratio differs from one. [TDR08]

For instance, a separation between electrons and pions is crucial for the measurement of the proton form factor in the time-like momentum regime. The exclusive reaction $\bar{p}p \to e^+e^-$ is dominated six orders of magnitude by the background process $\bar{p}p \to \pi^+\pi^-$ [Zim18]. The separation between electrons and hadrons implies a wide dynamic range of the energy measurement (10 MeV to 15 GeV) and a low pileup probability at event rates of upto 100 kHz in the barrel part and the backward part of the EMC [TDR08].

1.4.4 Background Suppression by Muon Filtering

The EMC consists of very dense material, where electromagnetic interacting particles deposit energy for every covered distance. Consequently, the EMC material can also be utilised as an additional muon filtering element in front of the muon range system. This is in particular important for the μ/π separation in the measurement of the time-like proton form factors via the reaction $\bar{p}p \to \mu^+\mu^-$. By excluding the EMC material, an degradation of the relative uncertainty in the measurement of G_E from 13.8 % to 40.2 % and for G_M from 7.2 % to 19.9 % at a beam momentum of 1.5 GeV/c was revealed by feasibility studies [Zim18]. Consequently, the EMC absorption capability is crucial for the measurement.

1.4.5 Particle Property Determination

Energy Determination

Subsection 1.4.3 has already introduced the importance of a precise E/p-measurement. A sufficient electron and positron separation from pions is only possible if the uncertainty on the energy measurement is negligible compared to the uncertainty of the

momentum measurement. The aimed momentum resolution of the straw tube tracker system is $\sigma_p/p \sim 1\,\%$ [E$^+$13]. Consequently, the energy resolution of the calorimeter has to be $\sigma_E/E \leq 1\,\%$ for high energies. Furthermore, $\bar{\text{P}}$ANDA typical final states such as π^0 and η need to be measured with uncertainties of better than 8 MeV and 30 MeV, respectively. Only by this, a reasonable final state decomposition can be achieved. Overall, the $\bar{\text{P}}$ANDA electromagnetic calorimeter must have a relative energy resolution (Subsection 3.1.4) of better than 2.5 % at 1 GeV [TDR08].

Particle Direction Determination

The energy determination of a particle is always a summation of partial energies in adjacent detector crystals. The electromagnetic shower profile can be reconstructed from the distribution of the partial energies in the different detector crystals. Consequently, the point of entrance of the particle can be reconstructed and thus the particle direction. A sufficient spatial resolution is essential to separate final state particles. The needed spatial resolution for the three calorimeter parts, the backward EMC, the barrel EMC and the forward EMC (Figure 1.2) should not exceed 10°, 2° and 0.5°, receptively. The requirement implies a single crystal threshold of lower than 3 MeV [TDR08].

1.5 Contribution of this Work to the $\bar{\text{P}}$ANDA Electromagnetic Calorimeter Technology

All technologies presented in this thesis were developed to fulfil the requirements on the electromagnetic calorimeter. Consequently, the actual detector components (Chapter 3) were chosen and optimised for the needed specifications. The development resulted in the construction of an EMC prototype. Furthermore, the signal processing methods, which are introduced in Chapter 4, play a vital role in the achievement of the requirements. The fulfilment of the demands is verified by both detailed simulations in Chapter 5 and extensive beam tests at the Mainz Microtron with the EMC prototype in Chapter 6.
The developments also serve the so-called FAIR Phase-0 experiment, which is introduced in Chapter 2. In Chapter 7, a feasibility study for FAIR Phase-0 by using the technologies developed in this work is performed.

2 Measurement of the Pion Transition Form Factor at MAMI

The illustration shows the FAIR Phase-0 version of the $\bar{P}$ANDA backward EMC. Within the Phase-0 programme at Mainz, it is planned to measure the electromagnetic transition form factor (TFF) of the pion at the Mainz Microtron Facility (MAMI). The EMC will measure a scattered electron and a pion of an exclusive reaction.

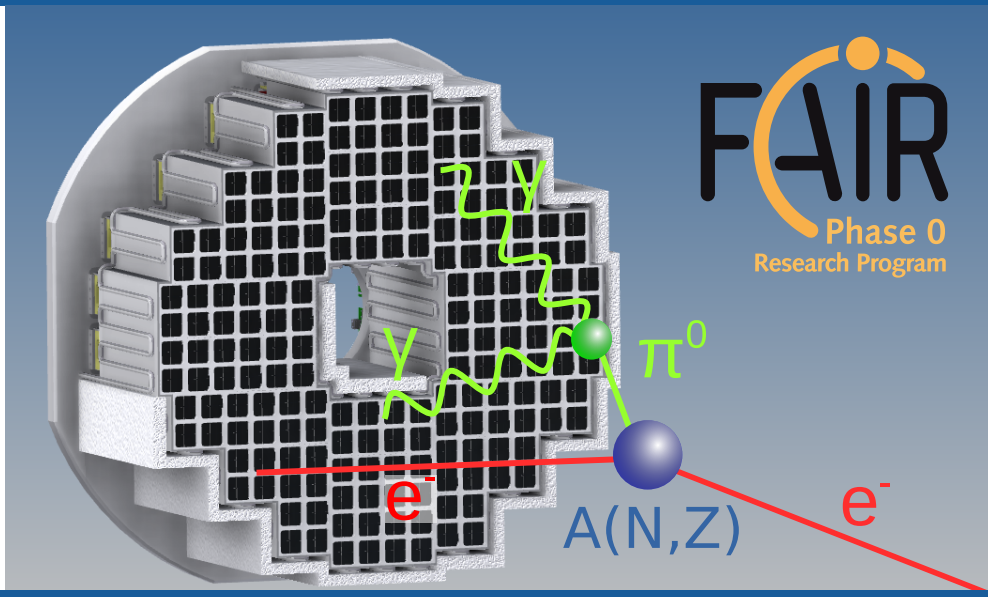

During the preparation phase of FAIR (Chapter 1), it is planned to use thoroughly developed detector components in other experiments. This project is called FAIR Phase-0.
The backward electromagnetic calorimeter of $\bar{P}$ANDA (Chapter 3) has been selected for such an experiment. It is envisaged to measure the electromagnetic transition form factor (TFF) of the pion in the Primakoff π^0 electroproduction. The pion electromagnetic TFF describes the $\pi^0\gamma\gamma$-coupling, where both photons are virtual. A precise measurement of the double-virtual TFF can help to reduce the uncertainty in the calculation of the hadronic light-by-light (HLbL) scattering [HHK$^+$18]. The HLbL scattering is one of the hadronic contributions to the Standard Model calculation of the anomalous magnetic moment of the muon a_μ^{SM}, which describes the deviation of the muon Landé factor g_μ from 2.
The discrepancy between the measurement of the anomalous magnetic moment of the muon $a_\mu^{\mathrm{Exp.}}$ [B$^+$06] and its SM calculation [AHKN12], [GSSK13] ,[Jeg19] is about four standard deviations, which is known as the $g_\mu - 2$-puzzle. The largest uncertainties in the SM calculation come in particular from the hadronic contributions, which need to be calculated in the non-perturbative regime of QCD, where the systematics is often not under control. One possible approach is to use dispersion relations to calculate the hadronic contributions to the scattering amplitudes from experimental data [PV14] [CHK$^+$14].
In the following, the $g_\mu - 2$-puzzle will be introduced by the discussion of both the Standard Model calculation of a_μ^{SM} and its measurement $a_\mu^{\mathrm{Exp.}}$. Afterwards, the connection of the muon TFF to the HLbL contribution of a_μ^{SM} via a dispersive approach will be addressed. Subsequently, the Primakoff π^0 electroproduction, which gives access to the muon TFF, will be presented. Moreover, experimental and kinematic constraints, which enhance the sensitivity to the pion TFF, will be concluded. The chapter closes with a discussion about the envisaged realisation of the experiment.

2.1 The Anomalous Magnetic Moment of the Muon

The magnetic moment $\vec{\mu}$ of a charged spin-$\frac{1}{2}$ particle can be experimentally determined to test the Standard Model. It is defined as:

$$\vec{\mu}_l = g_l \frac{e\hbar}{2m_l}\vec{S}, \quad l = e, \mu, \tau \tag{2.1}$$

Whereby $\vec{S} = \frac{\vec{\sigma}}{2}$ is the particle spin, which is described by the Pauli spin operators $\vec{\sigma}$ [Pau27], and the Landé factor g_l is the observable of interest. The Dirac-theory [Dir28] for relativistic spin-$\frac{1}{2}$ particles predicts a Landé factor of exactly $g_l = 2$. However, measurements revealed a difference from the value 2. The deviation of g_l from 2 is the anomalous magnetic moment:

$$a_l = \frac{1}{2}(g_l - 2) \tag{2.2}$$

2.1.1 Standard Model Calculation

The SM can explain the anomaly by considering higher-order corrections. J. Schwinger calculated the leading (one loop) QED correction of the anomalous magnetic moment in 1948 [Sch48]. He determined a value of $a_e = a_\mu = \frac{\alpha}{2\pi} \approx 0.001\,161\,41$. The corresponding Feynman diagram for the muon is shown in Figure 2.1.

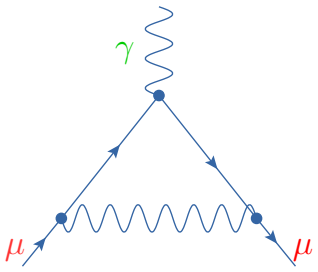

Figure 2.1: The first order (one loop) QED correction to $g_\mu - 2$. This and all following Feynman diagrams follow the convention to have the time-axis horizontally.

However, the Standard Model not only contains QED but also Electroweak (EW) and Quantum Chromodynamics (QCD). Thus, the SM prediction for a_μ^{SM} is the sum of the three contributions:

$$a_\mu^{\mathrm{SM}} = a_\mu^{\mathrm{QED}} + a_\mu^{\mathrm{EW}} + a_\mu^{\mathrm{QCD}} \tag{2.3}$$

In 2012 the most precise QED calculation for a_μ^{QED} was published by Aoyama et al. [AHKN12]. There, the anomalous magnetic moment of the muon was calculated to $\mathcal{O}(\alpha_{\mathrm{em}}^{10})$ to a value of $a_\mu^{\mathrm{QED}} = 116\,584\,718\,951(80) \times 10^{-14}$. The QED contribution to a_μ^{SM} is by far the most dominant one ($> 99.99\,\%$ of a_μ^{SM}). Furthermore, the uncertainty is small ($\mathcal{O}(10^{-13})$) compared to the following contributions.
Gnendiger et al. [GSSK13] calculated the electroweak contribution to a_μ^{SM} up to the two-loop level. They found a value of $a_\mu^{\mathrm{EW}} = 153.6(1) \times 10^{-11}$, which is only $0.001\,‰$

of a_μ^{SM}. However, the uncertainty is of $\mathcal{O}(10^{-11})$ and thus two order of magnitudes larger compared to the QED uncertainty.
The perturbative approach, which works well for QED and EW, generally can not be applied to QCD. The strong coupling constant only becomes small enough at very high energies, which is known as the asymptotic freedom. One technique to calculate the QCD contribution to a_μ^{SM} is a first-principle approach using Lattice QCD. Jegerlehner [Jeg19] found for the most dominant hadronic contributions, which are the hadronic vacuum polarisation (HVP) and the hadronic light-by-light scattering (HLbL), the values are $a_\mu^{\mathrm{HVP}} = 68\,946(325) \times 10^{-12}$ and $a_\mu^{\mathrm{HLbL}} = 1034(288) \times 10^{-12}$ respectively[1]. In both cases, the uncertainty is in $\mathcal{O}(10^{-10})$ and thus they are the biggest uncertainty of the whole a_μ^{SM} calculation. An overview of the uncertainties in the SM calculation is shown in Table 2.1.

2.1.2 Measurement at Brookhaven National Laboratory

In 2006 the most precise measurement of $a_\mu^{\mathrm{Exp.}}$ was performed by Bennett et al. [B$^+$06] at the Brookhaven National Laboratory. For this purpose, protons were accelerated to a momentum of 24 GeV/c by the Alternating Gradient Synchrotron (AGS). The accelerated protons were used to produce charged pions on a nickel target. The pions decay preferentially into muons. The muons were selected by an energy filter and filled into a storage ring. Due to parity violation in weak decays, the electrons, which are emitted in the muon decay are correlated to the muon spin. Consequently, the muon spin precession frequency ω_s was determined. Finally, the anomalous magnetic moment is derived by $a_\mu = -\frac{m}{e}\frac{\omega_s - \omega_c}{B}$. Whereby ω_c being the cyclotron frequency, m the mass of the muon, e the elementary charge and B the applied magnetic field. The final result was found to be $a_\mu^{\mathrm{Exp.}} = 116\,592\,089(63) \times 10^{-11}$.
In Table 2.1, the value for a_μ^{SM} is calculated by using [AHKN12], [GSSK13] and [Jeg19], which were discussed in the previous section, and compared with the experimental result from [B$^+$06]. The comparison reveals a four standard deviation discrepancy between SM and measurement.

2.1.3 Hadronic Contributions to $g_\mu - 2$ in a Dispersive Approach

The first-principle calculations of the muon anomalous magnetic moment are currently not able to give satisfying results in terms of uncertainties (Table 2.1). This is because of their calculation in the non-perturbative regime. As a result, the systematics of many of these processes are not under control. However, experimental data can be used to constrain the hadronic uncertainties. The approach is to express a_μ through an integral over data.

[1] In February 2020 a new lattice-QCD calculation of the HVP contribution was published by Borsanyi and others [B$^+$20]. They determined a value of $a_\mu^{\mathrm{HVP}} = 71\,240(631) \times 10^{-12}$. By utilising this value, the discrepancy between the SM calculation and measurement of a_μ diminishes to about one standard deviation. The result is the subject of current discussions. At the moment, it is necessary to wait until further theory groups confirm or disprove the result.

Contribution	Some Representatives			Error $[10^{-10}]$
a_μ^{QED}	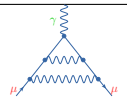	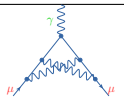	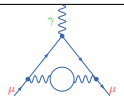	0.008 [AHKN12]
a_μ^{EW}	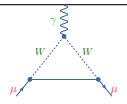	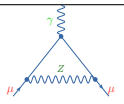	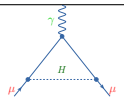	0.10 [GSSK13]
a_μ^{QCD}				
a_μ^{HVP}	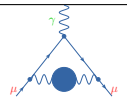	Vacuum Polarisation		3.25 [Jeg19]
a_μ^{HLbL}	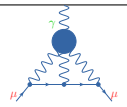	Light-by-Light		2.88 [Jeg19]
$a_\mu^{\text{HVP HO}}$	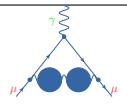	HO Vacuum Polarisation		0.06 [Jeg19]

Comparison	Value $[10^{-10}]$	Error $[10^{-10}]$
a_μ^{SM}	11 659 178.2	4.3
$a_\mu^{\text{Exp.}}$[B$^+$06]	11 659 208.9	6.3
$\lvert a_\mu^{\text{SM}} - a_\mu^{\text{Exp.}} \rvert$	30.9	7.6
Discrepancy	4σ	

Table 2.1: The table shows the uncertainties of the different contributions to a_μ^{SM}. The value of a_μ^{SM} was calculated by using [AHKN12], [GSSK13] and [Jeg19]. The QED uncertainty is by far the smallest followed by the EW uncertainty. The hadronic uncertainties are larger due to their non-perturbative calculation. The lower part of the table shows the comparison between SM prediction and measurement.

One example of such an integral is shown for the leading-order HVP contribution to a_μ [Pau14]:

$$a_\mu^{\text{HVP LO}} = \left(\frac{\alpha m_\mu}{3\pi}\right)^2 \int_{4m_\mu^2}^{\infty} \frac{ds}{s^2} K(s) R(s), \quad \text{where} \quad R = \frac{\sigma_{\text{tot}}(e^+e^- \to \text{hadrons})}{\sigma(e^+e^- \to \mu^+\mu^-)}. \tag{2.4}$$

Besides the muon mass m_μ and a known kinematical factor $K(s)$, the measured cross section $e^+e^- \to$ hadrons directly enters the calculation. Furthermore, the $1/s^2$ energy dependency indicates high sensitivity to the experimentally well known lower part of the hadronic spectrum.
Nevertheless, it is not possible to express the HLbL contribution to a_μ in the sense of Equation 2.4. Thus, the uncertainty of the HLbL contribution is in the same order of magnitude compared to the HVP contribution (Table 2.1), although it is suppressed by one power of α. However, a dispersive approach was applied to the HLbL amplitude

recently [CHK+14] [PV14] [HHK+18]. The approach allows expressing the HLbL contribution to quantities, which can be extracted from precise $\gamma^*\gamma^* \rightarrow$ meson related cross section measurements. Related to those cross sections is the coupling between the two photons and light pseudoscalar mesons, which is described by electromagnetic transition form factors (TFF). The FAIR Phase-0 experiment at Mainz is designed to measure the double-virtual electromagnetic transition form factor of the pion, which represents the $\pi^0\gamma\gamma$-coupling.

2.2 Hadronic Light-by-Light Scattering

The general diagram of the hadronic light-by-light (HLbL) scattering is shown in Figure 2.2a. The single-meson poles, such as π^0, η and η' (Figure 2.2b), are the simplest singularities of the HLbL tensor, whose residues are determined by the double-virtual transition form factors [HHK+18].

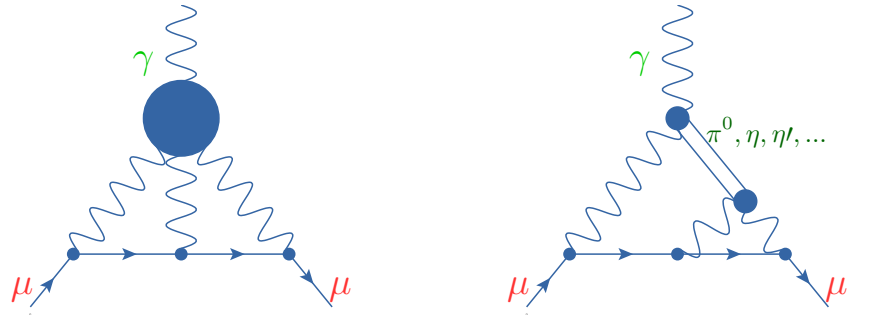

(a) General diagram for HLbL (b) Dominant subprocesses in HLbL

Figure 2.2: The hadronic light-by-light scattering process.

The pion-pole contribution is the numerically dominant contribution and would be fully determined if the double-virtual pion TFF could be measured for all (relevant) space-like momenta [HHK+18]. In Figure 2.3 the transition of a π^0 into two photons is shown. The coupling is described by the electromagnetic TFF $F_\pi(q_1^2, q_2^2)$.

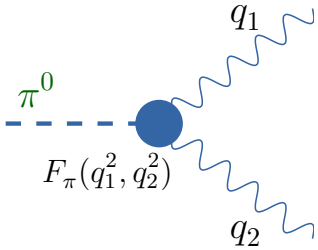

Figure 2.3: The Feynman diagram shows the transition of a π^0 into two photons. The process is characterised by the electromagnetic transition form factor $F_\pi(q_1^2, q_2^2)$. In contrast to the π^0 decay, where the photons are real (q_1^2,$q_2^2 = 0$), the photons of the HLbL scattering are virtual (q_1^2,$q_2^2 \neq 0$). Thus, the q_1^2 and q_2^2 dependency of $F_\pi(q_1^2, q_2^2)$ has to be determined.

Since the photons within the HLbL scattering are virtual (q_1^2,$q_2^2 \neq 0$), the q_1^2 and q_2^2 dependency of $F_\pi(q_1^2, q_2^2)$ has to be determined. For instance, $F_\pi(q_1^2, q_2^2)$ can be measured in the Primakoff π^0 electroproduction, which is a contribution to the coherent nuclear pion production.

2.3 The Coherent Nuclear Pion Production

One possible way to produce neutral pions is the coherent nuclear pion production:

$$e^- + A(N,Z) \rightarrow e^- + A(N,Z) + \pi^0 \tag{2.5}$$

where an electron excites a nucleus. Subsequently, the nucleus de-excites by emitting a pion. The nucleus must remain intact during the process (Figure 2.4).

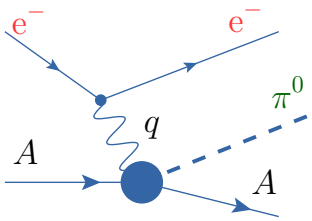

Figure 2.4: The diagram shows the coherent nuclear pion production. An electron excites a nucleus, which subsequently de-excites by emitting a pion and stays intact. One contribution to the process is the Primakoff pion electroproduction.

The Primakoff π^0 electroproduction is one contribution to the coherent nuclear pion production and gives access to the double-virtual TFF of the pion. Thus, the kinematics of the experiment has to be optimised for this process.

The Primakoff π^0 Electroproduction

In the Primakoff kinematics, a π^0 is produced in the interaction of an electron with the Coulomb filed of a nucleus [GM73]. At leading order in QED, the scattering amplitude is given by the diagram in Figure 2.5.

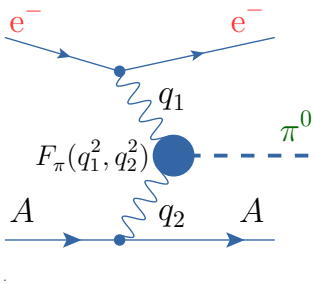

Figure 2.5: The diagram shows the leading order contribution to the Primakoff π^0 electroproduction. An electron interacts with the Coulomb field of a nucleus, which leads to the emission of a neutral pion. q_1 describes the momentum transfer between the electron and the pion and q_2 the momentum transfer between the nucleus and the pion. The process gives access to the double-virtual π^0 electromagnetic transition form factor $F_\pi(q_1^2, q_2^2)$.

Due to the additional two vertices, a factor of $1/\alpha$ suppresses the Primakoff electroproduction contribution to the coherent pion production. However, the extra propagator is proportional to $1/q_2^2$. Thus, the Primakoff electroproduction contribution can be enhanced by minimising q_2. Under the assumption of negligible recoil energy of the nucleus, the differential cross section of the Primakoff electroproduction is [GM73]:

$$\left(\frac{d^5\sigma}{dE_f d\Omega f d\Omega_\pi}\right)^{EP} = \frac{\lambda(q_1^2,q_2^2)}{8\pi^3 v_i}\alpha^2 Z^2 |\vec{p_\pi}| \frac{E_f}{E_i}\frac{1}{q_1^4 \vec{q_2}^4} \cdot \left[2(\vec{p_i}\vec{r})(\vec{p_f}\vec{r}) + \frac{1}{2}r^2 q_1^2\right] |F_{\mathrm{em}}(\vec{q_2}^2)|^2 \tag{2.6}$$

with v_i being the velocity of the incoming electron and α the fine structure constant. $\lambda(q_1^2, q_2^2)$ is the momentum dependent coupling constant, which is, up to constant factors, the electromagnetic transition form factor: $\lambda(q_1^2, q_2^2) \propto |F_\pi(q_1^2, q_2^2)|^2$. A further important characteristic of Equation 2.6 is the quadratic Z-dependency. The differential cross section increases by using a highly charged nucleus as target.
The indices i and f correspond to the initial state and the final state of the electron. Consequently, the four-momentum transfer from the electron to the pion is $q_1 = p_i - p_f$. The index π indicates the outgoing π^0 and the four-momentum of the pion reads $p_\pi = (E_\pi, \vec{p}_\pi)$. With this definition, the four-momentum transfer to the nucleus is $q_2 = q_1 - p_\pi$. In both cases the momentum transfers are space-like:

$$q_1^2 = -Q^2 < 0 \quad \text{and} \quad q_2^2 < 0 \tag{2.7}$$

Moreover, $\vec{r}$ is a space-like vector with $\vec{r} = (0, \vec{q_1} \times \vec{p_\pi})$ and $F_{\text{em}}(\vec{q_2}^2)$ is the nuclear electromagnetic form factor, which solely depends on the momentum transfer $\vec{q_2}^2$.

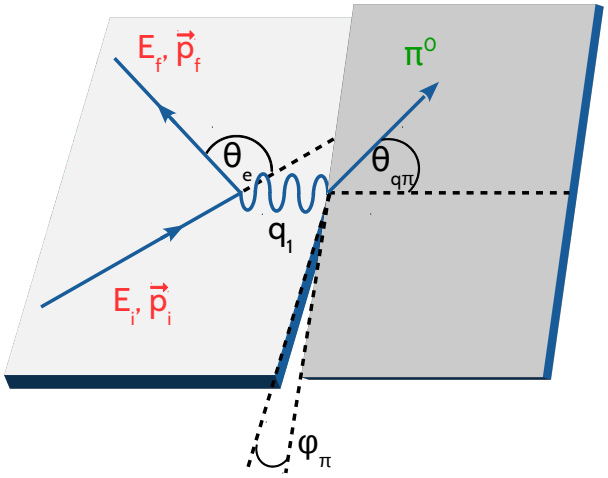

Figure 2.6: The illustration shows the kinematics of the Primakoff process in the laboratory frame. There are two important angles: Θ_e, which is the angle between incoming and outgoing electron momenta, and $\Theta_{q\pi}$, which is the angle between the direction of the momentum transfer q_1 and the outgoing π^0 momentum. The differential cross-section for the Primakoff process peaks at small $\Theta_{q\pi}$, which motivates a measurement of the π^0 near the forward direction.

Due to the high mass of the target nucleus, its recoil energy can be neglected. Thus, the four-momentum transfer to the target nucleus is given by $q_2 \simeq (0, \vec{q_2})$. By utilising the momentum conservation relation $\vec{q_1} = \vec{p_\pi} + \vec{q_2}$ it follows:

$$\vec{q_2}^2 = 2E_\pi^2 - q_1^2 - m_\pi^2 - 2\sqrt{E_\pi^2 - q_1^2}\sqrt{E_\pi^2 - m_\pi^2}\cos\Theta_{q\pi} \tag{2.8}$$

where $\Theta_{q\pi}$ is the angle between the momentum transfer $\vec{q_1}$ and the pion momentum in the laboratory frame.
Since the Primakoff electroproduction contribution enhances by minimising q_2^2 (Figure 2.5) and the kinetic energy of the nucleus can be neglected, $\vec{q_2}^2$ needs to be minimised. Applying this condition to Equation 2.8 results in a higher sensitivity for the Primakoff contribution at small $\Theta_{q\pi}$.

2.4 Background Processes and Total Cross Section

The primary background process to the coherent nuclear pion production is the incoherent nuclear pion production. In the incoherent case, the electron also interacts with the nucleus but knocks-out one ore more nucleons of the nucleus (Figure 2.7). Consequently, the kinematics differs from the coherent process and can be distinguished from it.

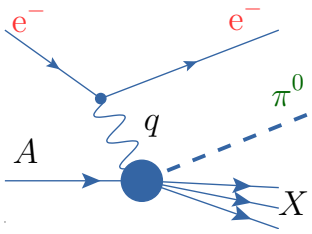

Figure 2.7: The diagram shows the incoherent nuclear pion production. In contrast to the coherent production, one or more nucleons are knocked-out of the nucleus. Thus, the kinematics of the incoherent process differs from the coherent process and can be distinguished from it.

In Figure 2.8 the differential cross sections of the different contributions are plotted against the momentum transfer to the nucleus ($\vec{q_2}^2$) for a medium momentum transfer $-q_1^2 = Q^2 = 0.03\,\mathrm{GeV}^2$. The calculation assumes a Tantalum target and an electron scattering angle between 5° and 15°. Furthermore, the ϕ-integration for both the pion and the electron has already been performed [CGM+20].

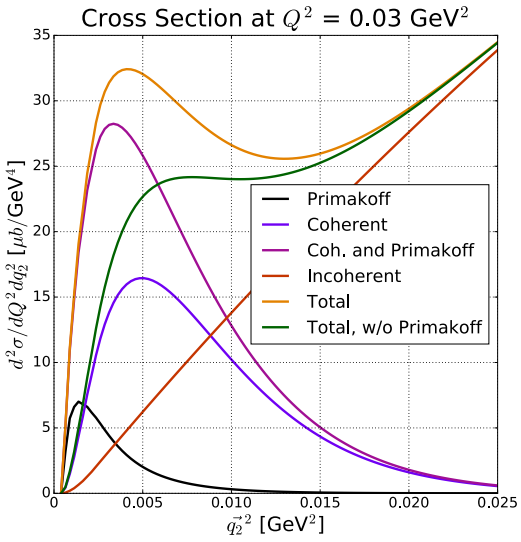

Figure 2.8: The plot shows the different contributions to the π^0 electroproduction for $Q^2 = 0.03\,\mathrm{GeV}^2$. The calculation is done for a Tantalum target and a scattering angle between 5° and 15°. Furthermore, the ϕ-integration has already been performed. The Primakoff process contributes to the coherent nuclear pion production and interferes with the incoherent pion production. The incoherent contribution is distinguishable from the Primakoff process, while the coherent contribution peaks similarly to it. However, the total cross section behaves differently without the Primakoff contribution. Thus, separation is possible. [CGM+20]

The plot shows the isolated Primakoff contribution (black curve), which contributes to the coherent pion production (without Primakoff: light purple). The minimisation of the momentum transfer to the nucleus ($\vec{q_2}^2$) enhances the Primakoff contribution. Consequently, the conjunction of both (dark purple) peaks more dominantly compared to a simple summation of the two curves (light purple + black).

The incoherent contribution (red curve) differs from coherent contributions and is small for low momentum transfers to the nucleus and increases for larger momentum

transfers. Thus, the incoherent contribution lifts the tail of the total cross section (orange curve).
For comparison, the total cross section is additionally plotted excluding the Primakoff contribution (green curve). The green curve differs significantly from the total cross section with the Primakoff contribution (orange curve). Consequently, the isolation of the Primakoff contribution is possible. [CGM+20] shows, that such a distinction is possible for Q^2-values between $0.01\,\mathrm{GeV}^2$ and $0.05\,\mathrm{GeV}^2$.

2.5 Realisation of the Experiment

A possible experiment for the determination of the pion electromagnetic transition form factor in the Primakoff kinematics has to detect the scattered electron with energy E_f and the pion with energy E_π. Due to its high mass, the nucleus stays predominately at rest. Consequently, the pion energy is approximately the beam energy E_i minus the energy of the scattered electron:

$$E_\pi \simeq E_i - E_f \tag{2.9}$$

The calorimeter can measure the energy and the point of entrance of the incoming particles. With the information about the point of entrance and the target coordinate, the momentum direction can be calculated. Consequently, the calorimeter determines both the energy E_f and the scattering angle of the electron.
Due to the short lifetime of the pion ($\tau_\pi = 8.30(19) \times 10^{-17}\,\mathrm{s}$ [N+18]), it immediately decays via the most probable decay mode ($98.823(34)\,\%$ [N+18]) into two photons. The two photons carry the invariant mass of the pion E_π. In the center of mass system of the pion, the two photons are oriented back to back ($\sphericalangle_{\mathrm{cms}}(\gamma_1, \gamma_2) = 180°$). However, in the laboratory system, they are boosted in the forward direction and can both be measured with the calorimeter, which allows the determination of the scattering angle of the pion.
By comparing the measurable observables (E_f, E_π, Ω_f and Ω_π) with the required observables E_f, Ω_f and Ω_π in Equation 2.6, it can be seen that the system is overdetermined. However, an overdetermined system is always beneficial for a measurement.

2.5.1 Kinematics

As already mentioned, a possible measurement of $F_\pi(q_1^2, q_2^2)$ has to be performed for a limited momentum transfer to the nucleus. By minimising the momentum transfer to the nucleus $\vec{q_2}$ (Equation 2.8), the following conditions for the kinematics can be derived [CGM+20]:

1. The pion energy E_π should be maximised. This is given for large beam energies E_i and small energies of the scattered electron E_f (see Equation 2.9). The MAMI accelerator (Section 6.1) can provide energies of up to 1508 MeV. However, smaller energies in the order of 1200 MeV are still considered to optimise the calorimeter acceptance.

2. The measurement has to be performed at low Q^2 in order to limit the value of $|\vec{q_2}|$. Furthermore, the expression $Q^2 = 2E_iE_f(1 - \cos\Theta_e)$ can be derived by neglecting the electron mass. Here, Θ_e is the polar angle of the scattered electron in the laboratory system. Since E_i is large and E_f is limited from below due to the energy acceptance of the detector, Θ_e has to be rather small. Consequently, the momentum transfer $\vec{q_1}$ will also have a small polar angle (Θ_q).

3. $\Theta_{q\pi}$ should be within a few degrees for optimal sensitivity to the Primakoff contribution. In combination with a small angle of the momentum transfer Θ_q to the pion follows a small angle for the pion momentum itself.

4. Due to point one, the pion energy is high. Therefore, the two photons of the pion decay will be highly boosted into forward direction.

2.5.2 Setup at the A1 Experimental Hall

The A1 experimental hall (Subsection 7.1.1) of the Mainz Microtron offers attractive conditions for the planned experiment. At A1, fixed-target experiments with electron energies of up to 1508 MeV can be performed. Furthermore, A1 offers great freedom in the choice of the target. Since a high Z target improves the cross section of the Primakoff electroproduction (Equation 2.6), it is planned to use Tantalum $^{181}_{73}$Ta. With its high melting point of 3290 K, Tantalum is suitable for high beam currents, which allows for a measurement with a high luminosity.
As shown in the previous section, the pion is emitted in the forward direction. Thus, it is planned to arrange a modified version of the $\bar{\text{P}}$ANDA backward EMC (Figure 3.16) around the exit beam pipe. In Figure 2.9 the planned installation is illustrated.

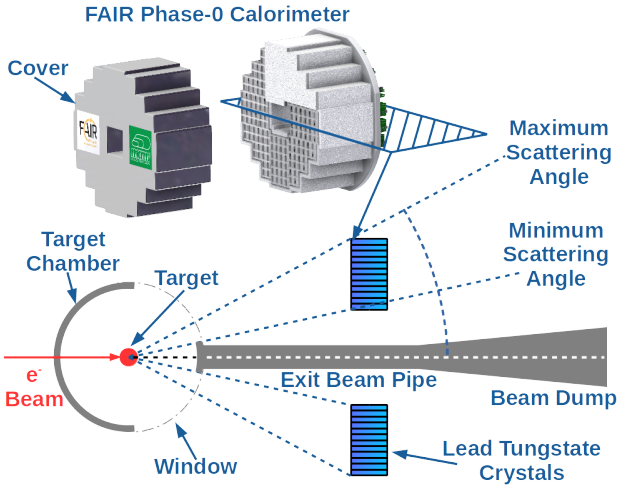

Figure 2.9: The illustration shows the planned arrangement of the FAIR Phase-0 version of the $\bar{\text{P}}$ANDA backward calorimeter for the measurement of the electromagnetic transition form factor $F_\pi(q_1^2, q_2^2)$ of the pion. The current design foresees a polar angle coverage of 5° to 15°. Thus, $F_\pi(q_1^2, q_2^2)$ can be measured in the Q^2-range of 0.01 GeV^2 to 0.05 GeV^2 for an electron beam energy of 1508 MeV.

All final state particles are measured with the EMC. However, at a standalone operation of the EMC it is not possible to distinguish between electrons and photons. Since it is crucial to reconstruct the invariant pion mass from the two decay photons, it is necessary to distinguish them from the electron. Consequently, a further detector

system in front of the calorimeter is foreseen. A prototype based on plastic scintillators with a silicon photomultiplier readout gives promising results [Gra18]. In contrast to the EMC, a plastic scintillator is only sensitive to electrons. Thus, the separation between electrons and photons is possible.

2.5.3 Acceptance and Effective Cross Section

The calculation in [CGM+20] and ongoing simulation indicate a sufficient detector acceptance for both the electron and the two photons from the pion decay for an electron beam energy of 1508 MeV. In Figure 2.10 the π^0 detection probability due to the photon angle acceptance is shown as a function of the pion energy E_π and the pion angle Θ_π. The plot shows an acceptance for the pion at angles above 5° of more than 40 % for pion energies between 800 MeV and 1200 MeV. The corresponding electron energies (Equation 2.9) are in the range between 300 MeV and 700 MeV.

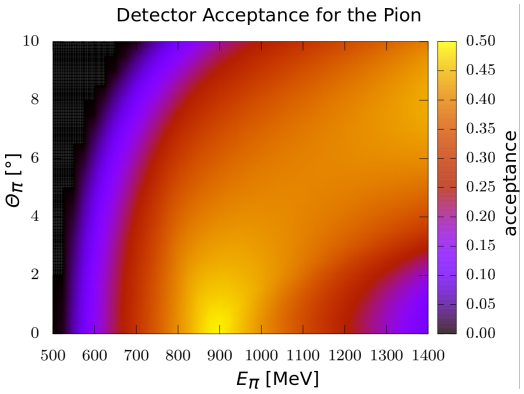

Figure 2.10: The plot shows the detection probability of the pion as a function of the pion energy E_π and the pion polar angle Θ_π. The plot indicates an acceptance of more than 40 % for pion energies between 800 MeV and 1200 MeV for polar angles above 5°. The corresponding electron energies (Equation 2.9) are between 300 MeV and 700 MeV. [CGM+20]

In Table 2.2, the total cross section σ_{tot} (Figure 2.8) is listed for Q^2-values between 0.01 GeV^2 and 0.05 GeV^2. The calculation for the values includes the integration of $\vec{q}_2{}^2$ up to 0.015 GeV^2. Every Q^2-value refers to an integral interval of $[Q_0^2 - 0.005\,\text{GeV}^2, Q_0^2 + 0.005\,\text{GeV}^2]$. Finally, the effective cross section σ_{eff}, which involves the solid angle acceptance of the detector, is listed in the third column of Table 2.2 [CGM+20].

$-q_1^2 = Q^2$ [GeV^2]	σ_{tot} [nb]	σ_{eff} [nb]
0.01	10.076	2.951
0.02	4.579	0.936
0.03	2.635	0.483
0.04	1.664	0.257
0.05	1.068	0.127

Table 2.2: The first column shows the available momentum transfer region for the experiment. The momentum transfers refer to an interval of $\Delta Q^2 = 0.01\,\text{GeV}^2$, respectively. In the second column, the total cross section of the process (Figure 2.8) is listed. Finally, the third column shows the effective cross section, which involves the solid angle acceptance of the detector. [CGM+20]

3

Development Work for the Backward Electromagnetic Calorimeter of the $\bar{\text{P}}$ANDA Experiment

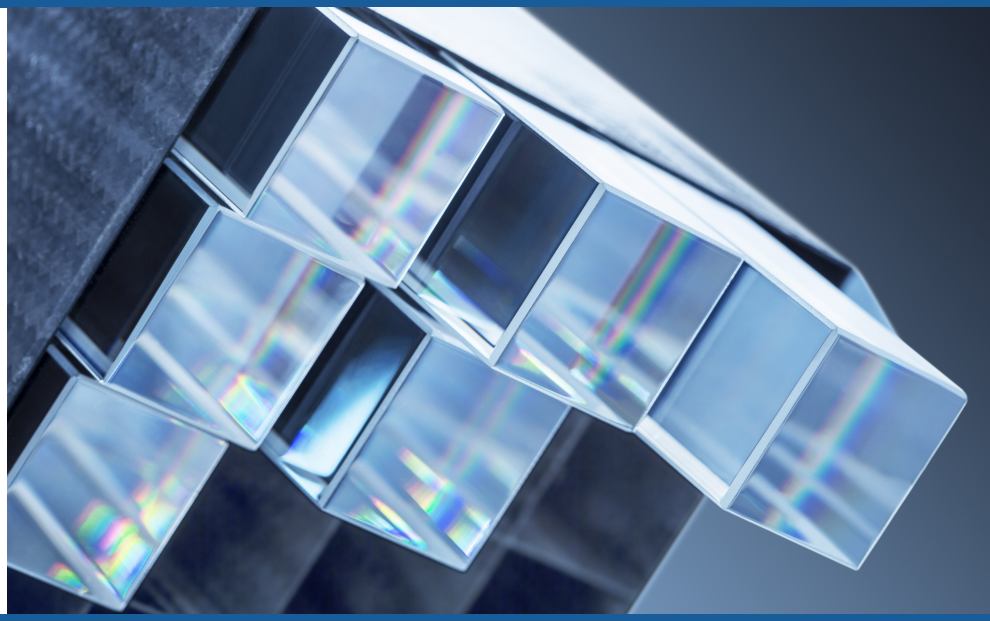

The picture shows a 4×4 carbon fibre reinforced polymer alveolus with lead tungstate crystals inserted. The interaction between these crystals and ionising particles produces light, the amount of which is proportional to the particle energy. The light is detected by avalanche photodiodes, where it is converted into charge. The charge is converted to an electrical signal.

Electromagnetic calorimeters are crucial detectors for nowadays high-energy experiments such as ATLAS [Mor19], CMS [Bii15] or $\bar{\text{P}}$ANDA (Chapter 1). They are dedicated to measuring the energy of charged particles and photons, which is necessary to reconstruct, e.g. lepton-pair and multi-photon channels.
The basic component of homogeneous calorimeters is always a luminescent material, which converts the energy of entering ionising particles into visible light. The amount of produced light is proportional to the energy absorbed by the medium through ionisation and atomic excitations. Typically, inorganic scintillators are used as active medium [KW16].
Depending on the application, a variety of scintillation materials can be considered. The material requirements for the $\bar{\text{P}}$ANDA calorimeter [TDR08] are, among others, high light yield and a short decay time of the scintillation light. Thus, a low energy threshold of 10 MeV and high event rates (500 kHz in the forward direction) can be achieved. The $\bar{\text{P}}$ANDA collaboration decided upon the material lead tungstate, which combines all desired characteristics.
In the context of this thesis, a modular Electromagnetic Calorimeter (EMC) was developed, which is based on lead tungstate. The main application of this EMC will be the backward electromagnetic calorimeter (Figure 1.2) of the upcoming $\bar{\text{P}}$ANDA experiment. Nonetheless, the modularity of the design and the performance of its components makes its usage for a measurement of the pion electromagnetic TFF at MAMI possible (Chapter 2). While writing this thesis, a modified version of the $\bar{\text{P}}$ANDA backward calorimeter is under construction.
In the following, the fundamental properties of homogenous electromagnetic calorimeters will be discussed. In Section 3.2, the components of the $\bar{\text{P}}$ANDA backward EMC will be presented by pointing out the modularisation approach. Finally, the calorimeter prototype will be introduced, which is the essential component in all laboratory and beam tests, which are presented in this work.

3.1 Homogeneous Electromagnetic Calorimeters

Homogeneous calorimeters deposit the energy of entering ionising particles within an active medium by an electromagnetic shower. The active medium converts the accumulated energy into detectable light by a scintillation process. Subsequently, the light is converted into charge by a photodetector. In this section, the phenomenon of electromagnetic showers, the scintillation process and the photodetection will be explained using components of the $\bar{\text{P}}$ANDA calorimeter. Finally, key properties such as relative energy resolution and spatial resolution will be addressed.

3.1.1 Electromagnetic Showers

Depending on the initial energy of the particle, the interaction with the scintillation material is not necessarily limited to one detector channel, which is one lead tungstate crystal equipped with two photosensors in the case of the $\bar{\text{P}}$ANDA EMC. On the contrary, the initial particle is converted into an electromagnetic shower, which has a lateral and a longitudinal extension. Thus, in general, the energy of a primary particle is distributed over several detector channels. The fundamental processes in electromagnetic showers are bremsstrahlung and pair production.

bremsstrahlung occurs whenever a charged particle is decelerated in the Coulomb field of a nucleus, while pair production corresponds to the conversion of a photon into an electron-positron pair.

Consequently, an electromagnetic shower is an alternating process between photons and electrons within a medium. In an electromagnetic calorimeter, a high conversion rate between photons and electrons/positrons is desired to deposit as much energy as possible within a small volume by multiply interactions with the crystal nuclei. Since the cross section for both bremsstrahlung and pair production is proportional to the square of the atomic number of the medium ($\sigma \propto Z^2$) [KW16], a high Z material is preferred for an electromagnetic calorimeter.

During the interplay between bremsstrahlung and pair production, the initial particle energy is more and more distributed to secondary particles. Thus, the energy per secondary particle decreases at every conversion generation. Since the cross section for pair production and bremsstrahlung are both proportional to the energy, the probability for these processes lower as the shower progresses. Consequently, ionisation becomes more and more dominant.

At the critical energy E_c, the energy loss driven by bremsstrahlung equals the energy loss driven by ionisation. The critical energy for the $\bar{\text{P}}$ANDA EMC scintillator material lead tungstate ($PbWO_4$) is $E_c(PbWO_4) = 9.64\,\text{MeV}$ [N$^+$18]. In Figure 3.1 the energy loss as a function of the particle energy (stopping power) for lead tungstate is shown.

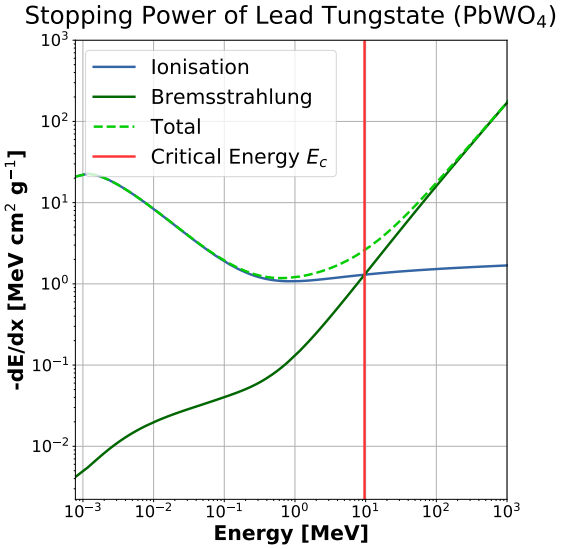

Figure 3.1: The plot shows the energy loss per distance as a function of the electron energy for lead tungstate. Ionisation is the dominant process for low energies (<10 MeV), while bremsstrahlung dominates at high energies (>10 MeV). The intersection between ionisation and bremsstrahlung defines the critical energy (E_c). The critical energy is important for the calculation of shower properties such as the Molière-Radius. The data for the plot was generated by using the software ESTAR [NT19b].

The electromagnetic shower development depends on the material. Good knowledge of both the longitudinal and the transversal spread distribution is important for the construction of a calorimeter. In the early days of particle detector physics, only empirical models and formulas were available. Nowadays, such empirical formulas are not needed anymore. Thanks to the progress in computer technology, particle interactions with matter can be simulated fast and very precisely. In the context of particle physics, the Geant4 toolkit for the simulation of the passage of particles through matter plays a vital role [CER19]. In Figure 3.2 an example of a Geant4 simulation of an electron hitting the EMC prototype (Section 3.3) is depicted.

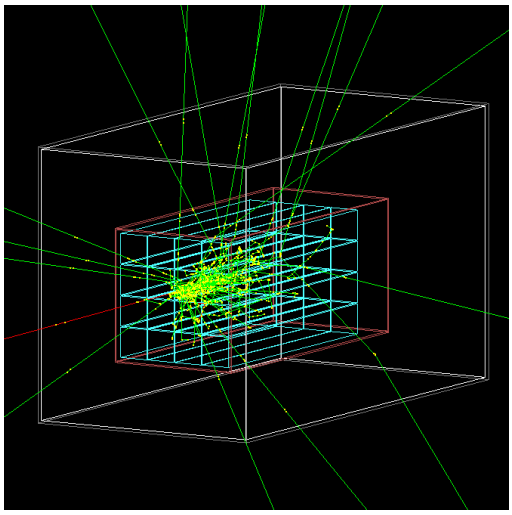

Figure 3.2: The visualisation of a Geant4 simulation shows the shower development of an electron with an energy of 855 MeV hitting the EMC prototype. The prototype consists of a 4×4 lead tungstate crystal matrix (here blue) and other material such as a copper cooling shell (red) and an aluminium cover (white) (Section 3.3). The green lines are trajectories of secondary particles. The highest density of green lines is within the crystal volume. Such simulations are crucial for both the construction of the EMC and the interpretation of beam data (Chapter 6).

Although simulations are the standard tool in detector physics, one important parameter for the transversal shower profile has to be mentioned. The Molière-Radius is defined

as:

$$R_M = \frac{E_s}{E_c} \cdot X_0, \tag{3.1}$$

whereby $E_s = 21.2\,\text{MeV}$ [KW16] and X_0 is the radiation length in which a particle has lost in average $1/e$ of its initial energy E_0. About 90 % of E_0 is deposited within a cylinder, which surrounds the shower axis with the radius R_M. The emission angle Θ in bremsstrahlung and pair production depends on the energy of the secondary particle:

$$\Theta \propto \frac{1}{\gamma} = \frac{m_e}{E}, \tag{3.2}$$

where γ is the Lorentz factor, m_e the electron mass and E the energy of the secondary particle [KW16]. Consequently, the transversal shower profile becomes wider as the shower progresses.

3.1.2 The Inorganic Scintillation Material Lead Tungstate

The choice of the scintillation material depends on parameters such as radiation length (X_0), light yield (LY), decay time and radiation hardness. The starting point for the $\bar{\text{P}}$ANDA electromagnetic calorimeter (EMC) was the need for a very dense material to achieve a compact setup. Furthermore, the material should handle high event rates and thus have a short decay time of the scintillation light. Due to the high radiation environment, the material needs to be as radiation-hard as possible. Finally, the light yield has to be as high as possible to achieve a sufficient energy resolution at all energies.
The chosen material was a compromise of the requirements. For instance, the need for a compact (dense) calorimeter limits the search to inorganic materials. On the other hand, inorganic materials have typically low decay times of the order of hundreds of nanoseconds. Nonetheless, the material lead tungstate $PbWO_4$ fits most of the requirements. Furthermore, there were many experiences gained by the electromagnetic calorimeters of CMS [Bii15], which uses optimised $PbWO_4$ crystals (PWO).
However, further optimisation of PWO was necessary because of its poor light yield. PWO at $-25\,°\text{C}$ only produces 0.8 % of the NaI(Tl) light yield[1] ([TDR08], table 4.1), which is too less to achieve the required particle threshold of $E_{\text{thrs.}} = 10\,\text{MeV}$ at $\bar{\text{P}}$ANDA.
The $\bar{\text{P}}$ANDA collaboration achieved a significant improvement of PWO through the enhancement of the structural perfection of the crystals and the optimisation of the doping composition. PWO-II at $-25\,°\text{C}$ has a light yield of 2.5 % of NaI(Tl) . Besides light yield, also the radiation hardness and the decay time were improved. A detailed treatise on the optimisation procedure can be found in the EMC TDR ([TDR08] 42 ff.). In Table 3.1 the most important parameters of PWO-II are listed.

[1] The generally accepted reference for inorganic scintillators is NaI(Tl). It generates 43000 photons per MeV. However, due to its slow decay time of 245 ns, NaI(Tl) is not suitable for fast calorimeters. ([KW16], table 13.3)

Parameter	Value	Unit
ρ	8.28	g/cm^3
X_0	0.89	cm
R_M	1.96	cm
E_c	9.64	MeV
τ_{decay}	6.5	ns
Scinti. Light λ_{max}	420	nm
Refractive Index $n(\lambda_{\text{max}})$	2.17	-
Relative Light Yield (LY)	2.5 ($-25\,°C$)	% (LY NaI(Tl))
Hygroscopic	no	-
dLY/dT	-3.0	%/°C
dE/dx (MIP)	10.2	$\text{MeV}\,\text{cm}^{-1}$

Table 3.1: The table shows the properties of PWO-II. It is very attractive for compact calorimeters since it has a high density ρ, a short radiation length X_0 and a small Molière radius R_M. The decay time τ_{decay} is unusually short for an inorganic scintillator. By cooling PWO-II to $-25\,°C$, its light yield improves by the factor 4.2 compared to room temperature. [TDR08][N$^+$18]

For comparison, the PWO-II crystals for the $\bar{\text{P}}$ANDA backward EMC are squared-shaped with a width of 2.47 cm and a length of 20 cm. Thus, they have more than 22 radiation lengths. Furthermore, the crystals are organised in clusters. For instance a 3×3 matrix has a width of 7.51 cm including a gap of 0.5 mm between the crystals. Thus, it covers almost a cylinder of two Molière-Radii ($d_{\text{cyl.}}$=7.82 cm).

The Scintillation Mechanism of Lead Tungstate

The scintillation mechanism of inorganic scintillators has its origin in the crystal lattice and the electronic band structure. The periodic structure of the crystal affects the energy levels of the crystal atoms. The complex deformation of the energy levels can be simplified with the help of the band model. In a first approximation, there is the valence band and the conduction band. The conduction band lies energetically higher than the valence band. The bands are separated from each other by an energy gap (E_g). Typical energy gaps of inorganic scintillators are between 4 eV and 12 eV [KW16].
Electrons can be excited from the valence band into the conduction band whenever the energy of an entering ionising particle exceeds the energy gap. Correspondingly, holes arise in the valence band due to the loss of electrons.
Luminescence of visible light is only possible if the crystal has luminescence centres with a smaller bandgap than E_g. Otherwise, possible scintillation light would again be absorbed. Luminescence centre can occur by the interaction of the incoming ionising radiation with crystal (an)ions and lattice defects (intrinsic luminescence). Alternatively, a luminescence centre can be induced by doping the crystal with other elements (extrinsic luminescence). In the case of $PbWO_4$, intrinsic luminescence caused

by the anion complex WO_4^{2-} [L+95] produces blue scintillation light (∼420 nm).

The potential curves for a luminescence centre are depicted in Figure 3.3. The illustration shows both the ground state and the excited state potential as a function of the lattice coordinate. Due to the solid-state environment of the luminescence centre, the potentials are shifted against each other. As a result, the excitation distance A-C differs from the optical transition B-D (Stokes-Shift).

A thermal de-excitation causes energy change between C and B. The electron can also reach point F by a further thermal excitation and drop down into the ground state A by thermal de-excitation (quenching). Cooling of the scintillator reduces quenching and thus increases the light yield. This effect is used for the $\bar{P}$ANDA EMC, which is operated at a temperature of −25 °C.

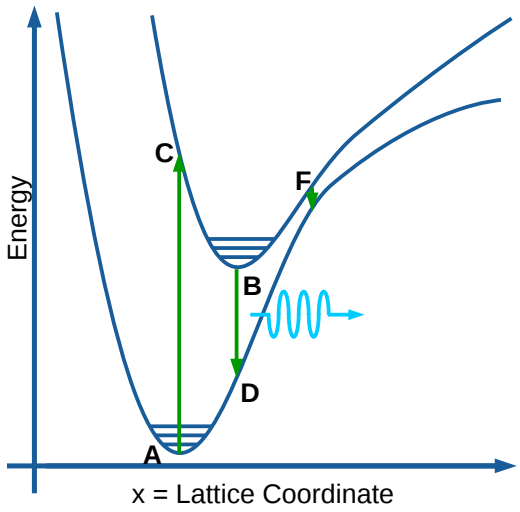

Figure 3.3: The illustration shows the potential curves of a luminescence centre as a function of the lattice coordinate. The ground state curve is shifted against the excitation curve due to the solid-state environment. Thus, the excitation path A-C has another corresponding wavelength than the optical transition path B-D. Due to thermal excitation within the excitation potential, the electron can reach point F, where both bands are close to each other. A thermal non-radiative de-excitation (quenching) can occur. Cooling of the scintillator reduces quenching. [Bir64]

Quenching Losses in Lead Tungstate

Quenching losses occur if electrons are trapped within trapping centres of the conductive band. The trapped electrons reduce the transmission of scintillation photons. Trapped electrons can drop into the valence band non-radiatively by thermal de-excitation. The cooling of the scintillation material, which improves the light yield (Figure 3.3) is counterproductive for the clearing of the trapping centres. Thus, the $PbWO_4$ crystals become less light transmissive over time in a radiative environment. A significant recovery under low temperatures (−25 °C) can not be observed ([TDR08] 52 f.). However, heating the calorimeter to clear the trapping centres is not viable, since it implies time-consuming data taking brakes. The more suitable solution is stimulated recovery. The crystal is illuminated by light, which clears the traps. In the case of $PbWO_4$ a stimulated recovery using blue light (420 nm) gives the best result [VDR09]. In Figure 3.4, a simplified model of the processes within the scintillator is depicted.

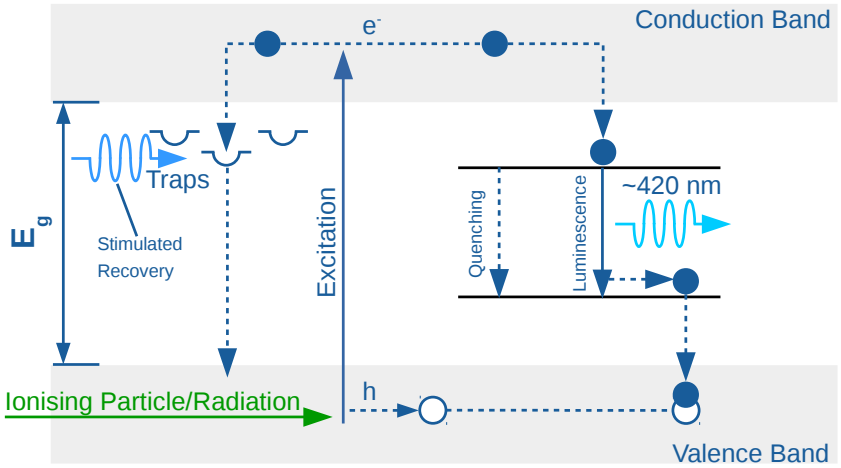

Figure 3.4: The illustration shows a simplified model of the luminescence process within the $PbWO_4$ scintillator. Ionising particles excite electrons from the valence band into the conduction band. At the same time holes occur within the valence band. The electrons can recombine with the holes in several ways. The desired way is recombination by using a luminescence centre and by emitting scintillation light. Nonetheless, non-radiative recombination is possible using a quenching centre. By cooling the scintillator, the probability of quenching is reduced. On the other hand, cooling decreases the probability of spontaneous recovering of trapped electrons within trapping centres. However, a stimulated recovery can be achieved by irradiating the crystal with blue light (420 nm). [KW16][Bir64][TDR08]

3.1.3 Photon Detection by Avalanche Photodiodes

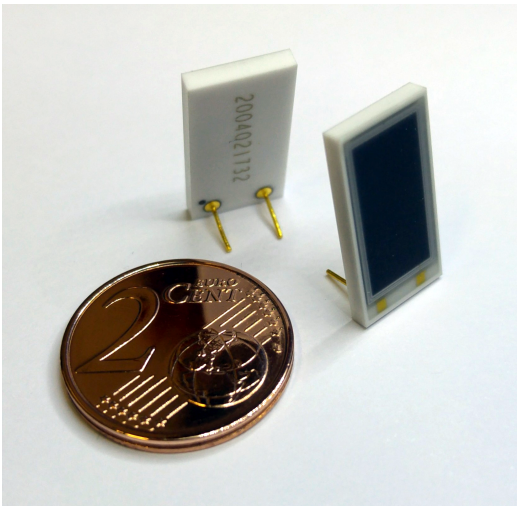

Figure 3.5: The photograph shows two S11048(X2) APDs from HAMAMATSU, which are used for the detection of scintillation photons. The active area is 14 mm × 6.8 mm (black area). The quantum efficiency is 70% for photons with a wavelength of 420 nm. Typical breakdown voltages are in the range of 375 V to 390 V. A proper characterisation is mandatory to operate the APD at the demanded gain and at a good working point. A table with all relevant specifications can be found under [HAM09].

Once the deposited energy is converted into photons, the photons need to be converted into charge to eventually generate an electrical signal, which is proportional to the deposited energy. For the $\bar{\text{P}}$ANDA EMC, this is done by Avalanche Photodiodes (APDs). Avalanche Photo Diodes (APDs) have appealing properties for electromagnetic calorimeters. They are mechanically robust devices with an intrinsic amplification. APDs are insensitive to magnetic fields [MMR+00]. Thus, they are usable in a magnetic environment. In Figure 3.5 two APDs of the type S11048(X2) from HAMAMATSU [HAM09], which are used for the $\bar{\text{P}}$ANDA EMC, are shown.

The Intrinsic Amplification of APDs

The avalanche effect within a high electric field zone is the origin of the intrinsic amplification of APDs. In contrast to a conventional p-n photodiode, an avalanche photodiode has an additional highly doped p^+-n^+ junction with a strong electric field at the boundary layer. In Figure 3.6 both the layer configuration of a typical APD and the electric field strength are depicted. The red (blue) color at the n^+ (p^+) layer indicates the positive (negative) charge density due to the diffusion from the p^+ (n^+) layer.

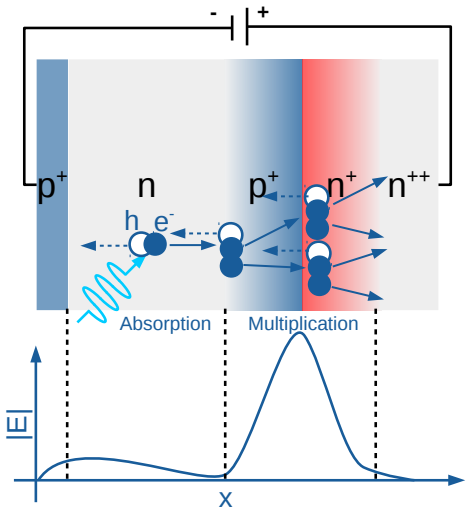

Figure 3.6: The illustration shows the layer configuration of a typical APD. The depleted n region absorbs incident photons by generating signal electrons. Due to the high voltage applied in blocking direction, the signal electrons drift into the high field region (p^+n^+). It comes to multiplication by the avalanche effect. Accelerated electrons generate secondary electrons, which themselves make further electrons. The charge on the readout electrode (n^{++}) can be converted into a signal by using a charge sensitive preamplifier.[KW16]

The detection of an incident photon begins with its absorption within the weakly doped and depleted n layer (space-charge region) by emitting a signal electron. Due to a reverse bias voltage, the electron drifts into the high field region. Within the high field region, the electron is accelerated and generates secondary electrons, which create further electrons. At the readout electrode, the charge can be collected and converted into an electrical signal by using a charge sensitive preamplifier (Subsection 3.2.2).

The APD Gain

By increasing the voltage, the holes within the p^+ layer are more and more attracted towards the negative pole and the electrons within the n^+ layer are more attracted towards the positive pole. Consequently, the barrier layer increases, which gives more space for the multiplication of signal electrons.

Depending on the applied voltage, APDs can be operated in the linear mode and the Geiger mode. For homogeneous calorimeters, only the linear mode is relevant, since the output charge of the APD has to be proportional to the number of produced photoelectrons and thus to the deposited energy. Typical APD amplifications (M) within the linear mode are in the order of 10^1 to 10^3.

For an application such as single-photon detection, APDs can be operated slightly above the nominal breakdown voltage, which is the Geiger mode. Thus, amplification factors of more than 10^5 are possible. Whenever the minimum amount of photons appears, the APD breaks down. Consequently, the output is not anymore proportional to the number of input photons. Special applications of APDs operating in the Geiger mode are Silicon Photomultipliers (SiPM). With an array of many APDs, they combine the high gain of photomultipliers with the advantages of semiconductors.

In Figure 3.7, the gain dependency from the bias voltage for a S11048(X2) APD is shown. The data were taken with the EMC prototype (Section 3.3) by performing a measurement using a pulsed light source (Appendix D).

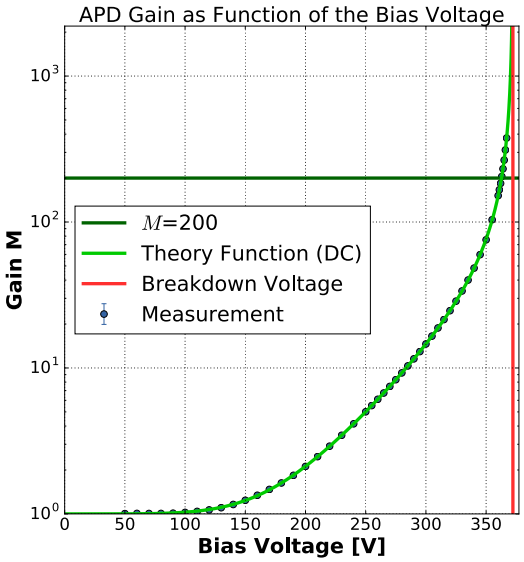

Figure 3.7: The plot shows the measured gain characteristics of an S11048(X2) APD at $-25\,°C$. The dark green line indicates a typical operating gain of $M = 200$. The measurement was performed by using the EMC prototype (Section 3.3). A proper APD characterisation is mandatory to operate the detector at a reliable operating point. In Appendix D a technique for a precise APD characterisation using a pulsed light source is presented.

Besides the bias voltage dependency, the operating temperature also has an impact on the APD gain. Different effects within the APD lead to an increase in gain of $2.2\,\%/°C$ by lowering the temperature. The number corresponds to a typical S11048(X2) APD, which operates at a gain of $M = 50$ [TDR08]. Consequently, APDs benefit from the cooling of the EMC.

The APD Signal to Noise Ratio

The signal to noise ratio of an APD is limited by the so-called shot noise. Shot noise happens when charged particles, which build as a whole a current, have to pass one by one a potential barrier. By increasing the bias voltage, the signal to noise ratio improves.
Due to an additional shot noise contribution driven by the avalanche effect (excess noise), the improvement of the signal to noise ratio is limited. Above a specific voltage, the signal to noise ratio starts to decrease again.
Laboratory measurements and several beam tests with the EMC prototype (Section 6.2) have shown that S11048(X2) APDs work stably at gains around $M = 200$. Moreover, a simulation framework was developed in this thesis (Chapter 5) to investigate the calorimeter performance as a function of different external parameters. One of these external parameters is the APD gain. The simulations show that the $\bar{\text{P}}$ANDA TDR requirements are met with an APD gain of $M = 200$.

3.1.4 The Relative Energy Resolution

The energy resolution is the essential characteristic of a calorimeter. It describes the minimum energy difference σ_E, at which another energy still can be distinguished from a first energy E. The quotient between energy difference and energy σ_E/E is the relative energy resolution.
The measurement of particle energies is a stochastic process. The shower particles in the active medium are eventually converted into N_S photoelectrons, which follow the Poisson distribution with the mean value $\langle N_S \rangle$ and the standard deviation $\sqrt{\langle N_S \rangle}$. Since the energy is proportional to the number of photoelectrons, $E \propto N_S$, it follows:

$$\frac{\sigma_E}{E} \propto \frac{\sqrt{N_S}}{N_S} = \frac{1}{\sqrt{N_S}} \propto \frac{1}{\sqrt{E}} \tag{3.3}$$

Besides the stochastic $1/\sqrt{E}$-contribution, also other factors play a role for the relative energy resolution. On the one hand, there is the electronic noise contribution, which describes the accumulated noise of the full readout chain. Since the noise level is constant, its contribution drops hyperbolically with the energy ($\propto 1/E$). On the other hand, there are mechanical and electronic irregularities and miscalibrations, which are summarised by a constant contribution to the energy resolution. With all these components, the energy resolution can be written as:

$$\frac{\sigma_E}{E} = \underbrace{a}_{\text{constant}} \oplus \underbrace{\frac{b}{\sqrt{E}}}_{\text{stochastic}} \oplus \underbrace{\frac{c}{E}}_{\text{noise}} = \sqrt{a^2 + \frac{b^2}{E} + \frac{c^2}{E^2}} \tag{3.4}$$

The $\bar{\text{P}}$ANDA EMC technical design report [TDR08] demands an energy resolution of:

$$\frac{\sigma_E}{E} \leq 1\,\% \oplus \frac{\leq 2\,\%}{\sqrt{E[\text{GeV}]}} \oplus \frac{\leq 3\,\text{MeV}}{E} \tag{3.5}$$

Therefore, the energy resolution is an important quantity to be measured in all detector test beams at MAMI. In Section 6.2 the achieved results with the EMC prototype will be discussed.

3.1.5 The Time Resolution

The $\bar{\text{P}}$ANDA EMC will operate in a so-called trigger-less mode, which means that every detector cell identifies events individually. Consequently, the later event-building depends on a precise timestamp determination. The measure for the time resolution is the RMS-value of differences between a theoretical (true) timestamp and measured timestamps.

The $\bar{\text{P}}$ANDA calorimeter TDR ([TDR08]) requires a time resolution of better than 1 ns for deposited energies higher than 60 MeV and better than 150 ps for deposited energies higher than 500 MeV.

The timestamp determination depends on the full readout chain, which includes the response of the preamplifier (Subsection 3.2.2) and the transmission of the analogue signal (Subsection 3.2.3) to the digitisation. The difficulty is to identify a characteristic feature within the signal pulse, even under noisy conditions. In the context of this thesis, digital signal processing algorithms (Section 4.4) were developed and implemented on Field Programmable Gate Arrays (FPGA) to achieve the time resolution requirements for the EMC. In Section 5.1 the capability of the parameter extraction algorithms are discussed.

3.1.6 The Spatial Resolution

The primary purpose of calorimeters is to measure particle energies. However, due to the granularity of the $\bar{\text{P}}$ANDA electromagnetic calorimeter, it can also determine the entrance position of particles with a spatial resolution in the order of a few millimetres. This is possible because electromagnetic showers spread over several detector cells. An optimisation of the position reconstruction of the EMC by using neuronal networks is currently under investigation [WolXX].

3.2 The Backward Electromagnetic Calorimeter of the $\bar{\text{P}}$ANDA Experiment

In the following, the components of the $\bar{\text{P}}$ANDA backward electromagnetic calorimeter will be explained. The components for the $\bar{\text{P}}$ANDA backward EMC will also find usage at the FAIR Phase-0 EMC. Consequently, the section will be finalised with the discussion of both the $\bar{\text{P}}$ANDA backward calorimeter layout and the FAIR Phase-0 layout.

3.2.1 The Single Crystal Unit

A single crystal unit contains one lead tungstate crystal with the dimensions of 24.7 mm × 24.7 mm × 200 mm, two avalanche photodiodes (Subsection 3.1.3), an Application-Specific Integrated Circuit (ASIC) based preamplifier, mounting supports, a shielding capsule for the electronics and a reflective foil, which surrounds the crystal. In Figure 3.8 an exploded view of a single crystal unit is depicted.

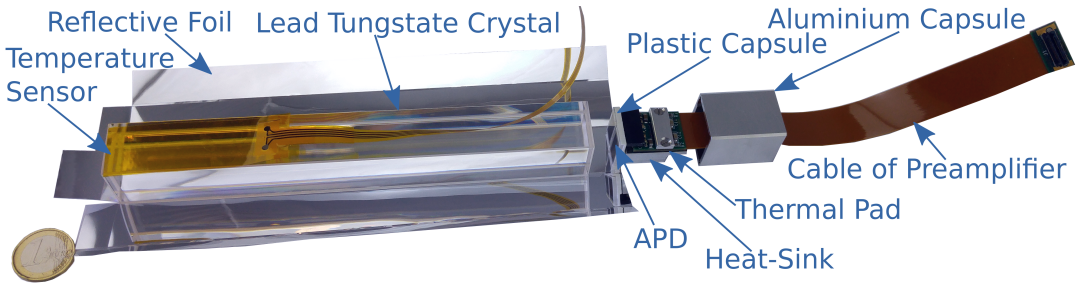

Figure 3.8: The photograph shows an exploded view of a single crystal unit. The avalanche photodiodes are attached to the end surface of the lead tungstate crystal by an optical glue. A 3D-printed plastic capsule defines the APDs positions. The plastic capsule is attached to the aluminium heat-sink, which carries away the heat from the preamplifier. The preamplifier is connected to the two APDs via connector pins and to the heat-sink via a thermal pad. The aluminium capsule houses all of these components, which are placed at the end of the crystal. The cable of the preamplifier is guided through an opening at the back of the aluminium capsule. An optical fibre connector is slid from the back into the aluminium capsule (not shown on the picture). The fibre connector ends precisely between the two APDs. All mechanical parts are screwed together. The crystal is wrapped with a reflective foil, which also encloses the front part of the aluminium capsule. Finally, some of the crystal units are equipped with a flat thermal sensor, which is fixed with adhesive tape on the outer side of the reflective foil (on the picture it is lying on the crystal for the sake of clarity).

The two APDs are held by a 3D-printed plastic capsule and attached to the crystal by an optical glue (Dow Corning® 3145 RTV). The plastic capsule is connected to the heat-sink, which also holds the preamplifier. Between preamplifier and heat-sink, a thermal pad (Bergquist® gap pad TGP 1500) ensures the thermal coupling. The pins of the APDs are connected to the input of the preamplifier. An aluminium capsule encloses all components but the crystal. In this way, the preamplifier is electromagnetically shielded.
The cable of the preamplifier is guided through an opening at the back of the aluminium capsule. An optical connector, which has four 200 μm quartz glass fibres in it, is inserted from the aluminium capsule backside and terminates between the APDs. The optical fibre connector is used for coupling test light pulses into the crystal.
The crystal is wrapped with a reflective foil (3M™ Specular Film DF2000MA), which

also slightly slips over the front part of the aluminium capsule. Some of the single-crystal units are equipped with flat ($\sim 0.2\,\mathrm{mm}$) PT100 temperature sensors [Nol14].

3.2.2 The Application-Specific Integrated Circuit Preamplifier

ASIC for P̄ANDA Front-End Electronics (APFEL) is a preamplifier for integrating the charge pulses produced by the APD. It was developed at the GSI Helmholtzzentrum in Darmstadt [Wie09] [FW11].

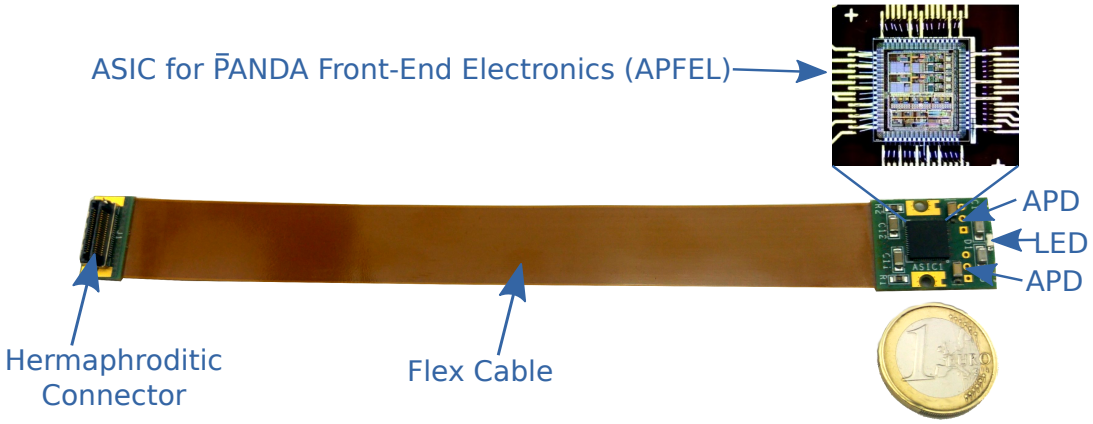

Figure 3.9: The photograph shows the ASIC for P̄ANDA Front-End Electronics (APFEL) and its PCB. The APFEL circuit operates two APDs. For each APD, the circuit provides a charge sensitive preamplifier and a shaper. There are two amplification gains (low gain and high gain) to cover the dynamic range of the calorimeter.

The APFEL has its target range of operation within the P̄ANDA EMC barrel and the backward EMC. Every single crystal unit is equipped with one APFEL chip.
The integrated circuit consists of two analouge readouts for two APDs. For every APD the circuit provides a charge sensitive preamplifier, a shaper and a differential output driver. To cover the expected dynamic energy range from 10 MeV to 7.3 GeV for the barrel part and the backward part of the P̄ANDA EMC ([TDR08]), the APFEL circuit provides two amplification gains. Thus, two differential outputs for every APD are available. In the following chapters, the two amplifications are called "Low Gain" (LG) and "High Gain" (HG). The ratio between the LG and the HG amplification is about 10.5.
The APFEL provides a programming line to set the baseline offset for every readout channel ($2 \times$ APD $\times$ (LG + HG)). In doing so, the signal can be moved inside the voltage input range of the following electronics.
The integrated circuit is packaged in a housing. The housing is soldered on the surface of a flexible Printed Circuit Board (PCB). On this board also a LED is located, which provides the light for the stimulated recovery (Subsection 3.1.2) of the crystal.
In the context of this thesis, a hardware based digital parameter extraction for APFEL

output signals was developed. Besides the description of the algorithms and implementation methods, also plenty of example APFEL pulse shapes can be found in Section 4.4.

3.2.3 The Distribution Boards

The distribution boards of the backward EMC drive the analogue signals from the preamplifier to Analogue to Digital Converters (ADCs, Subsection 4.1.1). Furthermore, they provide the communication with the APFEL chips, distribute the bias voltage to the APDs and give connections to the temperature sensors. For all these purposes, different PCBs were developed in collaboration with the electronics department of the Institute of Nuclear Physics in Mainz. There are three PCBs. Two of them are located close to the detector crystals and one is connected to the ADC.

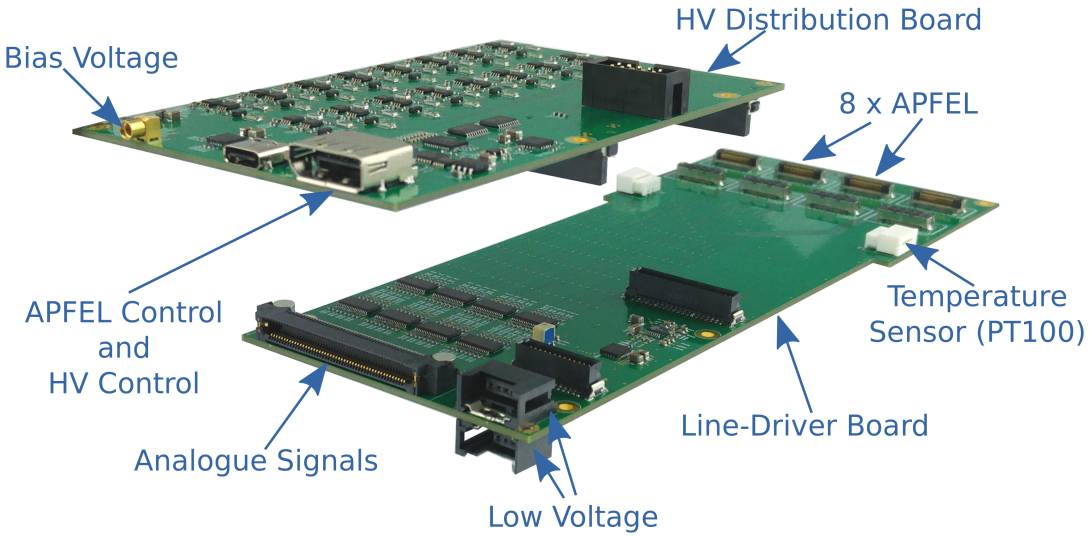

Figure 3.10: The photograph shows the line-driver board and the HV distribution board of the backward EMC front-end electronics. For reasons of clarity, the boards are disconnected on the picture. The line-driver board has eight hermaphroditic connectors for eight APFEL preamplifiers. Operational amplifiers boost the analogue signals from the preamplifiers. In addition to the preamplifier connectors, the line-driver board provides two connectors for two PT100 temperature sensors. On the other end of the line-driver board, a flat output connector for the analogue signals is located. The power connection is next to the signal connector. The HV distribution board is connected to the line-driver board and has three functions. Firstly, it provides a high voltage splitter circuit, which supplies 16 APDs with individual bias voltages. Secondly, it allows the communication and the programming of the APFEL chips. The APFEL preamplifier communication and the high voltage control are connected over separate busses but through the same cable. Thirdly, the board provides the connector for the temperature sensors.

The PCBs on the detector side are divided into a line-driver board and a HV distribution board. The HV distribution board is plugged on the top of the line-driver board (Figure 3.10). The line-driver board amplifies the analogue signals from eight APFEL preamplifiers to transmit them to the ADC. The HV distribution board is attached to the line-driver PCB and provides the bias voltage for 16 APDs, the APFEL preamplifier control and the temperature readout. The bias voltages for the APDs can be set individually.

The PCB on the ADC side is an adapter board (Figure 3.11), which connects the analogue signal cables with the entrance of the ADC. Furthermore, the adapter board offers the interface for the APFEL preamplifier programming and the bias voltage programming. The analogue detector signals are digitised and processed by the PANDA sampling ADC (SADC) board. In the context of this thesis, firmware for the sampling ADC board was developed (Chapter 4).

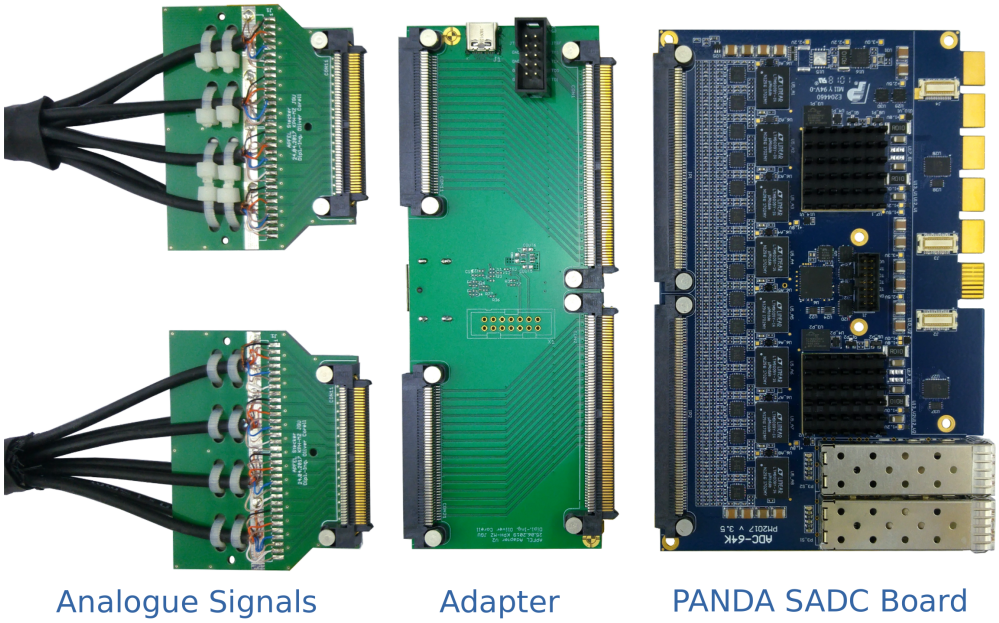

Figure 3.11: The photograph shows the adapter board of the front-end electronics with the entering signal cables and PANDA sampling ADC (Subsection 4.1.1). One signal cable transmits the signals from one line-driver board (eight single-crystal channels). Besides the signal transmission, the adapter board also provides the programming interfaces for the APFEL preamplifiers and the bias voltage splitter circuits.

3.2.4 The Submodule

The single crystal units are arranged in submodules. Such a submodule consists of up to 16 single-crystal units and is held together by a carbon fibre reinforced polymer alveolus. The alveolus is designed to be a stiff self-supporting structure with high accuracy in its dimensions and a low tendency for deflections. A plastic stopper at the front of the alveolus prevents the crystal units from sliding out of the alveolus. An aluminium insert closes the alveolus from the backside. The flex cable from the APFEL preamplifiers and the temperature sensor cables are guided through the insert. Both plastic stopper and insert are glued to the alveolus by a two-component epoxy resin adhesive. A spring mechanism guarantees a defined contact pressure between insert and crystal units.

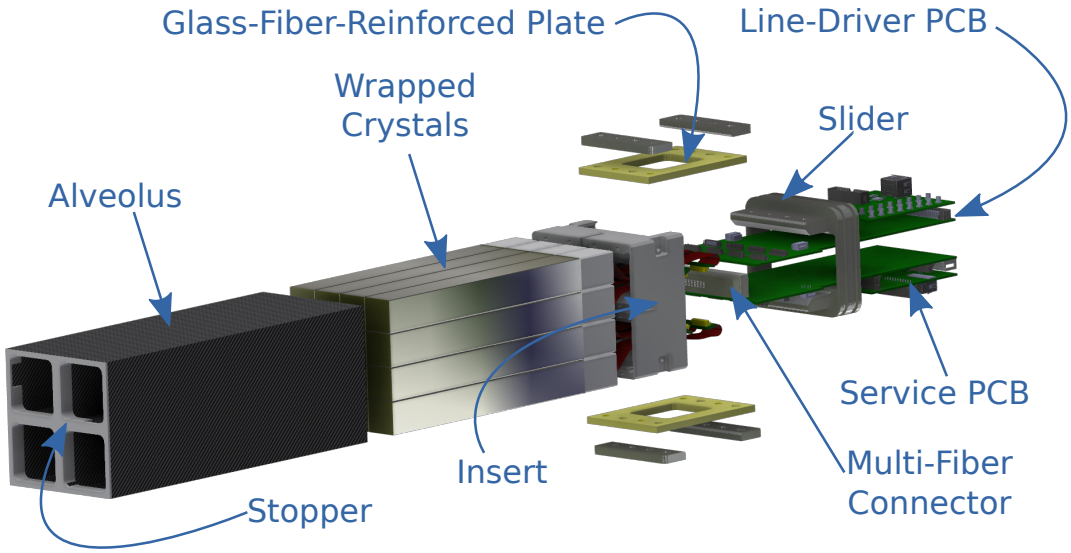

Figure 3.12: The exploded view shows a 4×4 submodule, which consists of 16 single crystal units. A carbon fibre-reinforced-polymer alveolus holds the crystal units together. A plastic stopper at the front and an aluminium insert at the rear side of the alveolus prevent the crystals from sliding. Two line-driver boards are glued back to back into an aluminium slider. The APFEL preamplifiers and the temperature sensors are connected with the line-driver boards. The optical fibres are led out by the multi-fibre connector. Finally, two glass-fibre-reinforced plates guarantee both the mechanical stability of the submodule and the thermal insulation between cold and warm detector volume.

The electronics part of the submodule is prepared separately. Two line-driver boards are slid back to back through the slit of an aluminium slider until a defined position. At their final position, the slider slit is filled with a light-tight epoxy resin adhesive. The alveolus unit and the electronics part are subsequently screwed together. The design was developed to connect the APFEL preamplifiers and the temperature sensor

cables conveniently with line-driver boards.
For every crystal unit, an aluminium optical connector is prepared, which contains four quarts fibres. The optical connectors are plugged into the aluminium capsules of the crystal units. The other side of the fibres culminates into a multi-fibre connector. The multi-fibre connector is plugged into the aluminium slider.
The mechanical connection between aluminium insert and slider is made by glass-fibre-reinforced plates which are screwed parallel to the line-driver boards. Besides the mechanical connection, the glass-fibre plates also ensure the thermal insulation between the cold and warm volume of the detector.
Besides the 4×4 submodule also other shapes were developed in order to approximate the hollow cylinder shape of the $\bar{\text{P}}$ANDA backward calorimeter. For the use at the FAIR Phase-0 experiment in Mainz, only 4×4 submodules will be used. In Figure 3.12 an exploded view of a 4×4 submodule is depicted. Furthermore, the different submodule versions for the $\bar{\text{P}}$ANDA backward EMC are depicted in Figure 3.13.

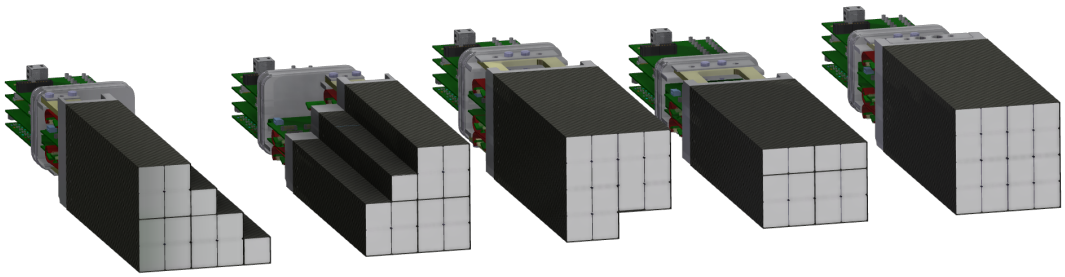

Figure 3.13: The computer-aided design shows the different submodule shapes, which are currently foreseen for the $\bar{\text{P}}$ANDA backward EMC. The different staircase shapes allow the hollow cylinder design of the $\bar{\text{P}}$ANDA backward EMC. For the FAIR Phase-0 experiment, only 4×4 submodules will be used.

3.2.5 Detector Layout for $\bar{\text{P}}$ANDA and FAIR Phase-0

The modular design of the EMC makes it possible to satisfy the boundary conditions of different experiments. For its usage as backward EMC at $\bar{\text{P}}$ANDA, the challenge is to fit as many crystals as possible into a small volume. The backward EMC will be assembled like a hollow cylinder. Inside its inner hole, it will enclose the support structure of the micro-vertex detector. The outer diameter will exactly fit inside the barrel part of the $\bar{\text{P}}$ANDA EMC (Figure 1.2).
For its usage at FAIR Phase-0, space limitation is not an issue. Quite the contrary, the design will include almost all available crystals to maximise the solid angle coverage. In addition, a round hollow cylinder shape is not necessary. Thus, the complexity can be reduced by only using 4×4 submodules. Although the mechanical design of the FAIR Phase-0 EMC will be easier than in $\bar{\text{P}}$ANDA, there are other challenges which

need to be addressed. For instance, at FAIR Phase-0, the EMC will operate in the forward direction. Thus, the EMC has to deal with much higher rates than in $\bar{\text{P}}$ANDA. In the following, the current layouts for both the $\bar{\text{P}}$ANDA backward EMC and the FAIR Phase-0 EMC are described in detail.

The $\bar{\text{P}}$ANDA Backward Electromagnetic Calorimeter Layout

The backward EMC as shown in Figure 3.14 will cover scattering angles from 140° to 170°. It consists of 524 lead tungstate crystals, which are organised in 36 submodules.

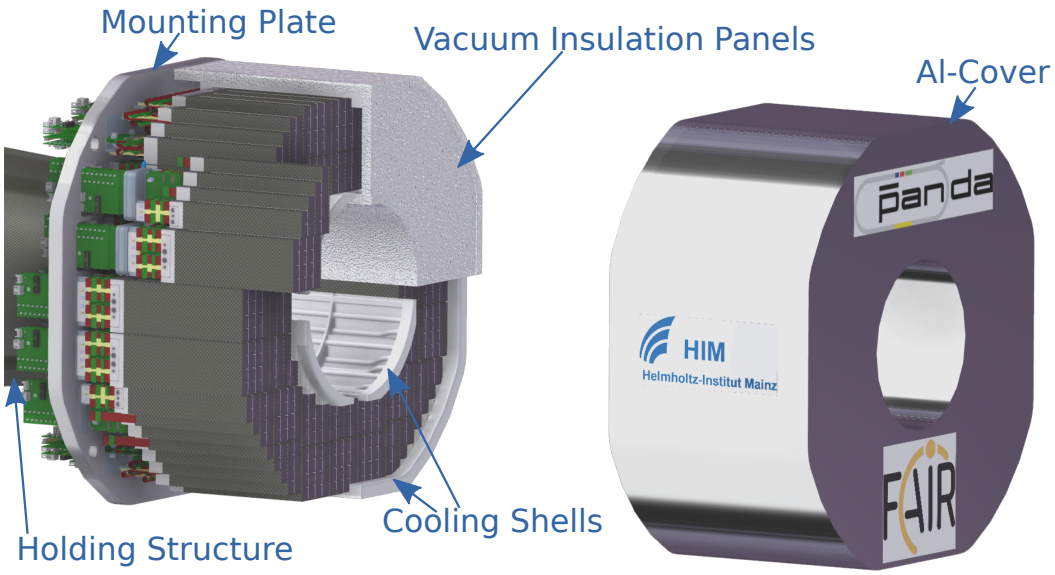

Figure 3.14: The exploded CAD drawing shows the design of the $\bar{\text{P}}$ANDA backward EMC, which will cover scattering angles from 140° to 170°. The design intends to have as many crystals as possible in a limited volume. The current design consists of 524 lead tungstate crystals distributed over 36 submodules. The resulting hollow cylinder is surrounded and lined by cooling shells and vacuum insulation panels. An aluminium cover encloses the detector volume. The outer and inner diameter are 884 mm and 322 mm, respectively.

The hollow cylinder shape of the $\bar{\text{P}}$ANDA backward calorimeter is achived, by utilising all available submodule shapes (Figure 3.13). The submodules are attached to a mounting plate. An aluminium cooling shell surrounds the resulting crystal ring. The front of the detector does not have an active cooling to reduce the dead material budget. Vacuum insulation panels encase the whole detector volume from the mounting plate surface up to the front of the submodules. The mounting plate is thermally decoupled by the glass-fibre-reinforced plates of the submodules (Figure 3.12). Finally, an aluminium cover encloses the whole detector. Thus, the detector volume can be

flooded with nitrogen gas to avoid ice formation from the air humidity. The complete backward calorimeter has an outer diameter of 884 mm, an inner diameter of 322 mm and a depth of 580 mm including the outer part of the electronics. A shielding box will house the electronics .
A movable holding structure holds the backward calorimeter. The holding structure has an extension arm with a length of 1150 mm and has to carry the weight of the calorimeter (approximately 0.7 t). Consequently, also the resulting torque due to the high leverage has to be considered. The holding structure is screwed via a tripod on precision rails. Both the rails and the tripod will ensure a precise fitting of the EMC into the $\bar{\text{P}}$ANDA detector (Figure 1.2). In Figure 3.15 the $\bar{\text{P}}$ANDA backward EMC on its holding structure is shown.

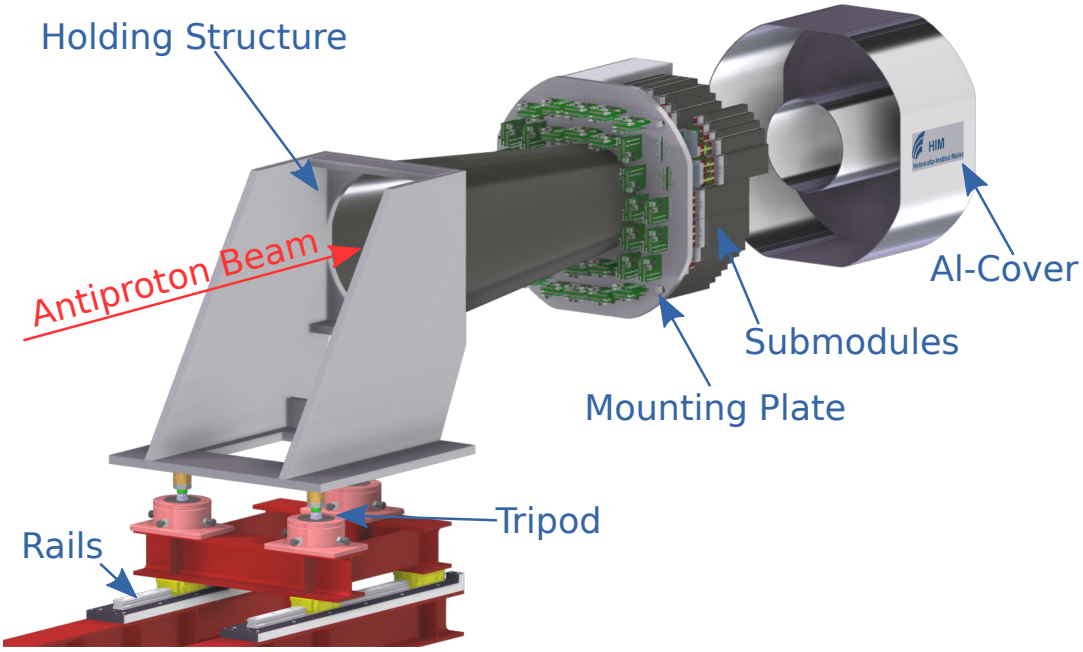

Figure 3.15: The exploded CAD drawing shows the $\bar{\text{P}}$ANDA backward EMC on its holding structure. The holding structure has to handle both the weight of the calorimeter (∼0.7 t) and the torque due to the extension arm. A tripod helps to fit the backward EMC precisely into the $\bar{\text{P}}$ANDA detector. The whole setup is mounted on rails to slide the backward EMC in and out of the $\bar{\text{P}}$ANDA spectrometer. The beam pipe of the antiproton beam goes through the centre of both the extension arm and the backward calorimeter.

The FAIR Phase-0 Electromagnetic Calorimeter Layout

The layout of the FAIR Phase-0 calorimeter is similar to the backward EMC design. However, at Phase-0, there is no need for a round hollow cylinder shape of the detector.

Thus, the design is simplified by using only 4×4 submodules. The current layout has 48 submodules, which can hold up to 768 lead tungstate crystals. Since there are only 700 crystals available, the outer submodules will not be completely filled with crystals. The calorimeter will be symmetrically filled beginning from the inner part. A possible symmetrical filling intends to use 640 crystals. The empty crystal places will be filled with aluminium dummies to ensure a good thermal coupling on the outer cooling shell. The width of the FAIR Phase-0 calorimeter is 930 mm, the inner diameter has a width across flats of 165 mm, and the full depth including electronics is 555 mm. The Phase-0 EMC will be mounted on a stable structure, which is not yet designed. In Figure 3.16 and in Section A.1 the current detector design is depicted.

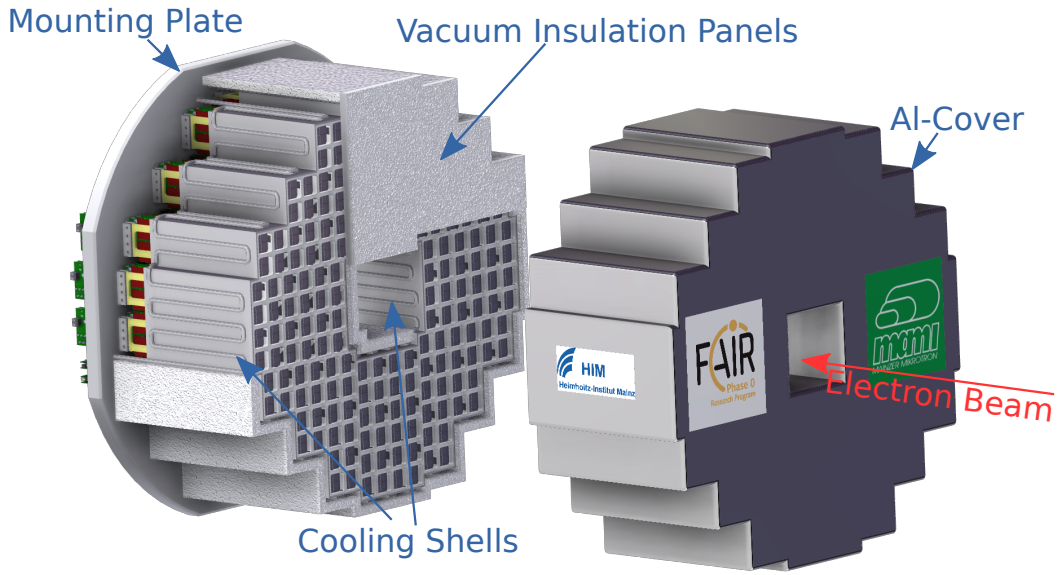

Figure 3.16: The CAD drawing shows the front side of the FAIR Phase-0 calorimeter. It consists of 48 4×4 submodules, which can hold up to 768 crystals. Since only 700 crystals are available, the submodules will be filled symmetrically beginning from the inner part of the calorimeter. A possible configuration holds 640 crystals. The empty spaces will be filled with aluminium dummies to increase thermal conductivity.

3.3 The Electromagnetic Calorimeter Prototype

To test the technological solutions presented in this work, a prototype EMC was built. The prototype is the further systematic development of "PROTO16", which was described in the author's master thesis [Nol14]. The main component of the new prototype is a 4×4 submodule, like it is shown in Figure 3.12. The further setup of the prototype is similar to the setup of both the $\bar{\text{P}}$ANDA backward calorimeter and

the FAIR Phase-0 calorimeter. Likewise, in the full calorimeters, the prototype has a mounting plate which is attached to a holding structure. The submodule is fixed on the mounting plate and is surrounded by a cooling shell and vacuum insulation panels. Finally, an aluminium cover closes the detector volume. In Figure 3.17 and Figure 3.18 photographs of the prototype are shown.
Although, the prototype design is very close to the $\bar{\text{P}}$ANDA backward calorimeter and the FAIR Phase-0 calorimeter, there are small modifications which are due to the development process. For instance, the alveolus is not glued to the insert but fixed with a clamping mechanism. Moreover, the optical multi-fibre connector is not in the centre of the slider (Figure 3.12) but attached next to it. The modifications are suitable for the prototype but not for a system composed of many submodules close to each other, where all submodule connections and services must stay within the projection of the alveolus to position the submodules edge on edge.
The prototype has all the necessary supplies and connections. Everything is connected to the prototype backside. The low voltage supply for powering the line-driver boards, the bias voltage for the APDs, the temperature readout, the preamplifier programming and the analogue signal cables leading to connectors on the shielding box. The optical multi-fibre connector and the cooling pipes are connected with plugs directly on the mounting plate. For the test with beam, two fluorescence plates are fixed on the prototype's outer box to make the beam spot visible for positioning the prototype.

3.4 Control, Monitoring and Data Acquisition

Due to the number of channels and the number of subsystems involved in the system operation, a slow control system is mandatory. Over the years of development, the slow control for the EMC became more and more enhanced and user-friendly. Almost all subsystems were by and by implemented into the so-called Experimental Physics and Industrial Control System (EPICS)[Fel14], which is also used by the $\bar{\text{P}}$ANDA collaboration. The EPICS framework provides a network traffic optimised detector control and monitoring. Furthermore, it supports data logging, and it is scalable by design. All relevant systems are accessible via a web interface. Thus, the setup process of the detector is very convenient.
The signal digitisation is performed with dedicated digitisation boards, developed at the University of Uppsala for the $\bar{\text{P}}$ANDA EMC [M$^+$17]. Since they are essential for this thesis's work, they will be described in detail in Section 4.2. They are based on fast analogue digital converters and Field-Programmable Gate Arrays (FPGAs). In the context of this thesis, both an FPGA firmware and a preliminary version of the DAQ software was developed (Chapter 4). Furthermore, the developments were tested with the EMC prototype (Chapter 6).

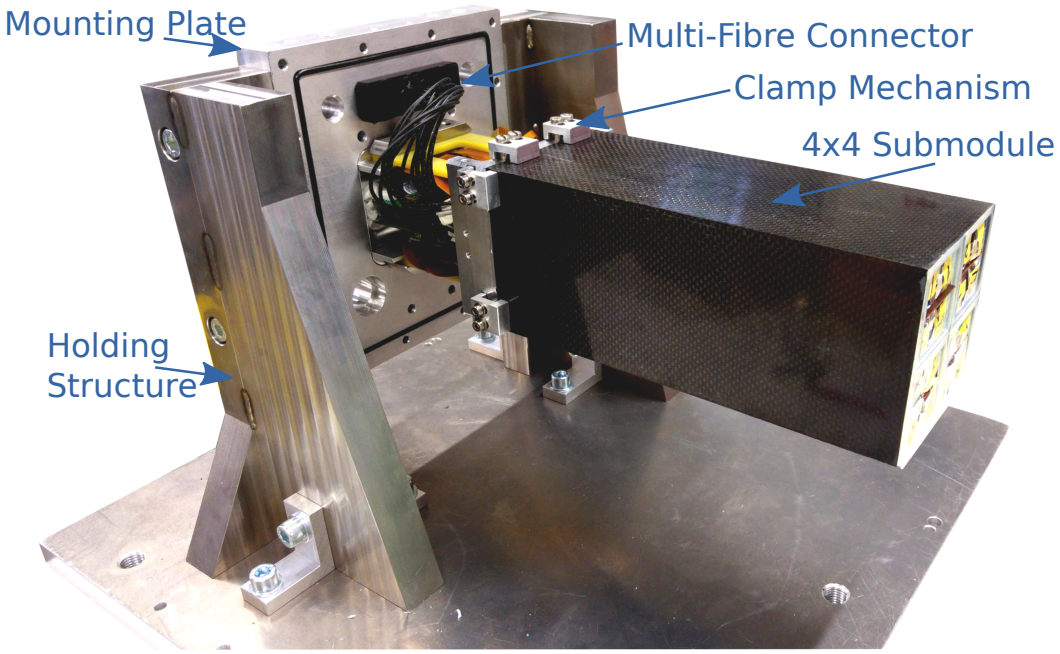

Figure 3.17: The photograph shows the open EMC prototype. The main component is a 4×4 submodule with 16 lead tungstate crystals. The submodule is mounted on a mounting plate, which is fixed to a holding structure. In contrast to the setup which will be used in $\bar{\text{P}}$ANDA and FAIR Phase-0, the alveolus is not glued to the insert but fixed by a clamping system. Furthermore, the optical multi-fibre connector is located beside the submodule slider and not in its centre. The mentioned modifications are due to the prototyping process. The further assembly can be seen in Figure 3.18.

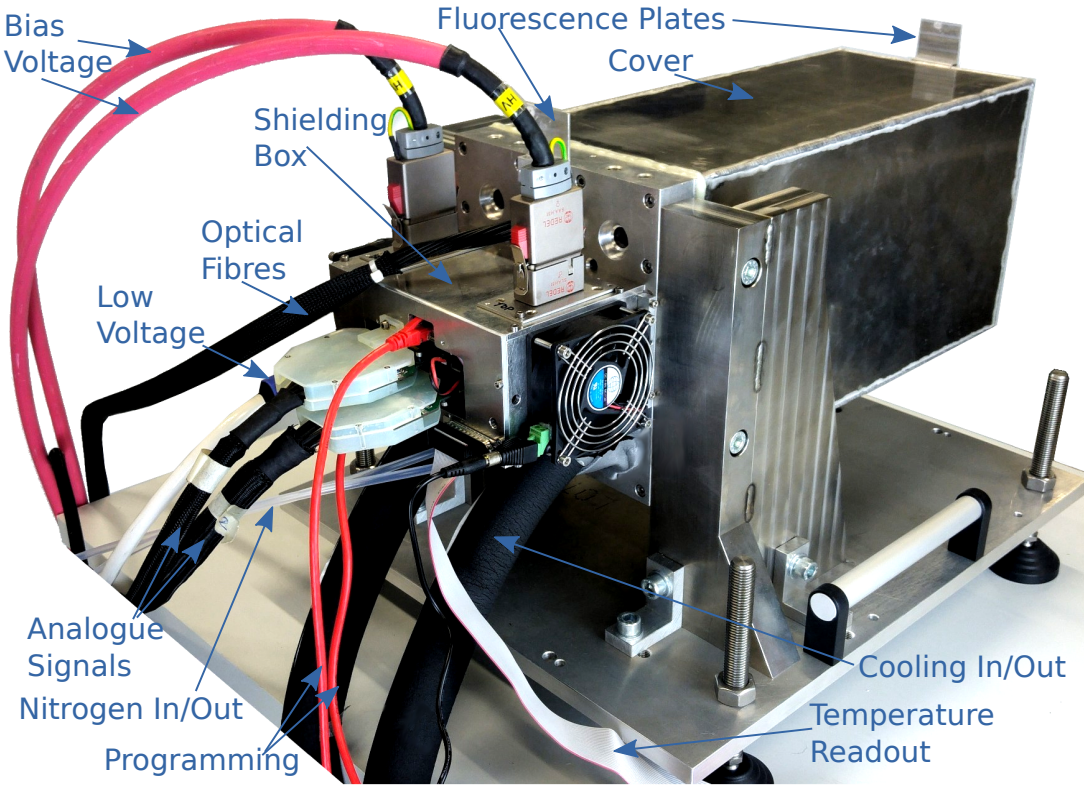

Figure 3.18: The photograph shows the backside of the EMC prototype with the complete cabling. Before closing the aluminium cover, a cooling shell was slid over the alveolus part of the submodule. The aluminium cover is lined with vacuum insulation panels. A shielding box surrounds the outer part of the front-end electronics. Besides the low and high voltage supply, the preamplifier programming lines, the optical fibres and the analogue signals cables, the prototype has insulated cooling pipes which supply the cooling shell with $-25\,^{\circ}\mathrm{C}$ cold ethanol. The detector is flooded with nitrogen, to avoid ice formation from the air humidity. The temperature inside the detector is monitored by flat temperature sensors (PT100). Two fluorescence plates are foreseen as a position reference for electron or photon beams.

4 Digital Processing of Electromagnetic Calorimeter Signals

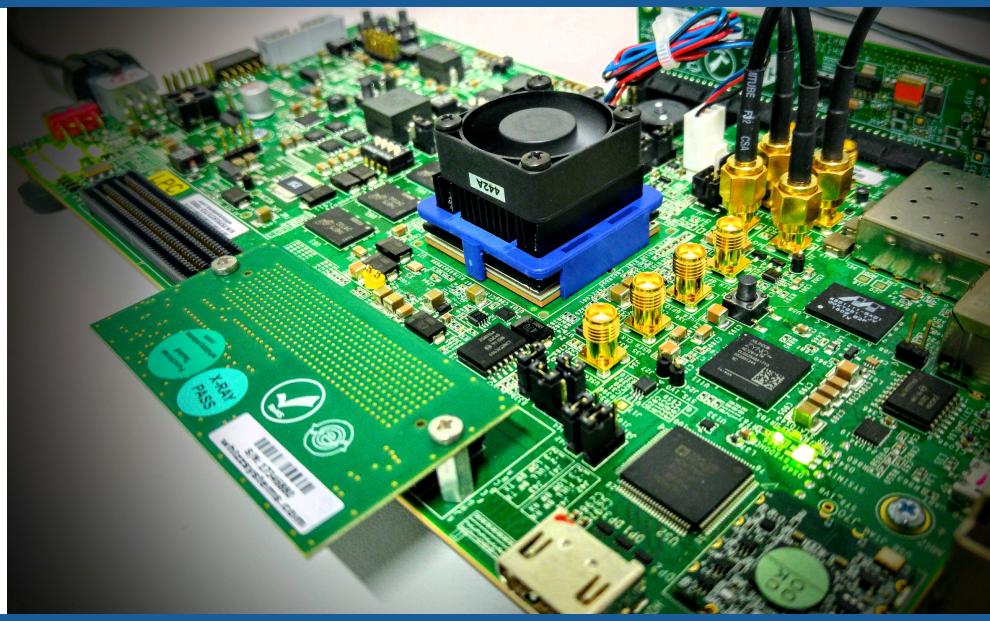

The picture shows a developer board, which has a Field-Programmable Gate Array (FPGA) on it. An FPGA consists of logic blocks, programmable interconnections, and input/output blocks. There are flip-flops and look-up-tables inside of the logic blocks. A logic system is realised by describing the behaviour of the logic blocks and their interconnections.

Nowadays, large-scale experiments are designed to cover multiple scientific goals. In contrast to past experiments with a dedicated trigger on a specific physics channel, they record various channels in parallel. Experiments like ATLAS or BESIII work with different hierarchies of triggers. The level one trigger collects information from the sub-detectors by which the data acquisition is initiated. A second trigger level does a more refined decision [A$^+$08][W$^+$09].
$\bar{\text{P}}$ANDA with its trigger-less concept will even go a step further. Every sub-detector system has to decide online which event is worth to record and which is not. The event building is made afterwards on computer nodes [TDR08].
In the context of this work, a Field-Programmable Gate Array (FPGA) based self-triggering readout system for the $\bar{\text{P}}$ANDA EMC was developed. It is specialised for extracting information from APFEL ASIC signals by using noise suppressing filters and customised extraction routines.
In this chapter, the relevant elements of digital electronics and the processing of digital data will be described. The introduction includes the basics of Analogue to Digital Converters (ADCs) and FPGAs. With the knowledge of the working principle of these devices, the $\bar{\text{P}}$ANDA Sampling ADC (SADC) board will be introduced.
Afterwards, the firmware for the $\bar{\text{P}}$ANDA SADC board, which was developed in this work will be presented by giving an overview of the data flow and essential modules. The section closes with a discussion about the FPGA utilisation of the current firmware implementation.
Since the signal smoothing with a Finite Impulse Response (FIR) filter is a key element of the signal processing on the SADC, the theory, including the terms of the transfer function and the impulse response, will be discussed in a dedicated section. Thanks to the technique of distributed arithmetic (DA), an implementation of high order filters on FPGAs was possible. For this reason, a software framework was developed to generate the DA hardware description for arbitrary FIR filters.
In the last part, the methods for detecting calorimeter preamplifier pulses and extracting both the amplitude and the time information will be discussed.

4.1 Digitisation and Processing of Digital Signals

For the measurement of particle energies with the electromagnetic calorimeter, different physical processes happen each after the other. A detailed explanation of the working principle of the calorimeter can be found in Chapter 3. At the end of the chain, the output of the detector is an analogue signal for every channel. The conversion of the analogue signals into a digital processable format is necessary. An ADC does this conversion. The principle of digitisation and the time-discrete structure of the signal after its conversion is essential to understand the digital signal processing on a Field-Programmable Gate Array (FPGA). In the following, the working principle of ADCs and FPGAs will be explained.

4.1.1 Working Principle and Characteristics of Analogue to Digital Converters

A sampling analogue to digital converter (ADC) converts an analogue voltage signal $g(t)$ in a series of samples g_n. The time distance between two samples is a constant value T. The reciprocal value of that constant T is the sampling frequency f_s.

$$f_s = \frac{1}{T} \tag{4.1}$$

The amplitude of a sample has an integer value within a certain range which is defined by the bit depth N_{bit}.

$$N_q = 2^{N_{\text{bit}}} \tag{4.2}$$

The ADC input voltage range is subdivided in N_q intervals of the width q. For example, a 14 bit ADC has an amplitude fragmentation of $2^{14} = 16384$ integers. Assuming an analogue input range of 2 V, a signal change of $q = 0.122$ mV can be resolved. The digitisation of an analogue signal in time and amplitude is illustrated in Figure 4.1.

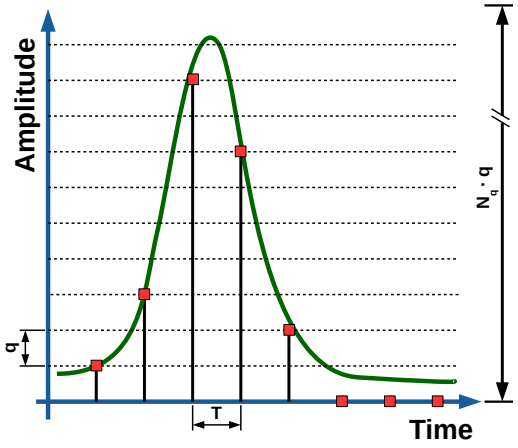

Figure 4.1: The illustration shows the digitisation of an analogue signal. A sample is taken after every clock period T. The resolution of the sample value is a function of the bit depth of the ADC. The higher the bit depth, the more digitisation intervals q divide the input range of the ADC.

The Digitisation Process

All ADCs have in common that they compare the input voltage with intrinsic reference values by using comparators. In the following, the process of digitisation is explained using the example of the direct conversion ADC also known as flash ADC. Direct means in this context that at every clock cycle a full sample is taken. For this fast digitisation of the analogue signal, $N_q - 1$ comparators are needed. An additional comparator can be used to indicate an overflow of the input range. The analogue voltage is fed to one input of every comparator. On the other input of the comparators, a reference voltage is applied. Between every two comparators, the reference voltage drops at a resistor (Figure 4.2) by the value of the digitisation distance q (Figure 4.1). The comparator decisions are fed to a logic gate network, which extracts the binary representation of the analogue input value.

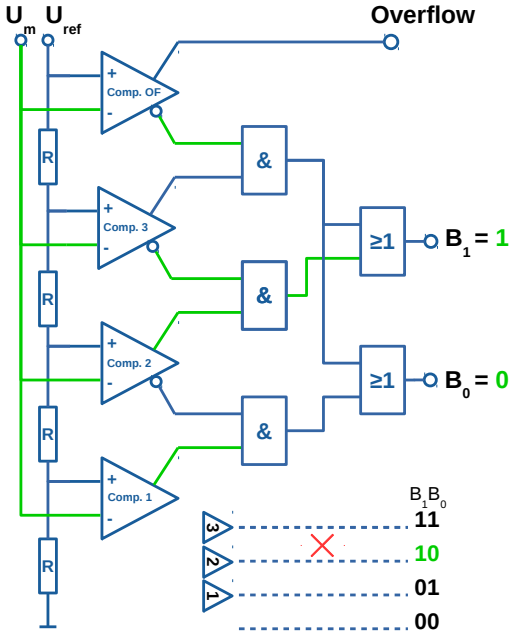

Figure 4.2: The circuit illustrates a two-bit ADC ($N_q = 4$). The analogue input voltage U_m is fed to comparators. The comparators examining U_m with a reference voltage U_{ref}. Considering an input voltage exceeds the first two reference stages (red cross), the comparator one and two indicate that U_m is greater than their specific U_{ref}. All other comparators output a NOT status. The three AND-gates transform the comparator states in a one-hot representation. Only one AND condition can be true at a time. The two OR-gates extract the binary value 10 which equals the decimal value 2.

The Nyquist Frequency and Digital Aliasing

Consider a function $g_1(t)$ which is digitised with a particular sampling frequency. Since the distance in time T between two samples is not zero, a second function $g_2(t)$ can be constructed, which fits in the same set of samples (Figure 4.3). This effect is called aliasing. Consequently, a limitation on the maximum frequency of the signal is needed to describe a function g with a finite set of numbers correctly. With the Nyquist frequency

$$f_{\text{nyquist}} = \frac{1}{2} \cdot f_s \tag{4.3}$$

the condition is defined as:

$$f_{\text{signal}} < f_{\text{nyquist}} \quad \text{or} \quad f_s > 2 \cdot f_{\text{signal}} \tag{4.4}$$

Whereby f_{signal} is the highest frequency component of g and f_s is the sampling frequency. This condition is also known as sampling theorem. A full discussion about the sampling theorem can be found in [SH99].

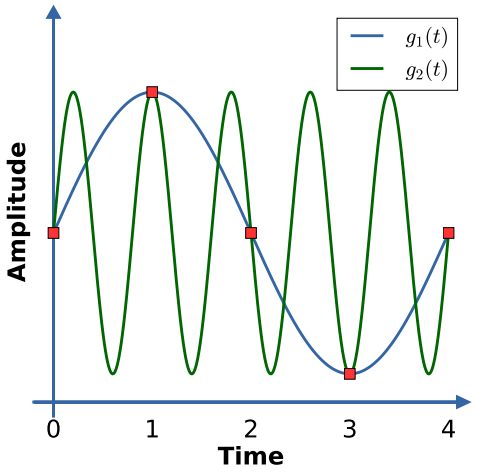

Figure 4.3: The plot shows the effect of aliasing. Due to the fact, that the distance between two samples is non-zero, it is always possible to find another function which also fits to the same set of samples. The sample set of the second function is an "alias" of the sample set from the first one. After the digitisation, it is not possible to distinguish one from the other. By using a sampling frequency, which is at least the double of the highest signal frequency aliasing can be avoided.

With the help of the sampling theorem, a proper sampling rate can be found for a certain analogue signal. Usually for detector pulses, the rising edge[1] contains the fastest components of the signal. For an estimation, it is enough to consider the duration of the rising edge. A typical APFEL preamplifier pulse has a rising edge duration of about 300 ns which gives a signal frequency of f_{signal} =3.3 MHz. Thus a sampling frequency of at least 6.6 MHz has to be chosen (Figure 4.4). Given nowadays data acquisition ADCs with sampling frequencies between tens and several hundred MHz it comes to an oversampling of the analogue signal. However, the oversampling helps to improve the signal to noise ratio [NK05]. This circumstance is used for the signal filtering in Subsection 4.4.2.

[1]The rising edge describes the transition of a signal between low to high. Generally, the baseline defines the low level of the signal.

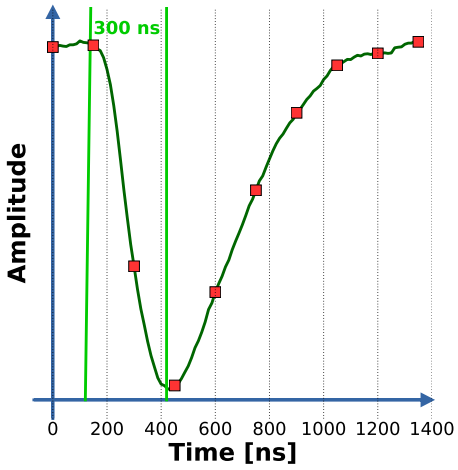

Figure 4.4: The plot shows a APFEL preamplifier pulse. The rise time is about 300 ns. The corresponding frequency of the rise time is $f_{\text{signal}} = 3.3$ MHz. By applying the sampling theorem, a sampling frequency of 6.6 MHz minimum has to be chosen. The red squares illustrate samples taken with the calculated sampling frequency. The set of samples fully describes the pulse, in particular its rising edge. However, noise with higher frequency components is overseen.

The Performance of Analogue to Digital Converters

Since a noise reduction method will be introduced in Subsection 4.4.2, the contribution of ADC limits and imperfections will be addressed in the following. Considering a perfect N_{bit} ADC, a digitisation uncertainty at the least significant bit (LSB) is given by design. When the analogue signal exceeds the last corresponding comparator, the actual amplitude is known within an interval of $\pm\frac{1}{2}q$ (Figure 4.2). By assuming a simple sawtooth as waveform within $\pm\frac{1}{2}q$, the Root Mean Square (RMS) of the digitisation noise amplitude is

$$U_{\text{N(RMS)}} = \frac{q}{\sqrt{12}} \tag{4.5}$$

In order to have a comparative value, the RMS of a sinusoidal signal with an amplitude A is used:

$$U_{\text{S(RMS)}} = \frac{A}{\sqrt{2}} = \frac{q \cdot 2^{N_{\text{bit}}}}{2 \cdot \sqrt{2}} \tag{4.6}$$

With the help of the signal power[2] and the noise power, the signal to noise ratio (SNR) is defined by:

$$\text{SNR} = \frac{P_{\text{signal}}}{P_{\text{noise}}} = \frac{U^2_{\text{S(RMS)}}}{U^2_{\text{N(RMS)}}} \tag{4.7}$$

By using equation (4.5) and (4.6) it follows:

[2]Electric power P is defined by the current I times the voltage U, which also can be written as $P = \frac{U^2}{R}$. It is frequent practice in signal theory to choose R=1Ω, which leads to $P = U^2$ [W].

$$\text{SNR[dB]} = 10 \cdot log_{10}(\text{SNR}) = 10 \cdot \log_{10}\left(\frac{3}{2} \cdot 2^{2\text{N}_{\text{bit}}}\right) \tag{4.8}$$

$$= 1{,}76 + 6{,}02 \cdot N_{\text{bit}} \tag{4.9}$$

For instance, a perfect 14 bit ADC has a signal to noise ratio of 86,05 dB. Nevertheless, real-world electronics has imperfections, for example, thermal fluctuations induce erratic excitations of charge which lead to thermal noise also known as Johnson-Nyquist noise. Another example is the $1/f$-noise which has its origin in semiconductor processes. The spectral density falls with $1/f$. Thus, it has an impact, especially at low frequencies. A more detailed introduction of these and other effects can be found in [NK05].

The Effective Number of Bits (ENOB) summarises all adverse effects and gives a measure for the ADC dynamics. Substituting the SNR with the measured quantity SINAD (Signal-to-Noise-and-Distortion Ratio) in Equation 4.8

$$N_{\text{bit}} \rightarrow \text{ENOB} \tag{4.10}$$

$$\text{SNR[dB]} \rightarrow \text{SINAD[dB]} \tag{4.11}$$

and solving it concerning the number of bits, ENOB is defined as

$$\text{ENOB} = \frac{\text{SINAD[dB]} - 1{,}76 \text{ dB}}{6{,}02} \tag{4.12}$$

The ENOB is frequency dependent, and thus a measurement for different frequencies is needed. Nowadays sampling ADCs have a resolution drop of one to two effective bits depending on the signal frequency.

The non-linearity of the digitisation process of an ADC is another crucial parameter. Thus, the Differential Non-Linearity (DNL) is introduced:

$$\text{DNL}_\text{n} = \frac{(U_{n+1} - U_n)}{q} - 1 \tag{4.13}$$

The DNL is the difference between the actual step width $(U_{n+1} - U_n)$ normalised to the voltage difference corresponding to one LSB and an ideal step width of exactly one LSB. For example, an actual step width of 0,5 LSB would lead to a DNL of -0,5 LSB. A skipping of a step would result in a DNL ≥ 1 LSB (Figure 4.5). The worst DNL indicates the quality of the ADC. A monotonic linear ADC fulfills the condition $|\text{DNL}_\text{n}| < 1$.

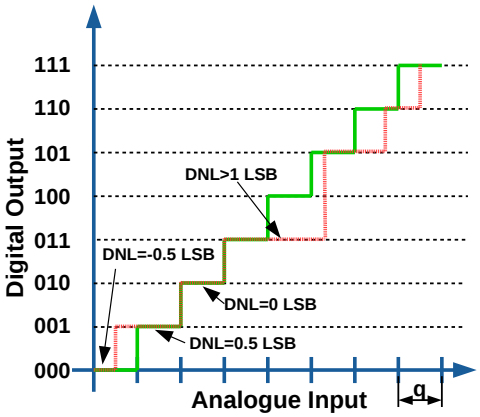

Figure 4.5: The illustration shows an example DNL for a 3-bit ADC. A perfect ADC (green) would increment its digital value whenever the input voltage exceeds one quantisation distance q. A real ADC behaves only approximately like this. The step width at which the digital value is incremented can differ from the ideal width of one q, corresponding to one LSB (red). A monotonic linear ADC has to fulfill the condition $|\mathrm{DNL_n}| < 1$.

Adding up all DNL_n values gives the Integrated Non-Linearity (INL):

$$\mathrm{INL_D} = \sum_{n=0}^{D} \mathrm{DNL}_n \tag{4.14}$$

$$= \frac{U_D - U_0}{q} - D \tag{4.15}$$

Whereby D is the obtained digital output value corresponding to the applied input voltage U_D. U_0 is the minimum analogue input analogous to an all-zero digital value. The difference between the digital output code D and the quotient of voltages defines the INL at D. The INL helps to perform an estimation of how much the ADC characteristics distorts the amplitude measurement of APFEL preamplifier pulses. A further discussion about ADC non-linearities can be found in [MIP01].

4.1.2 Working Principle of Field-Programmable Gate Arrays

Once the analogue signal is digitised it is necessary to reduce the amount of data to a minimum by preserving the useful information content. Since the data is already in a binary format, logic gate operations are used. As the ADC delivers one sample after every time interval T, which corresponds to one clock cycle, a clocked processing would achieve a continuous stream of processed data. The device of choice for such an application is a Field-Programmable Gate Array (FPGA). In the following, its structure and working principle will be explained.
The basic design of an FPGA consists of three types of components which are Configurable Logic Blocks (CLB), programmable interconnects and Input/Output (I/O) blocks. With these components, a configurable Integrated Circuit (IC) is realised. The customer[3] can describe a logic circuit by configuring the CLBs and the interconnections between them. In basic terms, CLBs consist of one Look-Up-Table (LUT), a D-type Flip-Flop (FF) and a Multiplexer (MUX).

[3]The configuration is done in the customer field. This is the origin of "Field" in Field-Programmable Gate Array.

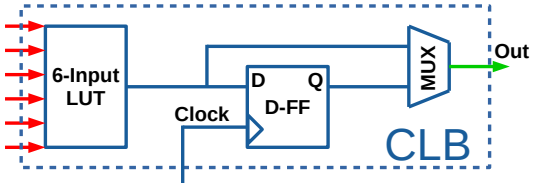

Figure 4.6: The illustration shows a Configurable Logic Block. A truth table defines the output of the Look-Up-Table (LUT) and thus the output of the CLB.

By setting a truth table and transferring it into the LUT every logic gate operation can be achieved. It is possible to choose a clocked flip-flop output or a clockless output by a multiplexer. The actual composition of a CLB differs between manufacturers and FPGA generations. For instance, the series 7 of Xilinx[4] provides a real 6-input LUT, distributed memory, shift registers, fast carry logic for arithmetic functions and wide multiplexers [Xil16]. Nowadays FPGAs feature hundreds of thousands of CLBs arranged in arrays allocated in several banks.

Programmable Switch Matrices (PSMs) connect the CLBs. A single PSM consists of a grid of lines. Every two lines have an intersection with six pass transistors. Thus, it is possible to connect the CLBs in many ways.

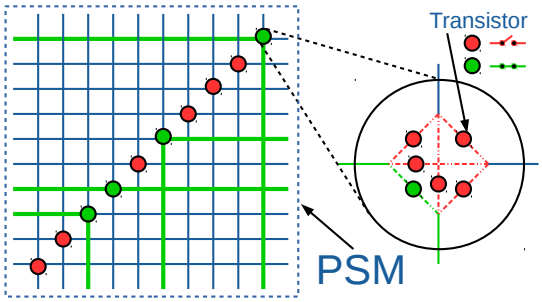

Figure 4.7: The figure shows a Programmable Switch Matrix. The PSMs are distributed between the CLBs. At an intersection inside a PSM, all possible connections between two lines can be made by transistors. It is possible to connect both neighbouring CLBs and not neighbouring CLBs.

Besides the CLB connections, there are additional interconnection types on an FPGA. The global routing distributes the clock and high-fan signals through the device. Especially for clock signals, it is desired to have a minimum of delays to provide the different blocks with a synchronous signal. Another interconnect is the I/O block routing, which surrounds the CLB array and connects the I/O blocks of the FPGA with the internal logic blocks.

The I/O blocks are connected with soldering pads on the bottom of the FPGA. Thus, communication to the outside world is possible. In general, FPGAs are soldered on a Printed Circuit Board (PCB), which connects it with other components such as ADCs, external clocks or high-speed data buses.

FPGAs have additional segments specialised for different tasks. For instance, Digital Signal Processing (DSP) slices use pre-implemented multipliers and accumulators to realise signal processing functions [Xil18a]. In the context of this thesis, DSP slices are used for different signal processing operations.

[4]There are many manufacturers on the market. Besides the market leader Xilinx, there is Intel PSG (Altera), Lattice and many more. In this thesis, manly Xilinx products are used. Thus, they are more frequently referenced.

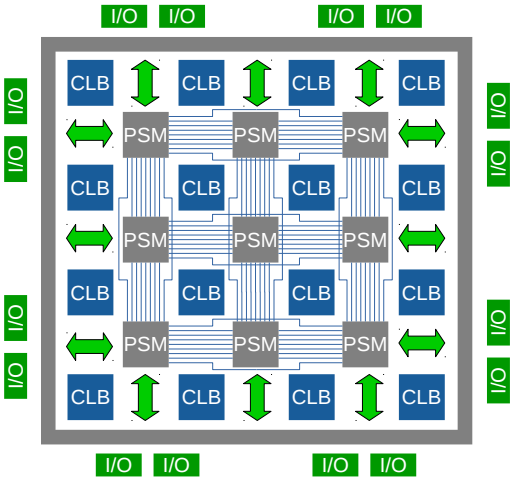

Figure 4.8: The illustration shows an FPGA with its essential components. Logic gate operations are performed by CLBs. To realise complex circuits PSMs interconnect the CLBs. The I/O block routing (grey frame) surrounds the array of the CLBs and connects the internal logic with the I/O pads. The global routing (here not drawn) supplies the FPGA blocks with clock and high-fan signals.

The configuration of an FPGA comprises different steps. First of all, a circuit design is needed. The designer has to develop the behaviour of the circuit. In contrast to the programming of a CPU runtime by using pre-defined logical structures, the logical structures themselves have to be designed. As a result, the development of an FPGA application is more time consuming, compared to a software solution. On the other side, there are benefits in using an FPGA. The hardware can be used more efficiently, and the application runs in real-time without interruptions from an operating system. Moreover, every single subprocess gets its area on the FPGA and is executed at every clock cycle. Thus, a real parallelisation for pipeline designs[5] is achieved.

The circuit design is written in a hardware description language (HDL). The most popular ones are Verilog and VHDL[6]. Besides the user-defined logic, additional code is needed. For instance, the communication with the I/O blocks or the clock setup has to be defined. This is done by Intellectual Property (IP) cores[7] provided by the FPGA manufacturer.

In a further step, the code is analysed by a synthesis tool [Xil18c] which generates a netlist. The next step is the implementation of the netlist, which includes the physical distribution of the logic elements and the routing of the signals [Xil17], on a specific FPGA device.

In the last step, a configuration file (bitstream) is generated. The FPGA is then subsequently programmed with the bitstream and performs the defined behaviour until a power off.

[5] A pipeline design is especially interesting for digital filters and continuous signal information extraction routines.

[6] Very High-Speed Integrated Circuit Hardware Description Language

[7] The availability depends on the licences of the user. JGU users have access to the essential IP cores from Xilinx.

4.2 The PANDA Sampling Analogue to Digital Board

The PANDA Sampling ADC (SADC) board was developed by the PANDA group of the University of Uppsala (Sweden) [M+17]. According to the PANDA calorimeter TDR [TDR08], it was designed to have a high channel density and low power consumption. The board offers 64 differential ADC channels with a resolution of 14 bit each. Eight commercial integrated circuits of type LTM9009Y-14 are used for this purpose. Every channel is digitised with a sampling rate of 80 MHz. The converted data are processed by two Xilinx Kintex-7 FPGAs and transmitted by two optical links to a data concentrator.

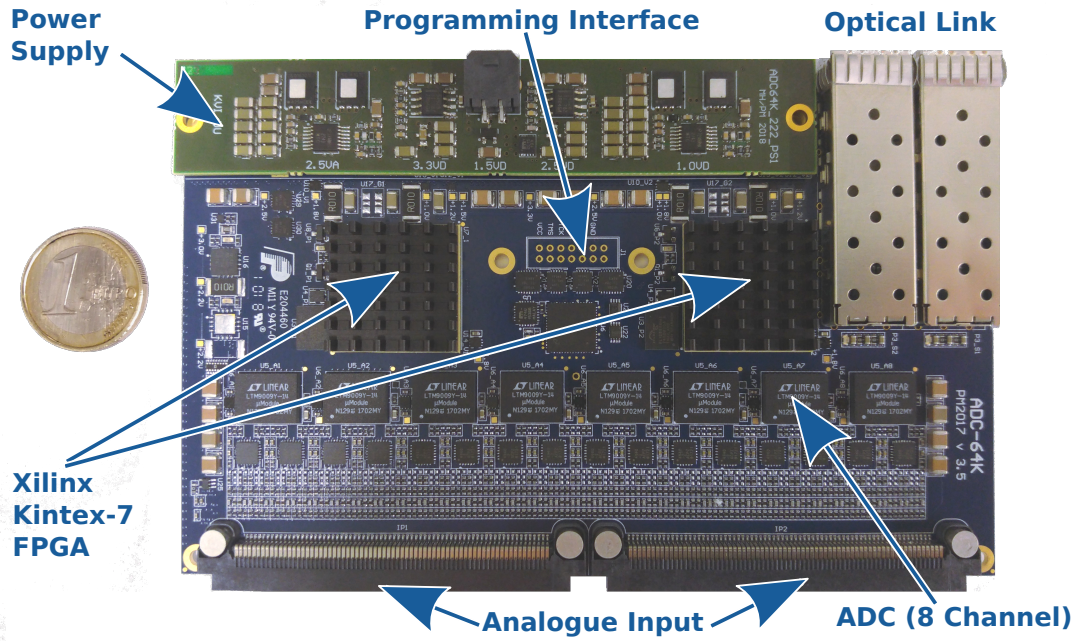

Figure 4.9: The photograph shows the latest version (PM2017 v 3.5) of the PANDA SADC board. It has eight LTM9009Y-14 [Cor18] chips on it. Every chip has eight differential ADC channels. Two Xilinx Kintex-7 FPGAs process 32 channels each. The processed data is transmitted via two optical links to a data concentrator.

The LTM9009Y-14 Analogue to Digital Converter Chip

The LTM9009Y-14 ADC is an eight differential channel simultaneous 14-bit sampling ADC chip. It is designed for digitising high frequency and wide dynamic range signals. The sampling frequency can be chosen in a range from 5 MHz up to 80 MHz. On the PANDA SADC board, it operates with the highest sampling rate.
The high resolution and therefore, the anticipated power consumption by using $2^{14} - 1$ comparators per ADC input channel excludes a simple flash ADC design (Subsection 4.1.1). The LTM9009Y-14 ADC subranges the 14-bit resolution into seven intervals,

which implies a latency of the digitised signal compared to the original analogue signal of six clock cycles [Cor18], which is 75 ns at a sampling frequency of 80 MHz.
A sample and hold (SH) element stores the input voltage temporarily for the digitisation at every stage. After the first stage, the digitised value is converted by a Digital to Analogue Converter (DAC) into a voltage. Afterwards, the voltage is subtracted from the stored voltage of the SH element. Subsequently, the residual voltage is passed to a further sample and hold element. The process repeats until all stages are fulfilled. Every stage performs the process at every clock cycle. Thus, a full 14-bit sample is available at every clock cycle. This process is also known as pipelining. Hence, the architecture is called pipeline ADC. In Figure 4.10 the functionality of a pipeline ADC is illustrated.

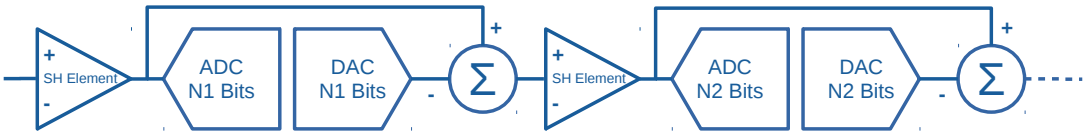

Figure 4.10: The illustration shows the operating principle of a pipeline ADC. In pipeline ADCs the ADC range is subdivided into intervals. At every interval a part of the input signal is digitised beginning from the Most Significant Bit (MSB), then converted into a voltage, subtracted from the original signal and passed to the next stage. The intermediate storage of residual voltages by the sample and hold elements allows the pipelining of the process. Thus, a full sample is available at every clock cycle. However, the samples have a constant latency compared to the analogue signal.

Finally, the ADC performance is summarised by using both the LTM9009Y-14 ADC datasheet and the ADC performance indications (Subsection 4.1.1). The extracted numbers are essential for the full simulation of the calorimeter output signals in Chapter 5.
In [Cor18] a typical Signal-to-Noise-and-Distortion Ratio (SINAD) is given at full scale as 72.6 dB, which corresponds to an effective number of bits of 11.77. The ADC has an analogue input range of 2000 mV. Thus, the effective resolution is 0.57 mV, which corresponds to 4.69 quantisation steps (q).
By utilising a typical signal energy calibration of 0.3 MeV/q, the ADC resolution refers to a single APD threshold of 1.41 MeV at low gain and 0.13 MeV at the high gain of the APFEL preamplifier.
According to [Cor18], the DNL (Equation 4.13) of the LTM9009Y-14 ADC is typically within the range of ±0.3 LSB and guaranteed to be smaller than ±0.8 LSB. Thus, the used ADC is sufficiently monotonic linear.
The typical INL of the LTM9009Y-14 ADC is within ± 1 LSB. Since the amplitude extraction of calorimeter signal pulses is a subtraction of the pulse extremum from the baseline, a worst-case error of the amplitude determination can be estimated. The worst INL, according to [Cor18], is at a difference of 6200 digitisation steps. Thus, the

error due to non-linearities in the amplitude determination is in the order of 2/6200 ($< \mathcal{O}(10^{-3})$). Smaller amplitudes profit from similar INL values for closely spaced output codes. As a result, the ADC contribution to the measurement accuracy can be neglected compared to other contributors such as preamplifier noise and transmission noise (Subsection 5.1.2).

The Kintex 7 Field-Programmable Gate Array

Two Kintex 7 FPGAs [Xil18b] were chosen for the $\bar{\text{P}}$ANDA SADC (Figure 4.9). The version number is XC7K160T-1FBG484C. Every FPGA processes 32 ADC channels. The FPGA has 162240 logic cells, which translate to 202800 CLB flip-flops.
With its 600 DSP (48E1[Xil18a]) slices (Subsection 4.1.2), 18 DSP slices per channel are available for digital signal processing. In the context of this thesis, methods were adapted to surpass the DSP slices limit. Thanks to Distributed Arithmetics (DA), high order filtering is possible, and DSP slices are saved for other operations. These methods are based on the distribution of operations in precalculated Look-Up-Tables (LUTs). Therefore, the number of LUTs, which is 101400, is also a crucial number.
The last important parameter of the used FPGA is the amount of RAM, which is 11700 kB. The implementation of the signal filtering and the extraction of signal parameters is fully pipelined, which means that interim results need to be cached in RAM. The actual needed RAM is a function of the number and depth of bit shift registers, which are used for intermediate filter values and derivatives. As an upper limit, 100 bytes per channel can be assumed. This leads to a RAM consumption of 3200 kB. Other modules, such as package builder and network implementation, do also need RAM. Anyhow, the overall RAM consumption is less than 50 % of the available RAM after the implementation of the introduced algorithms in Section 4.4.

Data Transmission by Optical Links

Two optical links connect the SADC with a data concentrator. Each FPGA sends the extracted signal parameters via a multi-gigabit transceiver (GTX), which can operate with up to 2 Gbit/s. Furthermore, the SADC slow control system communicates via the optical links with the FPGAs. Consequently, thresholds and other parameters can be adjusted. The SADC communication and the data transfer will be explained in more detail in Section 4.3.
Further information about the $\bar{\text{P}}$ANDA SADC can be found in [M$^+$17] and [Mü19].

4.3 Firmware for the Sampling Analogue to Digital Board

In the context of this thesis, firmware for the $\bar{\text{P}}$ANDA Sampling Analogue to Digital Board was developed. The firmware is capable of operating 32 ADC input channels of the $\bar{\text{P}}$ANDA SADC. Since two FPGAs are available on the board (Section 4.2), all 64 ADC input channels can be read out.

The firmware design is characterised by the efficient implementation of a high order Finite Impulse Response (FIR) filter, the well-adapted parameter extraction routines and its self-triggering concept. Both the extracted calorimeter data and the slow control system commands are transmitted by using UDP[8]-packages. Thus, a standard computer with optical network interfaces in combination with the right software can operate the $\bar{\text{P}}$ANDA SADC.

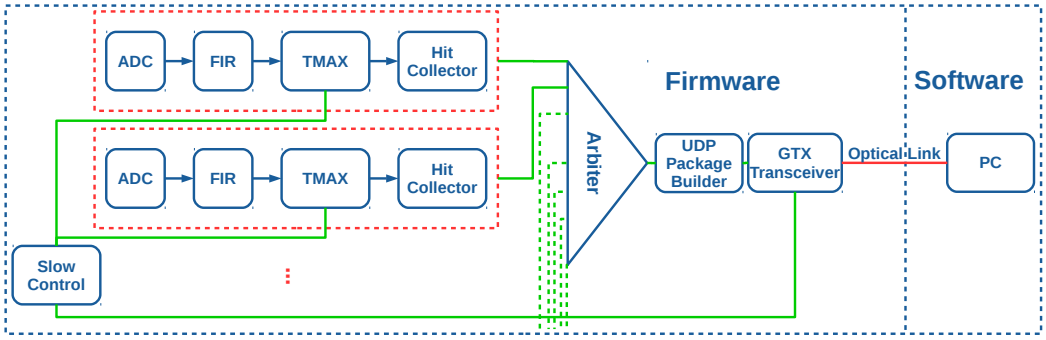

Figure 4.11: The illustration shows the core modules of the SADC firmware. The red dashed blocks represent one readout channel, respectively. There are 32 of these blocks per FPGA. After the filtering via the FIR module, the parameters are extracted by the TMAX module. The extracted parameters are stored in a buffer within the hit collector module. The arbiter periodically checks the hit collectors for new data. In the case of a full buffer, the bundle of hits is passed to the UDP package builder and transmitted to a computer by the GTX transceiver. The GTX interface is also used for the SADC slow control system, which allows setting thresholds and other parameters.

The illustration in Figure 4.11 shows the essential modules of the SADC firmware. General modules such as FPGA arbitration, Phase-Locked Loops (PLLs) and clock synchronisation are excluded in the illustration. More information about the excluded modules can be found in [Mü19]. Each FPGA on the $\bar{\text{P}}$ANDA SADC board reads out 32 ADC input channels. Thus, there are 32 readout instances (red dashed blocks in Figure 4.11) per FPGA.

The ADC provides one 14-bit data word with every 12.5 ns. The data words are carried to the FIR module, which performs the filtering of the raw signal. After the smoothing procedure, the parameters of the signal are extracted by the Time Measurement and Amplitude eXtraction (TMAX) module, which includes the hit detection, the amplitude extraction and the T_0 determination. The FIR module and the algorithms within the TMAX module are fully pipelined.

To understand pipelining, it helps to think of a discrete movement of a conveyor belt as depicted in Figure 4.12.

[8]User Defined Protocol

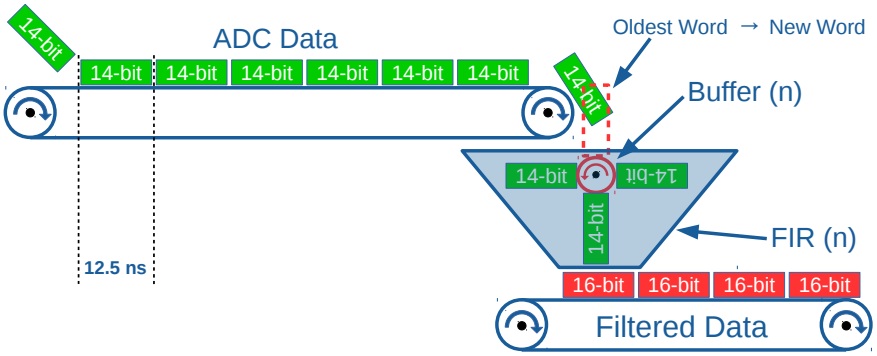

Figure 4.12: The illustration shows a part of the data flow on the FPGA represented as conveyor belts. The conveyor belts perform a quantised movement in time. The ADC provides a new 14-bit word every 12.5 ns. The process needs to be pipelined to guarantee a continuous output of the FIR filter. An n-coefficient FIR filter needs n 14-bit words to calculate one output word. Thus, a buffer is required, which stores the latest n-words. The buffer is updated every clock cycle by overwriting the oldest word with the newest word. The output of the FIR module are 16-bit words to improve the precession for further fix point arithmetics calculations within the following TMAX module.

The 14-bit words from the ADC are moved every clock cycle towards the FIR module. The n-coefficient FIR algorithm needs n 14-bit words to calculate one output word. A buffer within the FIR module is updated at every clock cycle by overwriting the oldest entry in the buffer. As a result, the FIR module always has n 14-bit words for calculating the output.
Every pipeline buffer adds a constant latency to the data stream. An increase in latency is still the price for pipelining. On the other hand, pipelining guarantees a continuous output at every clock cycle. The explanation of the FIR pipelining procedure is also correct for all other calculations within the TMAX module.
Whenever the hit detection path of the TMAX module indicates a hit, the hit information is moved to a collector module. Within the collector module, two things happen. On the one hand, a buffer with a defined size is filled up with the hit information. On the other hand, a clock domain change is performed. The reason is that the ADC, the FIR and the TMAX module work with a 80 MHz clock. In contrast, the GTX transceiver is clocked with 125 MHz. All modules are in the 125 MHz clock domain beginning from the arbiter.
Once the hit collector buffer has a defined amount of hits, it passes them to the arbiter module. The arbiter module is crucial since 32 channels have to use only one GTX transceiver. The arbiter periodically asks the 32 hit collectors one by one if data is available (round-robin scheduling). If a hit collector has a certain number of hits,

the information is passed to the UDP package builder. Finally, the UDP package is transmitted by the GTX transceiver to a computer, which serves as data-concentrator. The communication is bidirectional, which allows operating the slow control of the SADC board. For instance, the threshold for the TMAX hit detection can be set.

The Utilisation of the FPGA Resources

The Distributed Aritmetics (DA) implementation of the FIR allows to use the FPGA resources as efficiently as possible. The firmware occupies 58 % of the available look-up tables, 52 % of the available flip-flops and 19 % of the available DSP slices (Figure 4.13, Section A.3). This leaves some free resources for further algorithms. For example, the current firmware does not yet support baseline monitoring. Furthermore, the APFEL ASIC control is planed to be implemented on the FPGA. And finally, the FPGA resource consumption of the $\bar{\text{P}}$ANDA time distribution system (SODANET, [IKP09]) is not yet taken into account. However, the implementation software (Subsection 4.4.3), which was developed in this work, allows the filter optimisation by considering given hardware resources.

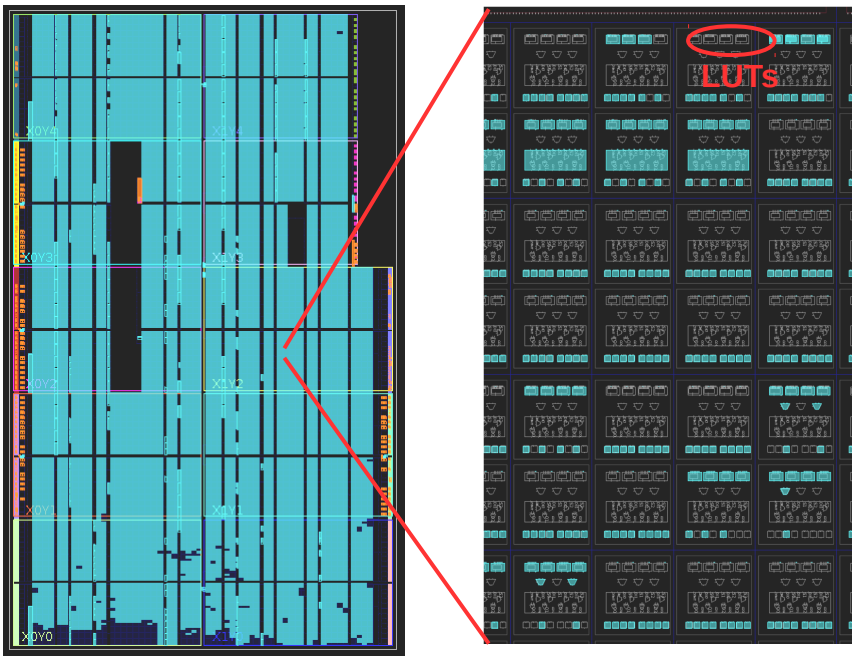

Figure 4.13: The picture shows the utilisation of the FPGA. The logic is distributed over the whole FPGA. Although, the FPGA seems very full (left picture, light blue blocks), a zoom shows that there are plenty of look-up tables, flip-flops and other blocks left. The firmware occupies roughly 50 % of the available resources. Exact numbers can be found in appendix Section A.3.

4.4 Digital Signal Processing Methods

As described in Chapter 3, the energy deposited in a calorimeter crystal is eventually converted into a current pulse by the APFEL preamplifier. The purpose of digital signal processing is to extract the essential signal parameters from the pulse such as the amplitude (H) and the time of occurrence (T_0). The event timestamp is especially crucial for the trigger-less readout. Furthermore, since the energy of an event is generally distributed over several crystals due to the spread of the electromagnetic shower, a sufficient T_0 determination is essential for the event energy summation.
Due to noise from the APFEL preamplifier and the transmission noise of the front-end electronics a proper signal parameter determination is difficult especially for low energy events. Even worse, noise at the entrance of the preamplifier also passes the amplifier transfer function which results into noise with the spectral structure similar to real calorimeter events. A detailed description of the calorimeter signal noise floor can be found in Chapter 5.
In Figure 4.14a and Figure 4.14b sample waveforms containing detector pulses and noise are shown.

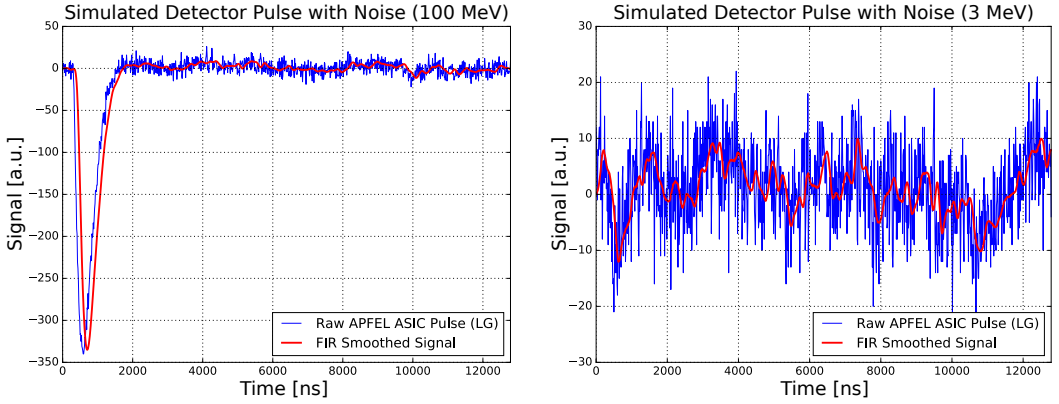

(a) Example APFEL ASIC pulse (100 MeV) (b) Example APFEL ASIC pulse (3 MeV)

Figure 4.14: The two plots illustrate the challenges of the signal parameter extraction. In both cases an APFEL ASIC pulse appears beginning at 300 ns. In the case of a 100 MeV signal (a), the pulse is easily distinguishable from the noise floor. In the case of a 3 MeV signal (b), it is much more difficult to discriminate whether it is a real pulse or just noise. The smoothed signal (red) increases the signal to noise ratio. The traces are created with the simulation framework, which is introduced in Chapter 5.

4.4.1 The Transfer Function and the Impulse Response

To resolve small energy amplitudes, the digitised detector signal needs to be smoothed. The idea is to map the noisy signal into a less noisy signal by using a transfer function. The behaviour of a Linear Time-Invariant (LTI) system, which transfers an input

function $f(t)$ to an output function $g(t)$, can be described with linear differential equations with constant coefficients:

$$\left[A_n \frac{d^n}{dt^n} + ... + A_1 \frac{d^1}{dt^1} + A_0\right] g(t) = \left[B_n \frac{d^n}{dt^n} + ... + B_1 \frac{d^1}{dt^1} + B_0\right] f(t) \tag{4.16}$$

With the help of the Fourier transformation

$$F(j\omega) = \int_{-\infty}^{\infty} f(t) e^{j\omega t} \tag{4.17}$$

the relation can be transformed into the frequency space. By using the relation

$$\frac{df(t)}{dt} \xrightarrow{\text{F.T.}} j\omega F(j\omega) \tag{4.18}$$

it follows

$$[A_n (j\omega)^n + ... + A_1 j\omega + A_0] G(j\omega) = [B_n (j\omega)^n + ... + B_1 j\omega + B_0] F(j\omega) \tag{4.19}$$

Finally, the transfer function in frequency space is given by

$$H(j\omega) = \frac{G(j\omega)}{F(j\omega)} = \frac{\sum_{i=0}^{n} B_i (j\omega)^i}{\sum_{i=0}^{n} A_i (j\omega)^i} \tag{4.20}$$

The term transfer function can also be used for time discrete systems. In Figure 4.15 the impact of a transfer function on both a continuous system and a discrete system is illustrated in terms of a filter.

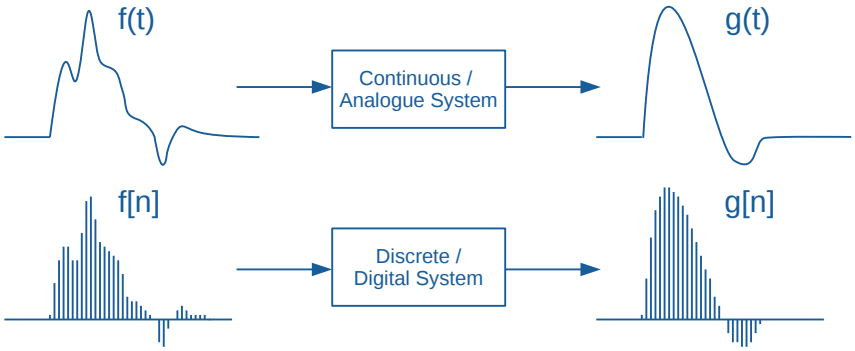

Figure 4.15: The illustration shows the transition of an input function into a output function by means of a filter. A filter is characterised by a transition function either realised as an analogue circuit for analogue signals or as a digital calculation scheme as it is implementable on an FPGA for digital signals.

Since every arbitrary input signal can be written as a sequence of impulses, every system is completely described by its response to one impulse. For a continuous system

an impulse is described by the Dirac delta function. The discrete counterpart of the Dirac delta function is defined as:

$$\delta_0[n] \mapsto \begin{cases} 1: & n = 0 \\ 0: & n \neq 0 \end{cases} \tag{4.21}$$

4.4.2 Finite Impulse Response (FIR) Filtering

As already mentioned in the introduction, it is mandatory to smooth the raw signal in order to perform a proper parameter extraction. The aim of this process is to increase the signal to noise ratio without distorting the time structure of the useful signal. Furthermore, the filter should not depend on the output function in order to avoid an excitation of the output due to a feedback loop.
A FIR filter meets all these requirements by guaranteeing a finite transient response. Thus, the filter output is stable after a finite settling time.
The basic idea is to design a transfer function, which passes the frequency components of the useful signal and blocks all other components. The challenge is to find the right degree of sharpness, which depends on the amount of filter coefficients. However, a large number of filter coefficients results in a higher resource consumption on the FPGA. Thus, the used filter will be a compromise between sharpness, damping and the usage of hardware resources.
A first example of FIR filtering is the generally known Simple Moving Average (SMA) filter:

$$y[n] = \frac{1}{N}(x[n] + x[n-1] + ... + x[n-(N-1)]) = \frac{1}{N}\sum_{k=0}^{N-1} x[n-k] \tag{4.22}$$

N given input values $x[k]$ with $k \in [0, N-1]$ are mapped to one output value $y[n]$ by averaging over $x[k]$. The weight factor $\frac{1}{N}$ applies to every element of the sum. To generalise this special case of a FIR filter, the weight factor restriction to be $\frac{1}{N}$ is removed, which results in:

$$y[n] = \sum_{k=0}^{M} A_k x[n-k] \tag{4.23}$$

with M being the order of the filter. There are $M+1$ input values needed to calculate one output value. With the right choice of the coefficients $A_k \in \mathbb{R}$ any filter characteristics (low pass, high pass, selective suppressing and passing of frequencies) can be achieved. By raising the filter order M, both the damping of undesired frequencies against useful frequencies and the band sharpness increase. The band sharpens describes how close two frequency bands (for instant pass band and stop band) can be together. Since Equation 4.23 only consists of linear operations the FIR filter is a Linear Time Invariant

(LTI) system. Applying the discrete impulse function (Equation 4.21) onto the FIR system (Equation 4.23), it follows:

$$h[n] = \sum_{k=0}^{M} A_k \delta_0[n-k] = \begin{cases} A_n & : n \in [0, M] \\ 0 & : \text{else} \end{cases} \tag{4.24}$$

The impulse response $h[n]$ of a FIR filter equals its filter coefficients A_n. By applying Equation 4.24 on Equation 4.23 the convolution sum of the filter is written as

$$y[n] = \sum_{k=0}^{M} h[k] \cdot x[n-k] \tag{4.25}$$

The convolution sum is the calculation scheme for computing the effect of the impulse response on the input signal. The filter needs a certain time period until the full set of coefficients is convoluted with the corresponding number of samples. This time period is called settling time and in the case of a FIR filter it is:

$$n_{\text{set}} = M \tag{4.26}$$

To better understand the concept of the convolution sum and the settling time an example is discussed in the appendix in Section A.2.

Frequency and Phase Response

The frequency response describes the desired pass and stop band characteristics, while the phase response describes the frequency dependent time shift between input and output signal. Ideally, all frequency components are shifted linearly. In this case, the filter has a linear phase behaviour.
By performing a discrete-time Fourier transformation (DTFT) of $h[k]$ the frequency response is given as:

$$H(\hat{\omega}) = \sum_{k=0}^{M} h[k] \cdot e^{-j\hat{\omega}k}, \tag{4.27}$$

whereby $\hat{\omega}$ is the normalised angular frequency with $\hat{\omega} = \frac{\omega}{f_s}$. The phase response $\Theta(\omega)$ can be determined by computing the ratio between real and imaginary part of $H(\hat{\omega})$. It can be shown that every FIR filter with an even or an odd number of coefficients and a symmetric impulse response has a linear phase behaviour [Sel]:

$$\Theta(\omega) = -G\omega \tag{4.28}$$

With the group delay between the input and output signal of:

$$G = \frac{M}{2} \tag{4.29}$$

In Chapter 5 the specific band ranges for the 20 coefficient FIR filter, which is used in both the hardware implementation and the software based simulation framework are introduced. Moreover, in Figure 5.10 the frequency response of this particular FIR filter is depicted.

The Pole-Zero Diagram

A pole-zero diagram helps to visualise the filter response. For discrete-time systems, Equation 4.20 can be expressed as:

$$H(z) = \frac{B_0 + B_1 z^{-1} + ... + B_n z^{-n}}{A_0 + A_1 z^{-1} + ... + A_n z^{-n}} \tag{4.30}$$

with $z = e^{j\hat{\omega}}$, which is the parameter of the z-transformation[9]. Equation 4.30 is a quotient of polynomials. Since polynomials can always be factorised, the zeros (factors in the numerator of Equation 4.30) and poles (factors in the denominator of Equation 4.30) can be identified and displayed on the complex z-plane. A FIR filter has M zeros and M poles. All poles are located at $z = 0$, which guarantees the stability of the system[10].

The different signal frequency components are located along the unit circle. The lowest signal frequency is at point z = (1,0). By moving the z variable in the anti-clockwise direction, the corresponding signal frequency increases. The maximum frequency is achieved at point (-1,0), which corresponds to the half of the sampling frequency f_s or in terms of the normalised angular frequency to $\hat{\omega} = \pi$.

The scaling of the filter's output amplitude at a certain signal frequency is defined by the product of the distances from the z value to the zeros.

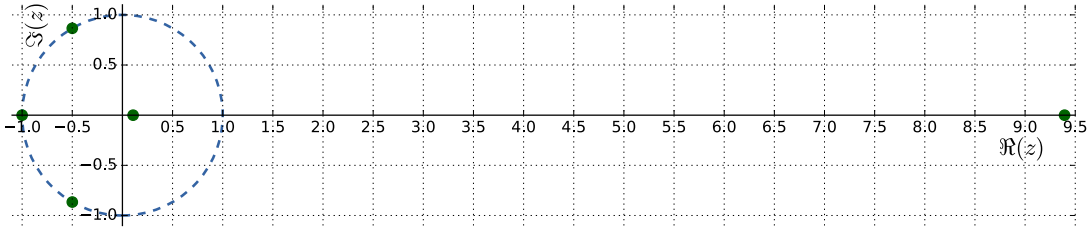

Figure 4.16: The pole-zero diagram for the example in appendix Section A.2 ($M = 5$). There are five zeros distributed on the complex plane. The sampling frequency is normalised to 2π. Starting from point (1,0) the signal frequency increases in the anti-clockwise direction. At point (-1,0) half of the sampling frequency (π) is achieved. The product of the distances between z value and the zeros defines the scaling of the amplitude for a certain signal frequency component. The M poles at $z = 0$ are not drawn.

[9]The z-transformation is the counterpart of the Laplace transformation for discrete-time systems. A deep treatise can be found in [SH99].

[10]Generally, a pole on the right half-axis of the complex plane would induce an increasing response to an impulse function instead of a abating response. Moreover, poles, which are not on the real axis would cause oscillations on the output. This happens in Infinite Impulse Response (IIR) filters.

The Determination of the FIR Coefficients

With the help of the Remez-Algorithm, developed by J.H. McClellan and T.W. Parks [MP05], the FIR filter coefficients can be determined. The algorithm needs the desired band ranges and the desired number of coefficients as input. The algorithm determines the filter coefficients with an iterative approach. In this work the Python SciPy Signal Remez implementation was used [Com19].

4.4.3 Efficient Filter Implementation via Distributed Arithmetics

Besides its many advantages, discussed in Subsection 4.4.2, a FIR filter has the disadvantage of a tremendous FPGA resource consumption.
The approved way to implement a FIR filter on nowadays FPGAs is to use Digital Signal Processing (DSP) slices [Xil18a]. DSP slices are logic networks, which are specialised to perform operations as the following:

$$O_{\mathrm{MAC}} = a + b \cdot c \tag{4.31}$$

The output O_{MAC} is the result of a multiplication and addition (accumulation). Such operations are also called MAC (Multiply-Accumulate). Considering the convolution sum of FIR filters (Equation 4.25) it is obvious, that MAC operations are needed to calculate the filter output. In Figure 4.17, the calculation scheme of a DSP implementation is depicted.
To calculate the output of a $(M+1)$-coefficient filter, $M+1$ multiplications and $M+1$ accumulations are needed. Thus, $M+1$ DSP slices are needed [Oss16].
The FPGA on the $\bar{\mathrm{P}}$ANDA SADC (Xilinx XC7K160T) has 600 DSP slices for 32 ADC input channels. Therefore, 18 DSP slices per channel are available. Besides filtering, DSP slices are also needed for other algorithms. For example, parts of the time path of the TMAX block are realised with DSP slices.
Consequently, another implementation method has to be used to have both a high order FIR filter for every channel and available DSP slices for other tasks.
In the early days of digital signal processing, the only way to implement more complicated calculations on digital devices was to use the method of Distributed Arithmetics (DA) [Whi89]. The underlying idea of DA is to use read-only memory (look-up tables) (Subsection 4.1.2) to store the output of recurrent calculations. Loosely speaking, the output of multiplications and sums are stored in LUTs. Thus, there is no need for costly gate networks such as DSP slices, which calculate the result again and again. Indeed, the actual implementation is much more challenging compared to the DSP implementation. For instance, only parts of the calculation's output can be stored in a single LUT. Thus, the arithmetic is distributed over many LUTs over the FPGA.
In the context of this thesis a software package was developed, which generates the DA hardware description for arbitrary FIR filters. Thus, it is possible to create the best (highest order) FIR filter which still fits on the FPGA. Consequently, the DSP slices are left free for other calculations. In the following, the fundamental steps for the distributed arithmetic implementation of a FIR filter are discussed.

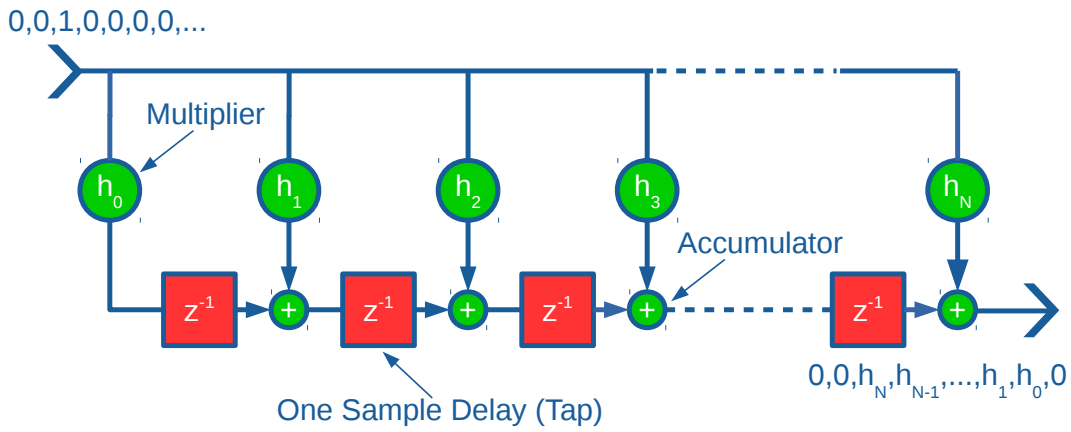

Figure 4.17: The illustration shows the implementation scheme of a FIR filter with DSP slices. The combination between a multiplier and an accumulator is called MAC (Multiply-Accumulate). Furthermore, a one sample delay between the individual MAC stages (also called tap in the established literature) ensures the proper accumulation of the interim results. The notation z^{-1} corresponds to the z-transformation, where a n-sample delay is transformed into z^{-n}. This becomes more clear by comparing the scheme with the FIR convolution sum in Equation 4.25 and the FIR example in Table A.1, where a lower row is moved one position to the right compared to its previous row. This row movement is realised by the taps.

Rewriting the FIR Convolution Sum

The fundamental FIR equation is:

$$y[n] = \sum_{k=0}^{M} A_k x[n-k] \tag{4.32}$$

with A_k being coefficients and x_k being the input samples. The binary expression of x_k is:

$$x_k = \sum_{l=0}^{N-1} b_{kl} 2^l \tag{4.33}$$

with b_{k0} being the least significant bit (LSB) and $b_{k(N-1)}$ being the most significant bit (MSB). Whereby N is the word width. Taking Equation 4.32 and Equation 4.33 together and interchanging the sums it follows:

$$y[n] = \sum_{l=0}^{N-1} \left[\sum_{k=0}^{M} A_k b_{(n-k)l} \right] 2^l \tag{4.34}$$

whereby the term inside the brackets

$$\sum_{k=0}^{M} A_k b_{(n-k)l} \tag{4.35}$$

has only a finite number of possible results. Since b_{kl} can only be either 1 or 0, there are only 2^{M+1} possible outcomes. After the calculation of all possible outcomes of Equation 4.35, a look-up table is built, which maps the binary input signature to an output value V_i. This becomes more clear by considering the following example:

Example 4.1 *A FIR filter with three coefficients is considered, which means that* $M = 2$ *and* $k \in [0,1,2]$. *The possible values for Equation 4.35 are shown in Table 4.1.*

Possible result	Binary signature	Value
1	**000**	$A_0 \cdot \mathbf{0} + A_1 \cdot \mathbf{0} + A_2 \cdot \mathbf{0} = V_0$
2	**001**	$A_0 \cdot \mathbf{0} + A_1 \cdot \mathbf{0} + A_2 \cdot \mathbf{1} = V_1$
3	**010**	$A_0 \cdot \mathbf{0} + A_1 \cdot \mathbf{1} + A_2 \cdot \mathbf{0} = V_2$
4	**011**	$A_0 \cdot \mathbf{0} + A_1 \cdot \mathbf{1} + A_2 \cdot \mathbf{1} = V_3$
5	**100**	$A_0 \cdot \mathbf{1} + A_1 \cdot \mathbf{0} + A_2 \cdot \mathbf{0} = V_4$
6	**101**	$A_0 \cdot \mathbf{1} + A_1 \cdot \mathbf{0} + A_2 \cdot \mathbf{1} = V_5$
7	**110**	$A_0 \cdot \mathbf{1} + A_1 \cdot \mathbf{1} + A_2 \cdot \mathbf{0} = V_6$
8	**111**	$A_0 \cdot \mathbf{1} + A_1 \cdot \mathbf{1} + A_2 \cdot \mathbf{1} = V_7$

Table 4.1: The table shows all possible results ($2^{M+1=3} = 8$) for Equation 4.35 for a three coefficient FIR filter. The table can be seen as look-up table, which maps a binary signature (second column) to an output value V_i (third column).

The key point is, that the weighted accumulation of Equation 4.32 is transformed to a bit by bit summation. It helps to think about it as $M + 1$ input samples, which lie on the top of each other. Whereby the bits are aligned according to their weight in the binary number system as depicted in Table 4.2.

Sample	2^{N-1}	2^{N-2}	...	2^4	2^3	2^2	2^1	2^0
x_0	0	1	...	1	1	0	0	0
x_1	0	0	...	1	1	1	1	1
x_2	0	1	...	0	1	0	0	1
output	V_0	V_5	...	V_6	V_7	V_2	V_2	V_3

Table 4.2: The table shows the origin of the binary input signature of the look-up table (Table 4.1). For a three coefficient FIR filter, three input samples are aligned according to their weight in the binary system. The filter output is then the sum over the LUT outputs weighted with their position in the binary system (2^l).

The filter output is the sum over the LUT outputs (columns in Table 4.2) weighted with their position in the binary system. The weighting according to the position in

the binary system is simply a bitshift, which can be implemented in a very efficient way on FPGAs. For the Example 4.1 with the given samples in Table 4.2 it follows:

$$y[n_{\text{example}}] = V_0 \cdot 2^{N-1} + V_5 \cdot 2^{N-2} + ... + V_3 \cdot 2^0 \tag{4.36}$$

Summarising the above, it has been shown that many costly multiplications (Figure 4.17) can be substituted with look-up tables, bitshifts and summations. The price for this efficient implementation is the much more complicated hardware description. Therefore a software package was developed to simplify the process and is explained in the following.

Software Package for FIR Filter Implementation

The DA description software generates the hardware description for an arbitrary FIR filter. The user chooses the desired band ranges (pass band, transmission band and stop band) and the desired order of the filter. As described in Subsection 4.4.2, the software framework uses the Remez-Algorithm ([MP05]) to determine the filter coefficients.
In practice, a high order FIR filter is desired. For instance, the current implementation of the Mainz firmware offers a 20-coefficient FIR filter ($M+1 = 20$) for every single ADC input channel (Subsection 5.2.1). Thus, there are 2^{20} possible results for Equation 4.35, which definitely can not fit into a single look-up table.
The workaround is, to segment the large look-up table (address width = $M + 1$) into N_{LUT} smaller once.

$$N_{\text{LUT}} = \frac{M+1}{L_{\text{size}}} \tag{4.37}$$

with L_{size} being the address width of the sub look-up tables. Depending on the architecture, nowadays FPGAs offer LUTs with address widths of up to 6 bits (Subsection 4.1.2).
As a function of the input parameters, the software defines the sub look-up table size in the way, that the result of Equation 4.37 is without a remainder and close (smaller or equal) to the LUT address width limit of the FPGA.
In a further step, the software generates the sub look-up tables and the hardware description of the DA implementation. The DA implementation consists of a pipeline buffer (Figure 4.12), which holds $M + 1$ samples at a time. The samples are aligned as shown in Table 4.2. The columns, which represent the binary weight position are connected piecewise to the sub look-up tables. In contrast to Example 4.1 the result of the calculation is distributed over several look-up tables. Thus an additional adder needs to accumulate the interim results. The output of the adder is V_i. In Figure 4.18 an example of the procedure is depicted. A $M + 1 = 4$ look-up table is split into $N_{\text{LUT}} = 2$ look-up tables of the size $L_{\text{size}} = 2$.
After the short detour, the process ends equally to an one look-up table calculation (Table 4.2). The final result is again the sum over all V_i's by weighting them with their appropriate 2^l factor (Equation 4.36).

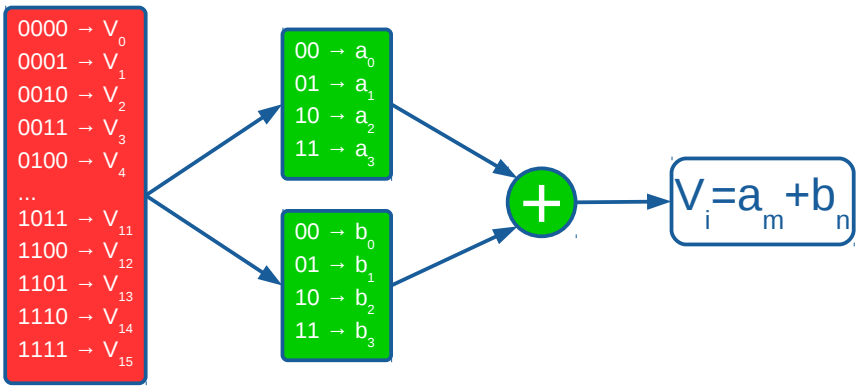

Figure 4.18: The illustration shows the splitting of a $M+1=4$ look-up table into $N_{\mathrm{LUT}}=2$ sub look-up tables of the size $L_{\mathrm{size}}=2$. The DA description package finds the best subdivision of the main look-up table automatically. Furthermore, it calculates the output values of the sub look-up tables.

In the particular case of the current implementation of a FIR filter with $M+1=20$ coefficients, the DA description package has performed a subdivision into $N_{\mathrm{LUT}}=4$ sub look-up tables of the size $L_{\mathrm{size}}=5$.
As final step, the software executes a test bench, which tests the DA implementation by comparing the filter response with known values.

4.5 Time Measurement and Amplitude Extraction

The Time Measurement and Amplitude eXtraction (TMAX) algorithm is a collection of routines which actually perform both the hit detection and the parameter extraction, i.e. the amplitude information and time information of a calorimeter pulse. It is applied to the FIR filtered signal. The algorithm collection can handle positive and negative preamplifier pulses. However, the explanation in the following refers to negative pulses. The central idea of the algorithm is to perform a derivation with a subsequent integration. Thus, the direct current (DC) component of the baseline disappears. This approach avoids a baseline follower. A second reason for the derivation is the pileup reduction. The TMAX algorithm is capable to detect pileup on the falling edge of the calorimeter preamplifier pulse. The design of the algorithm targets a subsequent amplitude recovery of pileup pulses on the falling edge. As it will be shown in the beam test results in Chapter 6, the TMAX algorithm makes high detector rate measurements ($\sim$100 kHz) possible.
The essential derivation (D) at the FIR filtered signal (T) is defined as:

$$D[i] = T[i] - T[i-r] \tag{4.38}$$

The derivation parameter r needs to be in a certain window to be sensitive to the rising

edge. Furthermore, it should be a power of two to perform an efficient implementation on the FPGA.
The next step is to invert the derivative and blocking all positive components. With the help of the Heaviside function Θ:

$$\Theta(x) \mapsto \begin{cases} 0: & x < 0 \\ 1: & x \geq 0 \end{cases} \tag{4.39}$$

it follows:

$$D^*_{\text{inv}}[i] = -\Theta(D[i]) \cdot D[i] \tag{4.40}$$

The sum

$$D_s[i] = D[i] + D^*_{\text{inv}}[i] \tag{4.41}$$

cancels out the falling edge of the pulse. By summing up D_s whenever it is smaller than zero the integral function F_{TMAX} can be written as:

$$D_s[i] \mapsto \begin{cases} F_{TMAX}[i] = F_{TMAX}[i-1] + \frac{D_s[i]}{r} & : D_s[i] < 0 \\ F_{TMAX}[i] = 0 & : D_s[i] = 0 \end{cases} \tag{4.42}$$

In Figure 4.19 the different components of the integral function for a derivative parameter of $r = 4$ are shown.

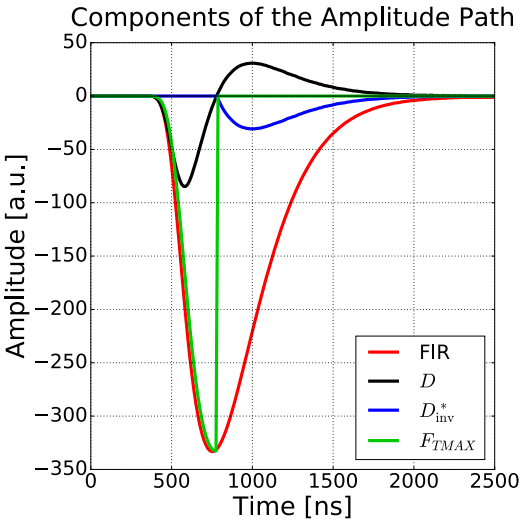

Figure 4.19: The figure shows the components of the integral function F_{TMAX} for a derivative parameter $r = 4$. The extracted amplitude is a candidate for a hit. It has to be ensured that it is a true hit. In particular for small energy pulses close to the noise floor, it becomes much more challenging to make a decision. Thus, the hit detection path was developed to perform a proper discrimination.

All following algorithms will use the integration function F_{TMAX} or components of it for different tasks, which run in parallel on the FPGA. Thus, the further description of the algorithms is divided into paths.

4.5.1 The Hit Detection Path

The discrimination between true hits and noise hits is performed by the hit detection path. A good parameter of a true hit is defined by its time under threshold. It is the number of samples i_t during which F_{TMAX} is smaller than zero (Equation 4.42). If the time is too short or too long, then it is most likely a noise hit. To adapt the time under threshold condition even more to the APFEL preamplifier pulse shape, a weight function λ_t was developed. The idea behind this function is to weight signal shapes, which appear like a rising edge of an APFEL pulse stronger than other shapes. The time under threshold condition is implicitly included due to the peak position of the weight function. Pulses, which have a proper time under threshold are stronger weighted than others. The weight function is an empirical function and defined as:

$$\lambda(i_t) \mapsto \begin{cases} e^{A_t \cdot i_t} & : i_t \leq P_t \\ M_t \cdot e^{-A_t(i_t - P_t)} & : i_t > P_t \end{cases} \tag{4.43}$$

With P_t being the maximum position and M_t the maximum amplitude of the function. P_t and M_t are connected through the relation $A_t = \frac{log(M_t)}{P_t}$. In Figure 4.20 an example for a weight function with the parameters $P_t = 28$ and $M_t = 2$ is depicted.

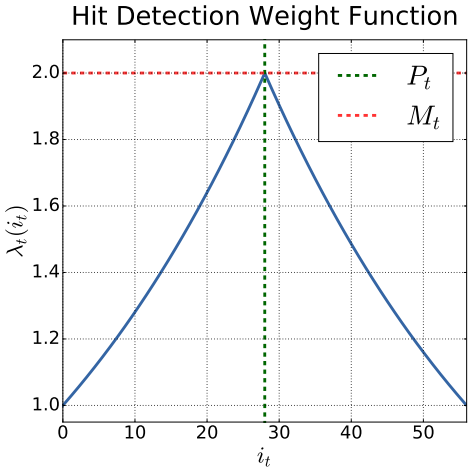

Figure 4.20: The illustration shows the weight function of the hit detection path with the parameters $P_t = 28$ and $M_t = 2$. The weight function is used to calculate a weighted sum with the extraction function F_{TMAX} whenever the extraction function is smaller than zero. If both, the time under threshold and the pulse shape are similar to an APFEL preamplifier theory pulse, the weighted sum peaks stronger compared to a noise hit pulse. This behaviour can be seen in Figure 4.21.

A $P_t = 28$ refers to a peak position at 350 ns for an ADC with a sampling rate of 80 MHz. This is slightly more than the typical rising time of 300 ns of an APFEL preamplifier pulse. The trigger is set on the weighted sum:

$$R_t = \sum_{k=0}^{i_k} \lambda_t[k] \cdot F_{TMAX}[k] \tag{4.44}$$

If R_t exceeds the threshold ts while F_{TMAX} is smaller than zero, the event is identified as a hit. There is a threshold ts for both the APFEL preamplifier low amplification (ts_L) and the high amplification (ts_H). For a more intuitive usage, the thresholds can

be set in units of ADC channels (q) or in units of energy (MeV), if the APD gain is known. The threshold is internally converted within the FPGA hardware description into a value that it is comparable with R_t. In Figure 4.21 an example of the hit detection capability for low energy (3 MeV) events is illustrated. The plot is done with the simulation framework, which will be introduced in Chapter 5.

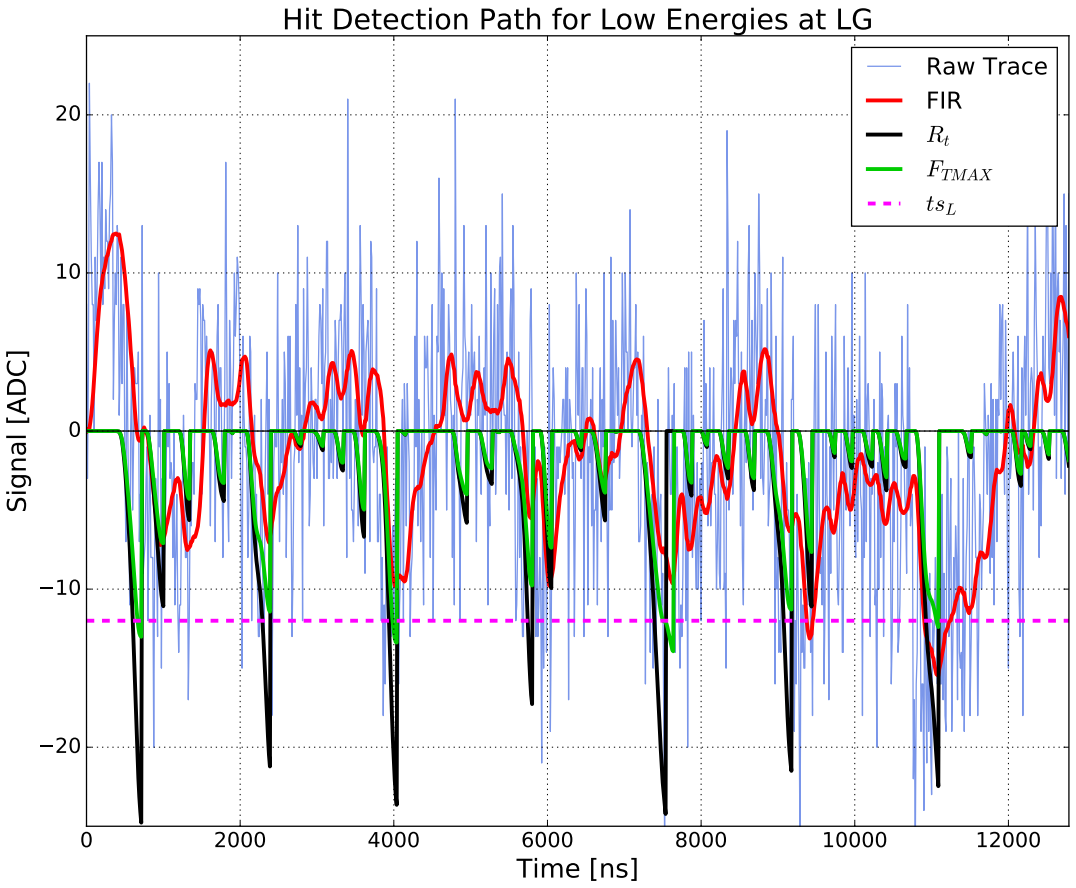

Figure 4.21: The plot demonstrates the pulse recognition for low energy (3 MeV) pulses at low gain amplification. The hit detection parameters are $P_t = 28$ and $M_t = 2$. Seven input pulses are distributed on the trace with a distance of 1700 ns between each other. The weighted sum R_t peaks stronger at true hits compared to noise hits. At the true hits, the amplitude of R_t (black) is about twice the amplitude of the integral function F_{TMAX} (green). In contrast to noise hits, where R_t and F_{TMAX} peak with a similar amplitude. The passing of the threshold ts_L defines the recognition of the hit. The plot is generated by using the simulation framework, which will be introduced in Chapter 5.

4.5.2 The Amplitude Path

The amplitude path directly uses the integral function F_{TMAX} to determine the amplitude value. The amplitude path continously updates a register with the current value of F_{TMAX} whenever it is smaller than the previous value. The register is rested whenever F_{TMAX} becomes zero.
In parallel to the amplitude path, the hit detection path performs the discrimination. If the hit detection path indicates a hit, the last value within the register before the reset defines the amplitude of the event. Afterwards, the hit amplitude information is collected with the hit time information.

4.5.3 The Time Path

The time path is designed to determine the occurrence time T_0 of the pulse. The idea is to use a unique point within the pulse shape which is not amplitude (energy) dependent. The theoretical function of the PANDA APFEL preamplifier is given by:

$$f(x) = -A \cdot e^{\frac{-N(x-\delta)}{\tau}} \cdot \left(\frac{x-\delta}{\tau}\right)^N, \tag{4.45}$$

with the parameters δ, τ, N and A. The shift parameter δ describes the starting point of the pulse. The rising time is defined by the parameter τ. Furthermore, the parameter N has an impact on the decay time and A is related to the pulse hight H and the parameter N via:

$$A = H \cdot e^N \tag{4.46}$$

Since it is not possible to determine the starting point δ within the noise floor, T_0 is extracted at the first inflexion point ($f''(x) = 0$) I of the pulse:

$$T_0 = \delta + I \tag{4.47}$$

with

$$I = \frac{\tau(\sqrt{N} - 1)}{\sqrt{N}} \tag{4.48}$$

The realisation of the time path is done by the determination of the zero transition of the second derivative D' of the FIR smoothed signal. The step width of $T = 12.5$ ns at a sampling frequency of 80 MHz limits the time resolution. Thus, a linear interpolation between two time-discrete values of $D'[i]$ is implemented:

$$T_0 = i_0 + \frac{D'[i_0]}{D'[i_0] - D'[i_1]} \tag{4.49}$$

with i_0 and i_1, being the samples right before and after the zero transition of $D'[i]$.

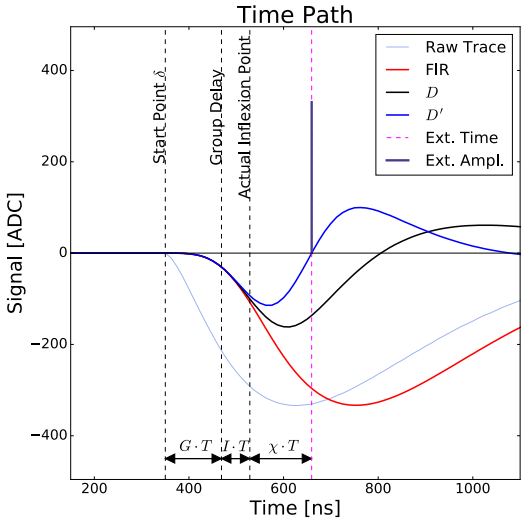

Figure 4.22: The illustration shows the T_0 determination of an APFEL preamplifier pulse. The time path is applied on the FIR filtered signal. T_0 is extracted at the zero transition of the second derivative D'. Compared to the actual input pulse start position δ, the extracted time T_0 is shifted by three constants: The FIR group delay G, the duration to the inflexion point I and χ, which is a function of the parameters N, τ and r. χ can be determined numerically.

The extracted T_0 is shifted compared to the original starting point δ of the input pulse. On the one hand there is the group delay G caused by the FIR filtering (Equation 4.29). On the other hand, T_0 is extracted at the first inflexion point of the pulse, thus I has to be subtracted from T_0 to obtain the starting point of the pulse. Due to the numeric determination of the second derivative, the zero transit is shifted by the value χ. Whereby χ is a function of N, τ and r and can be numerically computed for a specific parameter set.
The total shift is:

$$T_{\text{shift}} = T \cdot (G + I + \chi) \tag{4.50}$$

The different time shift contributions are displayed in Figure 4.22.

4.5.4 Pileup Detection and Correction

The $\bar{\text{P}}$ANDA EMC TDR ([TDR08]) requires a single crystal hit rate of up to 100 kHz for the barrel and backward part of the EMC. The probability for k events in an interval ΔT at a rate R follows the Poisson distribution:

$$P_\lambda(k) = \frac{\lambda^k}{k!} \cdot e^{-\lambda} \tag{4.51}$$

Whereby $\lambda = \Delta T \cdot R$. The probability for one or more additional events ($k \geq 1$) at the full pulse length ($\Delta T = 1500$ ns) at $R = 100$ kHz is

$$P_\lambda(k \geq 1) = 1 - P_\lambda(k = 0) = 13.9\,\%.$$

The TMAX algorithm can detect pileup hits on the falling edge of the pulse. The minimum time distance between the first and the second hit is a function of both the derivative parameter r and the FIR filter characteristics.
A typical value for the minimal time between hits is about 450 ns. Pulses, which are closer together than this, can not be distinguished and appear as one pulse with a higher amplitude.

In Figure 4.23 an example for a second pulse on the falling edge of a pulse is depicted. The second pulse has a smaller extracted amplitude compared to the first pulse. Thus, the amplitude of the second pulse needs to be corrected.

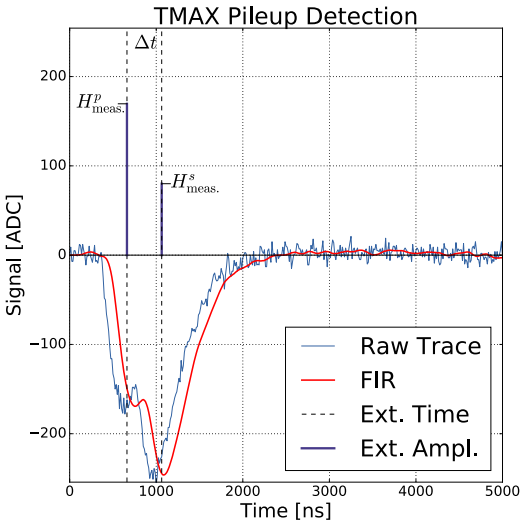

Figure 4.23: The plot shows a second pulse on the falling edge of a first pulse. Both the first and the second pulse represent an energy of 50 MeV. The time distance between the pulses is Δt. The extracted amplitude of the second pulse is smaller than its actual height. However, with the information of the extracted amplitudes $H^p_{\text{meas.}}$ and $H^s_{\text{meas.}}$ together with Δt an offline amplitude correction for the second pulse is possible. In Chapter 6, this method is used to operate the EMC prototype under high rate conditions.

The time path of the TMAX algorithm is able to determine the appearance times T_p of the primary pulse and T_s of the second pulse, thus the time difference $\Delta t = T_s - T_p$ can be computed. With the amplitude information of the first pulse $H^p_{\text{meas.}}$ and the second pulse $H^s_{\text{meas.}}$ in combination with the time difference Δt, an offline amplitude correction can be performed:

$$H^s_{\text{corr.}} = H^s_{\text{meas.}} \cdot \Sigma(H^p_{\text{meas.}}, H^s_{\text{meas.}}, \Delta t) \tag{4.52}$$

with Σ being the correction function. In Chapter 6 a first approach for the determination of the correction function is made by using beam data. Furthermore, a detailed discussion about pileup and dead time of the EMC can be found in Section 6.6.

5 Simulation of Signal Processing Algorithms

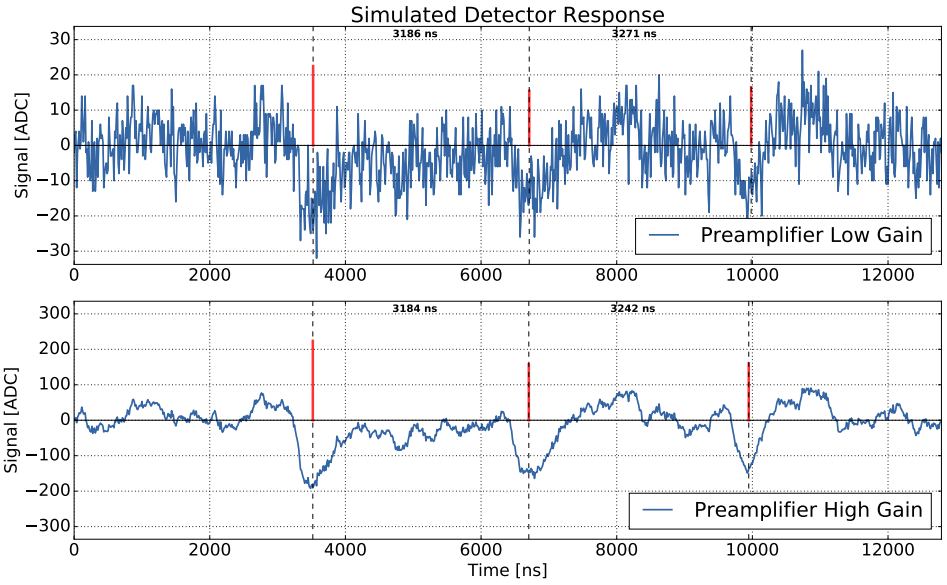

The plots show simulated single APD detector traces with 5 MeV *events for the APFEL preamplifier high gain and low gain. The red bars indicate both the found hits on the trace and their extracted heights. The simulation of the detector response is important for the development of pulse parameter extraction algorithms and the validation of these algorithms under defined conditions.*

In an early stage of the development of parameter extraction algorithms for APFEL preamplifier pulses, the need for a detector response simulation framework has manifested. The aim was to simulate the detector response as accurately as possible. For this reason, the detector response was extensively studied in the laboratory. Furthermore, the software signal processing routines were optimised to behave as similarly as possible to their counterparts on the FPGA. The framework has been improved over the years in terms of the accuracy of the simulation and its usability. As a result, the software package was embedded into PandaRoot, which is the simulation, reconstruction and analysis framework of $\bar{\text{P}}$ANDA.

In the following the key elements of the software modules, which are the realistic signal generator and the implementation of the APFEL preamplifier parameter extraction routines, will be explained. After the explanation, a comparison between simulation and measurement will be given.

The second part of this chapter focuses on the validation of the signal processing routines, which were introduced in Chapter 4. After the motivation of the used parameters for the FIR filter and the extraction routines, the simulation procedure will be introduced.

The simulation gives access to detector parameters as a function of the APD gain. For instance, the noise hit rate and the detection efficiency are accessible. Noise hists are signal fluctuations due to noise, which are recognised as pulses (events), while the efficiency is the ratio between detected real hits and all possible real hits. Furthermore, the time resolution and energy-pulse height dependency can be addressed.

With this information, the parameter extraction performance can be compared with the $\bar{\text{P}}$ANDA TDR requirements and the real detector can be adjusted accordingly. The chapter closes with a summary of the validation results in tabular form.

5.1 Detector Response Simulation Framework

The simulation framework is capable of simulating both realistic detector signals and the parameter extraction as it is introduced in Chapter 4. Realistic means in this context that the most dominant detector characteristics are considered for the simulation of APFEL preamplifier pulses. The software implementation of the parameter extraction resembles as close as possible the behaviour of the hardware implementation on the FPGA.
The framework can be used to generate arbitrary pulse sequences and test the response of the parameter extraction. Thus, a comparison between input (energies and times) and output (amplitudes and timestamps) can be made quickly. Furthermore, the optimisation of parameters and performance studies can be done.
In the following, first, the realistic signal generator will be introduced and subsequently, the software implementation of the APFEL pulse parameter extraction.

5.1.1 Realistic Signal Generator

The relevant information in the detector signal is in the APFEL preamplifier pulse shape. This information is disturbed by noise from various sources. A realistic signal generator has to simulate both the useful APFEL preamplifier pulse and the relevant noise components.
The theoretical pulse shape of APFEL preamplifier pulses is described by Equation 4.45. However, the function is repeated here for the sake of clarity:

$$f(x) = -A \cdot e^{\frac{-N(x-\delta)}{\tau}} \cdot \left(\frac{x-\delta}{\tau}\right)^N \tag{5.1}$$

The pulse parameters N and τ are extracted from fits to waveforms, recorded with a real detector. The shift parameter δ sets the pulse occurrence time. The pulse height is proportional to the parameter A. In Figure 5.1 an example of a 50 MeV (APD gain 200) signal without noise is depicted. The occurrence time δ is set to zero.

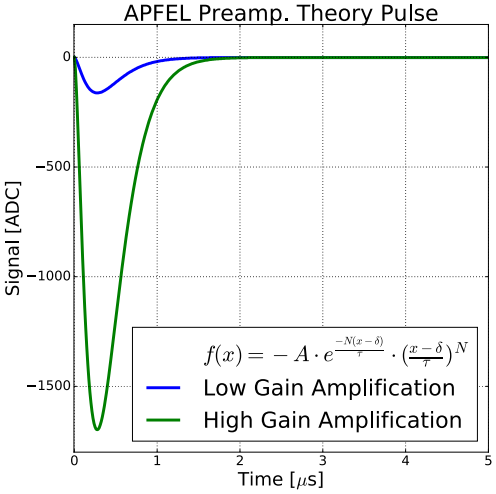

Figure 5.1: The plot shows a 50 MeV (APD gain 200) signal without any noise, which is generated by the signal generator. The signal generator always produces an output for the low gain amplification and an output for the high gain amplification. The fixed parameters N and τ as well as the ratio between high gain and low gain was determined with detector data. The parameter δ and A are used to define the occurrence time and the pulse height.

The pulse height contains the energy information of an event. Thus, a conversion function α is needed, which translates a pulse height in units of ADC steps [channel] into a corresponding energy [MeV].

$$\alpha = \frac{q}{M \cdot LY_{-25\,^\circ\mathrm{C}} \cdot A_{\mathrm{eff.}} \cdot Q_{\mathrm{eff.}} \cdot e \cdot G_{\mathrm{ASIC}}} \quad [\mathrm{MeV/channel}] \tag{5.2}$$

q [mV/channel] is the digitisation step size of the ADC. M is the APD gain without a unit. $LY_{-25\,^\circ\mathrm{C}}$ is the light yield of the lead tungstate crystal at $-25\,^\circ\mathrm{C}$ in units of [$\mathrm{n_{photo.}}$/MeV]. A_{eff} [%] is the effective area coverage of an APD on the front face of a lead tungstate crystal. Q_{eff} [$\mathrm{n_{elec.}}/\mathrm{n_{photo.}}$] is the quantum efficiency of the used APDs. e [C] is the elementary charge which converts the number of electrons $n_{\mathrm{elec.}}$ with the APFEL preamplifier gain G_{ASIC} [$\mathrm{mV\,C^{-1}}$] into a voltage [mV]. The corresponding values of the mentioned parameters are summarised in Table 5.1.

Parameter	Value	Unit	Source
q	0.122	mV/channel	[Cor18]
M	≥ 1	-	-
$LY_{-25\,^\circ\mathrm{C}}$	500	$\mathrm{n_{photo.}}$/MeV	[TDR08]
$A_{\mathrm{eff.}}$	16	%	[HAM09]
$Q_{\mathrm{eff.}}$	0.70	$\mathrm{n_{elec.}}/\mathrm{n_{photo.}}$	[HAM09]
e	$1.602\,176\,634 \times 10^{-19}$	C	[NT19a]
G_{ASIC}	0.22×10^{15}	$\mathrm{mV\,C^{-1}}$	[Wie19]

Table 5.1: The table shows the values of the parameters of Equation 5.2.

By using Equation 5.2, it follows for the pulse height H in units of ADC channels:

$$H = \frac{E\ [\mathrm{MeV}]}{\alpha(M)} \quad [\mathrm{channel}] \tag{5.3}$$

Together with Equation 4.46 the final result for the parameter A is:

$$A = E\ [\mathrm{MeV}] \cdot \alpha(M)^{-1} e^{N} \tag{5.4}$$

5.1.2 Signal Noise Model

The signal noise has different origins. On the one hand, there is the noise from the ADC, which reduces the effective resolution of the ADC (Subsection 4.1.1). Furthermore, the line-driver board (Figure 3.10) has active components and transmits the signal from the APFEL preamplifier to the ADC over several meters of cables. Finally, the most dominant source of noise is the APFEL preamplifier itself.
All the mentioned noise sources have a characteristic spectral density. For example, white noise at the entrance of the APFEL preamplifier is also transformed by the preamplifier transfer function. Thus, the time structure of the APFEL preamplifier noise is similar to the time structure of the useful signal.

A measurement was performed to determine the different noise contributions. The setup consisted of the $\bar{\text{P}}$ANDA SADC (Section 4.2), the calorimeter line-driver electronics and an APFEL preamplifier, which was equipped with two biased (380 V) APDs. In Figure 5.2 the spectral densities for the different noise sources are shown. The displayed spectra were generated by performing a Fast Fourier Transformation (FFT) of the baselines, each with $N = 1024$ samples. 120 FFTs have been averaged for all setups to allow for a clear determination of the noise floor. Generally, an FFT analyses N samples to extract information about the whole signal. This is done by theoretical infinitesimal repetitions of these N samples. As a result, the theoretical signal has discontinuities on the borders, which are also known as leakage errors. A window can be applied to the time domain samples before the FFT to reduce the leakage errors. All FFT results in this work were generated by using a hann window [Sch16].

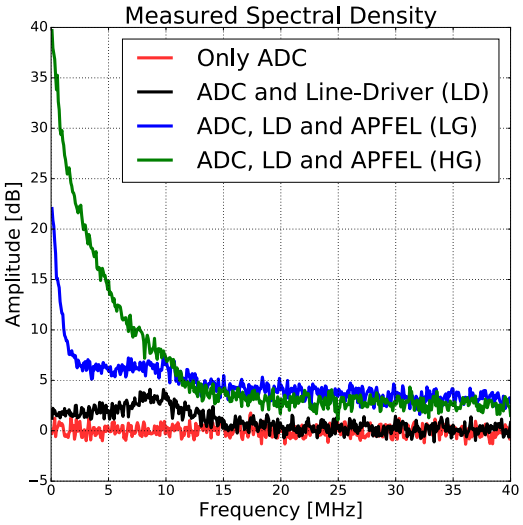

Figure 5.2: The plot shows the measured spectral density for different setups. The ADC contribution is negligible compared to the overall noise level. Thus, the signal baseline taken with the ADC alone, is set as a reference (0 dB). The line-driver board contributes to the region between 5 MHz and 15 MHz. The most dominant contributions come from the APFEL preamplifier. These are different depending on the amplification factor. Realistic noise is generated by using the composed spectral density distributions (LG, HG) as input.

The procedure for simulating a realistic noise floor is to generate baselines by mixing frequency components according to the measured composed spectral density.
The spectral density is subdivided into small frequency intervals (I_i). Every frequency interval is assigned to a cosine which is oscillating with the corresponding frequency. From the technical point of view, it refers to the real part of an inverse FFT. The simulation model assumes uniformly distributed phases. A random generator generates the phase ϕ_i for a particular cosine. The output cosine ($C(I_i)$) contributes with a certain amplitude to the overall spectral density. Thus, the amplitude of the generated cosine has to be weighted with the corresponding power from the measured spectral density $P(I_i)$ [dB].

$$C(I_i) = cos_{I_i}(x + \phi_i) \cdot 10^{\frac{P(I_i)[\text{dB}]}{20}} \tag{5.5}$$

Finally, the composed noise floor T_{noise} is the sum over all components:

$$T_{\text{noise}} = \sum_{i=1}^{N_I} C(I_i) \tag{5.6}$$

whereby N_I is the number of intervals. There are 1024 possible intervals from the FFT. However, to reduce computing time, the current implementation reduces the number of intervals by a factor of two. Thus, $N_I = 512$ intervals are used for the simulation. In order to illustrate Equation 5.6, a baseline is depicted in Figure 5.3. The plots show the same baseline including frequency intervals up to 1 MHz, 5 MHz and 40 MHz, respectively.

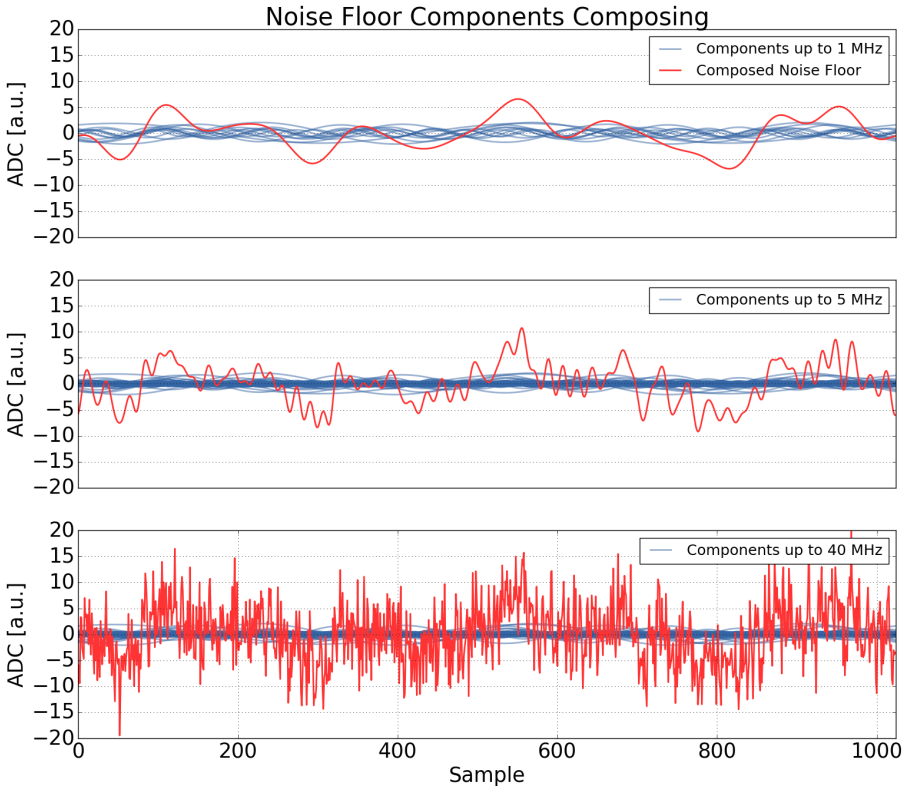

Figure 5.3: The three plots show the composition of the noise floor at low gain amplification with three different bandwidths. According to the spectral density (Figure 5.2), the various components contribute with different amplitudes to the overall noise.

One hundred twenty traces were generated with the method just described to validate the noise generating procedure. An FFT analysis processed the traces. The comparison between the measured and simulated spectral densities can be seen in Figure 5.4. The simulated spectral densities follow the measured spectral densities in a good agreement. In particular, the relevant part (< 10 MHz) is well reproduced. Nevertheless, there is a discrepancy at higher frequencies of about 3 dB. Since a finite impulse response filter with a cut-off frequency of 7.2 MHz will be applied on the signals, the deviation can be neglected.

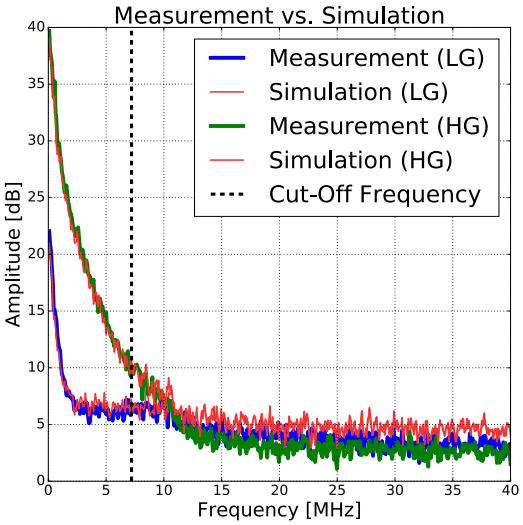

Figure 5.4: The plot shows the comparison between the measured and the simulated spectral densities. In either case, 120 baselines for the high gain and the low gain were analysed. The simulations fit the measured spectra to a decent extend. Especially the low-frequency components ($< 10\,\mathrm{MHz}$) show a good agreement. Nevertheless, there is a discrepancy at higher frequencies of about 3 dB. Since a finite impulse response filter with a cut-off frequency of 7.2 MHz will be applied on the signals, the deviation can be neglected.

Besides the frequency domain, a comparison between measurement and simulation can be made in the time domain. Of course, it is much more difficult to identify the time structure of the noise floor by just looking at baselines. Anyhow, the comparison of the baseline projection along the time axis gives at least a hint for the simulation quality. In Figure 5.5 measured and simulated baselines are compared.

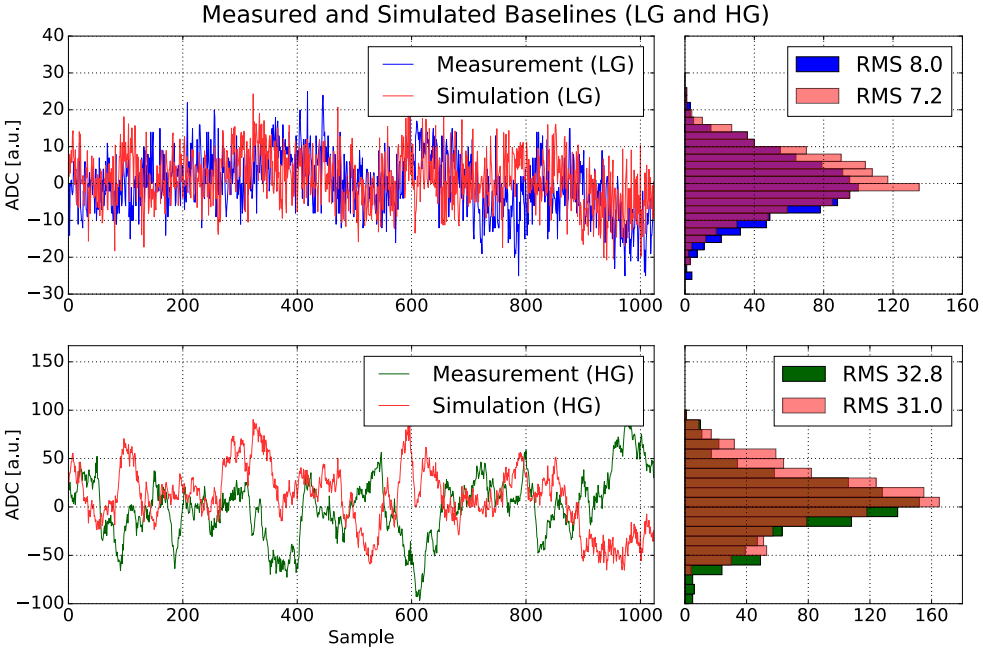

Figure 5.5: The plot shows the time structure comparison between a simulated and measured baseline for both high gain and low gain amplification. By considering the baseline histograms, a good agreement in terms of the RMS can be identified.

5.1.3 Merging of Simulated Pulse and Simulated Noise Floor

The last step is to merge the generated noise floor with the theoretical pulse shape. For every simulated detector hit a new baseline is generated. Furthermore, the output resolution of the signal generator is reduced in order to simulate the resolution limits of the ADC. In Figure 5.6 a complete simulated 50 MeV detector event is depicted.

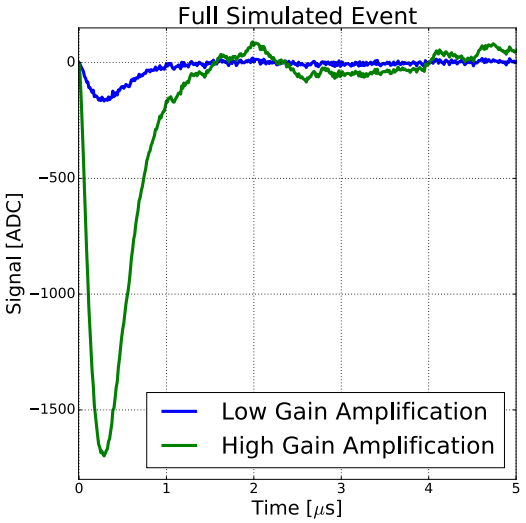

Figure 5.6: The plot shows a simulated 50 MeV detector event with a realistic noise floor. The event generator uses the spectral density of real detector baselines to simulate the noise floor for the APFEL high gain and low gain amplification. The spectral densities from the low and high gain baselines differ. The high gain signal has a more substantial contribution of low-frequency components, which is in agreement with the measured spectral density in Figure 5.2.

5.1.4 Software Implementation of the Parameter Extraction

The software implementation of the parameter extraction includes both, the finite impulse response filter (Subsection 4.4.2) and the TMAX algorithms (Section 4.5). The modules are designed to easily change configuration parameters such as coefficients of the FIR filter or the extraction parameters of the TMAX modules. Furthermore, all precision issues, which are present on digital devices, are considered. More precisely, the high precision floating point calculations, which are common for nowadays CPUs are artificially worsened to a fixpoint calculation as they are used on FPGA devices. Thus, the output of the software parameter extraction can be directly compared with the output of the FPGA. More information about the software package and how to use it can be found in [Nol19].

5.1.5 Comparison between Measurement and Simulation

A comparison between real detector measurements and simulation will be made in the following to validate the results of the simulation framework. As a first crosscheck 120 simulated and 120 measured baselines were passed to the parameter extraction software. In both cases, the number of noise hits as a function of the hit detection threshold was counted. The average number of noise hits should be similar for simulated baselines and measured baselines. In Figure 5.7, the ratio between the average number of noise hits between measured baselines and simulated baselines as a function of the hit detection threshold are drawn. The threshold was scanned between 0 MeV and 3.5 MeV for the

low gain amplification and between 0 MeV and 2.5 MeV for the high gain amplification. Since the probability for noise hits decreases by increasing the threshold, the absolute number of noise hits is smaller for higher thresholds. Thus, the statistical uncertainties also increase for ratios at higher thresholds. As it will be shown in the further course of this chapter, for a typical APD gain of 200 a noise hit rate of about 150 kHz in the low gain amplification and about 40 kHz in the high gain amplification for a hit detection threshold of 2.5 MeV are expected. Consequently, a 10 %-band as it is drawn in Figure 5.7 corresponds to ±15 kHz in the low gain amplification and to ±4 kHz in the high gain amplification at a threshold 2.5 MeV.

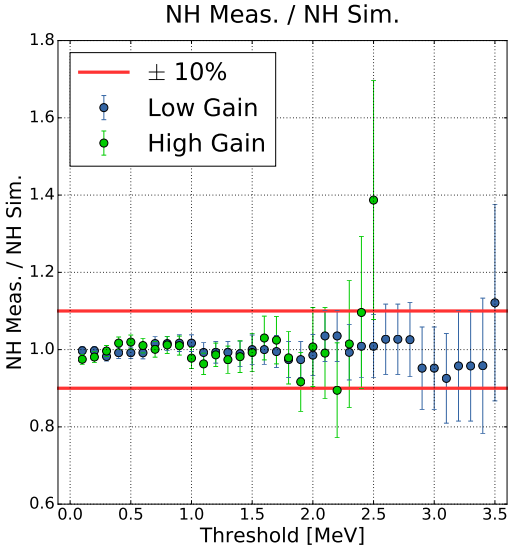

Figure 5.7: The plot shows the ratio of the average number of noise hits between measured baselines and simulated baselines. The noise hits were extracted with the software implementation of the parameter extraction. Most of the ratios are close to one and within a 10 %-band. The few outliers agree within the error bars with the band. The larger errorbars for ratios at higher thresholds can be explained due to the lower statistics because of the lower noise hit probability at higher thresholds.

As a second measure for the simulation quality, the relative energy resolution (Subsection 3.1.4) is considered. The important parameter for the following discussion is the electronic noise term (c in Equation 3.4). In the case of the simulation, energy spectra for a single APD channel were generated in the low gain amplification. The APD gain was set to $M = 150$ and the hit detection threshold was set to $th_L = 2.5\,\text{MeV}$. From the energy spectra, both the position and the standard deviation of the spectra were extracted. Consequently, the relative energy resolution for the simulation is determined according to Subsection 3.1.4. Since the simulation only includes the electronic noise term c, the relative energy resolution function becomes:

$$\frac{\sigma_E}{E} = \frac{c}{E} \tag{5.7}$$

The energy resolution for a 3×3 crystal matrix was determined to compare the simulation with measurement. A detailed explanation of how such a measurement is done by using the MAMI accelerator is given in Chapter 6. For the analysis, only data from one APD per crystal was used since the simulation was also performed for only one APD channel. Equally to the simulation, the APD gain was set to $M = 150$ and the hit detection threshold was set to $ts_L = 2.5\,\text{MeV}$. The measured relative energy resolution is shown in Figure 5.8.

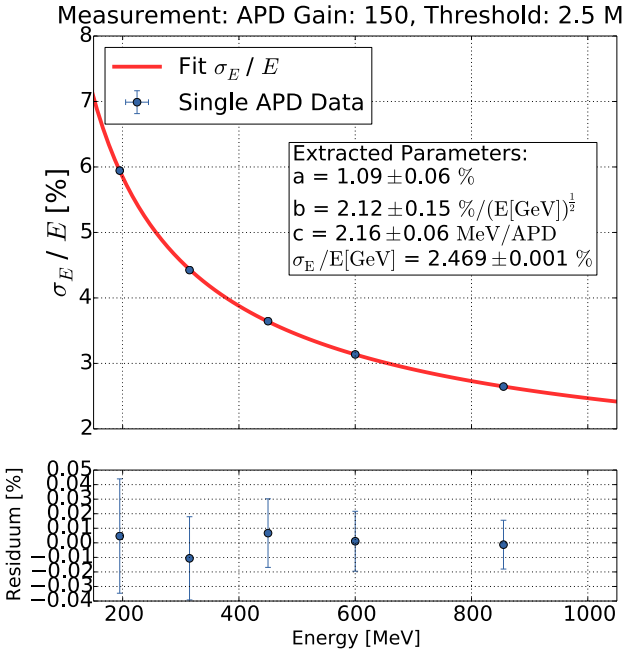

Figure 5.8: The plot shows the measured relative energy resolution for a 3×3 crystal matrix. A detailed explanation of the measuring process by using the MAMI accelerator is given in Chapter 6. The measurement was performed with the same APD gain ($M = 150$) and the same hit detection threshold ($ts_L = 2.5\,\text{MeV}$) as it was set in the simulation. Furthermore, only one APD per crystal was used for the analysis to compare the measurement with the simulation.

In contrast to the simulation, the measured relative energy resolution contains the statistical fluctuation term (b in Equation 3.4) and the constant term (a in Equation 3.4). Thus, Equation 3.4 is rearranged to isolate the c/E part:

$$\frac{c}{E} = \sqrt{\left(\frac{\sigma_E}{E}\right)^2_{3\times3} - a^2 - \frac{b^2}{E}} \tag{5.8}$$

Here, $\left(\frac{\sigma_E}{E}\right)^2_{3\times3}$ is the measured relative energy resolution at energy E using a 3×3 crystal cluster. The parameters a and b are extracted from the energy resolution fit in Figure 5.8. Since the noise of different APD channels is summed quadratically, the single APD channel noise for a 3×3 crystal matrix is a factor $\sqrt{9}$ smaller than the cluster noise.

By correcting the measured relative energy resolution following the discussion above, the c/E part for a single APD channel is extracted and depicted together with the simulated c/E dependency in Figure 5.9. The extracted c parameter from the simulation is 2.095(6) MeV while the extracted c parameter from the measurement is 2.16(6) MeV.

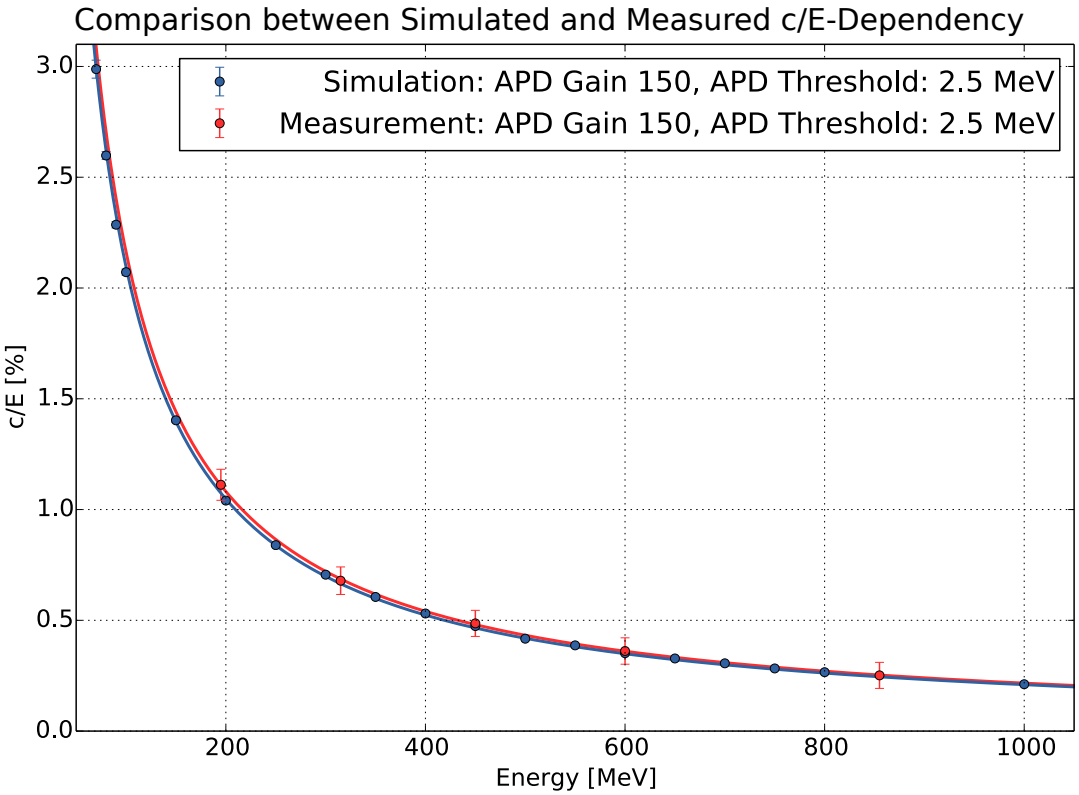

Figure 5.9: The plot shows the comparison of the single APD channel electronic noise contribution to the relative energy resolution for both simulated and measured data. In both cases, the APD gain was $M = 150$ and the APD threshold was $ts_L = 2.5\,\mathrm{MeV}$. Simulation and measurement are in good agreement within the uncertainties.

5.2 Performance of Parameter Extraction for Electromagnetic Calorimeter Preamplifier (APFEL) Signals

The detector response simulation framework allows for validating the APFEL preamplifier parameter extraction algorithms under defined conditions. Beforehand, the simulation framework was used to find suitable parameter sets for both the FIR filter and TMAX algorithms. However, this process was always an interplay with the hardware implementation on the FPGA. For example, the number of FIR coefficients was increased until the FPGA implementation tool was no longer able to fit the needed logic on the FPGA. By adding some headroom, the current FPGA implementation offers a 20-coefficient FIR filter for every channel. In the following, the utilised input parameters are motivated. Subsequently, the simulation procedure for parameter validation is described. Finally, the simulation results for the detector noise hit rate, the detector efficiency, the time resolution and the energy-pulse height dependency

are shown. The results differ by using different APD gains due to changes in the signal to noise ratio. Thus, the simulations were performed for a variety of APD gains. Nevertheless, the discussion refers to a typical APD gain of $M = 200$. In the course of the section, it will be referred to results with other APD gains in Appendix B.

5.2.1 Parameter Set for FIR Filtering

The usage of FIR filtering aims to reduce high-frequency noise while preserving the pulse shape. The fastest component of the useful signal is within the rising edge of the pulse. The rising time of about 300 ns leads to an average frequency for the fast pulse components of f_{fast}=3.333 MHz.
An ideal filter would let pass all frequency components up to f_{fast} and stop all higher frequencies. As already explained in Subsection 4.4.2, the convergence of a realisable filter to an ideal filter is a function of the number of the filter coefficients. The more coefficients, the sharper the filter bands. Furthermore, boundary conditions such as available logic on the $\bar{\text{P}}$ANDA SADC FPGA need to be considered.
As a result, a filter with 20 filter coefficients was selected. The passband was chosen from 0.0 MHz to 1.0 MHz, which does not cover the fastest components of the signal. However, in combination with the transition band [1.0 MHz, 7.2 MHz], most of the fast signal frequency components are conserved as it is shown in the filter's frequency response in Figure 5.10. The stopband starts about 1 MHz after the Nyquist frequency for f_{fast} at 7.2 MHz. The chosen bands are summarised in Table 5.2.

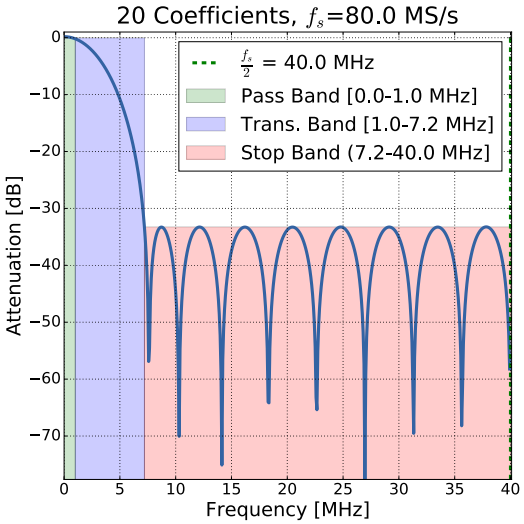

Figure 5.10: The figure shows the frequency response of the implemented FIR filter. The passband is between 0.0 MHz and 1.0 MHz. The transmission band is between 1.0 MHz and 7.2 MHz. The damping at the highest useful signal frequency is less than 4 dB. The stopband starts at 7.2 MHz. The choice is a compromise between filter sharpness, damping and the available resources on the $\bar{\text{P}}$ANDA SADC FPGAs.

Finally, the pole-zero diagram (Subsection 4.4.2) of the filter transfer function is shown in Figure 5.11. Most of the zeros are placed around the unit circle on the complex plane to achieve the low pass characteristics of the filter. This characteristic can also be found for simple moving average filters, where all zeros are symmetrically distributed along the unit circle. However, two zeros are placed asymmetrically on the real $\Re$-axis to obtain the high attenuation of more than 33 dB between passband and stopband as it can be seen in the filter's frequency response in Figure 5.10.

Band	Lower Limit [MHz]	Upper Limit [MHz]
Pass	0.0	1.0
Transision	1.0	7.2
Stop	7.2	40.0

Table 5.2: The table shows the chosen band ranges for the FIR filter. These band ranges are also used for the current hardware implementation on the $\bar{\text{P}}$ANDA SADC board FPGAs.

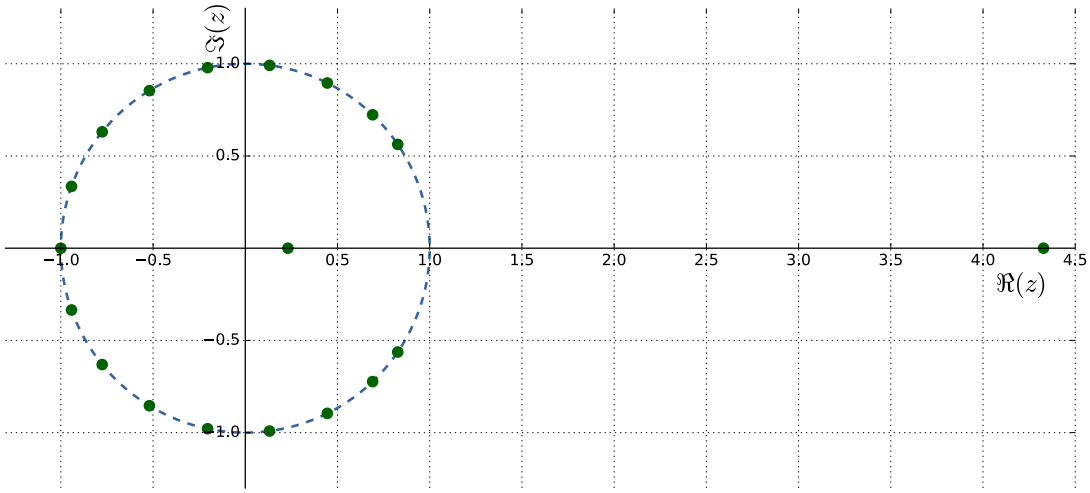

Figure 5.11: The pole-zero plot shows the positions of the zeros of the implemented FIR filter. The poles are all at (0,0) and not drawn here. The sampling frequency is normalised to 2π. This means, 0π refers to a sampling frequency of 0 MHz, π to the Nyquist frequency and 2π to the maximum sampling rate of the ADC, which is 80 MHz. From coordinate (1,0), the frequency increases in the anti-clockwise direction. At coordinate (-1,0), half of the maximum sampling frequency (40 MHz) is obtained. Most of the zeros of the transfer function are placed around the unit circle to suppress high frequencies. Two zeros are placed outside the unit circle along the $\Re$-axis to achieve the high attenuation of more than 33 dB between passband and stopband (Figure 5.10).

5.2.2 Time Measurement and Amplitude Extraction Parameters

The TMAX parameter set includes the derivative parameter r and the two hit detection parameters P_t and M_t. The particular set, which is motivated in the following, is used for both the validation test and the current hardware implementation on the FPGA. The derivative parameter r was optimised concerning the hit detection efficiency η (Subsection 5.2.4) for 3 MeV events for a hit detection threshold of 2.5 MeV. In Figure 5.12 the detection efficiency as a function of the parameter r is plotted. By

increasing the parameter r beginning from $r = 1$, the efficiency increases as well and has a maximum at $r = 6$. However, in contrast to the software implementation of the parameter extraction, where r can be any positive integer value, r has to be powers of two in the case of the FPGA hardware implementation. This is because of the derivative normalisation, where a division by r is performed. Divisions, which are multiple of two, can efficiently be implemented on FPGAs with bit shifts. Thus, the value of parameter r has been chosen to $r = 4$.

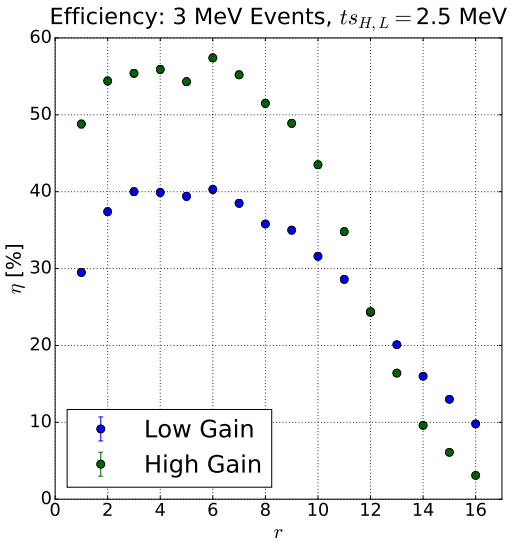

Figure 5.12: The plot shows the simulated hit detection efficiency for 3 MeV events in both the low gain amplification and the high gain amplification. The detection efficiency increases by increasing the parameter r until its maximum at $r = 6$. For even higher r's the efficiency falls quickly. In contrast to the software implementation, the hardware implementation only supports r values which are powers of two. This is because the derivative is normalised by dividing it with r. The r parameter, which is used on the FPGA and in the following software simulations is $r = 4$.

The hit detection parameter P_t includes the duration of the rising edge of the APFEL preamplifier pulse implicitly. Since the duration of the rising edge is about 300 ns and the time between samples is 12.5 ns, the value of P_t should be about 24. However, due to the characteristics of the weighting function (Equation 4.43), the value is slightly bigger than 24. Scans as presented for the parameter r were also performed for P_t. The scans revealed an optimum value of $P_t = 28$ which refers to a time of 350 ns. The parameter M_t defines the maximum value of the weighting function. Thus, the strength of the weighting of true hits over noise hits is defined. A value of $M_t = 2$ has been chosen and gives suitable results as shown in Figure 4.21.

5.2.3 Simulation Procedure

The idea of the pulse processing validation is to generate traces with well-defined events by using the simulation framework. These simulated signals are processed with the FIR filter and the TMAX algorithm. The extracted pulse parameters can subsequently be compared with the input values. As shown in Figure 5.13, three simulated calorimeter events are placed on the trace. The distance between the simulated pulses is exactly 3200 ns, which is more than twice of a complete pulse length. Consequently, interference between the events is excluded. A hit is considered a true hit if it is within a hit detection window. Additionally, an interval of $I_{\mathrm{NH}} = 6750$ ns after the pulse sequence is used to determine the noise hit rate. In order to achieve statistical significance, 4000

traces for a specific input parameter set are generated. Thus, up to 12000 pulses can possibly be detected from the software implementation of the TMAX algorithm per input parameter set. The varied input parameters are:

- The APD gain (M)
- The event energy (E)
- The hit detection threshold (ts_L and ts_H)

The APD gain has an impact on the signal to noise ratio. The event energy refers to the energy, which is measured within one crystal by using one single APD. By varying the hit detection thresholds both the noise hit rate and the detection efficiency are affected. The extraction performance is validated by comparing its results with the $\bar{\text{P}}$ANDA TDR requirements. Furthermore, by using the results of the simulation, the real detector can be set to an optimal operating point.

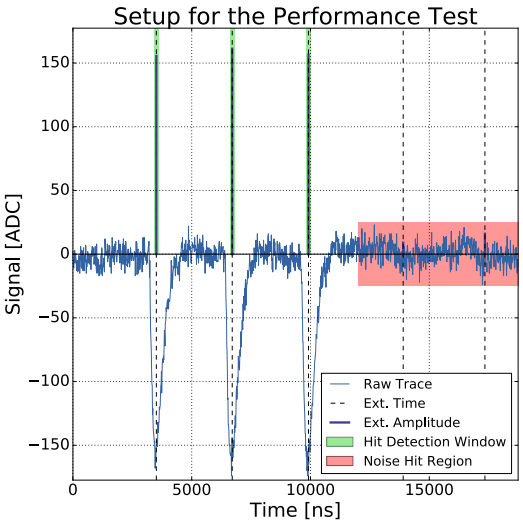

Figure 5.13: The plot shows a simulated example trace as it is used for the performance test. Three simulated calorimeter events with a defined energy and appearance time are placed on the trace. The trace is processed by the software implementation of the FIR filter and the TMAX algorithm. The extracted pulse parameters can subsequently be compared with the input values. Moreover, 6750 ns of the trace (red) is used to determine the noise hit rate for a particular input parameter set. Four thousand traces are generated and processed for every parameter set.

5.2.4 Noise Hit Rate and Efficiency

Baseline fluctuations due to noise that are identified as hits by the signal processing algorithms are called noise hits. The noise hit rate and the detection efficiency are entangled parameters and both a function of the hit detection threshold.
If the threshold is too high, the probability of pulse recognition of real hits decreases. On the other hand, the noise hit rate also decreases. If the threshold is low, the probability of detecting real hits increases. On the other hand, the noise hit rate can exceed the rate limit of data acquisition. Thus, it is indispensable to find a compromise between noise hit rate and efficiency. In the following, the result of the threshold scan for an APD gain of $M = 200$ is presented. The used hit detection thresholds are in between 0.5 MeV and 3.5 MeV. Scans for other APD gains can be found in Appendix B.

The noise hit rate R_{NHR} is computed by the quotient of the number of detected noise hits N_{NH} and the interval length I_{NH}:

$$R_{\mathrm{NHR}} = \frac{N_{\mathrm{NH}}}{I_{\mathrm{NH}}} \tag{5.9}$$

The detection efficiency η is determined for 3 MeV events since the $\bar{\mathrm{P}}$ANDA TDR [TDR08] requires a single channel threshold of smaller or equal 3 MeV. η is defined as the ratio between detected hits and generated hits. A detected hit is considered as identified if the reconstructed timestamp lies within a window I_{true}, which encloses the theoretical occurrence time of the pulse. The used window width is motivated by the time resolution distribution for 3 MeV pulses (Subsection 5.2.5) and ranges from -100 ns to $+100$ ns from the theoretical occurrence time T_0 (Figure 5.13, green windows). By lowering the TMAX hit detection threshold, both the efficiency and the noise hit rate increase. In Figure 5.14 the outcome of the threshold scan for APD gain $M = 200$ is shown.

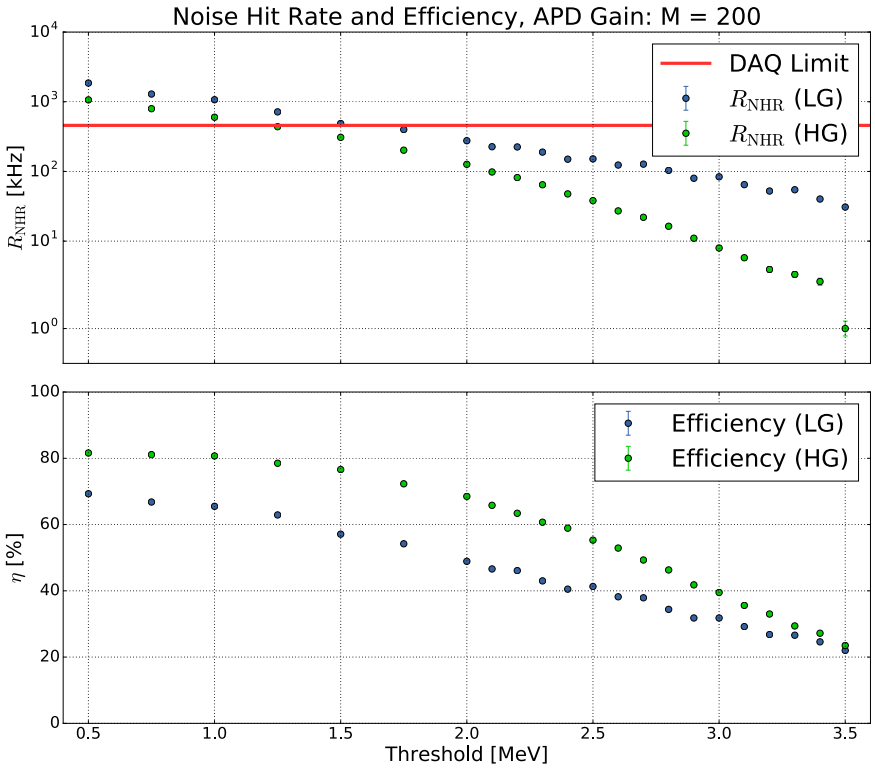

Figure 5.14: The plots show the simulated noise hit rate (upper plot) and the simulated detection efficiency (lower plot) for 3 MeV events and an APD gain of 200 as a function of the hit detection threshold for both the low gain amplification (LG) and the high gain amplification (HG). The DAQ limit refers to a useful signal rate of 100 kHz, at which 458 kHz are left for noise hits. The noise hit rate y-axis is plotted logarithmically.

For instance, an efficiency of 72.3 % with a noise hit rate of 202 kHz at a threshold of 1.75 MeV is possible. Depending on the specific implementation on the FPGA (Section 4.3), a single-channel noise hit rate of up to 458 kHz can be handled by the data acquisition. The estimation refers to the most likely implementation for $\bar{\text{P}}$ANDA, at which one optical link of the SADC transmits the data for all 64 channels. 558 kHz events per channel can be transmitted at a bandwidth of 2 Gbit/s and an event size of 56 bit. Subtracting 100 kHz for the useful events, 458 kHz are left for noise hits. However, the operation point of the data acquisition should not lie at its limit. Nevertheless, a noise hit rate between 100 kHz and 250 kHz is acceptable.
If a detection efficiency of 72.3 % is not sufficient, there are two ways to increase the efficiency even more. For instance, a higher APD gain increases the efficiency until a certain extent due to the increase of the signal to noise ratio. The problem here is that the APD could operate at its limit, close to its breakdown voltage.
A better solution is an online comparison of the timestamps of different APD hits within one crystal. Since noise hits are uncorrelated, most of these hits will not pass the comparison within an interval $I_{\text{comp.}}$. The potential of an online timestamp comparison is illustrated in Figure 5.15.

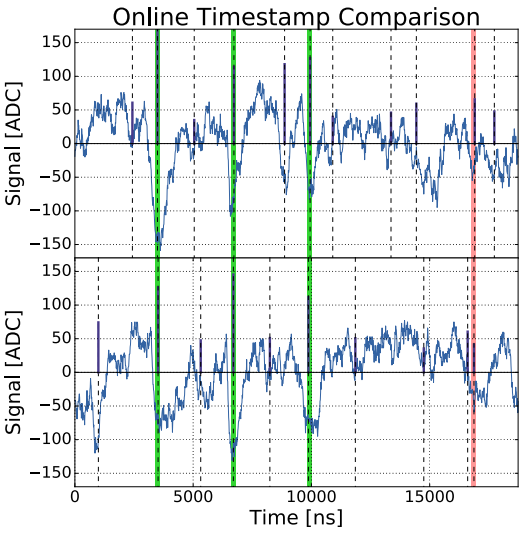

Figure 5.15: The plot shows the effective noise hit reduction through the timestamp comparison of different APD hits within one crystal. The green intervals show hits, which are considered as real hits. All other hits are uncorrelated (eight in the upper plot and seven in the lower plot). Therefore, only one noise hit (red interval) survives after the comparison. Thus, the noise hit rate is drastically reduced, and the data acquisition can operate far below its rate limit. As a result, a lower threshold can be set, which results in higher detection efficiency. The illustration was created with the simulation framework.

By utilising the online comparison approach, the noise hit rate drops by the factor:

$$D_{\text{drop}} = 1 - P_\lambda(k)^2 = 1 - \lambda^2 \cdot e^{-2\lambda} \tag{5.10}$$

with $\lambda = I_{\text{comp.}} \cdot R_{\text{NHR}}$ and $P_\lambda(k)$ being the Poisson distribution (Equation 4.51) with $k = 1$.
Considering the example of APD gain 200, the detection efficiency is 80.7 % at the threshold of 1 MeV (high gain amplification). The noise hit rate in this case is 599 kHz (Figure 5.14), which would exceed the data acquisition capability. By introducing a comparison interval of $I_{\text{comp.}} = 200$ ns, the noise hit rate drops by $D_{\text{drop}} = 98.9\,\%$ to 6.8 kHz. In Figure 5.16 the impact on the noise hit rate by using an online timestamp

comparison is depicted. In contrast to Figure 5.14 the y-axis of the noise hit rate is not anymore logarithmic.

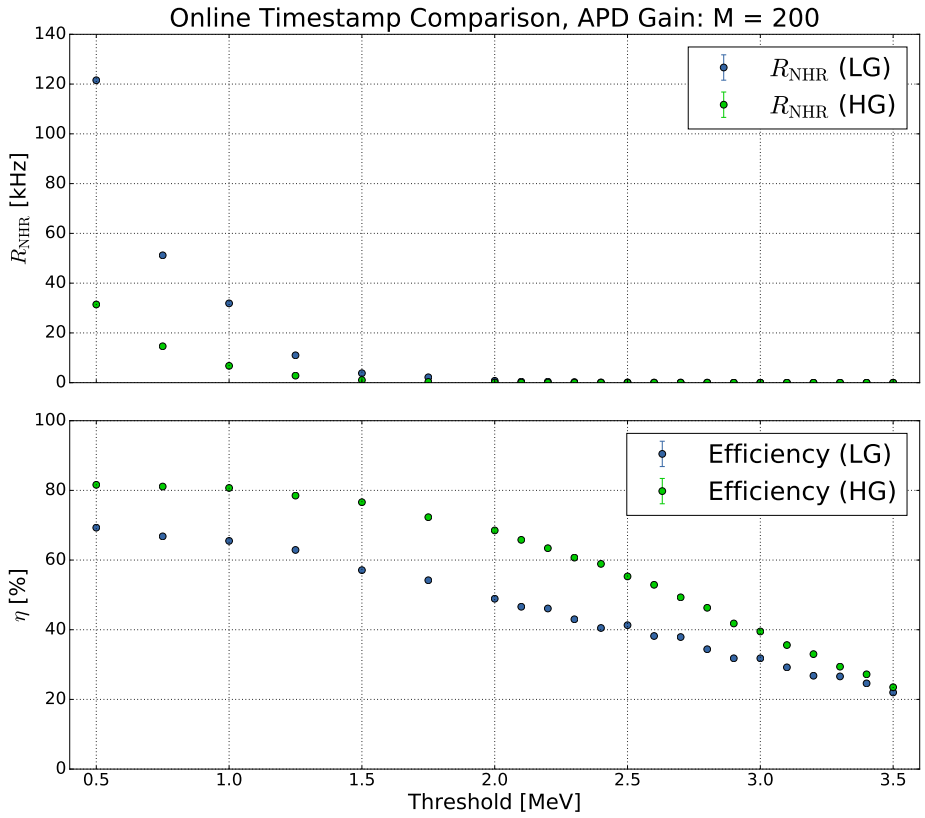

Figure 5.16: The plots show the simulated noise hit rate (upper plot) and the simulated efficiency (lower plot) for an APD gain of 200 as function of the hit detection threshold for both the low gain amplification (LG) and the high gain amplification (HG). In contrast to Figure 5.14 the technique of the timestamp comparison of the signals from two APDs are used with a comparison interval of $I_{\mathrm{comp.}} = 200\,\mathrm{ns}$. Thus, the noise hit rate drops significantly. All noise hit rate points are well beneath the data acquisition limit. As a result, a lower threshold can be chosen, which leads to a higher efficiency.

Although an online timestamp comparison would decrease the noise hit rate significantly, there are disadvantages. One of them is the softening of the redundancy of the detector, which means that both APDs of a crystal need to operate. If one APD fails, the noise hit rate will increase again. On the other hand, the implementation of such an online comparison on the FPGA would demand a lot of buffer RAM. The feasibility of the hardware implementation has to be studied.

5.2.5 Time Resolution

Since the $\bar{\text{P}}$ANDA calorimeter will operate in a self-triggering mode, its time resolution is crucial. Firstly, it is important to associate hits to the right events to perform a correct cluster energy summation. Secondly, the calorimeter events have to be merged with other $\bar{\text{P}}$ANDA sub-detector events. Finally, a sufficient time resolution helps to suppress noise hits (Subsection 5.2.4). The TDR requires a time resolution of 1 ns for energy deposits above 60 MeV and 150 ps for energies above 500 MeV [TDR08]. The time resolution depends strongly on the APD gain. In the following discussion again an APD gain of 200 is assumed.
The determination of the time resolution data was done, as explained in Subsection 5.2.3. The key element here is that the theoretical occurrence times T_0 of the pulses are well known. The theoretical times T_0 are then subtracted from the extracted times $t_{\text{ext.}}$:

$$\Delta t = t_{\text{ext.}} - T_0 \tag{5.11}$$

Subsequently, the time resolution is identified as the RMS of the Δt distribution. In Figure 5.17 the time distribution and thus the time resolution for 60 MeV events at APD gain 200 is shown. Moreover, in Figure 5.18 the time resolution as function of the energy for APD gain 200 is plotted.

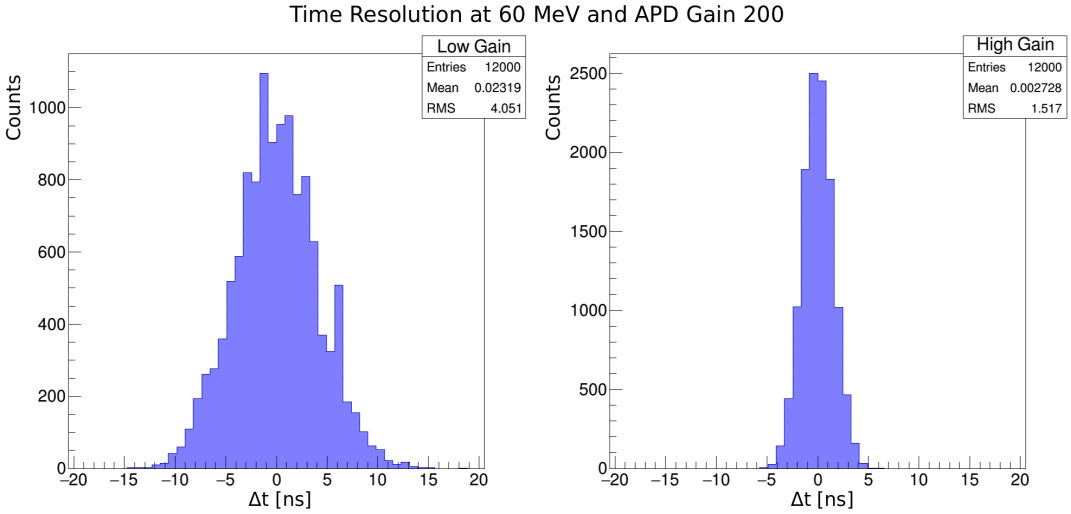

Figure 5.17: The plots show the simulated time spectra for the low gain amplification (left) and the high gain amplification (right) at 60 MeV for APD gain 200. The RMS values of the distributions are the measure for the time resolution.

The achieved time resolutions for 60 MeV and 500 MeV at high gain amplification are 1.517(10) ns and 182(1) ps, respectively. The time resolutions for higher deposit energies agree with the TDR requirement.

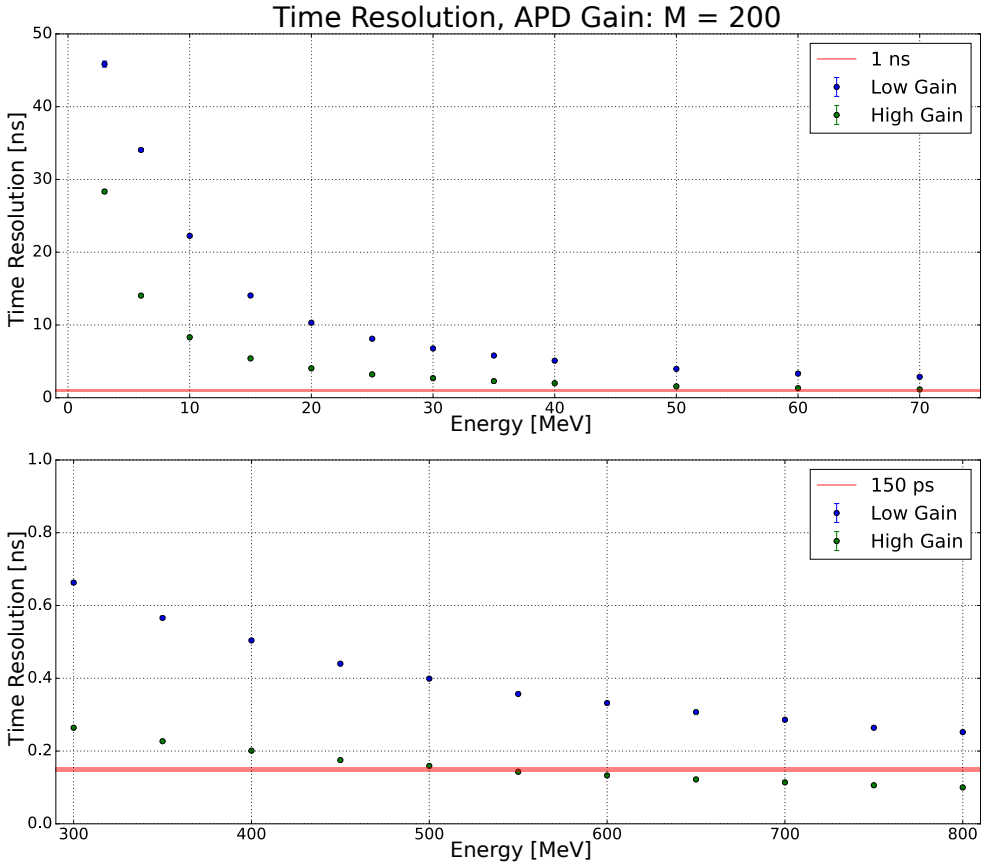

Figure 5.18: The plots show the simulated time resolutions for different deposited energies. The TDR aspires a time resolution of 1 ns and 150 ps for energy deposits above 60 MeV and 500 MeV, respectively. The TDR requirements are met with APD gain 200 and surpassed at higher gains (Appendix B). Nevertheless, the more crucial parameter is the time resolution at low energies, which has a huge impact on the cluster building quality.

With higher APD gains, even better time resolutions are possible, which can be seen in Appendix B. However, depending on the APD characteristic, gains much higher than 200 implies the operation of the APD close to its breakdown voltage.
Another important topic in the context of the time resolution is the cluster summation. Due to the electromagnetic shower, the deposited energy is distributed over several crystals. To sum up the partial energies, the timestamps of the different crystal hits need to be compared. The energy resolution improves if small energies also contribute to the sum. Thus, the time interval for the summation I_{sum} should be oriented towards the time resolution at the single-channel threshold of 3 MeV. Considering Figure 5.18, the time resolution at 3 MeV is 28.34(23) ns. By setting the interval to $I_{\text{sum}} = \pm 1 \cdot \text{RMS}$, 68 % of the 3 MeV partial energies contribute to the sum. Which means that almost

every third 3 MeV event is not considered for the sum. An interval of $I_{\text{sum}} = \pm 2 \cdot \text{RMS}$ would already include 95 % of the 3 MeV partial energies, which has a positive impact on the energy resolution.
However, the above numbers only relate to identified hits. The probability for the identification is the efficiency η. The efficiency increases by lowering the single-channel threshold, which increases the noise hit rate (Subsection 5.2.4) at the same time. As a result, a too free choice of the summation interval I_{sum} would, on the one hand, increase the probability of involving small energies to the sum. On the other hand, it would increase the likelihood for noise hits, which then also contribute to the sum and thus degrade the energy resolution. Therefore, the energy resolution will improve by lowering the threshold until a certain point and then degrade again. This behaviour is addressed in Chapter 6, where beam tests with the EMC prototype are discussed.

5.2.6 Energy-Pulse Height Dependency

As the last validation test, the energy-pulse height dependency of the parameter extraction will be addressed in the following. The data were generated according to the description in Subsection 5.2.3.
Subsequently, a histogram for every energy and every amplification factor (high gain and low gain) was generated and fitted with a Gaussian. As an example, the amplitude distribution for a deposited energy of 100 MeV at APD gain 200 is shown in Figure 5.19.

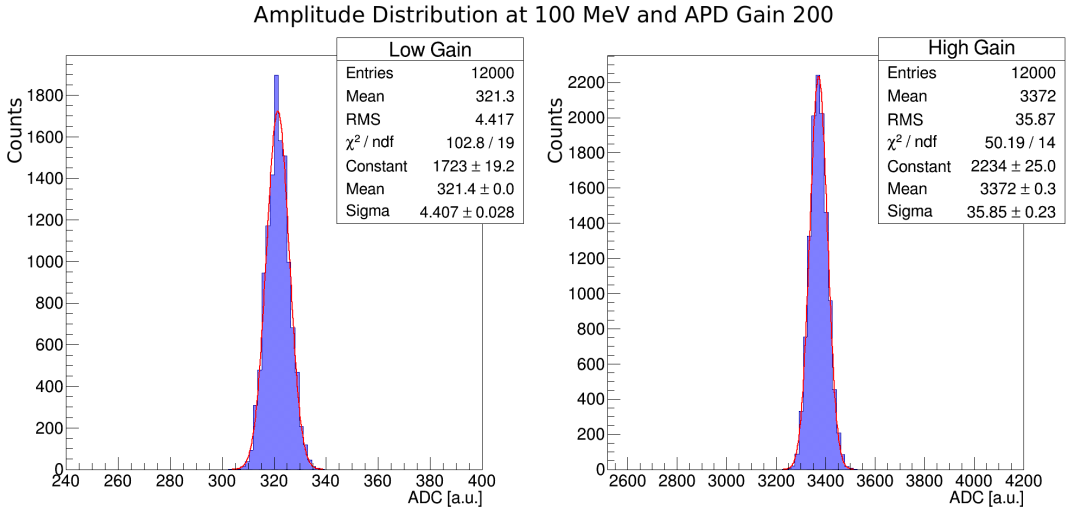

Figure 5.19: The simulated amplitude distributions (low gain, high gain) for a deposited energy of 100 MeV are shown. The histograms are fitted with a Gaussian. The extracted parameters (mean and standard deviation) are used to determine the linearity and the relative resolution for a specific APD gain.

The reason for using a Gaussian fit instead of just using the sample mean and standard deviation are the low energy amplitude distributions. Since low energies are close to the threshold, the amplitude distribution is cut on its left side (Figure B.9). Thus, the mean is slightly shifted to higher amplitudes, and the standard deviation is slightly smaller compared to a not cut distribution. A Gaussian fit, which excludes the cut side of the distribution gives access to the pure mean and standard deviation. Amplitude distributions, which are further away from the threshold, are fitted symmetrically.
The extracted means of the amplitude distributions are subsequently plotted against the input energies of the simulation. The result for APD gain 200 is shown in Figure 5.20. A linear fit was performed for high gain and low gain amplification, respectively. The two lower plots show the residua of the fits. A dashed magenta line demonstrates the ADC limit. In the case of APD gain 200, the absolute values of the residua are always smaller than 160 keV. For deposited energies above 100 MeV the absolute values of the residua are smaller than 50 keV. In any case, the non-linearity is at least one order of magnitude smaller than the single-channel threshold of 3 MeV. Thus, the linearity of the parameter extraction can be seen as more than sufficient. Linearity plots for other APD gains can be found in Appendix B.
Finally, all relevant results of the parameter extraction validation are summarised in Table 5.3.

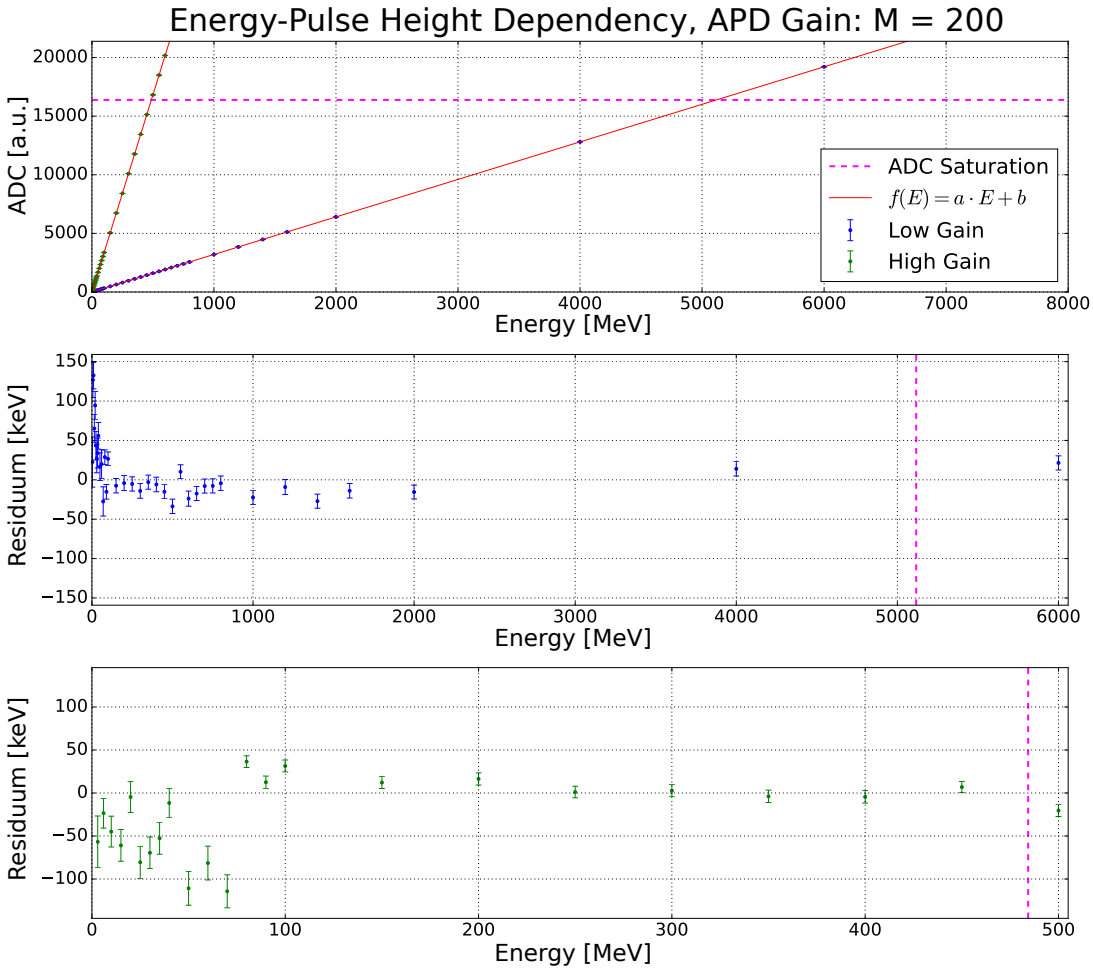

Figure 5.20: The plots show the simulated energy-pulse height dependency for APD gain 200. The upper plot shows the mean of the extracted amplitude distributions (Figure 5.19) plotted against the input energies of the simulation. A linear fit for the high gain and low gain amplification was done respectively. The absolute values of the residua are always smaller than 160 keV. For energies depositions above 100 MeV, the absolute of the residua are smaller than 50 keV. The non-linearities are at least one order of magnitude smaller than the single channel threshold of 3 MeV.

Parameter	Achieved Value						TDR	Unit
APD Gain	150		200		250		-	-
Preamp. Gain	LG	HG	LG	HG	LG	HG	-	-
Noise Hit Rate	Threshold: 2.5 MeV							
Single	331.1(26)	160.9(20)	151.44(200)	38.07(110)	67.93(145)	5.52(45)	-	kHz
Dual ($I_{\text{comp.}} = 200\,\text{ns}$)	1.27(5)	0.16(1)	0.13(1)	<0.01	<0.1	<0.01	-	kHz
Efficiency	Deposited Energy: 3 MeV							
Threshold: 2.5 MeV	39.6	50.4	41.3	55.3	42.4	58.5	-	%
Threshold: 1.5 MeV	55.9	65.9	57.1	76.6	61.5	83.9	-	%
Time Resolution								
60 MeV	5.369(35)	1.998(13)	4.051(26)	1.517(10)	3.176(21)	1.198(8)	1	ns
500 MeV	635(4)	239(2)	477(3)	182(1)	380(2)	144(1)	150	ps
Non-Linearity	Upper Limit							
Dep. Energies $< 100\,\text{MeV}$	635.12(23)	288.24(179)	138.24(70)	134.80(7)	162.17(7)	103.66(73)	-	keV
Dep. Energies $\geq 100\,\text{MeV}$	64.81(3)	41.31(27)	44.90(3)	21.62(27)	44.78(3)	21.05(26)	-	keV

Table 5.3: The table summarises the results of the parameter extraction performance simulation.

6 Prototype Tests at the Mainz Microtron MAMI

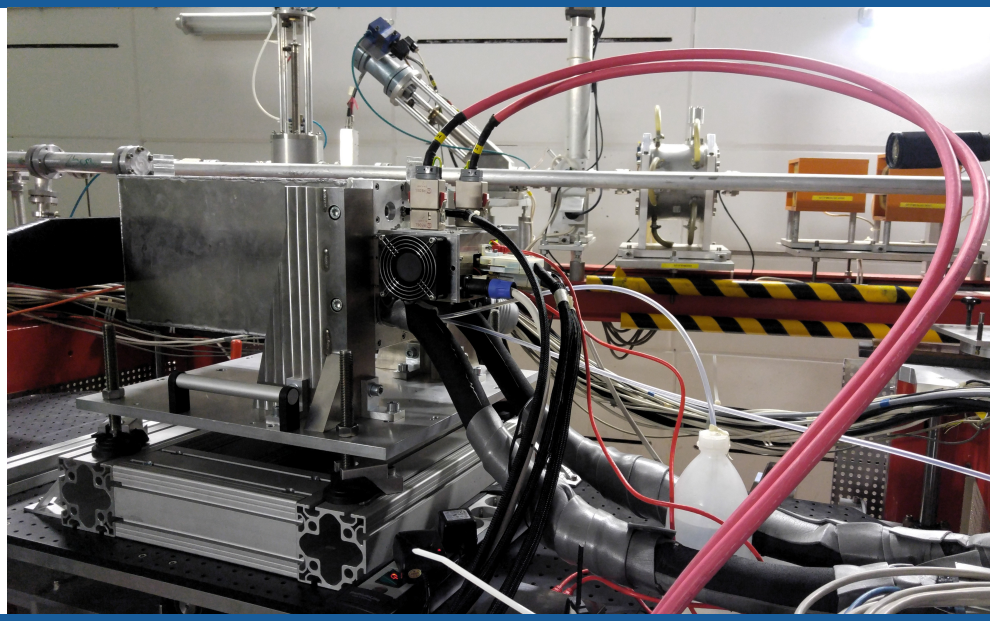

The picture shows the backside of the EMC prototype at the Mainz microtron facility. The prototype is the miniaturised version of the EMC and consists of all relevant parts. The essential component is a 4×4 EMC submodule with 16 crystal units. The prototype was used in many laboratory tests and beam tests to benchmark and improve the EMC technology.

In the context of this thesis, an electromagnetic calorimeter (Chapter 3) was developed. The development included the digital processing of the detector signals (Chapter 4). Besides laboratory tests, the Mainz Microtron (MAMI) was utilised to examine the calorimeter and its full readout chain under real conditions. MAMI can produce electrons and photons in a wide energy range. Thus, it is the perfect tool for benchmarking an electromagnetic calorimeter.

Five beam tests with the EMC prototype at MAMI have been performed between 2014 and 2018. Also, the prototype was used in two test beams in 2018 in the context of feasibility studies for the FAIR Phase-0 experiment (Chapter 7). Furthermore, three additional beam tests were dedicated to detector components tests. Thus, about 500 h of tests at MAMI were devoted to the EMC development. In the following, a short introduction to the Mainz Microtron accelerator will be given with emphasis on the X1 extraction beamline. Furthermore, the test setup for the EMC prototype benchmarking at the X1 extraction beamline will be described.

The central part of this chapter is the discussion of the most relevant results of the beam tests. Besides the characterisation of the EMC in terms of relative energy resolution and linearity, the benchmarking of the digital signal processing (Chapter 4) will be presented. The discussion includes the maximum recording rate, the effective detector dead time, the pileup probability at high rates and the pileup handling.

6.1 The Mainz Microtron Accelerator Facility

The Mainz Microtron (MAMI) facility is a recirculating electron accelerator which uses the Race Track Microtron (RTM) principle [MAM19]. The idea is that electrons pass through a linear accelerator several times by increasing their momenta at every transition. Two dipole magnets deflect the electron beam by 180° each to return the electrons to the linear accelerator.
The maximum achievable energy is limited by both the magnetic field strength and the dimensions of the dipole magnets. Between 1979 and 2006 MAMI was upgraded with ever-larger RTM structures, which are arranged in series. The key features of MAMI are its electron beam brilliance, its continuous-wave beam and its high beam current of up to 30 μA for polarised electrons and up to 200 μA for unpolarised electrons [Aul11]. In Figure 6.1 a schematic view of the Mainz Microtron is shown.

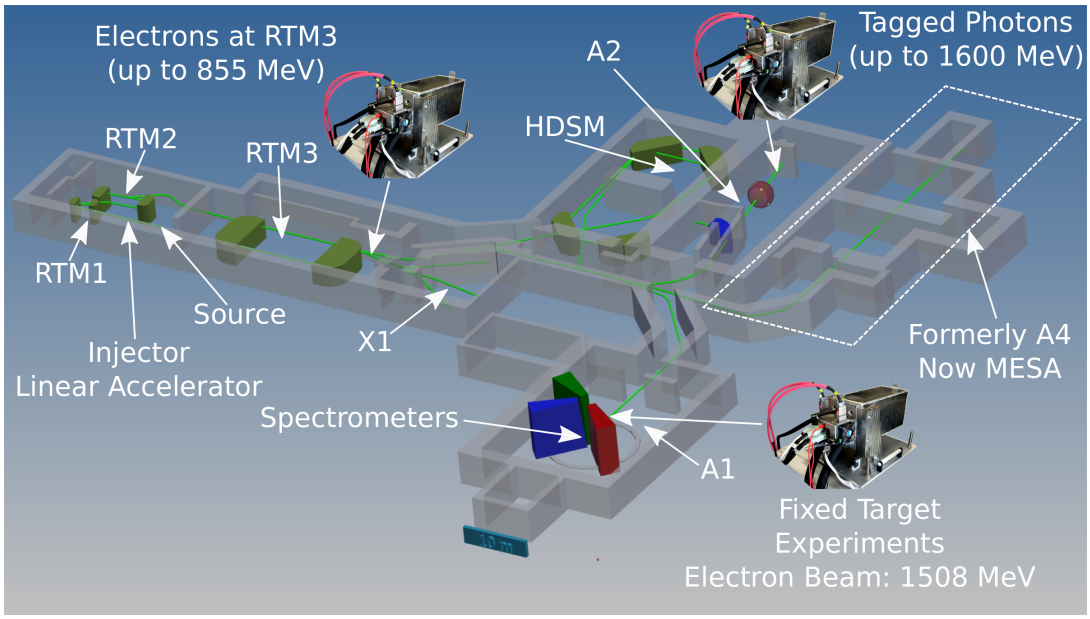

Figure 6.1: The schematic view shows the Mainz Microtron Accelerator Facility (MAMI). It consists of three stages of race track microtrons (RTM1, RTM2 and RTM3) and one stage of a Harmonic Double-Sided Microtron (HDSM). There are three active experiments located on the facility. The X1 experiment produces brilliant X-rays, the A2 experiment studies hadron reactions by using tagged photons and the A1 group performs electron scattering at nucleons and nuclei. Also, all locations where the EMC prototype was tested are shown.

In the following, the different MAMI stages are discussed. The electrons are provided by an electron source, which has two modes of operation. On the one hand, unpolarised electrons can be produced by thermal emission. On the other hand, polarised electrons can be generated by the photoelectric effect using a laser. The electrons are subsequently

accelerated by the injector linear accelerator and fed into the first RTM structure.
The RTM1 accelerates the electrons to an energy of 14 MeV. Subsequently, the electrons are guided to RTM2. The beam leaves RTM2 with an energy of 183 MeV and enters the third stage of MAMI (RTM3).
At the exit of RTM3, the X1 experiment is located, which can access electron energies between 195 MeV and 855 MeV with a step width of 15 MeV. X1 produces brilliant X-rays by using the undulator principle. With its two dipole magnets with a weight of 450 t each, the RTM3 magnets are almost at spatial limits for the available hall. Consequently, the Harmonic Double-Sided Microtron (HDSM) comes into play, which is the last accelerator stage of MAMI. Instead of using two dipole magnets, the HDSM uses four dipole magnets, each with a bending angle of 90°. Furthermore, the HDSM has two linear accelerator structures, which are located on opposite sides of the ring. The second linear accelerator operates with twice the frequency (second harmonic) of the first linear accelerator. The HDSM principle almost doubles the electron energy compared to the maximum output energy of RTM3 (855 MeV) by only increasing the magnet weight by 11 % (4 x 250 t)[Jan06]. There are two ongoing experiments, which use the output electron beam of the HDSM. At A2, electrons with an energy of up to 1600 MeV are converted into photons via bremsstrahlung. A2 studies hadron reactions by scattering photons on nuclei and nucleons. A1 uses electrons with energies of up to 1508 MeV. In the experimental hall, three magnetic spectrometers are used to perform electron scattering experiments at nuclei and nucleons. All magnetic spectrometers are rotatable around the target.

6.2 Beam Tests with the Prototype Calorimeter

During the years of development, several beam tests were performed with the EMC prototype at the Mainz Microtron facility. The first test was done in 2014 using energy tagged photons at A2 [Nol14]. Afterwards, the space right behind RTM3 at the X1 extraction beamline (Figure 6.1) became the central location for experiments with the prototype. This location has attractive features for electromagnetic calorimeter tests. Firstly, the location provides a monochromatic electron beam with a maximum energy spread (1σ) of 13 keV [Jan06]. The spread is about two orders of magnitude smaller than the EMC energy detection threshold. Thus, the determination of detector characteristics is not limited by the accelerator properties.
Secondly, the beam spot is well collimated with a spread of less than 1 mm, which is important to determine beam location dependencies of the measurements.
Furthermore, the intensity of the electron beam is precisely tunable to very low values. Thus, the detector can be placed directly in the beam. Moreover, the experimentalist has full control over the beam and the freedom in accessing the experimental area. Finally, the setup area provides plenty of space for detector support structures, cameras, remote-controlled movable tables, rotatable platforms and all subsystems, which are needed to operate the detector.
Alongside detector tests at A2 and X1, also fixed target scattering experiments were

performed with the EMC prototype in the context of a FAIR Phase-0 feasibility study at A1, which will be discussed separately in Chapter 7. The following focuses on the setup and the results from the RTM3 beam tests. Whereby from Section 6.3 to Section 6.5 data from the July 2015 beam test was used. The data for the high rate measurements in Section 6.6 stem from the August 2018 beam test.

6.2.1 Experimental Setup at the MAMI Detector Test Facility

For a beam test at RTM3, the extraction beamline is opened and sealed with a flange. The prototype is installed at the location of the removed beamline. Thus, the EMC prototype is placed directly in front of the opened extraction beamline. Consequently, the electron beam can be pointed directly into the crystal matrix. A movable table can change the detector position in horizontal (X) and vertical (Y) direction. A plastic scintillator can optionally be placed between the extraction beam pipe and the EMC prototype. As a result, a triggered data recording is possible. Furthermore, the plastic scintillator can be used as event rate detector. An illustration of the basic setup is shown in Figure 6.2. Furthermore, a photograph of the setup is given in Figure 6.3.

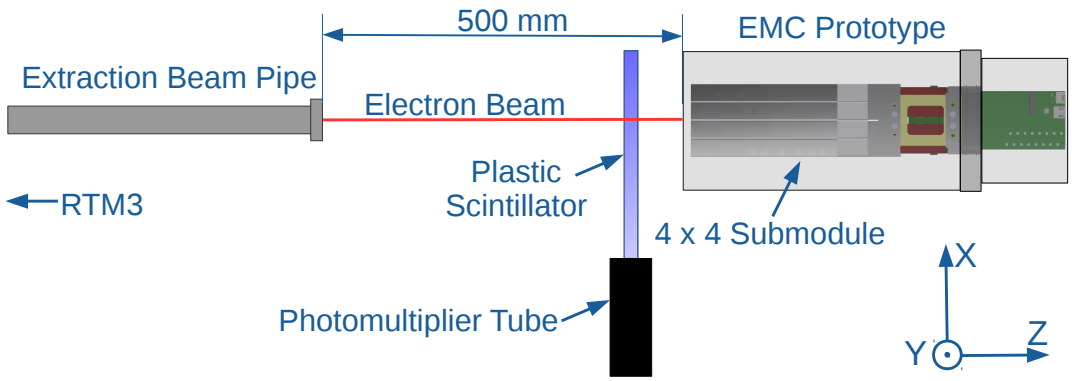

Figure 6.2: The illustration shows the basic setup of a test beam at the X1 extraction point. The EMC prototype is placed directly in front of the extraction beam pipe. A movable table provides the possibility to place all individual crystals into the electron beam. A plastic scintillator can optionally be placed between extraction beam pipe and EMC prototype. By changing the electron energy and tuning the beam current, a variety of tests can be performed.

The EMC prototype is connected with all necessary supplies, as shown in Figure 3.18, which include low voltage, high voltage, cooling, nitrogen, optical fibers and programming lines. Furthermore, the analogue signal cables are connected to the data acquisition, as shown in Figure 3.11. The detector with all its subsystems can be monitored and controlled from the counting room.

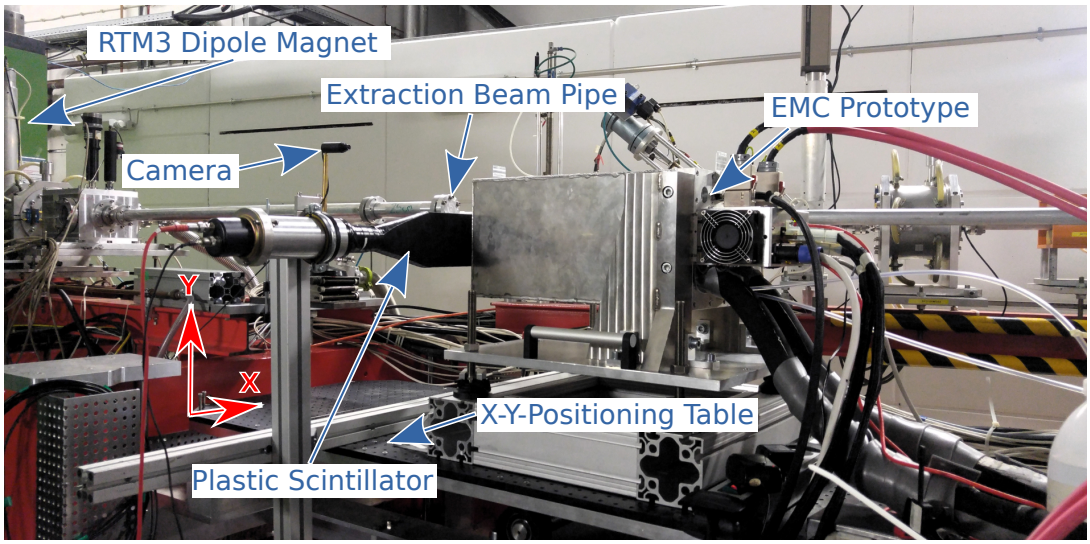

Figure 6.3: The photograph shows the experimental setup for prototype tests at the X1 extraction point (Figure 6.1). Here, electrons are detected by placing the detector directly in front of the extraction beam pipe. A table allows a precise movement to arbitrary positions within the crystal matrix. A plastic scintillator between the prototype and the exit beam pipe can be used as a trigger or as a detector for the event rate. Several radiation-hard cameras allow the observation of the experiment from the counting room.

6.2.2 Alignment of the Prototype

It is intended to move the EMC prototype and thus its crystal matrix to defined positions. For instance, it is mandatory to point the electron beam onto the centre of every single crystal to perform a proper detector calibration (Subsection 6.2.4). Consequently, the detector position has to be known as good as possible. The procedure, which is described in the following, aims for a detector alignment with a precision in the order of one millimetre.

During the installation of the experiment, the detector is aligned by using a laser beam, which is parallel to the extraction beam pipe. After the alignment, the crystal matrix is parallel to the extraction beam pipe. By using a level, the detector is aligned with the horizontal plane.

The final reference is determined by using the electron beam itself. Therefore, the beam points onto the fluorescence plates of the detector, which are described in Section 3.3. The fluorescence plates have a defined relative position to the crystal matrix. When the beam spot becomes visible in the centre of the reticle of the front and the rear fluorescence plate, the zero-position is defined. The procedure is illustrated in Figure 6.4. The photograph was taken from an observation monitor in the counting room.

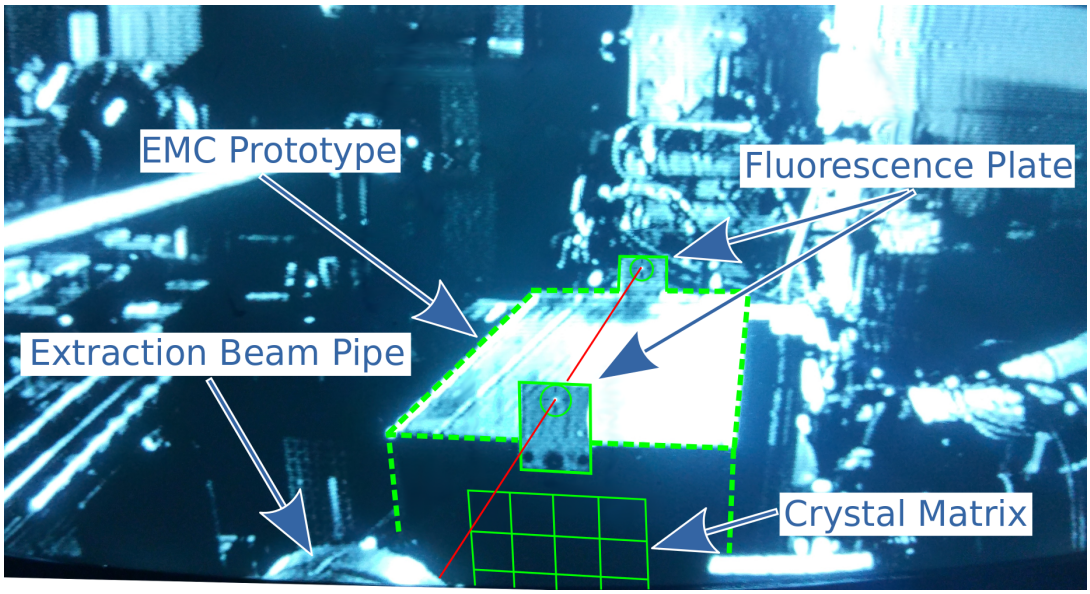

Figure 6.4: The photograph shows the reference determination for the movable table. The picture was taken during a beam test from an observation monitor in the counting room. The corresponding camera was attached to the extraction beam pipe, pointing to the front face of the detector (Figure 6.3). The fluorescence plates of the EMC prototype are moved into the electron beam (red line). The appearance of luminous points in the centre of the reticles on both plates indicates the zero-point. Red and green lines were superimposed to the original picture to facilitate the understanding.

6.2.3 Data Taking Procedure

A variety of tests can be performed with the setup just introduced. On the one hand, the accelerator can be set to different energies and currents. On the other hand, the detector has several parameters, which can be scanned to characterise its response.
Before the actual data taking, a signal quality check is performed by the observation of the live-monitor. In Figure 6.5, an example output of the live-monitor for a single electron event is depicted.
The 16 plots correspond to the 16 crystals of the EMC prototype. Each trace in a plot corresponds to one of the two APDs on the crystal. The traces are the digitised output of the low amplification of the 16 APFEL preamplifiers (Subsection 3.2.2). The accelerator was set to the energy of 855 MeV. All detector APDs were set to gain 150 (Subsection 3.1.3). The beam pointed to the centre of crystal 9. Thus, crystal 9 has the highest signal amplitude. As expected, some of the neighbouring crystals detect parts of the electromagnetic shower (Subsection 3.1.1).
Two alternative modes of data taking were used for recording the prototype response. In the first mode, full traces were recorded with the so-called MBS-system ([JAM17] and [Nol14]), as shown in Figure 6.5. Therefore, the plastic scintillator with the

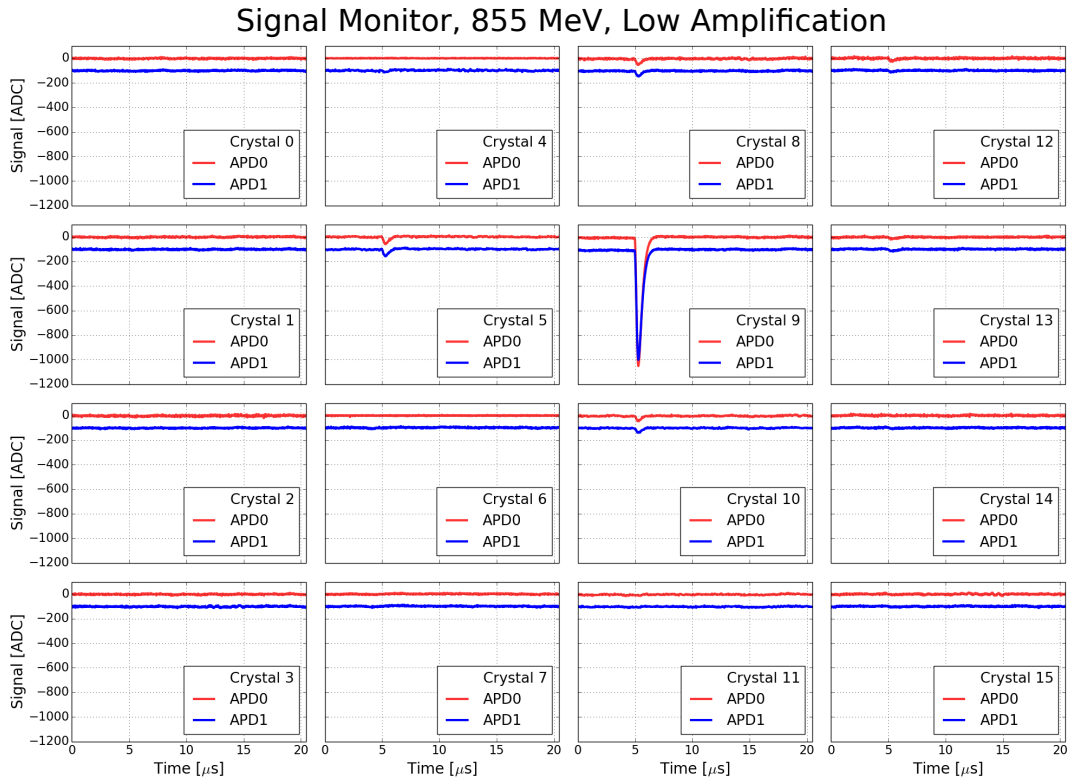

Figure 6.5: The plots show the digitised signals from the APFEL preamplifiers for a 855 MeV electron event. Here, one trace corresponds to one APD. Since the electron beam pointed directly into crystal 9, it has the highest signal pulse amplitude. However, some of the neighbouring crystals also detect parts of the shower leakage. Note: The baselines were moved to similar Y-positions in the offline analysis.

Photomultiplier Tube (PMT) readout serves in coincidence with the prototype as an external trigger. The event information is extracted in an offline analysis with the methods presented in Section 4.4.

In the second mode, data can be taken with the $\bar{\text{P}}$ANDA digitisation board with the firmware, which was developed in this work (Section 4.3). The online event information extraction is identical to the extraction at the offline analysis of the recorded traces. However, since only hit information (amplitude and timestamp) is transmitted, the needed data bandwidth is much smaller. Thus, it can be recorded with much higher event rates (Section 6.6).

For every data taking, also all detector status data are recorded by the slow control system. The records include the APD bias voltages, which are strongly related to the APD gains, the low voltages for the electronics, the detector temperature distribution and the movable table coordinates.

6.2.4 Single-Crystal Energy Calibration

The average pulse height at a given electron beam energy for central crystal events differs from one crystal to the other. The reasons for this are differences in the crystal light yield, the optical coupling of the APDs to the crystal and variations in the electronic parts. Furthermore, inaccuracies in the characterisation of the APDs lead to differences in the APD gains. For further analysis of the beam data, it is crucial to ensure the comparability of the different detector channels.

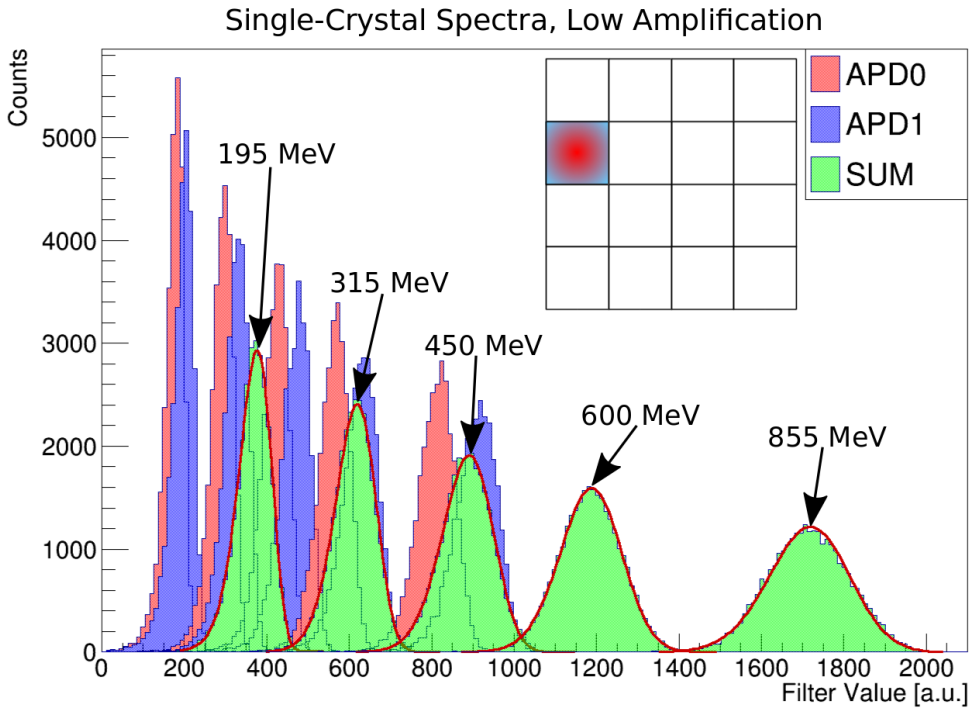

Figure 6.6: The plot shows the pulse height histograms for different electron beam energies in the low gain amplification for a single crystal. The red spot in the 4×4 grid indicates the position of the crystal within the 4×4 crystal matrix from the beam perspective. The pulse height values in arbitrary units are determined by the parameter extraction routine, introduced in Section 4.4. The average pulse heights (histogram position) at a given electron beam energy differs for the two APDs. However, the sum of the individual pulse heights defines the single-crystal response (green histograms) for specific energy. By fitting the histograms of the single-crystal responses with the Novosibirsk function and extracting the position of the maxima, the single-crystal energy calibration can be determined.

Since every crystal was centred on the beam, an individual single-crystal energy calibration can be performed. The procedure assumes that on average in every crystal, the same energy is deposited. For a specific crystal and a particular electron beam

energy, the extracted pulse heights are filled in a histogram for both APDs. The sum of the extracted pulse heights (arbitrary units) of both APDs defines the single-crystal response to a given particle energy. In Figure 6.6 both the APD histograms and the single-crystal response histograms for different electron beam energies are shown.

The single-crystal response histograms (green) are fitted with the Novosibirsk function:

$$f(x) = p_0 \cdot \exp\left\{-\frac{1}{8}\left[C \cdot a \cdot \ln\left(1 - \frac{p_3}{p_2}(x - p_1)\right)\right]^2 - 2\left(\frac{1}{a}\right)^2\right\} + p_4, \tag{6.1}$$

with $a = \operatorname{arcsinh}(\frac{p_3 \cdot C}{2})$ and $C = 2\sqrt{2\ln(2)}$. Whereby p_1 is the position of the histogram maximum and p_2 is related to the distribution width.

The extracted maxima of the single-crystal response histograms (p_1) are proportional to the deposited energies. Since a single-crystal does not measure the beam energy but only a fraction of it, the expected deposited energy needs to be determined by a Geant4 simulation. Consequently, the single-crystal responses can be plotted against the expected deposited energies to extract the single-crystal energy calibration. The result of the simulation is depicted in Figure 6.7.

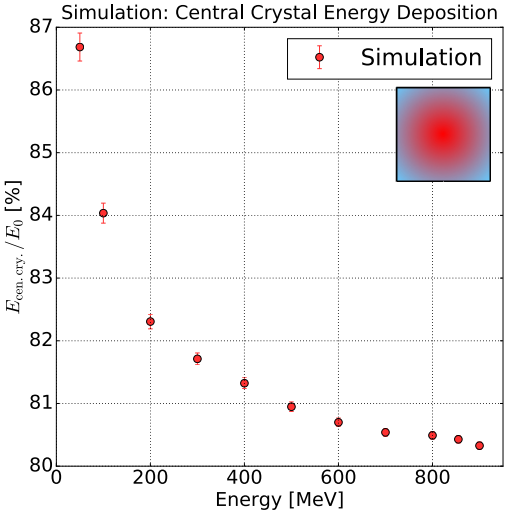

Figure 6.7: The plot shows the fraction of the deposited energy in a single crystal as a function of the beam energy. For instance, an electron only deposits 80.4 % of its 855 MeV into a crystal, when hitting the crystal centrally. The plot is generated by using data from a Geant4 simulation. The results are used to plot the expected deposited energies against the distribution positions (Figure 6.8), which leads to the single-crystal energy calibration.

As an example, the procedure is depicted for one crystal in Figure 6.8. The single-crystal calibration plots for the other crystals can be found in Figure C.1. The process is also done for the APFEL preamplifier high amplification signals (Figure C.2 and Figure C.3). As a result, the exact ratio between low and high amplification is determined for every crystal. Since small energies are recorded with the high amplification and high energies are recorded with the low amplification, the determined ratio is important for the later data analysis.

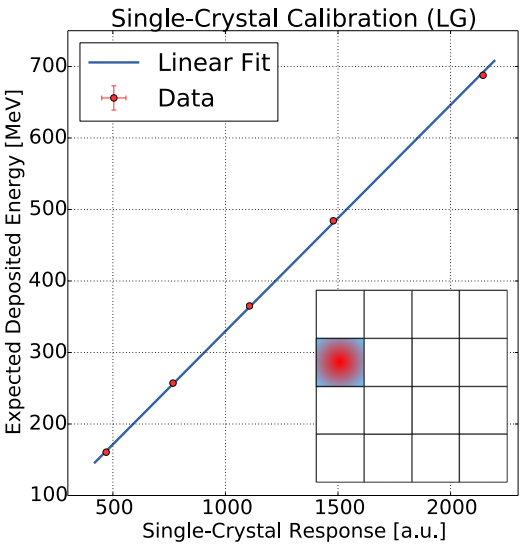

Figure 6.8: The plot shows the single-crystal calibration for one of the 16 detector crystals. The single-crystal response is plotted against the expected deposited energy from the simulation (Figure 6.7). The procedure is done for every single crystal. Thus, a crystal response normalisation can be performed, which allows an appropriate summation of partial energies within a crystal cluster (Subsection 6.2.5). The procedure is also done for the APFEL preamplifier high amplification. Consequently, the ratio between low amplification and high amplification can be determined.

6.2.5 Cluster Energy Determination

To measure particle energies with the calorimeter, it is not enough to only look on the crystal where the particle has entered (central crystal). Due to the average spatial spread of the electromagnetic shower (Subsection 3.1.1), the particle energy is distributed over the central crystal and its neighbouring crystals. As a result, the measured energy of the central crystal and the energies, which are measured with the neighbouring crystals, need to be summed up. With the single-crystal energy calibration (Figure 6.8), the different detector crystal responses are normalised. In Figure 6.9, a so-called sum spectrum for a 3×3 crystal matrix is shown. The summation was performed after the normalisation of the single-crystal responses. Also, the contributions of the central crystal and the neighbouring crystals to the sum are drawn.

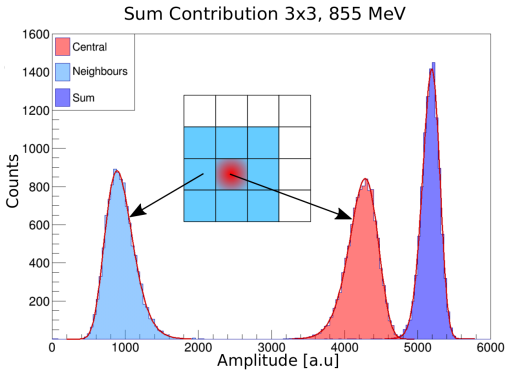

Figure 6.9: The plot shows the distribution of the contributions from the central crystal and the sum of its neighbours for 855 MeV electron events. At the example, the central crystal contains 82.78(5) % of the signal. The sum spectrum has a much less prominent tail to lower energies because the shower leakages for a 3×3 crystal cluster are much smaller than for a single crystal.

The sum spectra play the central role for the characterisation of the EMC prototype. For instance, the relative energy resolution (Section 6.3) or the detector linearity (Section 6.5) can be derived. Such a characterisation always refers to a defined cluster

geometry. For instance, the 4×4 crystal matrix of the EMC prototype can be subdivided into four 3×3 matrices. A 3×3 matrix has a central crystal and is surrounded by eight neighbouring crystals.

In Figure 6.10 the sum spectra for all recorded electron beam energies and all four 3×3 matrices of the prototype are depicted. The plots refer to a specific parameter set of the prototype (APD gain and hit detection threshold).

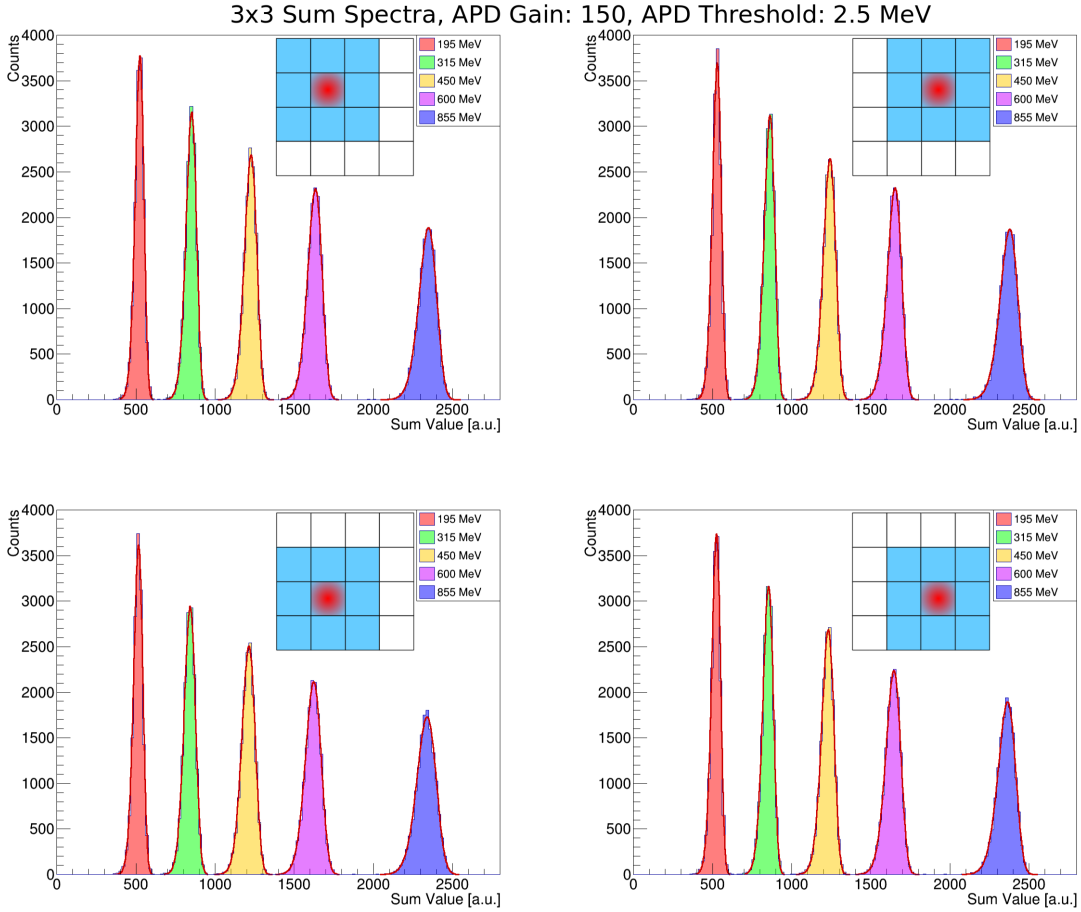

Figure 6.10: The plot shows energy spectra obtained by summing the signals from 3×3 crystal events for a specific prototype parameter set (APD gain and hit detection threshold). The procedure was done for five electron beam energies (195 MeV, 315 MeV, 450 MeV, 600 MeV and 855 MeV). Central characterisation parameters such as the relative energy resolution can be derived from such energy spectra as a function of the detector parameter set. For instance, the dependency of the relative energy resolution on the hit detection threshold is discussed in Section 6.4.

6.3 Relative Energy Resolution of the Prototype

With the help of the cluster sum spectra (Figure 6.10), the relative energy resolution can be extracted according to the definition in Subsection 3.1.4. The spectra are fitted with the Novosibirsk fit function (Equation 6.1) to extract both the spectra peak positions ($\mu_{\text{Sum}} \equiv p_1$) and the spectra widths ($\sigma_{\text{Sum}} \equiv p_2$). The peak positions of the sum spectra are proportional to the beam energies ($\mu_{\text{Sum}} \propto E$). Thus, the relative energy resolution is:

$$\frac{\sigma_E}{E} = \frac{\sigma_{\text{Sum}}}{\mu_{\text{Sum}}} \tag{6.2}$$

By fitting the above ratio with the relative energy resolution function (Equation 3.4), the different contributions to the resolution can be extracted. In Figure 6.11 an example for such an energy resolution fit for a specific detector parameter set is depicted.
As explained in Subsection 3.1.3, the signal to noise ratio of an APD improves with higher gains (higher bias voltages). A better signal to noise ratio also improves the relative energy resolution of the EMC. However, the improvement of the signal to noise ratio is limited by the excess noise (Subsection 3.1.3). The operating gain for the APDs in the $\bar{\text{P}}$ANDA calorimeter will be in the range of approximately 150 to 250. The data for Figure 6.11 were taken at a gain of 150 for all APDs. Such a moderate gain leaves headroom for compensating possible energy resolution drops due to the ageing of components in the final $\bar{\text{P}}$ANDA calorimeter after years of operation.
The hit detection threshold defines the minimum pulse amplitude of hits to be stored. As mentioned in Subsection 4.5.1, there is a correlation between the detection efficiency and the noise hit rate. The relative energy resolution improves if real hits are added to the sum and degrades if noise hits are added to the sum. A detailed discussion about the impact of the hit detection threshold on the relative energy resolution will be done in the next section. The data for Figure 6.11 were taken for a hit detection threshold of 2.5 MeV.
From the fit to the data, the following results are obtained. The relative energy resolution at 1 GeV is 2.207(6) %, which is already better than the $\bar{\text{P}}$ANDA TDR ([TDR08]) requirement (2.5 % at 1 GeV). The stochastic term also surpasses the TDR requirement (1.83(45) %/$\sqrt{\text{E[GeV]}}$ compared to 2 %/$\sqrt{\text{E[GeV]}}$). The constant term agrees with the TDR requirement within the uncertainty (1.08(14) % compared to 1 %). The single-crystal noise term is better than the requirement (2.02(15) MeV compared to 3 MeV). The results for the other three 3×3 crystal matrices of the EMC prototype can be found in Appendix C.

6.4 Relative Energy Resolution: Threshold Dependency

The results, which were discussed in the previous section, correspond to the same APD channel threshold of 2.5 MeV for both preamplifier amplifications. However, by lowering the threshold, it becomes more likely that small leakage energy portions of the

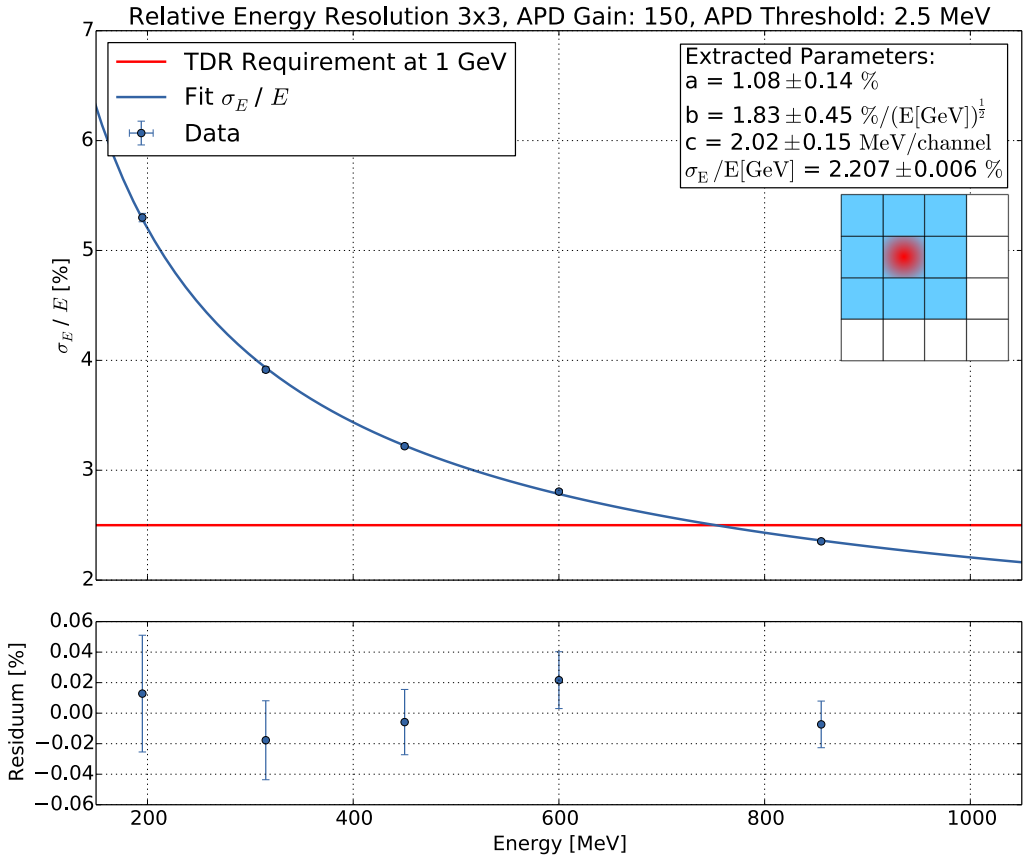

Figure 6.11: The plot shows the relative energy resolution of the EMC prototype as a function of the beam energy for a 3×3 crystal cluster. The APDs were set to gain 150 and the hit detection threshold was set to 2.5 MeV. The relative energy resolution at 1 GeV is better than the $\bar{\text{P}}$ANDA TDR ([TDR08]) requirement (2.207(6) % compared to 2.5 %). The stochastic term (see Subsection 3.1.4 for explanations) is also better than the requirement (1.83(45) %/$\sqrt{\text{E[GeV]}}$ compared to 2 %/$\sqrt{\text{E[GeV]}}$). The constant term agrees within the uncertainty with the requirement (1.08(14) % compared to 1 %). The results for the other three 3×3 crystal clusters of the EMC prototype can be found in Appendix C.

electromagnetic shower are detected in the border of a crystal cluster. As a result, the shower leakage reduces, and thus the relative energy resolution improves. On the other hand, the noise hit rate increases by lowering the threshold (Subsection 5.2.4). In the case of a too high noise hit rate, two effects can occur. Firstly, the data acquisition can reach its limits in terms of data throughput. Secondly, noise hits can erroneously be added to the cluster sum, which worsens the energy resolution.

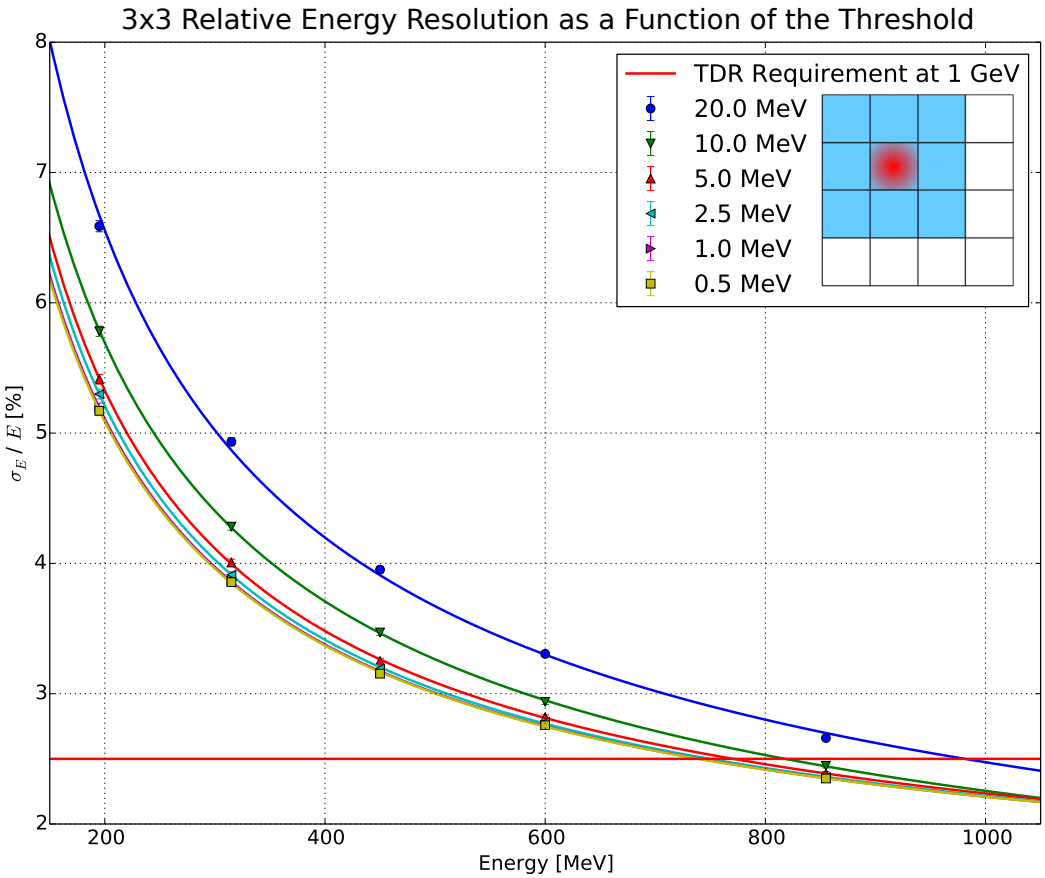

Figure 6.12: The plot shows the impact of the hit detection threshold on the relative energy resolution. The same threshold was applied on both the APFEL preamplifier low amplification and the high amplification. The relative energy resolution improves by lowering the threshold until a certain point. The lowering of the threshold below 1.0 MeV does not improve the energy resolution significantly.

For the analysis of the threshold dependency of the relative energy resolution, data recorded with the external trigger were used (Subsection 6.2.3). The outputs of such an externally triggered event are traces as demonstrated in Figure 6.5. There are two traces for every APD channel, which stem from the high gain and the low gain output of the preamplifier. Since there are two APDs per crystal, there are 64 traces in total for the 16 crystals of the EMC prototype.

By using the software implementation of the parameter extraction algorithm (Subsection 5.1.4), the amplitudes and the timestamps of all hits on the traces can be extracted as a function of the hit detection threshold. Furthermore, by using the single-crystal energy calibration data (Subsection 6.2.4), the hit detection threshold can be expressed in units of energy (MeV). Since the high gain amplification has

a better signal to noise ratio (Subsection 5.2.4), the high gain amplification is used to detect low energy events, while the low gain amplification is used for high energy events. Depending on the APD gain, the high gain amplification saturates at energies between 400 MeV (APD gain 250) and 900 MeV (APD gain 100). The data, which are discussed here, were recorded with an APD gain of 150. In this case, the high gain energy range reaches its limits at about 650 MeV.

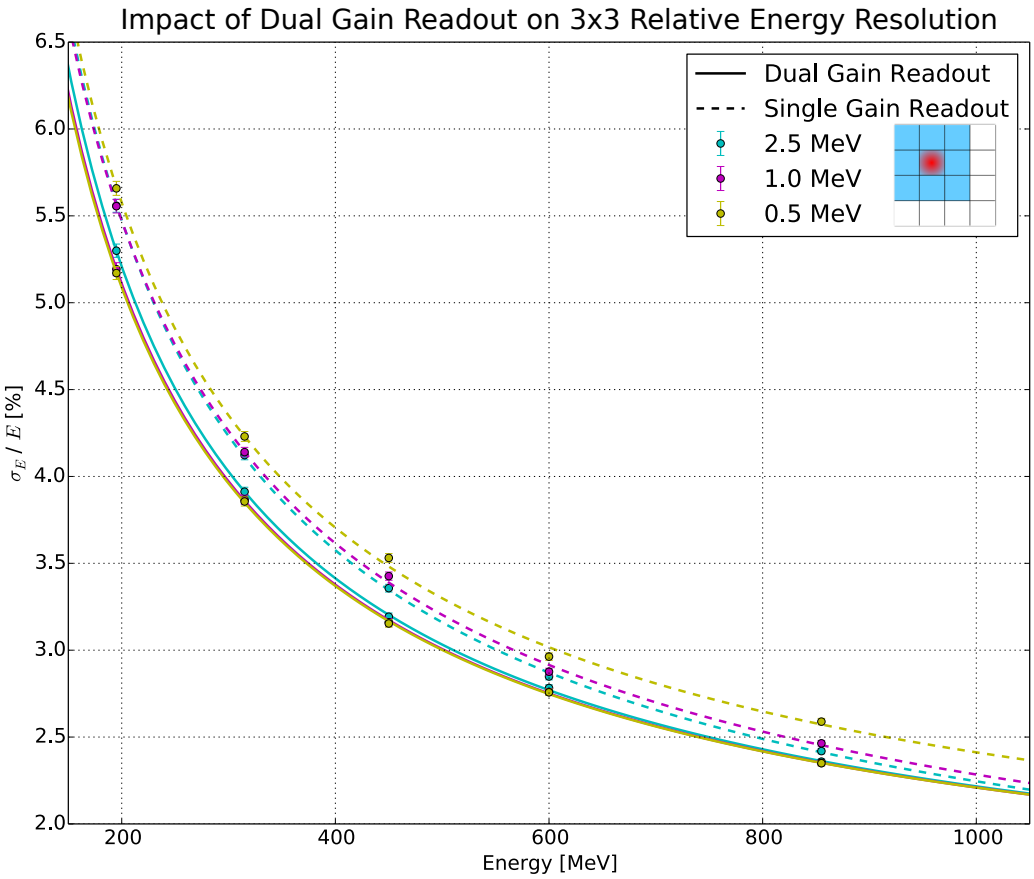

Figure 6.13: The plot shows the impact of the dual-gain readout compared to the single-gain readout (only low gain). Due to the better signal to noise ratio of the high amplification, the relative energy resolution always improves and in particular at low energies compared to the dual-gain readout. In the case of the single-gain readout, the energy resolution even worsens by lowering the threshold due to the summation of noise hits.

In a later particle physics experiment like $\bar{\text{P}}$ANDA, the hit detection threshold of the high gain will be set to a lower energy value compared to the low gain. However, for the threshold scan, both gains are set to the same hit detection threshold since high

noise hit rates are not an issue for offline analysis. Subsequently, a routine within the analysis detects saturation in the high gain and chooses the low gain amplification data in this case. This procedure is called dual-gain readout within this work. In Figure 6.12 the result of the threshold scan for a 3×3 cluster is depicted. The results for the other three 3×3 crystal matrices of the EMC prototype can be found in Appendix C.
As expected, the relative energy resolution improves by lowering the threshold. The resolution benefits from lower thresholds. Nevertheless, at thresholds lower than 1.0 MeV the improvement reaches its limit. The relative energy resolution curves for the thresholds 1.0 MeV and 0.5 MeV are almost congruent. Degradation of the relative energy resolution for a too low threshold can not be observed for the dual-gain readout. Nevertheless, this effect can be observed by using only the low gain amplification (single-gain readout). In Figure 6.13, the results obtained with single-gain readout and dual-gain readout are compared.
In the case of the single-gain readout, the relative energy resolution degrades by lowering the threshold below 2.5 MeV. This behaviour indicates that noise hits are added to the cluster sum.
As Figure 6.13 shows, the relative energy resolution always benefits from the dual-gain readout at all measured energies and all applied thresholds. Also, the data acquisition can be operated at a manageable noise hit level. By utilising the result from the simulation (Figure B.2), it can be shown that at an APD gain of 150 the noise hit rate for the high gain is well below the limit of the data acquisition (161 kHz at a threshold of 2.5 MeV). By using the online timestamp comparison (Subsection 5.2.4), the noise hit rate can be reduced to a few kHz.
In summary, the detector system is sensitive to changes of the single-crystal threshold down to 1.0 MeV using an APD gain of 150 in the dual-gain readout (Figure 6.12). However, considering rate limits of the data acquisition, an upper limit for the lowest single-crystal threshold of 2.5 MeV can be specified, which is 0.5 MeV lower than the $\bar{\text{P}}$ANDA TDR requirement of 3 MeV [TDR08].

6.5 Linearity of the Prototype Response

Besides the relative energy resolution, the linearity of the calorimeter response is a second important feature. The simulations in Subsection 5.2.6 have shown that the TMAX parameter extraction has a linear response to the input energy. The deviations from a perfect linearity are always smaller than 160 keV for energies below 100 MeV and smaller than 50 keV for energies above 100 MeV for an APD gain of 150 (Figure B.11). Nevertheless, the mentioned simulation only considers a single APD channel with the high and the low gain amplification. In a real measurement, other factors have to be considered. For instance, there are non-linearities in electronic components, miss-calibrations between detector channels or temperature drifts over the measurement time.
In the following the detector response as a function of the energy deposited into a 3×3 crystal matrix will be determined. In Subsection 6.2.4 it was already discussed that a

single crystal does not measure the beam energy but only a fraction of it. The same is true for a 3×3 crystal matrix. Of course, the fraction is higher in the case of a 3×3 crystal matrix. In order to determine the expected deposited energy in a 3×3 crystal matrix as a function of both the particle energy and the hit detection threshold, the result of a Geant4 simulation is used.

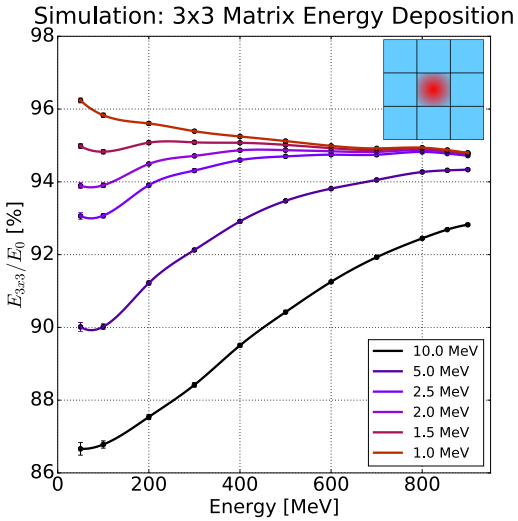

Figure 6.14: The plot shows the results of a Geant4 simulation. Displayed is the ratio between expected deposited energy in a 3×3 crystal matrix and the incoming particle energy. The different curves correspond to different hit detection thresholds. At higher incoming energies, the relative losses due to shower leakages decrease. At lower incoming energies, the contribution becomes more and more dominant. Thus, the ratio becomes smaller for higher thresholds.

The outcome of the simulation in Figure 6.14 shows two significant effects. For low hit detection thresholds, the fraction ($E_{3\times3}/E_0$) lowers for higher particle energies. At higher hit detection thresholds, the curves already start at a lower fraction and rise for higher energies. Since smaller particle energies also result in smaller energies in the neighbouring crystals, these smaller leakage energies are ignored due to the higher threshold. The curve shapes result from the interplay of the mentioned effects.

By using the simulation results, the expected deposited energy into the 3×3 matrix is determined for every beam energy for a specific hit detection threshold. For instance, at a beam energy of 195 MeV and a hit detection threshold of 5 MeV, 90.9 % of the energy (177 MeV) can be measured by a 3×3 matrix. Subsequently, the calorimeter response is determined by fitting the sum spectra (Subsection 6.2.5) with the Novosibirsk function (Equation 6.1) and extracting the maximum position of the peak. Finally, the calorimeter response is plotted against the expected deposited energy, extracted from the simulation. In Figure 6.15 this procedure is shown for a hit detection threshold of 5 MeV. The hit detection threshold was chosen to avoid inefficiencies in the hit detection. The non-linearity is in the order of 1 MeV and thus only in the order of a few per mil compared to the deposited energies. The linearity plots for the three other 3×3 cluster of the EMC prototype can be found in Appendix C.

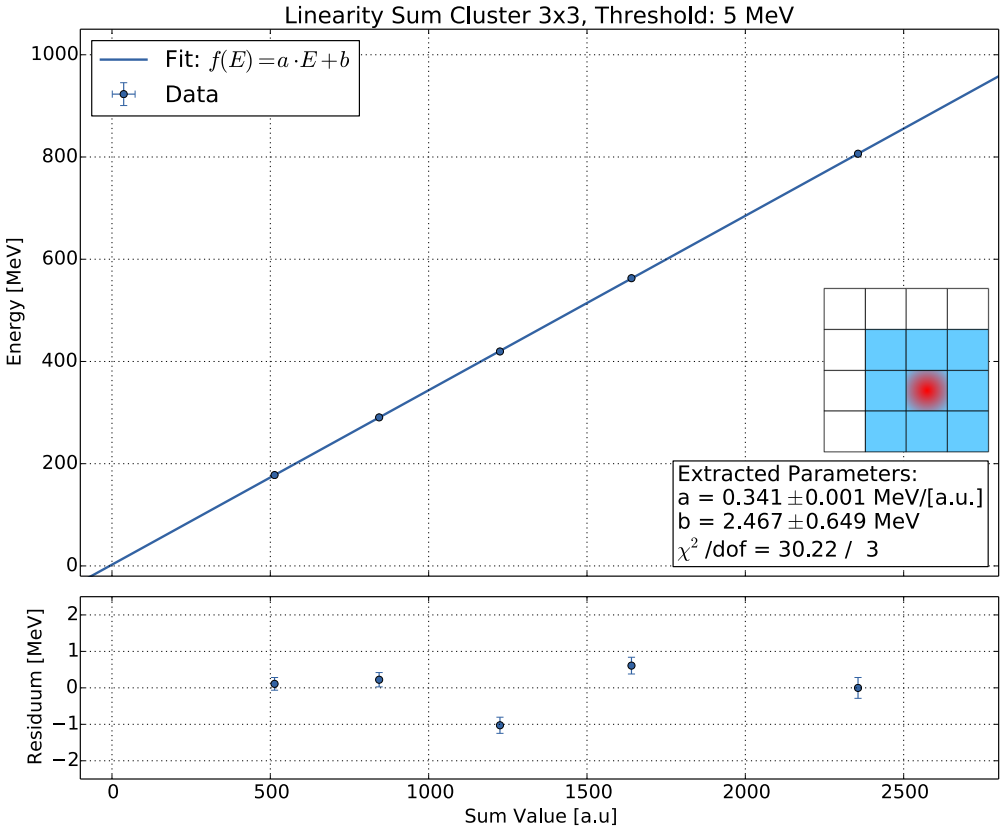

Figure 6.15: The plot shows the expected deposited energy versus the measured detector signal of the EMC prototype for a 3×3 crystal matrix. The threshold was set to 5 MeV. The expected deposited energies stem from a Geant4 simulation (Figure 6.14). The non-linearity of the prototype is in the order of a few per mil.

6.6 High Rate Measurements and Pileup Handling

The firmware, which was developed in this work (Chapter 4), gives the possibility to perform high rate measurements with the EMC prototype. The results of these high rate measurements are discussed in the following.

The limiting factor for the maximum achievable detector rate is not the data bandwidth of the readout but rather the duration of the leading edge of the APFEL preamplifier pulse, which has a width of about 300 ns. As explained in Section 4.5, the pulse recognition is based on the change of sign of the derivative of the FIR filtered signal. The shortest period between two separable pulses is about 450 ns at the current implementation. There are four relevant types of consecutive pulses, which are described in the following. Furthermore, an illustration of these types can be found in Figure 6.16.

1. A second pulse occurs after the decay time of the first pulse. The pulses can easily be separated.

2. A second pulse occurs within the separation limit. Thus, the pulse processing algorithm is not able to separate the pulses.

3. A second pulse occurs after the separation limit but before the first pulse is completely decayed. The pulses can be separated, but the extracted height of the second pulse is attenuated.

4. Two or more additional pulses occur within the time interval of the first pulse. A pulse separation depends on the pulse positions (similar to type 2 and type 3).

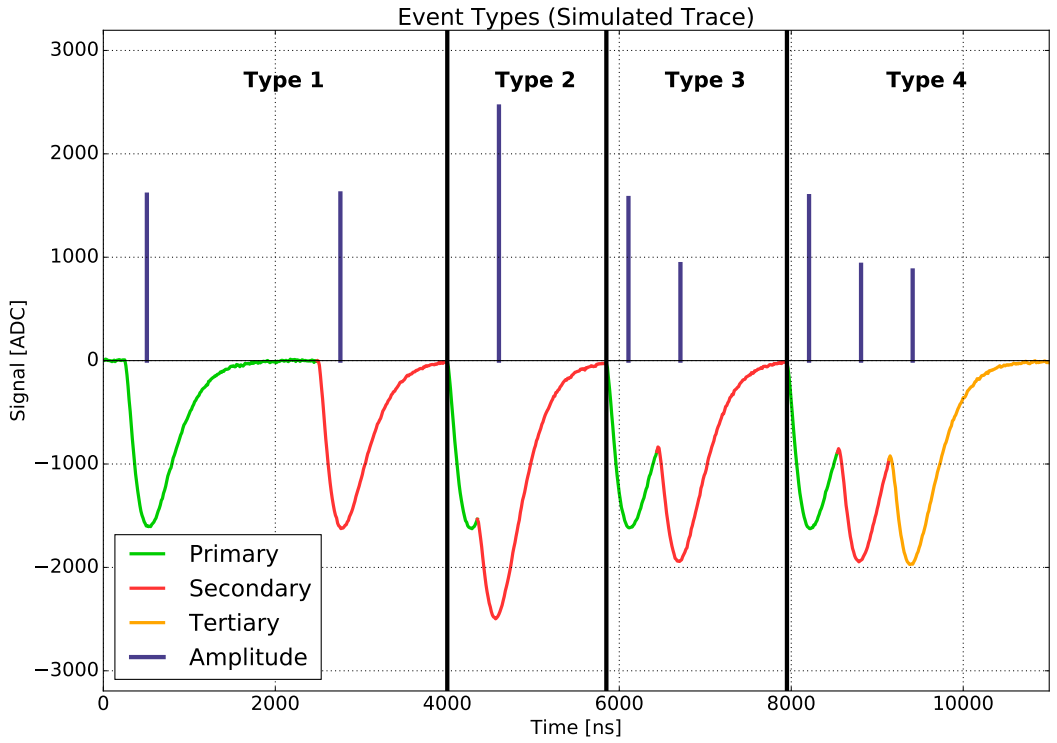

Figure 6.16: The illustration shows the most important time structures of consecutive pulses. All pulses have the same amplitude to demonstrate the impact of the time structure to the extracted values. The blue bars represent the extracted amplitudes and timestamps. Type 1 describes two pulses, which are not superimposed. Type 2 describes a second pulse, which occurs within the separation limit of the pulse processing algorithm. Type 3 described a second pulse after the separation limit but before the first pulse is wholly decayed. Type 4 describes two or more additional pulses within the time interval of a first pulse.

The different types occur with different probabilities depending on the event rate. The $\bar{\text{P}}$ANDA TDR [TDR08] requires an event rate of up to 100 kHz for the backward and the barrel part of the EMC. Thus, the probabilities for the different event types are determined for an event rate of $R = 100\,\text{kHz}$. The probabilities are calculated according to the Poisson distribution (Subsection 4.5.4) with k being the number of events within a time interval ΔT and λ being the product of ΔT and R. Δt is the time between consecutive pulses within ΔT. In Table 6.1 the results of the calculation is shown.

Type	Δt [ns]	ΔT [ns]	k	$\lambda = \Delta T \cdot 100\,\text{kHz}$	$P_{100\,\text{kHz}}$
1	[0,1500]	1500	0	0.150	86.1 %
2	[0,450]	450	1	0.045	4.3 %
3	[450,1500]	1050	1	0.105	9.5 %
4	[0,1500]	1500	≥ 2	0.150	1.0 %

Table 6.1: The table shows the probabilities of the different types of consecutive pulses calculated with the Poisson distribution. Type 1, 2 and 3 are calculated by using the time interval ΔT and the number of additional pulses k within it. Whereby Δt is the time between consecutive pulses within ΔT. For instance, type 1 has no consecutive pulse ($k = 0$) between $\Delta t = 0\,\text{ns}$ and $\Delta t = 1500\,\text{ns}$, which corresponds to the interval $\Delta T = 1500\,\text{ns}$. Type 3 has exactly one ($k = 1$) consecutive pulse after the separation limit of $\Delta t = 450\,\text{ns}$ but before the first pulse is completely decayed at $\Delta t = 1500\,\text{ns}$. Type 4 corresponds to two or more pulses within ΔT with $P_{100\,\text{kHz}}(\Delta T, k \geq 2)$.

In the following, the different event types will be used to interpret data from high rate measurements with the EMC prototype.
The basic setup for the measurement is described in Subsection 6.2.1. The electron beam was centred on one crystal of the crystal matrix. The plastic scintillator, as shown in Figure 6.2, was used for a rate reference measurement. The electron rate was adjusted by varying the beam current. An electron beam energy of 855 MeV was used during the whole test.
The output from the data aquisition is the event information, which contains the amplitude and the time information of the individual events. By using the event timestamps, the time Δt between consecutive events can be extracted in the offline analysis. The extracted amplitudes and the time differences to their previous events are subsequently plotted against each other event by event. In Figure 6.17 such an event-by-event scatter plot is shown for a detector rate of 110.35 kHz.
The red region above 1500 ns shows the type 1 events. Here, a pulse separation and amplitude determination is trivial. The broad straight distribution above (green and blue) shows type 2 events. These events generally can not be separated. In the particular case of a mono-energetic electron beam, they have an amplitude which is twice the value of type 1 events. The red snapping part below 1500 ns indicates type 3 events. For type 3, the amplitude of the second pulse is distorted due to the superposition with the first pulse. The green snapping part below type 3 indicates a

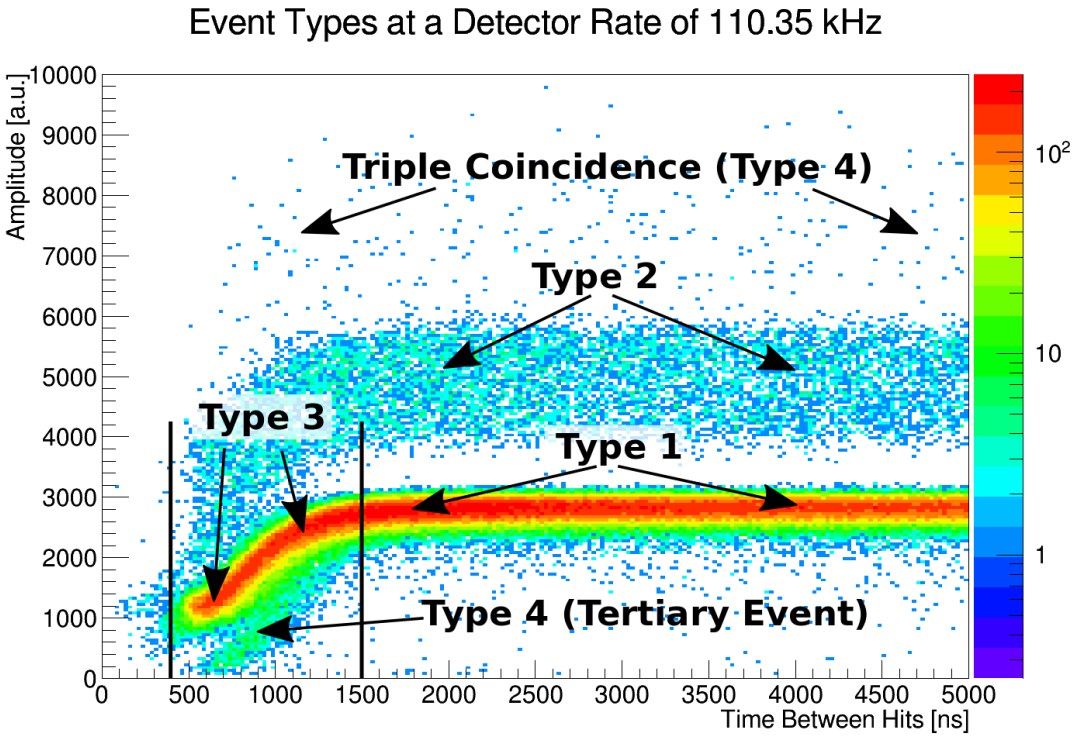

Figure 6.17: The two-dimensional histogram shows the relation between the extracted amplitude of an event and the time difference (Δt) to the previous event for mono-energetic events (855 MeV). The red part above 1500 ns shows type 1 events (see explanation in the text). The type 2 region shows pileup events, which can not be separated. The amplitude of type 3 events is smaller compared to type 1 events. However, type 3 events can be separated, and the amplitudes of the secondary pulses can be restored. The kink below type 3 events stems from tertiary events of type 4, which have even smaller amplitudes than type 3 events.

special case of type 4 events. A second pulse is located within the separation limit (type 2). In addition, a third pulse is located on the falling edge of the superimposed pulses. In this particular case, the amplitude of the third pulse is even more attenuated than the amplitude of the second pulse in type 3 events. Events with even higher amplitudes than type 2 events are a further category, where both the second and third pulse are located within the separation limit.

6.6.1 Pulse Amplitude Restoration

As shown in the previous section, the signal processing algorithm is capable of detecting a second pulse on the falling edge of a primary pulse. This case is denoted above as type 3 event. Due to the superposition with the falling edge of the primary pulse,

the extracted amplitude of the second pulse is attenuated (see Figure 6.16). In the following, a simple procedure will be presented, which makes the correction of the extracted amplitude of the second pulse for type 3 events possible.
As explained in Subsection 4.5.4 a correction function Σ is needed for the amplitude extraction of type 3 events. Σ has three inputs: the extracted height of the first pulse $H^{p}_{\text{meas.}}$, the extracted height of the second pulse $H^{s}_{\text{meas.}}$ and the time difference between the pulses Δt. The corrected amplitude of the second pulse can be calculated with:

$$H^{s}_{\text{corr.}} = H^{s}_{\text{meas.}} \cdot \Sigma(H^{p}_{\text{meas.}}, H^{s}_{\text{meas.}}, \Delta t) \tag{6.3}$$

Due to the measurement with mono-energetic electrons, a special case of equal amplitude heights for both the first and the second pulse is considered. In this particular case, the correction factor is only a function of the time difference Δt between the pulses.
The type 3 region in Figure 6.17 already characterises the attenuation of secondary pulses as a function of Δt. The approach is to fit the type 3 region with a high order polynomial function. Subsequently, the polynomial function is normalised to the undistorted pulse height, which is defined by the amplitude value of the type 1 region. The result is a function $A(\Delta t)$, which is depicted in Figure 6.18. Finally, the correction function Σ is:

$$\Sigma(\Delta t) = \frac{1}{A(\Delta t)} \tag{6.4}$$

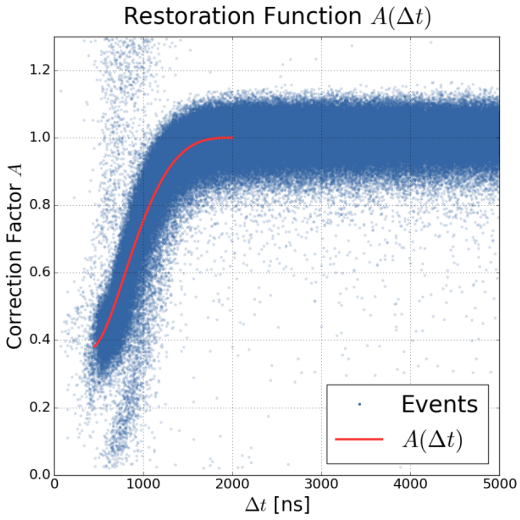

Figure 6.18: The plot shows the fit of the type 3 region in Figure 6.17. The function is determined by a ninth order polynomial fit. The correction curve applies for the case of mono-energetic events. In this case, the correction function only depends on the time difference Δt between the first and second pulse. A generally valid solution of Equation 6.3 can be determined with the simulation framework, which is discussed in Chapter 5. Nevertheless, this has not been done in this work.

The determined correction function only applies for mono-energetic events. However, by using the simulation framework (Chapter 5), a generally valid solution of Equation 6.3 can be determined by scans. Such a scan has to be done for all possible combinations of the energy (pulse height) of the first and the second pulse. Nevertheless, this has not been done in this work.

With the help of the fit in Figure 6.18, the type 3 events of Figure 6.17 can be corrected. The amplitudes of the second pulses are multiplied by $1/A(\Delta t)$. In Figure 6.19, the performance of this procedure is depicted. The uncorrected type 3 event amplitudes (blue histogram) move towards amplitude values of type 1 events, after applying the correction. Furthermore, the histogram for type 3 events becomes more symmetric (green histogram). By adding the corrected events to the type 1 events (red histogram), they are no longer considered as lost events (magenta histogram). However, the procedure slightly degrades the relative single-crystal energy resolution (5.226(6) % compared to 4.908(5) %) at 855 MeV. One reason for the degradation of the relative energy resolution is that type 4 events also have been corrected with the type 3 event restoration function. By considering Figure 6.17 or Figure 6.18 a slightly different course of the lower kink can be identified. Thus, a possible type 4 restoration function would be slightly different compared to the type 3 restoration function.
Nevertheless, the important result of this method is the possibility of reducing the effective pileup rate. Depending on the physics case, it can be chosen between a better energy resolution (ignoring type 3 events) or a better statistics (adding corrected type 3 events to type 1 events).

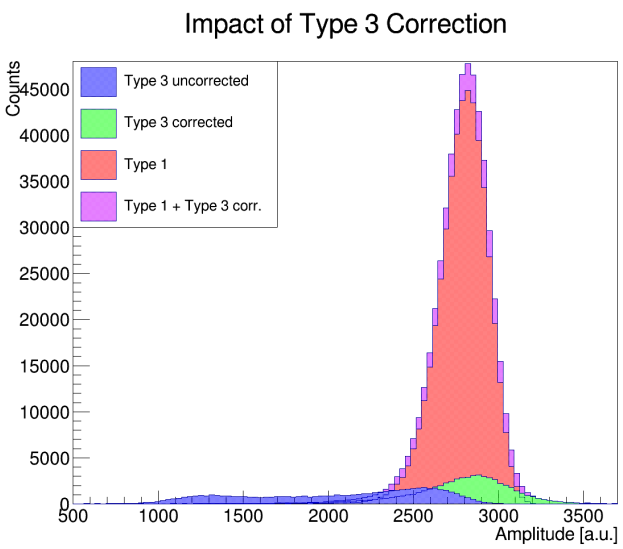

Figure 6.19: The plot demonstrates the impact of the type 3 correction. The blue histogram shows the broad distribution of uncorrected type 3 events, which is a consequence of the amplitude dependency from the time difference Δt (see Figure 6.17). After the correction (green histogram), the type 3 distribution moves towards the type 1 distribution (red histogram). Adding the corrected type 3 events to the type 1 events (violet histogram) results in a better statistics.

6.6.2 Dead Time of the Prototype

The dead time describes the time during which the detector readout is busy processing an event and not able to accept new events. All additional events within the dead time are considered as pileup and can not be distinguished from each other.
In order to determine the EMC prototype dead time, the event rate has to be measured with an additional detector. Therefore, the plastic scintillator with the photomultiplier readout comes into play (see Subsection 6.2.1). Typical photomultiplier tube pulses have a length of a few nanoseconds. Thus, their pileup probability is much lower

compared to the pileup probability of the EMC signal pulses (13.9 % at 100 kHz). For instance, the pileup probability for photomultiplier pulses with a length of 10 ns is less than one per mil at an event rate of 100 kHz. As a result, the inaccuracy of the event rate measurement with the plastic scintillator can be neglected.
For the analysis, the EMC detector rate $R_{\text{Det.}}$, is extracted from the timestamps of the event hits. The degradation of the measured EMC detector rate compared to the rate measured with the scintillator $R_{\text{Sci.}}$ can be described by:

$$R_{\text{Det.}} = R_{\text{Sci.}}(1 - \tau R_{\text{Det.}}) \tag{6.5}$$

Whereby τ is the dead time of the EMC prototype. The degradation of the measured EMC rate depends on the EMC rate itself. The higher the event rate in the EMC, the higher the probability for pileup. As a result, the number of non-distinguishable events increases and thus, the measured EMC detector rate does not increase linearly with the event rate.
In order to remove the $R_{\text{Det.}}$ dependency of the right side of Equation 6.5, the equation can be converted into:

$$R_{\text{Det.}}(R_{\text{Sci.}}, \tau, \epsilon) = \frac{\epsilon \cdot R_{\text{Sci.}}}{1 + \tau \cdot \epsilon \cdot R_{\text{Sci.}}} \tag{6.6}$$

Whereby ϵ is a factor introduced to account for inefficiencies in the scintillator readout. These inefficiencies resulted from a too high discrimination threshold, which was applied to the photomultiplier signals. In Figure 6.20, the fit of the data by using Equation 6.6 is shown.
The EMC prototype dead time is

$$\tau = 464(13)\,\text{ns}$$

The result agrees with the estimation for the signal processing detection limit of 450 ns.

6.6.3 Effective Pileup Probability of the Prototype

The $\bar{\text{P}}$ANDA TDR [TDR08] aims a pileup rate of 1 % at a single-channel detector rate of 100 kHz. Due to the length of 1500 ns of the APFEL preamplifier pulse, the pileup probability at this rate is 13.9 %. However, the signal processing procedure is able to detect pulses on the falling edge of the first pulse. In combination with an amplitude restoration as demonstrated in Subsection 6.6.1, this kind of pileup events can be considered as recovered. As a result, the effective pileup probability at 100 kHz decreases. However, the situation is different for one or more additional pulses within the dead time of 464(13) ns, which are not only lost but also affect the amplitude measurement of the first event (see Figure 6.16, type 2).
Nevertheless, according to the Poisson distribution the current pileup probability with corrected type 3 events at 100 kHz of the EMC prototype is:

$$P_{100\,\text{kHz}} = 4.53(12)\,\%$$

A further improvement is only possible if the signal processing algorithm is extended with an event type 2 separation based on slope changes on the rising edge of the superimposed pulses. However, it will be challenging to achieve the 1 % mark due to inefficiencies in the pulse detection under these conditions. Finally, all results of this chapter are summarised in Table 6.2.

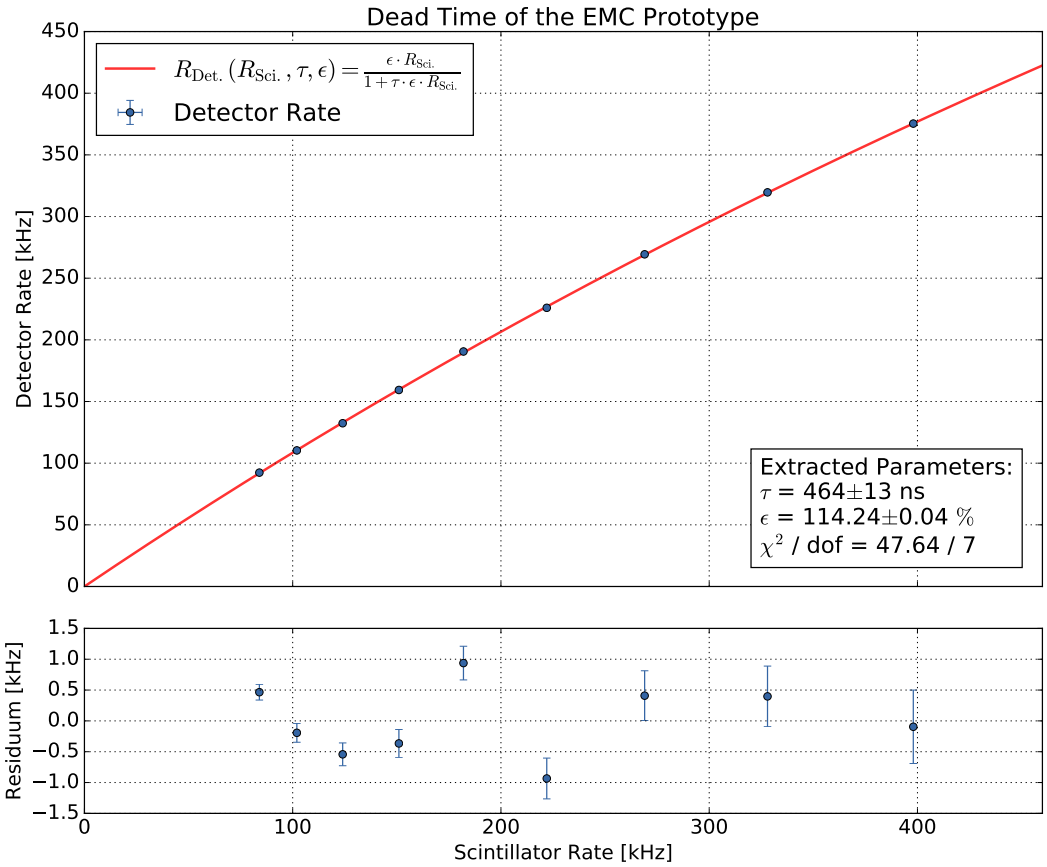

Figure 6.20: The plot shows the measured EMC detector rate as a function of the measured plastic scintillator rate. Equation 6.6 describes the relation between the different measurements and gives access to the dead time τ of the EMC prototype.

Parameter	Achieved Value			TDR	Unit
	Worst	Typical	Best		
Rel. En. Res.	According to Subsection 3.1.4				
σ_E/E at 1 GeV	2.440(14)	2.207(6)	2.190(2)	$\leq$2.5	%
Constant a	1.23(21)	1.08(14)	0.95(61)	$\leq$1	%
Statistics b	2.02(65)	1.83(45)	1.78(30)	$\leq$2	$\frac{\%}{\sqrt{E[\mathrm{GeV}]}}$
Noise per Channel c	2.14(9)	2.02(15)	1.92(60)	$\leq$3	MeV
Single Crystal					
Lowest Threshold	-	$\leq$ 2.5	-	$\leq$ 3	MeV
Non-Linearity					
Maximum	2.22(36)	1.26(24)	1.21(19)	-	‰
Timing					
Dead Time τ	-	464(13)	-	-	ns
Pileup $P_{100\,\mathrm{kHz}}$	13.9 (w/o corr.)	4.53(12)	-	1	%
Highest Event Rate	-	-	375.4(6)	100	kHz

Table 6.2: The table summarises the performance parameters of the EMC prototype. Values which are determined with different 3×3 crystal clusters are subdivided into "Worst", "Typical" and "Best" to get a better overview of the data. The "Typical" value is the second best result of the four 3×3 crystal clusters. On the right side, the requirements of the TDR are compared with the results. The results of the relative energy resolution and the non-linearity were determined with an APD gain of 150. The results for the timing were determined with an APD gain of 200. The worst-case for the pileup probability $P_{100\,\mathrm{kHz}}$ refers to the theoretical value, which would be achieved without a type 3 correction.

7

Exploratory Measurements for the FAIR Phase-0 Experiment at MAMI

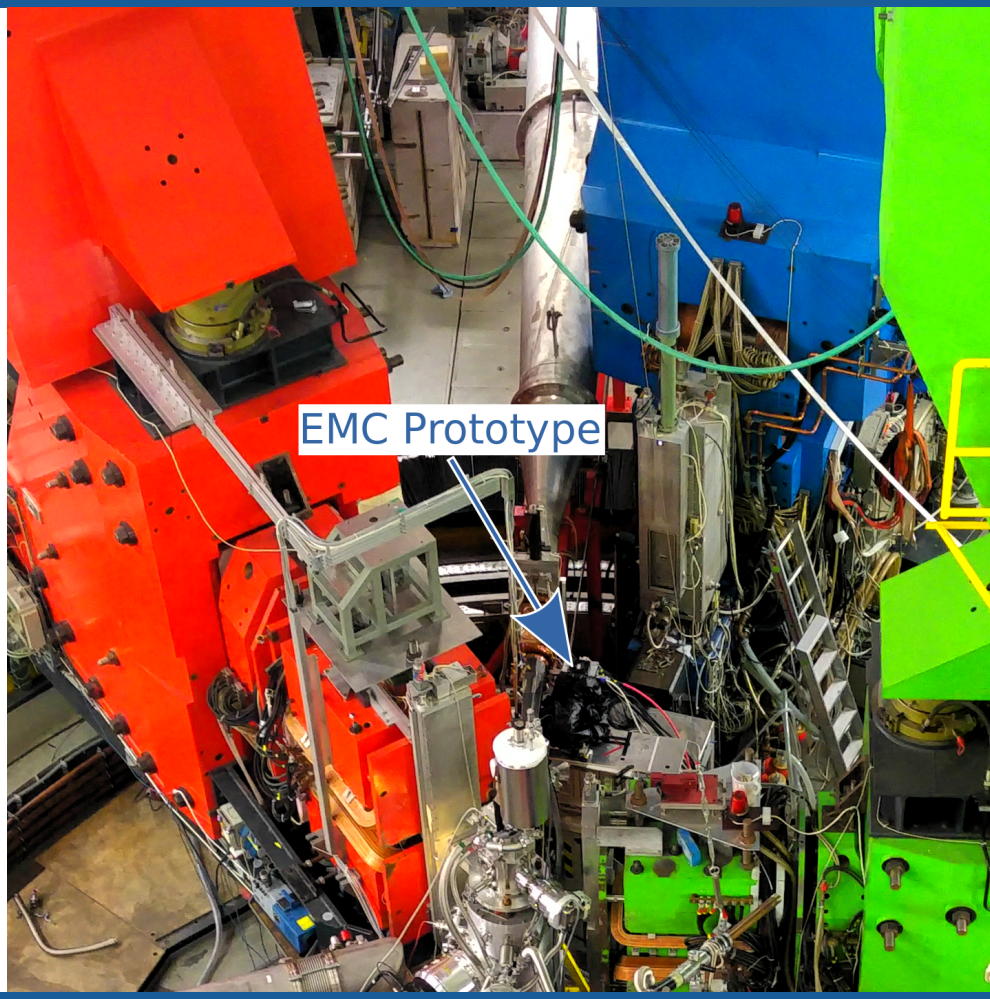

The picture shows the EMC prototype at a test beam at the A1 electron scattering facility at MAMI. The prototype is located behind a scattering chamber, which is surrounded by three magnetic spectrometers. The setup is designed to perform the first scattering experiment with the EMC prototype using carbon, tantalum and carbon-hydrogen targets. The test is a significant milestone on the way towards the FAIR Phase-0 experiment in Mainz. The results show the capability of the EMC to operate under small scattering angles as it is necessary for the measurement of the pion electromagnetic transition form factor.

The techniques, which were developed in this work, will not only find usage at the $\bar{\text{P}}$ANDA experiment but also at the upcoming FAIR Phase-0 experiment in Mainz, presented in Chapter 2. In the preparation of FAIR Phase-0, feasibility studies were performed, including both simulations and beam tests. A detailed discussion about the feasibility studies can be found in [Wol18] and [CGM$^+$20].

The aim of this chapter is the determination of the relative energy resolution as a function of the luminosity for the FAIR Phase-0 experiment in Mainz by using both measurement and simulation. Consequently, implications for the pion TFF measurement accessible luminosity and thus the measuring time can be derived.

At the beginning of the chapter, the test setup at MAMI will be discussed with emphasis on the measurement under small scattering angles. Small scattering angles imply a high rate of low energy background events.

Consequently, the analysis gives access to the energy distribution of low energy electrons and photons under small scattering angles. This is relevant since low energy events can superimpose with the final states of the exclusive reaction in Phase-0. The superposition, in turn, leads to amplitudes that are erroneously measured too high. Due to the fluctuation in the superimposed pulses, the relative energy resolution decreases. The probability for superpositions is a function of the rate of background events. The rate of background events is, in turn, a function of the luminosity.

7.1 Beam Tests for the FAIR Phase-0 Experiment

As presented in Chapter 2, the FAIR Phase-0 experiment aims at the measurement of the electromagnetic transition form factor of the pion by using the Primakoff π^0 electroproduction. The final states are the electron, which scatters on the nucleus and the two photons, which stem from the pion decay (Equation 2.5).
Due to kinematical constraints (Figure 2.3), the calorimeter has to be located in the forward direction. Consequently, a high rate of low energy background electrons and photons is expected. This low energy background affects the exclusive reaction measurement due to its superposition with signal pulses.
Besides others, this effect was studied with a scattering test at the A1 facility at MAMI by using the EMC prototype.

7.1.1 Test Setup at the A1 Spectrometer Hall at MAMI

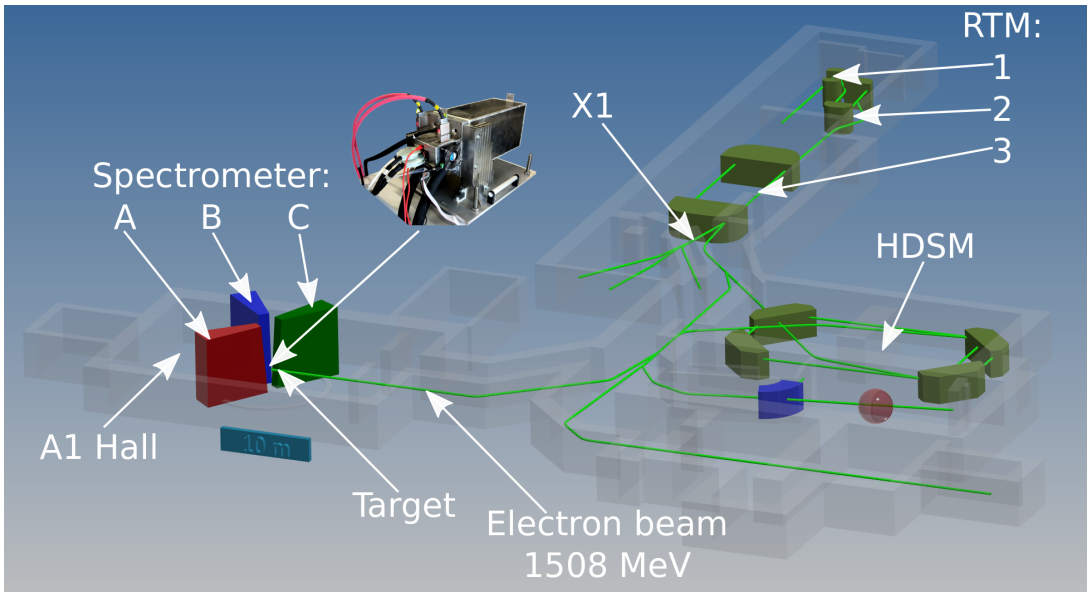

Figure 7.1: The schematic view shows the Mainz Microtron facility with the location of the EMC prototype for the FAIR Phase-0 feasibility test beam. The A1 experiment consists of three magnetic spectrometers (A, B and C), which surround a target vacuum chamber. For the test beam, the prototype was mounted on the support structure of spectrometer B. Consequently, the EMC prototype was adjustable along the scattering angle Θ. The crystal matrix was pointing in the direction of the target centre. Spectrometer A was used for a coincidence measurement, and spectrometer C was not used.

In Section 6.1, the Mainz Microtron (MAMI) was already introduced. Furthermore, the beam test at the X1 extraction point is discussed in Subsection 6.2.1. The beam

tests at X1 were performed by letting the electron beam hit the crystal matrix of the prototype directly.
At the A1 hall instead, the prototype was located behind a target under an adjustable scattering angle. The collision between the electron beam and the target results into the scattering of electrons and the production of secondary particles. Since the A1 hall is behind the last stage of MAMI (HDSM), see Figure 7.1, a beam energy of 1508 MeV was used for the experiment. In Figure 7.2 the location of the EMC prototype within the A1 hall is shown.

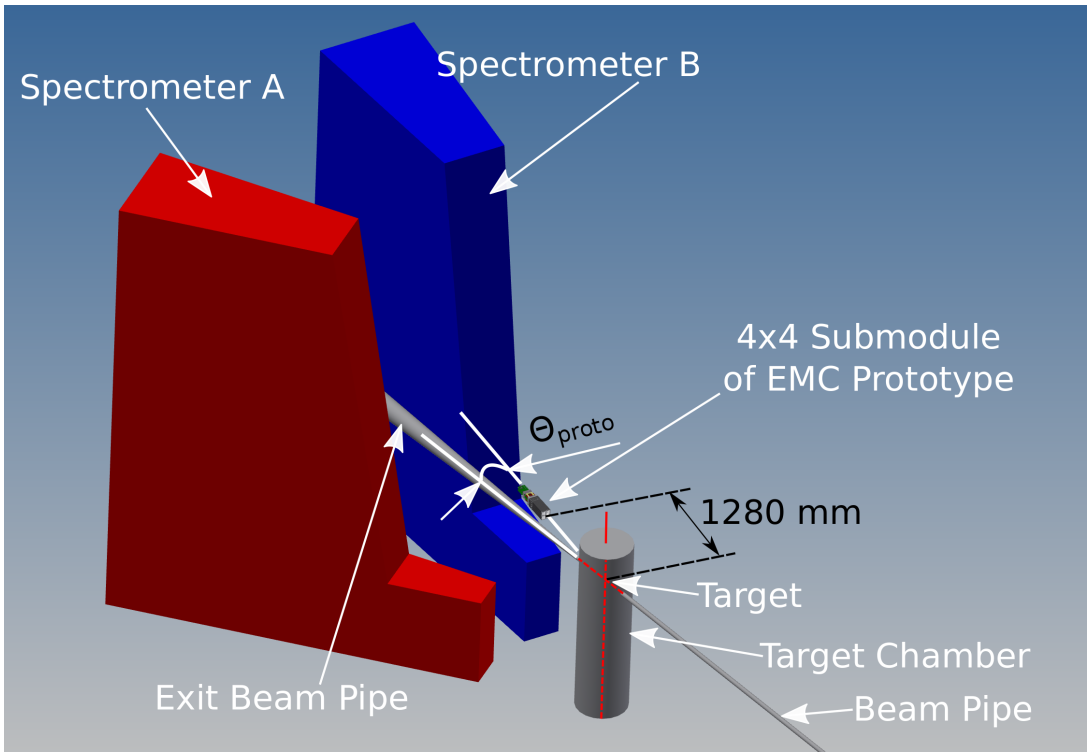

Figure 7.2: The illustration shows the test beam setup at the A1 hall at MAMI. For the test, only the spectrometers A and B were relevant. The spectrometer A was used for a coincidence measurement with the EMC prototype. The support of spectrometer B was used as a rotatable mounting for the EMC, because it assures a very good alignment of the prototype. The central axis of the 4×4 crystal matrix of the prototype was at the height of the beam. Furthermore, the central axis of the crystal matrix was parallel to the radial vector with its origin at the target. The angle between (exit) beam pipe and the central axis of the crystal matrix was defined by Θ_{proto}. The minimum angle was $\Theta_{\text{proto}} = 8.7°$. The distance between the target and the front surface of the crystal matrix was 1280 mm.

The A1 hall harbours three magnetic spectrometers (A, B and C). All spectrometers can be moved and be adjusted to different scattering angles around the target. Necessary

for the beam test were spectrometer A and B. The prototype was mounted on the support of spectrometer B. Consequently, a precise rotation along the scattering angle Θ_{proto} was possible. Besides, the rotation of the prototype could be done externally. With its width of 100.3 mm, the 4×4 crystal matrix covered a polar scattering angle of 4.5° and a solid angle of 6.13 msr.

In Figure 7.3 a photograph of the setup is shown. The EMC prototype was mounted on a movable positioning table, to perform a fine adjustment of its position. The movable table was mounted on the spectrometer B support via an aluminium structure. Similar to the beam tests at X1 (Chapter 6), the prototype was remotely controllable from the counting room.

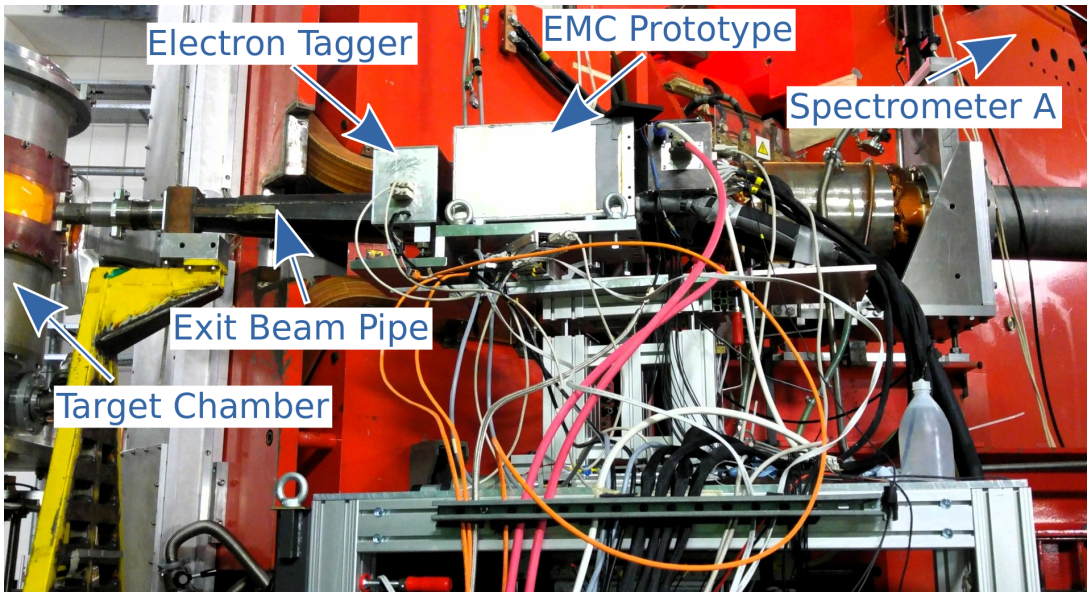

Figure 7.3: The photograph shows the setup for the FAIR Phase-0 feasibility study at the A1 hall at MAMI. The EMC prototype was mounted on a movable table to perform a fine adjustment of its position. The movable table is connected with the spectrometer B via an aluminium construction. In the front of the EMC prototype, the so-called electron tagger was mounted, which was used to distinguish between electrons and photons [Gra18].

The target system consists of a cylindric vacuum chamber at which both the beam pipe and the exit beam pipe are attached (Figure 7.2). A window in the forward direction (see the left side of Figure 7.3), allows scattered particles to exit the vacuum chamber. The window is covered with a thin layer of Kapton® to minimise the material budget. The target itself is in the centre of the vacuum chamber. An exchange mechanism allows for a remote switch of targets.

As explained in Chapter 2, a high Z target enhances the Primakoff π^0 electroproduction cross section. Thus, Tantalum $^{181}_{73}$Ta was used as target material. Due to its high

melting point (3290 K), it is suitable for measurements at high beam currents. Also, other targets were utilised for different purposes. Firstly, polyethene [-CH_2-CH_2-]$_n$ was used to measure the elastic electron-proton scattering on H nuclei under different scattering angles. The energy of the detected elastically scattered electrons is a function of the scattering angle. By performing a coincidence measurement with spectrometer A, an energy calibration of the EMC prototype was possible. For this, the prototype detected the elastically scattered electron, while the spectrometer measured the recoiled proton. Finally, $^{12}_{6}$C was used to perform a quasi-elastic scattering measurement. A complete discussion of the measurements with the different targets can be found in [Wol18]. The following section focuses on the low energy background measurement by using the $^{181}_{73}$Ta target.

7.1.2 Background Rate and Energy Distribution

Since the FAIR Phase-0 calorimeter will be installed at small scattering angles, a high background rate of low energy electrons and photons is expected. Consequently, the EMC prototype was placed as close as possible to the exit beam pipe, which corresponds to a scattering angle of $\Theta_{\text{proto}} = 8.7°$. As a result, the minimum angle between the exit beam pipe and the lateral surface of the crystal matrix was $\Theta_{\text{min.}} = 6.5°$. Thus, the test measurement addressed a scenario, which is close to the worst-case angle ($\Theta = 5°$, see Figure 2.9) for the low energetic background rate at FAIR Phase-0. For the test beam, a specially developed trigger unit was used, to allow triggering on the 16 individual detector crystals. The 16 logic output signals were fed to a VMEbus (Versa Module Eurocard-bus) scaler module to determine the individual rates in the calorimeter crystals. In Figure 7.4 the sum of the detector rates of the four central crystals of the 4×4 crystal matrix as a function of the beam current is depicted. The threshold, which was applied at the central crystals corresponds to an energy of approximately 150 MeV. The measurement reveals a good linear dependency of the total event rate on the beam current.

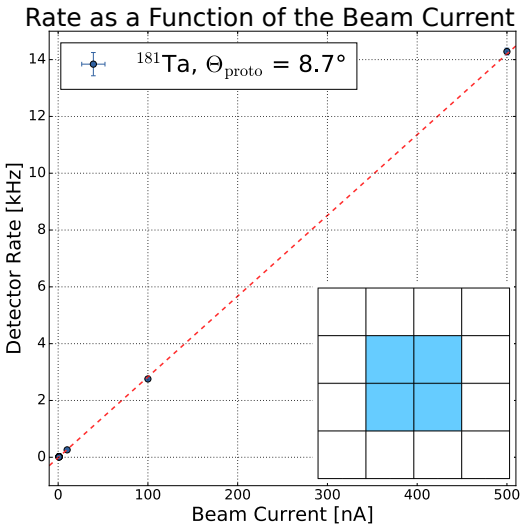

Figure 7.4: The plot shows the result of the total rate measurement for the $^{181}_{73}$Ta target. The EMC prototype was located at the smallest possible scattering angle $\Theta_{\text{proto}} = 8.7°$ to measure a close to worst-case scenario for the background. The plot shows the sum of the rates of the central crystals against the beam current. The applied threshold corresponds to an energy of approximately 150 MeV. The measurement reveals a good linear dependency of the total event rate on the beam current. [Wol18]

Besides the total event rate dependency on the beam current, the energy distribution of the low energetic background is essential for the following discussion. Luigi Capozza performed an analysis of recorded traces [Cap19]. He extracted the summed rate as a function of the event energy. Consequently, a particular rate for a given energy in Figure 7.5 is the sum over all rates until the given energy beginning at the highest energy. The analysis was done for three different beam currents.

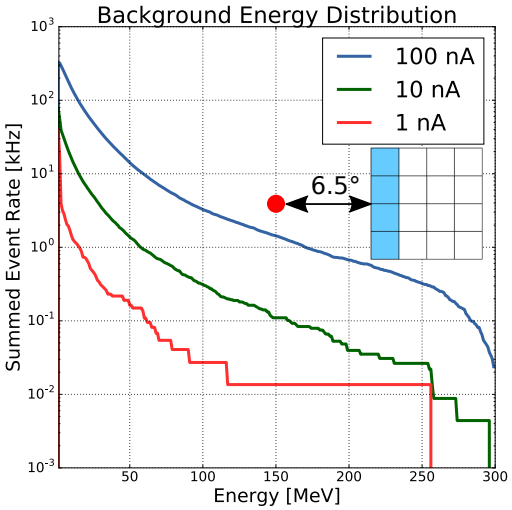

Figure 7.5: The plot shows the integrated event rate as a function of a given energy threshold. At the lowest energy, the full spectrum is integrated, which results in the total single-crystal event rate at the given current. The rates were determined by using a representative crystal of the crystal column, which is closest to the exit beam pipe (blue column in the illustration). At this column, the highest rates were measured since it was at the smallest scattering angles ($\Theta = 6.5°$ to $\Theta = 7.6°$). [Cap19]

The three curves in Figure 7.5 have approximately the same shape. Since there is a factor of 10 between the individual beam currents, the linear dependency between total rate and beam current can be seen again due to the equidistant offsets between the curves in the logarithmic plot.

7.2 Simulation of the Low Energy Background

In Section 6.6, the effect of pileup events to the output of the signal processing algorithm (Section 4.5) was studied. Generally, pileup can distort both the amplitude and the time determination of an event pulse.
The energies of the final states of the exclusive reaction in the FAIR Phase-0 experiment are in the order of a few hundred MeV, each. The frequency of the exclusive reaction is expected to be in the order of mHz. In contrast, the total rate of low energy background events can reach hundreds of kHz depending on the scattering angle and the beam current (Figure 7.5). Thus, it is very likely that the low energy background events will distort the measurement of the final states of the Primakoff reaction. There is a typical optimisation problem: The higher the beam current, the higher the event rate of the desired reaction. On the other hand, the higher the beam current, the higher the rate of low energy background events which distort the measurement. Thus, a trade-off has to be made between a sufficient energy resolution and a sufficient event rate.
The relative energy resolution of the EMC prototype was determined for all of its 3×3

crystal matrices in Section 6.3. The approach for the analysis is to use background-free data from the X1 measurement, which provide the energy distribution over the crystals for every single electron event. The X1 data are consequently deteriorated by adding low energy background events.

The crucial element is the simulation of all detector traces for every single event, which was recorded at the X1 test beam. Such an X1 event consists of the measured energies for each of the participating crystals within the 3×3 matrix. The measured energies are subsequently converted into pulses on traces including realistic noise by the signal generator (Subsection 5.1.1). The traces are then superimposed with background events. Subsequently, the traces are analysed by the software implementation of the pulse parameter extraction (Subsection 5.1.4). Afterwards, the extracted hits are used to generate 3×3 sum spectra (Subsection 6.2.5). Lastly, the relative energy resolution can be extracted. The concept of the analysis is illustrated in Figure 7.6.

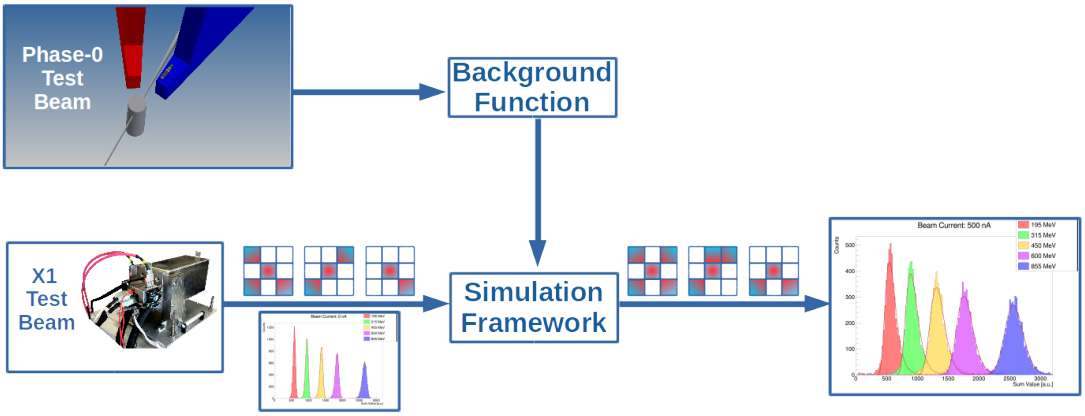

Figure 7.6: The illustration shows the concept for the determination of the 3×3 relative energy resolution at a given low energy background rate at small scattering angles for the FAIR Phase-0 experiment. The input is the background-free measurement from the X1 test beam. The information of events, which were measured with a 3×3 crystal matrix are fed to the simulation event by event. For every event, all detector traces (3×3 crystals × 2 APD × 2 amplifications = 36) are generated according to the measured energies (pulse heights) in the individual crystals. The traces are superimposed with low energy background event pulses according to the measurement from the FAIR Phase-0 test beam. Subsequently, the traces are analysed by the parameter extraction algorithm to generate 3×3 sum spectra.

The output of the analysis is the expected relative energy resolution for a 3×3 crystal matrix at small scattering angles as a function of the beam current.

7.2.1 Generation of Signal Traces

Since the electromagnetic shower is an erratic process, the energy distribution over the crystals differs from one event to the other. Consequently, a single event, which was measured with a 3×3 matrix at the X1 test beam, is characterised by both the pulse amplitude in the central crystal and the pulse amplitudes in the neighbouring crystals, which are in total nine different pulse amplitudes (see Figure 6.5). With the help of the single-crystal energy calibration (Subsection 6.2.4), these nine pulse amplitudes are translated into energies. As a result, the event is now specified by a list of nine energies.
The simulation methods, presented in Chapter 5, can generate realistic detector pulses on traces with realistic noise. There are two APDs, which are read out by two amplification stages per crystal. Consequently, for each crystal energy on the list, four detector signals are generated. As a result, 36 (3×3 crystals × 2 APD × 2 amplifications) detector signals need to be generated for each event.
The final element of the simulation is the introduction of the background hits according to the low energy background distribution (Figure 7.5), which was determined in the FAIR Phase-0 test beam. There are three steps needed to simulate the background hits:

1. The number of background hits is determined for the trace length of L_{Trace} by a Poisson random number generator. Furthermore, the generated number of background hits depends on the total rate. Since the total rate is proportional to the beam current (Figure 7.4), the total rate can be calculated as a function of arbitrary beam currents:

$$R(I_{\mathrm{Beam}}) = \frac{R_{100\mathrm{nA}}}{100\,\mathrm{nA}} \cdot I_{\mathrm{Beam}} \tag{7.1}$$

   where $R_{100\mathrm{nA}}$ is the total rate for the 100 nA-measurement (Figure 7.5). The 100 nA-measurement was chosen as a reference since, at this current, the impact from noise hits is negligible compared to the number of background hits.

2. The time of occurrence along the trace length L_{Trace} is determined for every single background hit with a uniform random number generator.

3. The energy amplitudes of every single background hit is determined by a second uniform random number generator, which generates a value between 0 and 1. The result is mapped to an energy amplitude by using the low energy background function (Figure 7.7).

Following the steps above, an individual background hit sequence is generated for every single crystal for every event. The background hit sequence is subsequently passed to the trace simulation. According to the sequence, pulses are generated and superimposed for all four signal traces (2 APD × 2 amplifications) of the crystal. By considering Figure 7.7, the probability for the occurrence of background events with energies above a specific limit can be determined. For instance, 95 % of the function

domain [0.05,1.00] results in energy amplitudes below 50 MeV. As a result, background hits with high energy amplitudes and thus a more extensive transversal shower profile are rare. Consequently, it is assumed that every crystal has its individual background hit sequence.
The background function is determined by the normalisation of the 100 nA-curve of Figure 7.5 to its maximum. After the normalisation, it has a value range between 0 and 1. Subsequently, the function is inverted. As a result, it has now a domain between 0 and 1 and the energy range of the low energetic background as value range. The function thus obtained is depicted in Figure 7.7.

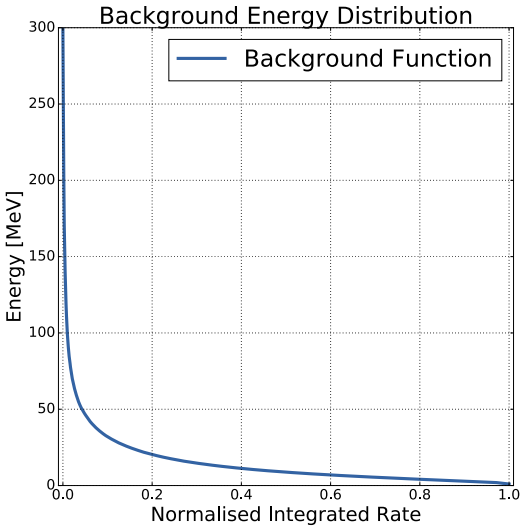

Figure 7.7: The plot shows the low-energy background function. It is determined by the normalisation of the 100 nA-curve of Figure 7.5 to its maximum. The result of the normalisation is subsequently inverted. The obtained function has its domain between 0 and 1. The value range of the function is the energy range of the low energetic background. The function is needed for the simulation of the energy amplitudes of the background hits. To this end, a random generator generates a value between 0 and 1, which is mapped to an energy amplitude by the background function.

In Figure 7.8, the impact of the background hits on traces for different beam currents is depicted. A 50 MeV-reference pulse is set on every trace at a defined position to see the effect of its superposition with background hits.

7.2.2 Impact on the Relative Energy Resolution

All 36 traces of every simulated 3×3 cluster event are analysed by the software implementation of the parameter extraction algorithm (Subsection 5.1.4). Consequently, the procedure to determine the relative energy resolution is identical to the procedure described in Chapter 6. Thus, sum spectra were generated as described in Subsection 6.2.5. The hit detection threshold was set to 1 MeV. In Figure 7.9 sum spectra for simulated 3×3 events for different energies and different beam currents are shown. "No Background" refers to a Phase-0 beam current of $I_{\mathrm{Beam}} = 0\,\mathrm{nA}$. As a result, these spectra only reflect the X1 measurement.
In Figure 7.10 the relative energy resolution plots for different beam currents are shown. Beside the simulations, also the measured relative energy resolution from the X1 beam test is shown. The data from this measurement were used as input for the simulation. As a reference, a simulation without any background was performed to compare measurement and simulation. The relative energy resolution curve from

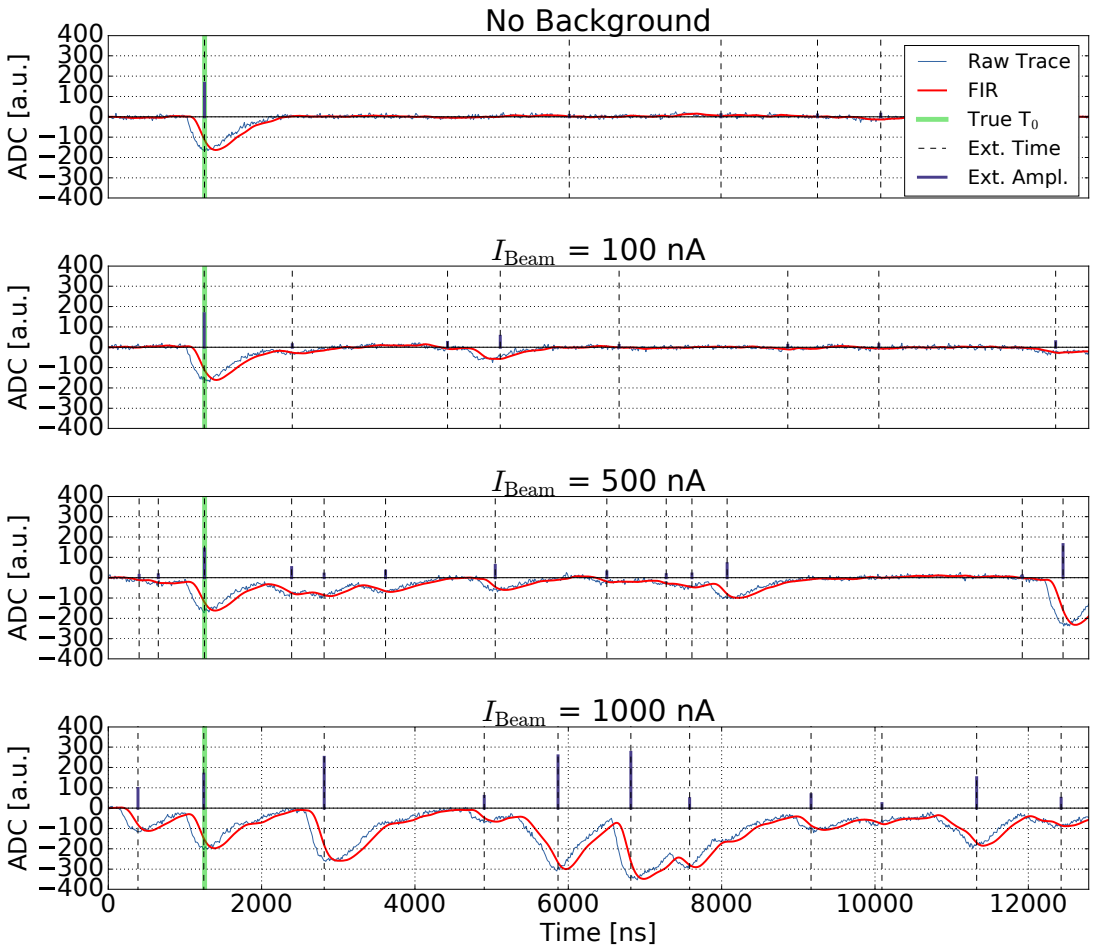

Figure 7.8: The plots show simulated traces in the low gain amplification for different beam currents. The upper plot shows a reference trace without background events. A 50 MeV reference event is placed at a defined position (green line) on every trace. For the simulation, the background hits are generated for every crystal. Thus, the same background sequence is applied on both amplification for both APDs. In order to simulate a full 3×3 cluster event, nine background sequences need to be generated.

the reference simulation lies slightly above the measured relative energy resolution curve. The reason for this is double counting of noise events because the input data of the X1 test also contains a certain amount of noise events. Thus, the result of the simulations gives an upper limit for the relative energy resolution for a 3×3 cluster at small scattering angles for different beam currents. Finally, the relative energy resolution at 1 GeV and 500 MeV is plotted against the beam current in Figure 7.11. An energy of 500 MeV was chosen, since the final state particles at FAIR Phase-0 have energies in this region. For instance, at $I_{\mathrm{Beam}} = 1000\,\mathrm{nA}$, a relative energy resolution of better than 10 % for deposited energies of 500 MeV can be achieved.

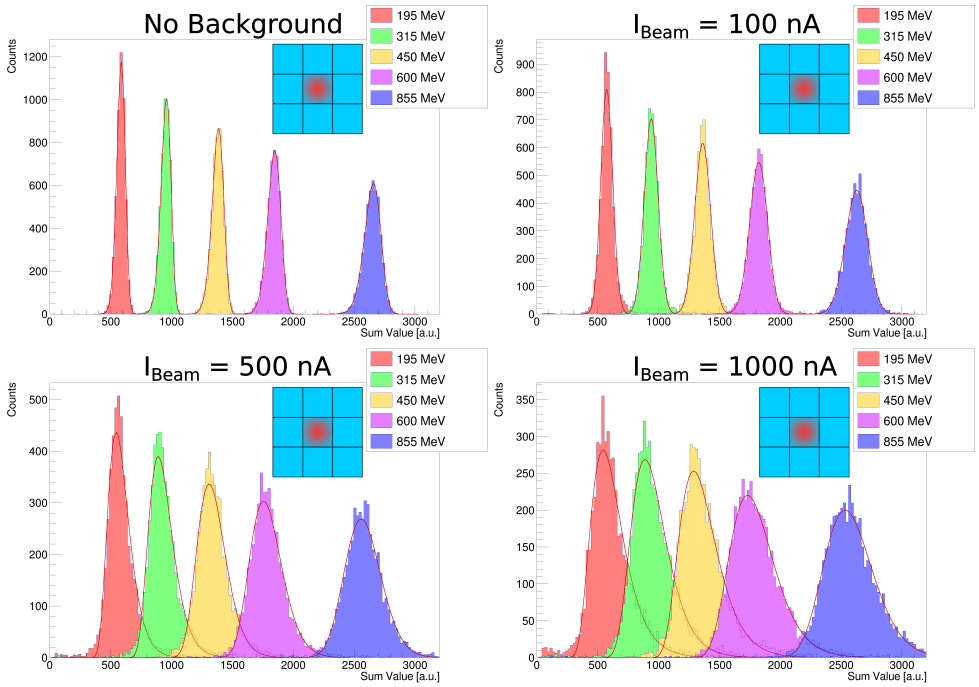

Figure 7.9: The plots show simulated 3×3 sum spectra for different beam currents. As a reference, simulated sum spectra without background are shown in the upper left plot. For every energy, 5000 cluster events were generated. For increasing beam currents, the distributions become broader. Due to superpositions between the signal pulse and background pulses, the extracted amplitude of the useful pulse is distorted. Similarly, the extracted timestamp of the useful pulse can be distorted, which can lead to cluster summation failures.

7.3 Implications for Luminosity and Measuring Time

The FAIR Phase-0 experiment in Mainz has a definite time constraint. In 2024[1], the installation of the calorimeter into the $\bar{\text{P}}$ANDA experiment is envisaged. Consequently, a high luminosity is demanded to measure the electromagnetic transition form factor of the pion in a reasonable time. The luminosity depends on the beam current I_{Beam} and the target properties:

$$L = \dot{N}_{\text{Beam}} \cdot n_{\text{Target}} \cdot d_{\text{Target}} \tag{7.2}$$

whereby $\dot{N}_{\text{Beam}}$ is the particle rate of the beam with $\dot{N}_{\text{Beam}} = \frac{I_{\text{Beam}}}{e}$ and with e being the elementary charge. The density of scattering centres is given by

$$n_{\text{Target}} = \frac{\rho_{Ta}}{m_{\text{Atom}}} \tag{7.3}$$

[1]Status at the time of writing this thesis.

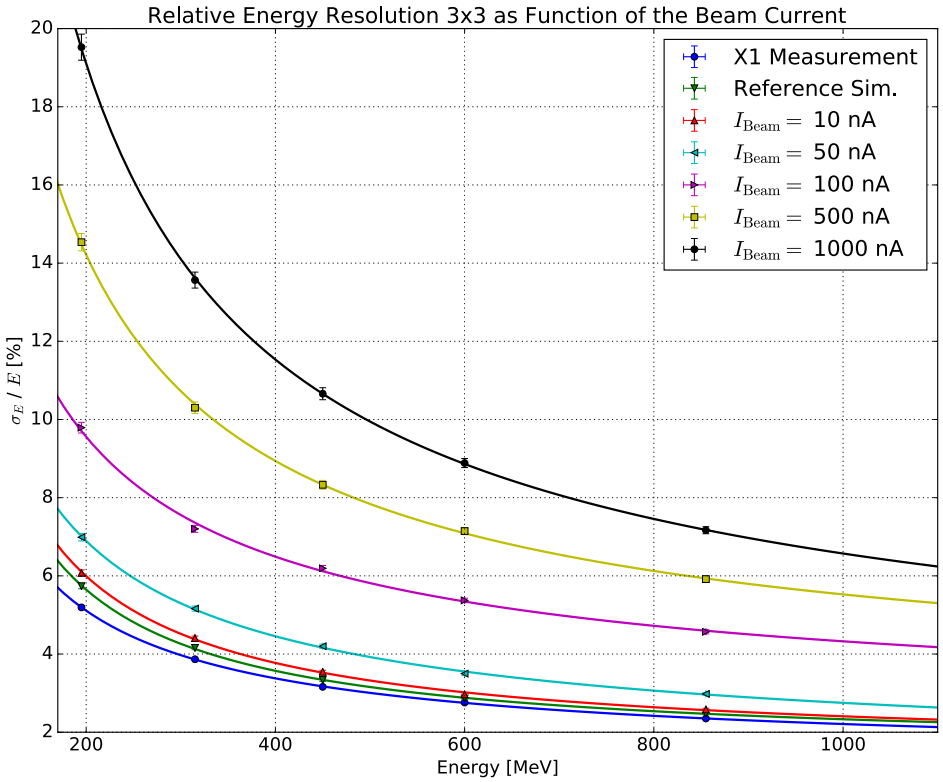

Figure 7.10: The plot shows the simulated 3×3 relative energy resolution for different beam currents. The curve from the reference simulation (green) lies slightly above the measured curve (dark blue). Thus, the results of the simulations can be seen as an upper limit for the 3×3 relative energy resolution for the FAIR Phase-0 experiment.

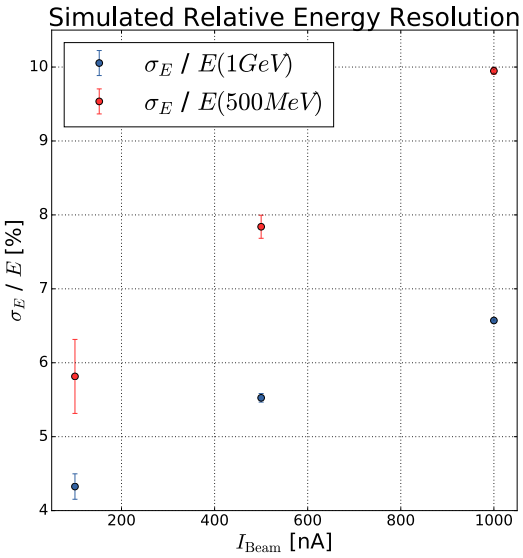

Figure 7.11: The plot shows simulated relative energy resolutions (3×3) for fixed deposited energies under small scattering angles ($\Theta_{\mathrm{proto}} = 8.7°$) as a function of the beam current. The relative energy resolution at 1 GeV without background events is about 2.2 % (Table 6.2). The relative resolution at deposited energies of 500 MeV was chosen, since the final states of the FAIR Phase-0 experiment (e^-, γ_1 and γ_2) have energies in this region (Section 2.5). The larger uncertainties at 100 nA can be explained by fluctuations at the 100 nA-simulation (see Figure 7.10).

here is $\rho_{Ta} = 16\,650\,\mathrm{kg/m^3}$ [N$^+$18] the density of the Tantalum target and $m_{\mathrm{Atom}} = 180.947\,88(2)\,\mathrm{u}$ [N$^+$18] its atomic mass. Finally, the luminosity is proportional to the target thickness, which was $d_{\mathrm{Target}} = 1.6\,\mu\mathrm{m}$ at the Phase-0 test beam.
In order to estimate the measuring time for the experiment, the event rate of the exclusive reaction R needs to be determined. The event rate is the product of the luminosity and the effective cross section σ_{eff} of the reaction:

$$R = L \cdot \sigma_{\mathrm{eff}} \tag{7.4}$$

The calculation of the effective cross section ([CGM$^+$20]) takes a preliminary acceptance of the Phase-0 EMC (Section 2.5) into account. The effective cross section ranges from 2.951 nb to 0.127 nb for the available Q^2-region, which is between $0.01\,\mathrm{GeV}^2$ and $0.05\,\mathrm{GeV}^2$ (Table 2.2).
The minimum measuring time T for the pion electromagnetic transition form factor at a particular momentum transfer is:

$$T = \frac{N}{R} \tag{7.5}$$

whereby N is the number of the measured events. The number of measured events, in turn, determines the relative statistical uncertainty with $\sqrt{N}/N$. In Figure 7.12, the minimum measuring time for the pion electromagnetic transition form factor for the different momentum transfers is depicted as a function of the beam current and the relative statistical uncertainty.
The measurements at different Q^2-values will be performed in parallel. Thus, the statistics for the measurements at lower Q^2-values would improve until the measurement of the highest Q^2-value has achieved a certain relative uncertainty mark.
As discussed in Section 2.5, the EMC has to determine the energy and the momentum direction of the final state particles. The precision on the energy and the momentum direction determination is strongly dependent on the relative energy resolution (Table 7.1). Consequently, the relative energy resolution affects the systematic uncertainty of the measurement. As a result, a trade-off between measuring time, statistical uncertainty and systematical uncertainty has to be done. However, further detailed simulations of the scattering processes and the detector response are needed to find the optimum. Such simulations are currently ongoing.

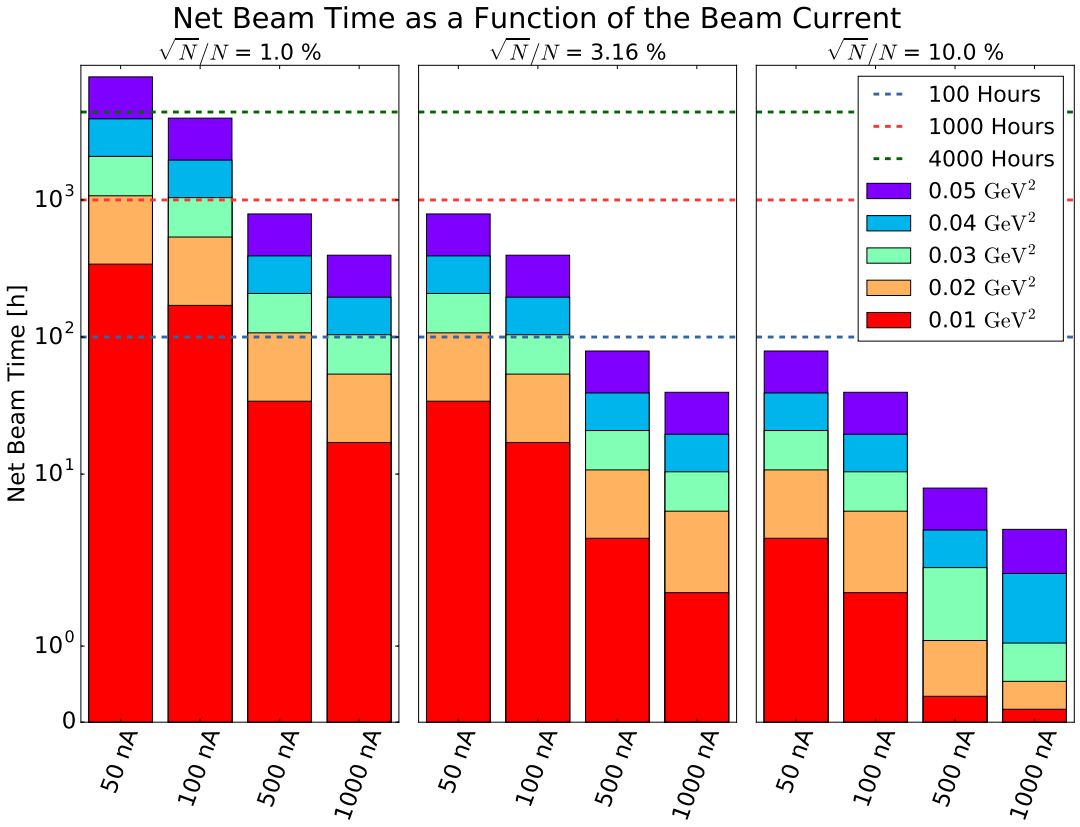

Figure 7.12: The plot shows the estimated net beam time, needed for the measurement of the pion electromagnetic form factor at different Q^2 as a function of the beam current and the relative statistical uncertainty. The measurements at various Q^2 values are performed in parallel. Thus, the statistics for the measurements at lower momentum transfers would improve until the measurement at the highest Q^2 has achieved a certain relative uncertainty mark.

I_{Beam} [nA]	L [μb^{-1}/s]	$\frac{\sigma_E}{E}$(500MeV) [%]	$\frac{\sigma_E}{E}$(1GeV) [%]
1000	55.34	9.94(5)	6.57(2)
500	27.67	7.84(16)	5.53(6)
100	5.53	5.86(50)	4.33(17)
50	2.77	3.92(10)	2.75(4)

Table 7.1: The table shows the results of the simulation of the relative energy resolution at small scattering angles for the FAIR Phase-0 experiment as a function of the beam current. The precision on the energy measurement and the momentum direction determination depends on the relative energy resolution. Consequently, the relative energy resolution affects the systematical uncertainty of the measurement.

8 Conclusion and Outlook

The development of the backward EMC of the $\bar{\text{P}}$ANDA detector and its preparation for a FAIR Phase-0 experiment was subject of this work. Thus, a prototype calorimeter was built, which provides all technologies and materials as they will be used in the final EMC. The essential development was the digital filtering and parameter extraction for the digitised EMC signals. For this purpose, a software-based test and development environment was created, which is characterised by the realistic simulation of both the digitised signals of the EMC preamplifier and the electronic noise background for the full readout chain. The simulation framework was used to optimise the digital processing methods and to obtain the parameter extraction performance as a function of detector settings, such as the avalanche photodiode gain and the energy detection threshold. Meanwhile, the software has also found its way into PandaRoot, which is the simulation framework for the $\bar{\text{P}}$ANDA experiment.
The digital signal processing methods were also implemented into the Field-Programmable Gate Arrays of the EMC digitisation board. Hence, a new firmware was developed, which provides for all EMC channels a self-triggering readout, signal smoothing by a high order filter with a finite impulse response (FIR), noise hit suppression and pileup handling. Furthermore, the firmware can manage event rates of up to 558 kHz per channel. The implementation of the high order FIR filter was only possible by utilising the method of distributed arithmetic (DA), which substitutes costly FPGA digital processing units (DSP slices) with look-up-tables, summations and bitshifts. Since the hardware description of the DA implementation is complex, software was developed, which generates the description for arbitrary filter parameters.
Several beam tests at the Mainz Microtron facility (MAMI) were performed, to test both the prototype calorimeter and the digital signal processing methods. Measurements at the MAMI detector test facility using an electron beam with energies between 195 MeV and 855 MeV produced the following results for a 3×3 crystal matrix. For comparison, the requirements of the $\bar{\text{P}}$ANDA EMC technical design report (TDR) are also given in brackets. The single-crystal energy threshold of the calorimeter is better than 2.5 MeV (TDR: 3 MeV), which allows for a measured relative energy resolution at 1 GeV of 2.207(6) % (TDR: 2.5 %). The constant term value is 1.08(14) % (TDR: 1 %), the stochastic term value is $1.83(45)\,\%/\sqrt{\text{E[GeV]}}$ (TDR: $2\,\%/\sqrt{\text{E[GeV]}}$) and the electronic noise contribution is 2.02(15) MeV (TDR: 3 MeV). Furthermore, the largest deviation in the linearity of the calorimeter is 1.26(24) ‰ over the entire measured energy range. By utilising a new pileup restoration approach, the pileup probability at an event rate of 100 kHz was reduced to 4.53(12) % compared to 13.9 % without correction. However, the TDR requires a pileup probability of 1 % at 100 kHz event rate for later experiment phases. A further convergence to this value is possible if the approach of the presented method is further generalised. Finally, the dead time of the detector was determined to 464(13) ns.

Almost all technologies presented in this work were being joined within a feasibility study for the measurement of the pion transition form factor (TFF) using a version of the $\bar{\text{P}}$ANDA backward EMC at MAMI. Thus, the EMC prototype was utilised for an exploratory measurement at the MAMI A1 spectrometer hall with an electron beam on a Tantalum $^{181}_{73}$Ta target. Since the later measurement of the pion TFF has to be performed for small scattering angles, the prototype was also placed at small angles. Consequently, the impact of low-energetic electron and photon background on the envisaged measurement was studied.
The test measurement gave access to the background energy distribution, which was implemented into the digital signal processing simulation framework. Subsequently, the background-free data from the measurement at the MAMI detector test facility was used as input for a simulation of the expected relative energy resolution for a 3×3 crystal matrix at small angles ($6.5° \leq \Theta \leq 7.6°$) as a function of the luminosity.
The determined relative energy resolution for the relevant particle energy of 500 MeV ranges from 3.92(10) % at a luminosity of $2.77\,\mu\text{b}^{-1}/\text{s}$ to 9.94(5) % at a luminosity of $55.34\,\mu\text{b}^{-1}/\text{s}$. In conclusion, the study shows the feasibility of the pion TFF measurement in terms of the detector technology used. Accordingly, it can be stated that the $\bar{\text{P}}$ANDA backward EMC can operate stably and reliably in an electromagnetic environment. However, further studies are needed. Currently, simulations with complete detector geometry are being conducted. Furthermore, the impact of the energy resolution on the particle angle determination has to be analysed to estimate the systematic uncertainty of the measurement.
The construction of the complete EMC for the pion TFF measurement is currently in progress. Many of the essential detector parts have already been produced. Moreover, submodules of the detector will be subjected to an extensive testing cycle after their assembly. The necessary hardware and software for the testing cycle are currently being prepared. Furthermore, the complete digitisation hardware is already available in Mainz. However, the FPGA firmware has to be modified in terms of scalability. Furthermore, the data from up to 2800 (700 crystals × 2 APDs × 2 amplifications) digitisation channels need to be concentrated. First explorations for such a data concentrator system are ongoing. Furthermore, development is also required in the areas of the electron-photon separation, front-end electronics and slow control.

Appendices

Appendix A

Hardware

A.1 Design of the FAIR Phase-0 Calorimeter

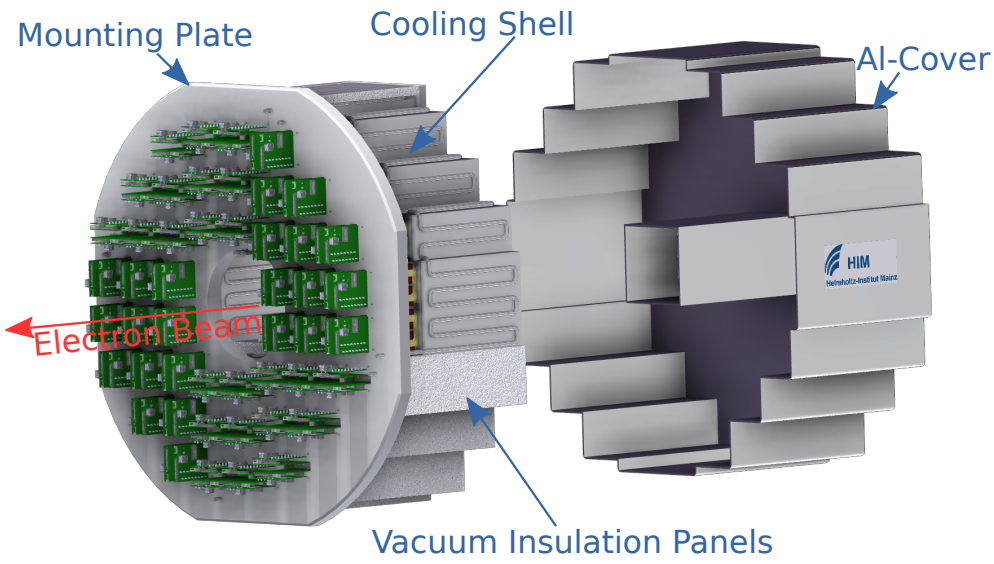

Figure A.1: The CAD drawing shows the backside of the FAIR Phase-0 calorimeter. The outer part of the electronics will be housed within a shielding box. The beam pipe goes through the centre of the calorimeter.

A.2 Illustrative Example of FIR Filtering

A FIR filter of order $M = 5$ with $M + 1 = 6$ coefficients and a settling time of $n_{\text{set}} = 5$ is considered.

$$x[n] = [2,2,1,1,2,3] \quad h[n] = [-0.2,1.5,3.2,3.2,1.5,-0.2] \tag{A.1}$$

The chosen coefficients describe a low pass filter with symmetric impulse response ($h[0 + l] = h[M - l], l \in [0,1,2]$). In Table A.1 the different steps of building the convolution sum from the samples $x[n]$ and the impulse response $h[n]$ are listed. Furthermore, in Figure A.2, the procedure is visualised for the first two calculations.

n		0	1	2	3	4	5	6	7	8	9	10
$h[0] =$	-0.2	-0.4	3.0	6.4	6.4	3.0	-0.4	0.0	0.0	0.0	0.0	0.0
$h[1] =$	1.5	0.0	-0.4	3.0	6.4	6.4	3.0	-0.4	0.0	0.0	0.0	0.0
$h[2] =$	3.2	0.0	0.0	-0.2	1.5	3.2	3.2	1.5	-0.2	0.0	0.0	0.0
$h[3] =$	3.2	0.0	0.0	0.0	-0.2	1.5	3.2	3.2	1.5	-0.2	0.0	0.0
$h[4] =$	1.5	0.0	0.0	0.0	0.0	-0.4	3.0	6.4	6.4	3.0	-0.4	0.0
$h[5] =$	-0.2	0.0	0.0	0.0	0.0	0.0	-0.6	4.5	9.6	9.6	4.5	-0.6
$y[n]$		-0.4	2.6	9.2	14.1	13.7	11.4	15.2	17.3	12.4	4.1	-0.6

Table A.1: The convolution sum of the impulse response $h[n]$ and the input signal $x[n]$ is shown. The row values are calculated by the multiplication of the corresponding impulse response value with every input sample. The next lower row is shifted by one cycle to the right. The filter value $y[n]$ is the sum over column n. The first two output values $y[0]$ and $y[1]$ are underlined in green. They are also illustrated in Figure A.2.

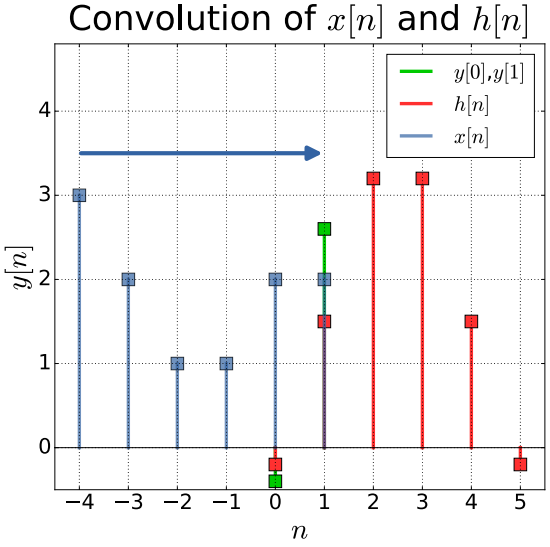

Figure A.2: The plot shows the convolution of the input signal $x[n]$ with the impulse response $h[n]$. The signal is *slid* over the impulse response. The certain filter output at time n is calculated as shown in Table A.1. At $n = 5$, the first complete filter value after the settling time n_{set} is available (Table A.1, gray column). For the calculation of the filter output from ADC samples, the settling time does not play a role. Even high order filters are settled after a view hundreds of nanoseconds.

A.3 Resource Utilisation of the PANDA Digitisation Board

The following diagram and the following table show the resource utilisation of the firmware of the FPGAs for the PANDA digitisation board (SADC). The firmware consumes about 50 % of the available hardware, which let plenty of space left for not yet implemented features such as baseline monitor and readout synchronisation between different SADCs.

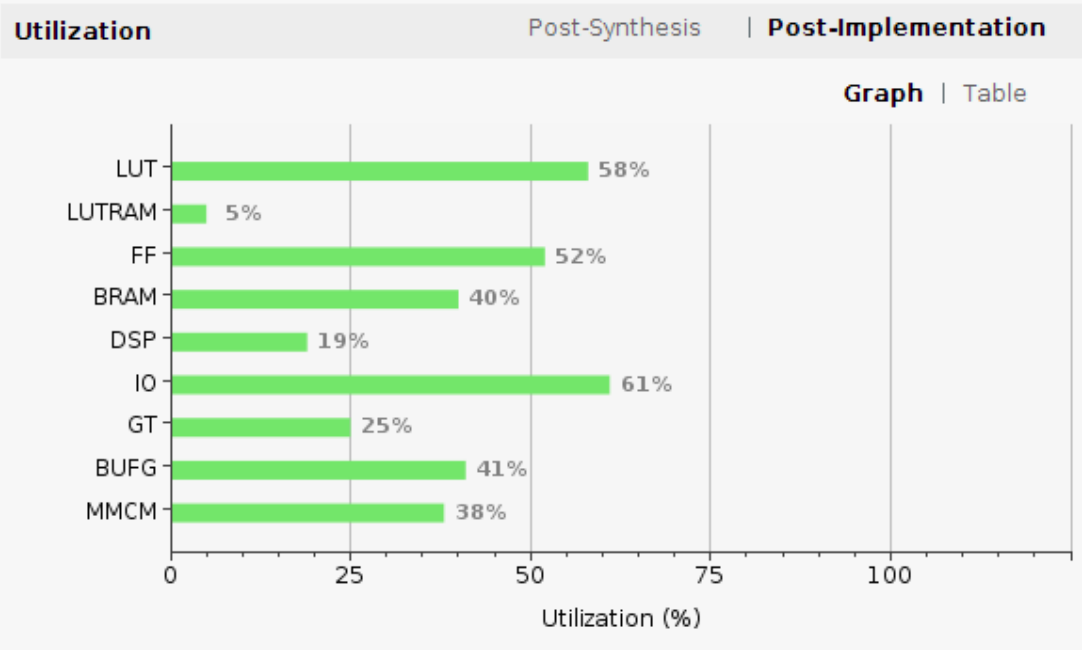

Figure A.3: FPGA resources consumption of the presented firmware.

Utilization Post-Synthesis | **Post-Implementation**

Graph | **Table**

Resource	Utilization	Available	Utilization %
LUT	59032	101400	58.22
LUTRAM	1767	35000	5.05
FF	105895	202800	52.22
BRAM	131	325	40.31
DSP	112	600	18.67
IO	175	285	61.40
GT	1	4	25.00
BUFG	13	32	40.63
MMCM	3	8	37.50

Figure A.4: FPGA resources consumption of the presented firmware.

Appendix B

Simulation of Signal Processing

The discussion of the simulation of signal processing methods in the main text was done for a typical APD gain of 200. However, depending on the needs in the later experiment, also other gains can be considered. Thus, the simulations were also made for the APD gains 100, 150, 250 and 300.

B.1 Noise Hit Rate and Efficiency

The following plots show the simulated noise hit rate and the simulated detection efficiency as a function of the hit detection threshold for different APD gains.

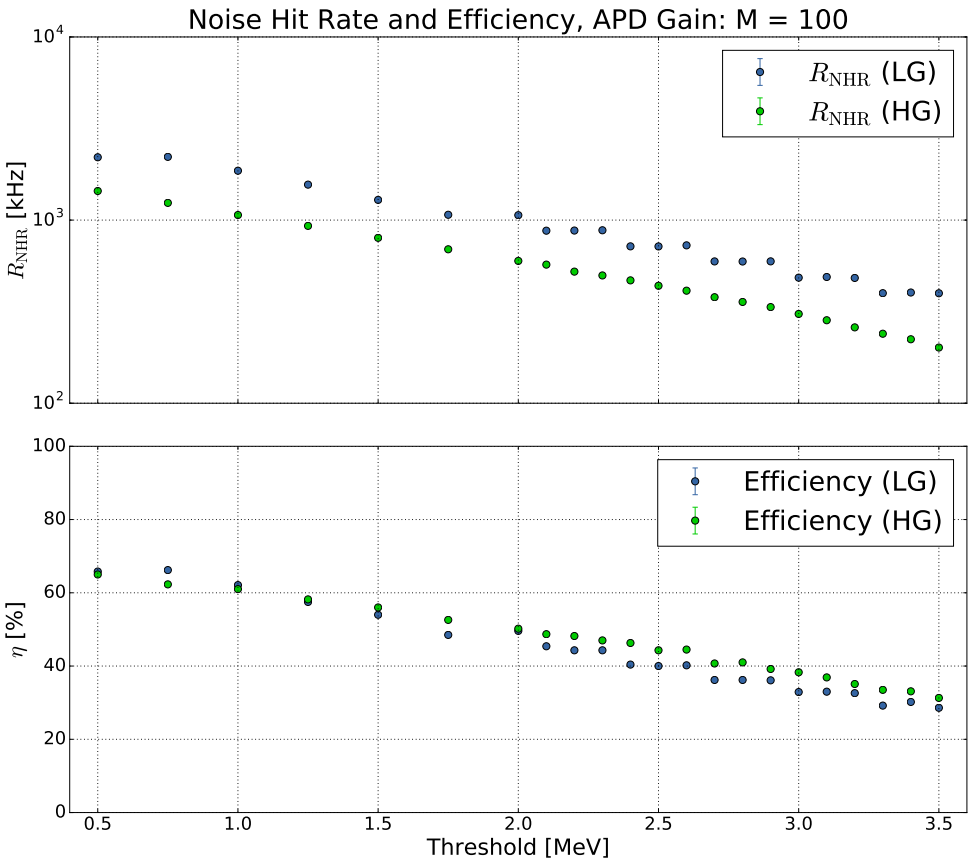

Figure B.1: Noise hit rate and efficiency for APD gain 100.

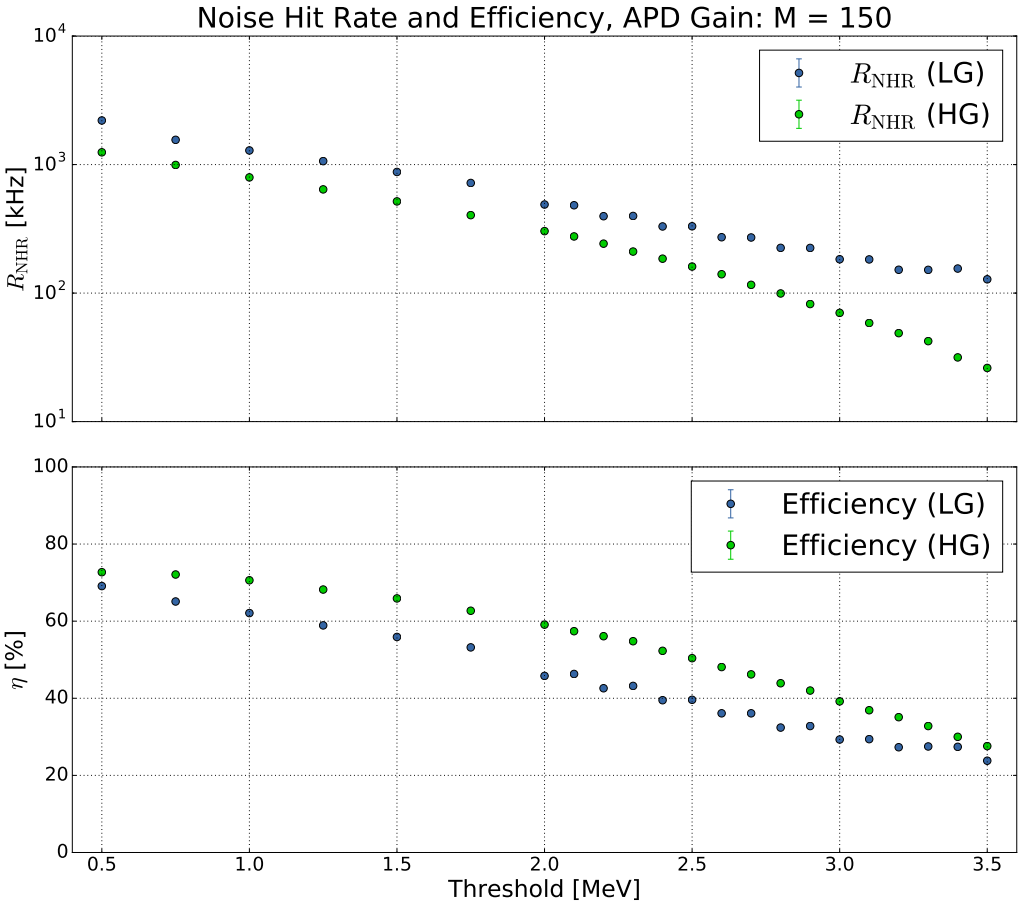

Figure B.2: Noise hit rate and efficiency for APD gain 150.

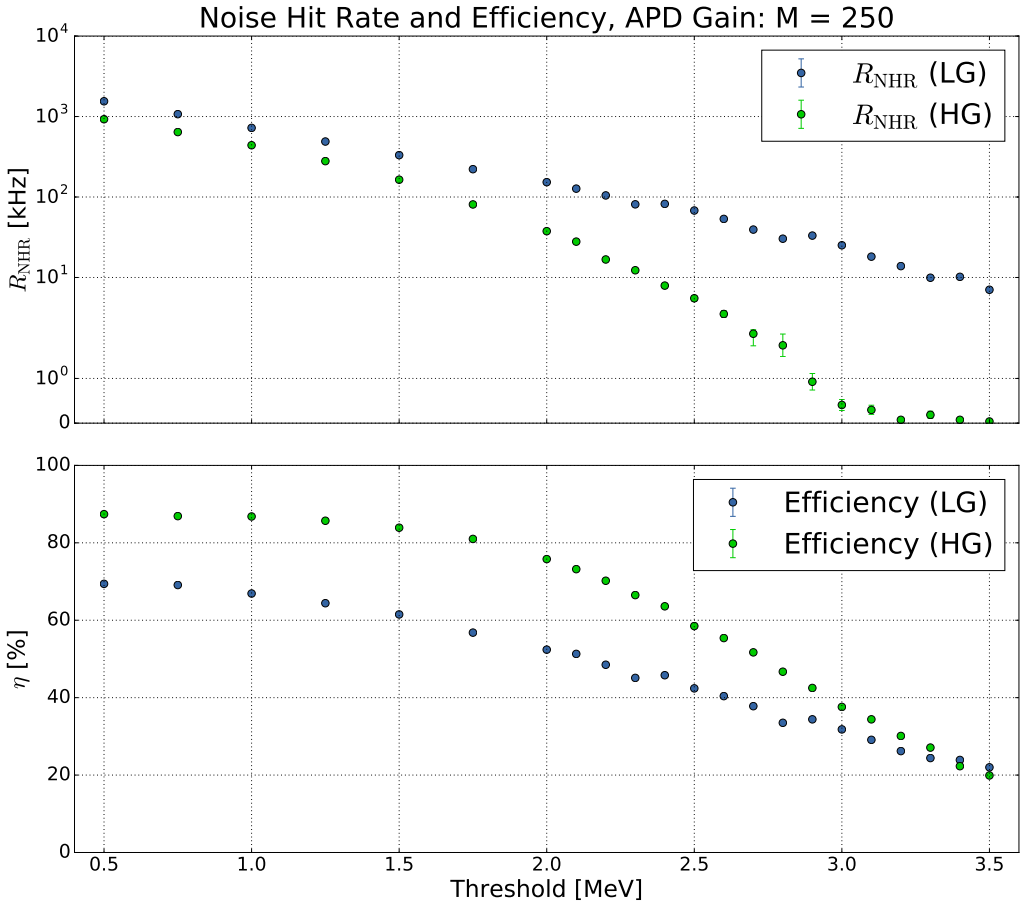

Figure B.3: Noise hit rate and efficiency for APD gain 250.

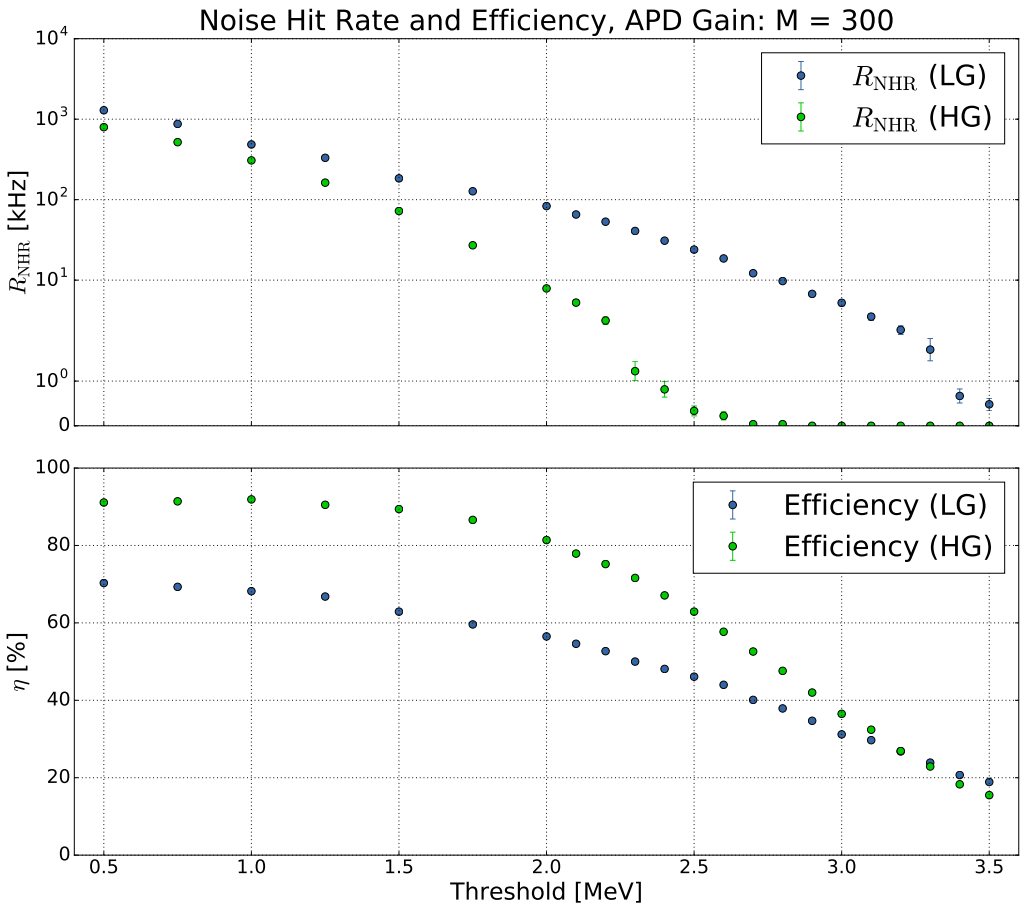

Figure B.4: Noise hit rate and efficiency for APD gain 300.

B.2 Time Resolution

The following plots show the simulated time resolution as a function of the deposited energy for different APD gains.

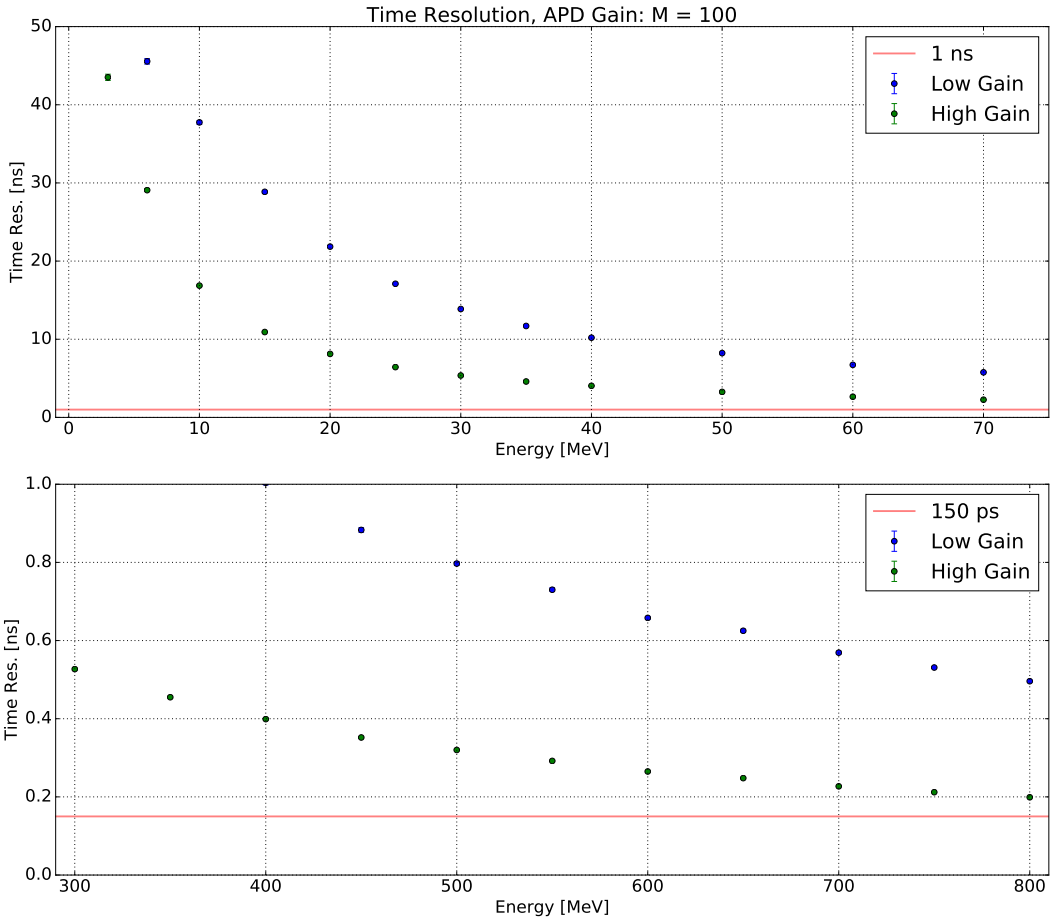

Figure B.5: Time resolution for APD gain 100.

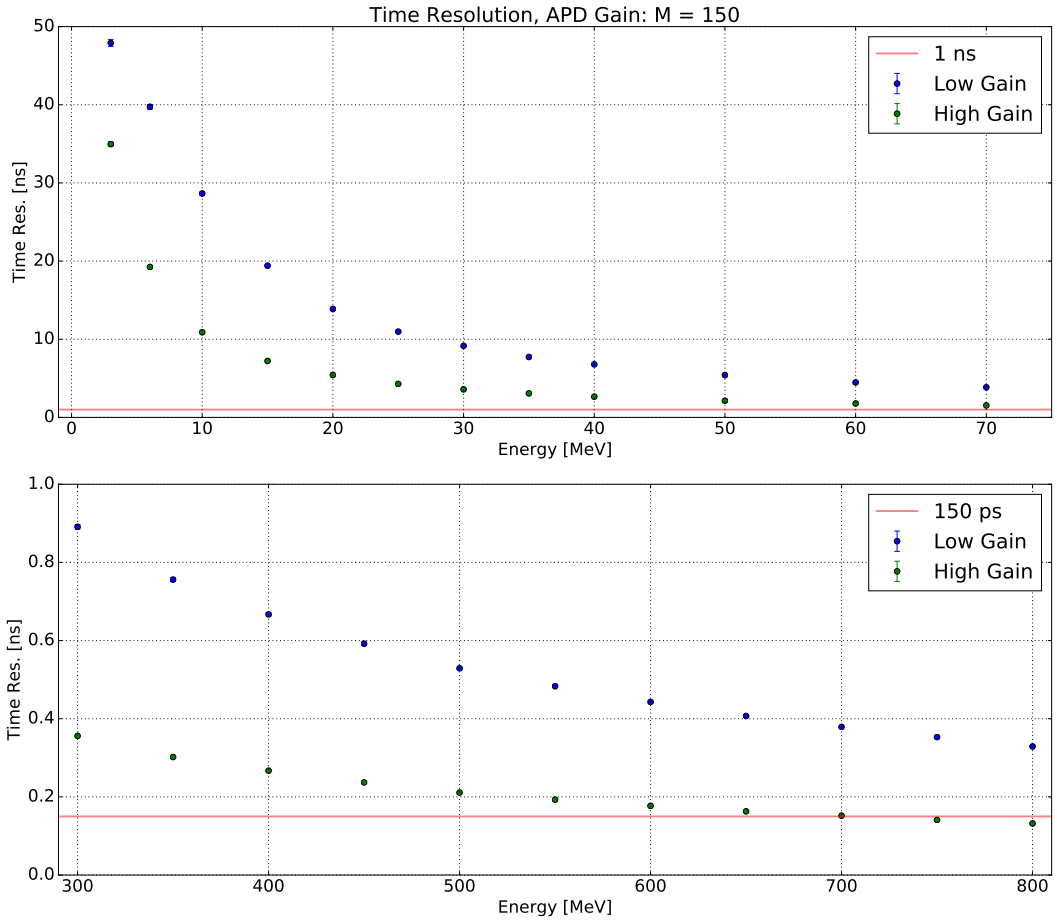

Figure B.6: Time resolution for APD gain 150.

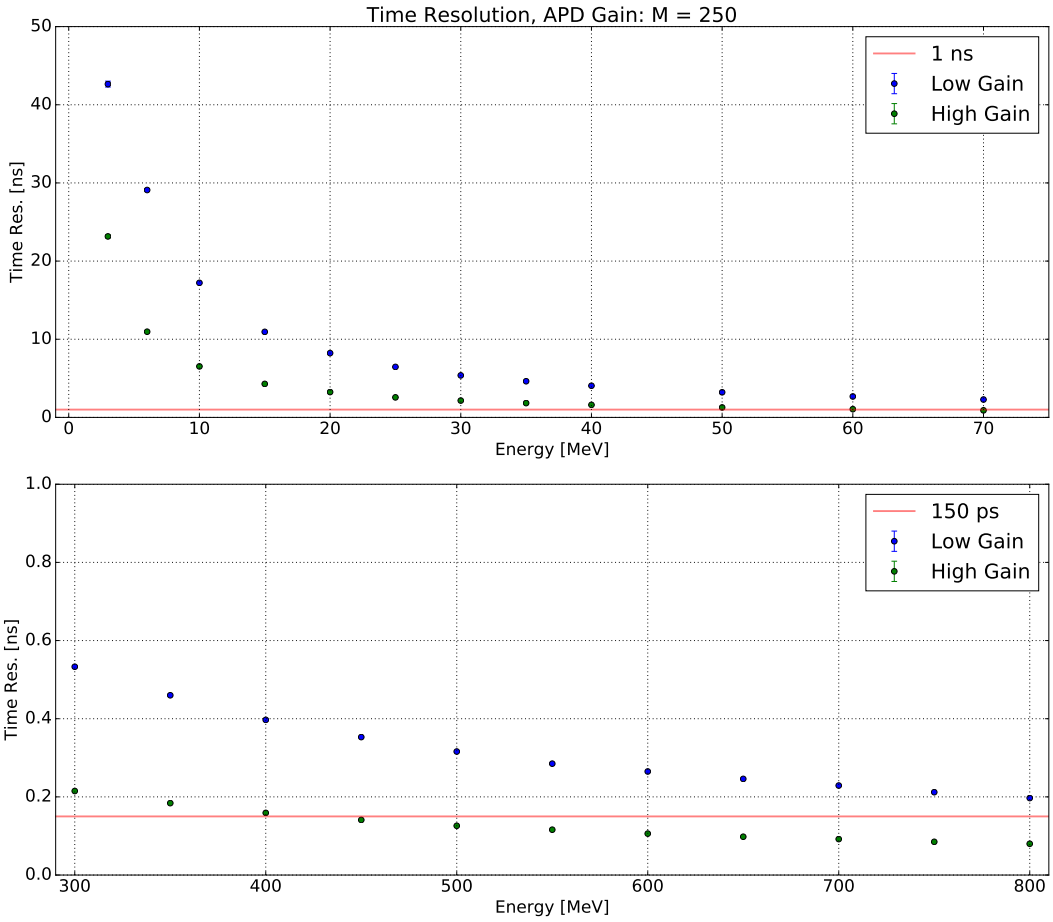

Figure B.7: Time resolution for APD gain 250.

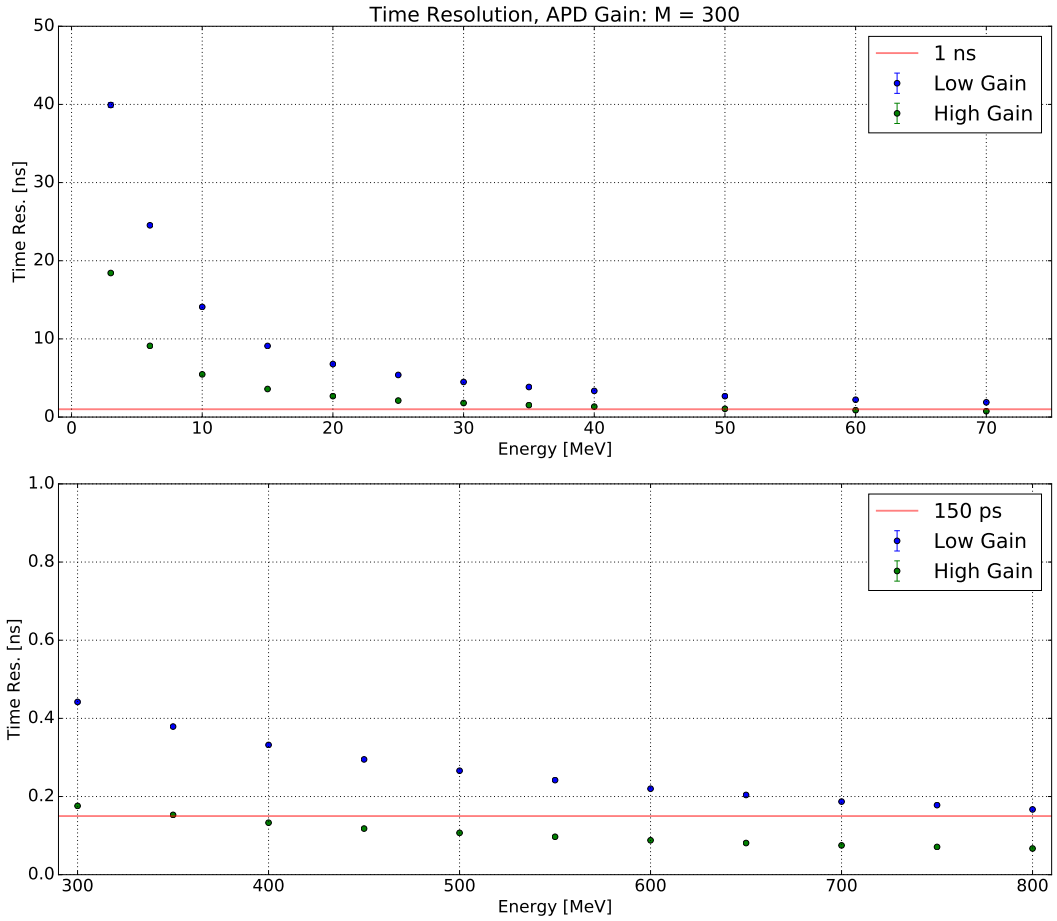

Figure B.8: Time resolution for APD gain 300.

B.3 Energy-Pulse Height Dependency

In the following, the simulated energy-pulse height dependency for different APD gains is shown. Furthermore, Figure B.9 demonstrates the fit procedure for signals close to the threshold.

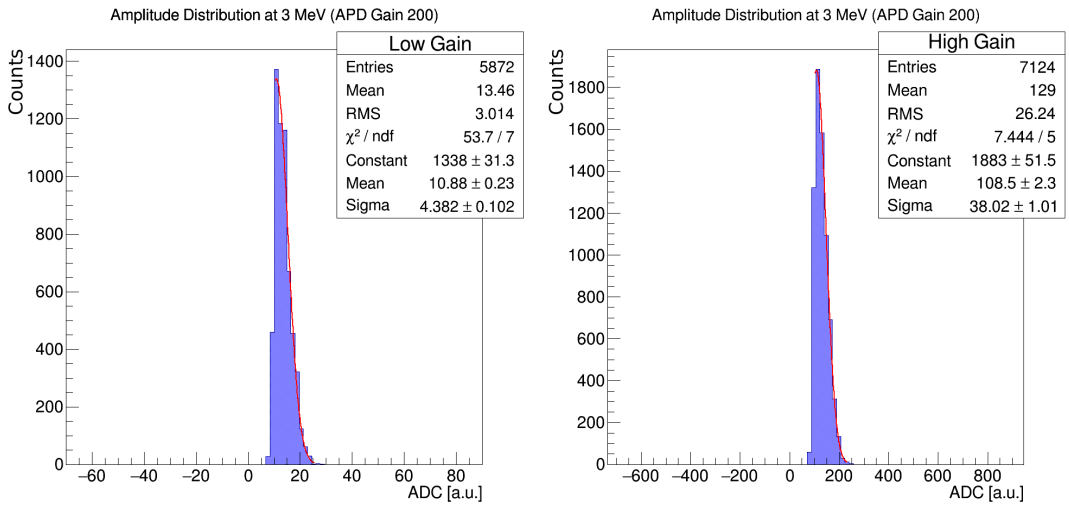

Figure B.9: The plot shows the distribution of the extracted amplitudes for deposited energy of 3 MeV at APD gain 200. Since the signal is close to the threshold, the distribution is cut off on its left side. Thus, the mean and the RMS of the distribution is falsified. A Gaussian fit, which excludes the cut side of the distribution gives access to the pure mean and sigma.

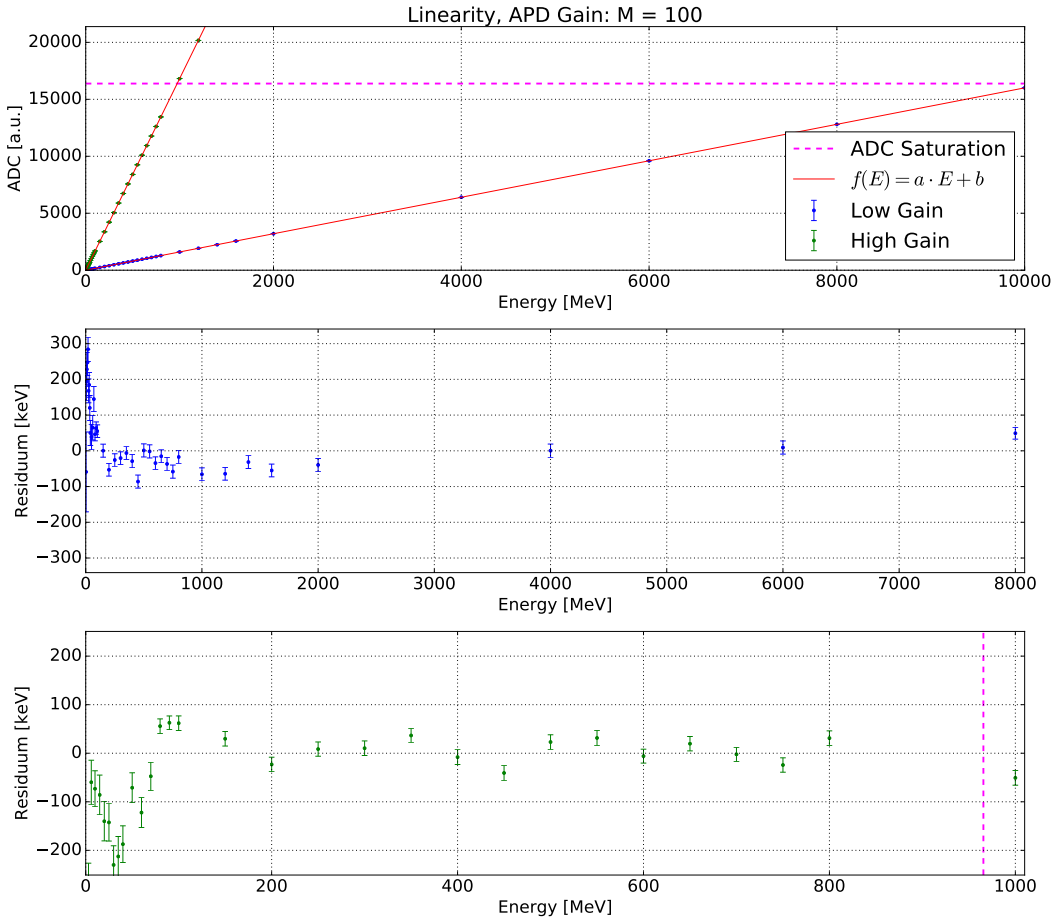

Figure B.10: Linearity for APD gain 100.

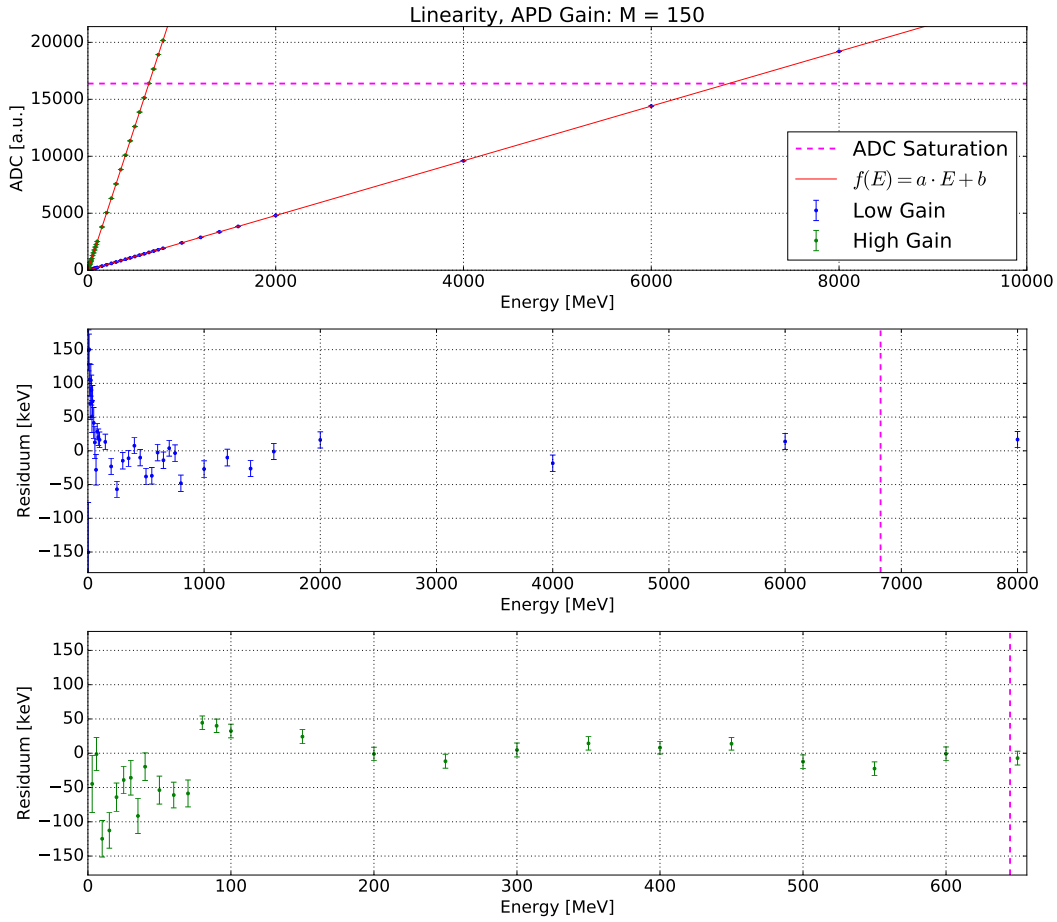

Figure B.11: Linearity for APD gain 150.

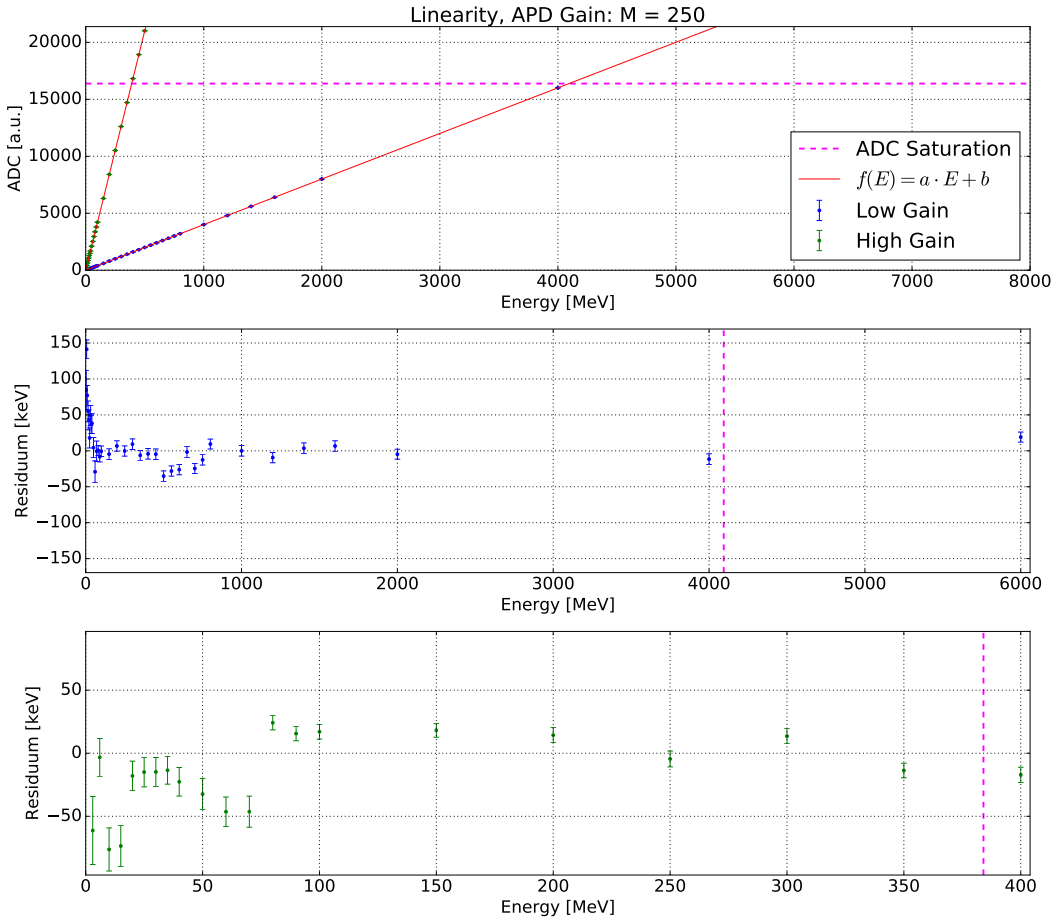

Figure B.12: Linearity for APD gain 250.

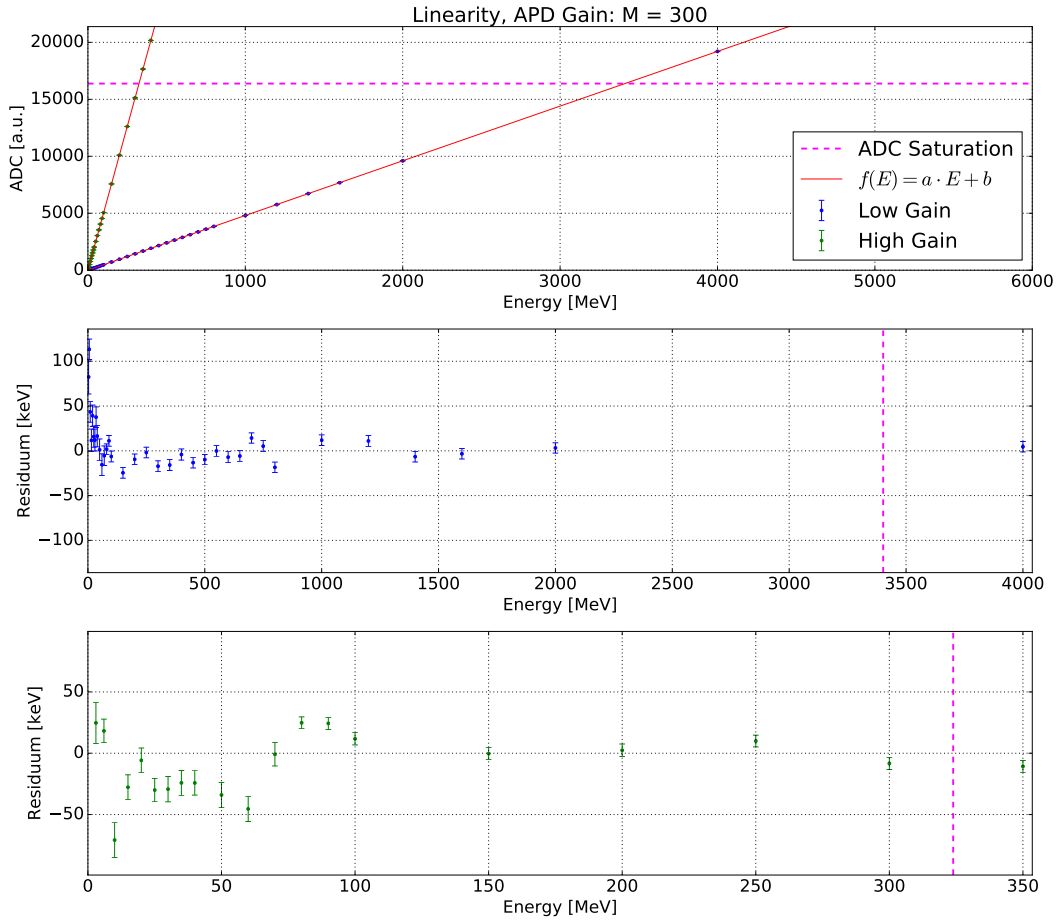

Figure B.13: Linearity for APD gain 300.

Appendix C

Measurements with the Prototype

In the following, further results of the measurements with the EMC prototype are shown. The discussion in the main text was done for an example 3×3 crystal matrix. However, the EMC prototype has four 3×3 crystal matrices. Thus, the results from the remaining three matrices are shown here.

C.1 Single-Crystal Calibration

The analysis of beam data demands a variety of steps. One of these steps is the single-crystal energy calibration, which was demonstrated for an example crystal in the main text for the low gain amplification of the preamplifier. In Figure C.1, the calibration curves for all crystals of the prototype in the low gain amplification are shown. Furthermore, Figure C.2 shows single-crystal spectra recorded in the high gain amplification for an example crystal. Also, the single-crystal energy calibration has to be performed in the high gain to combine data from the two amplifications. The single-crystal energy calibration for all crystals in the high gain is depicted in Figure C.3.

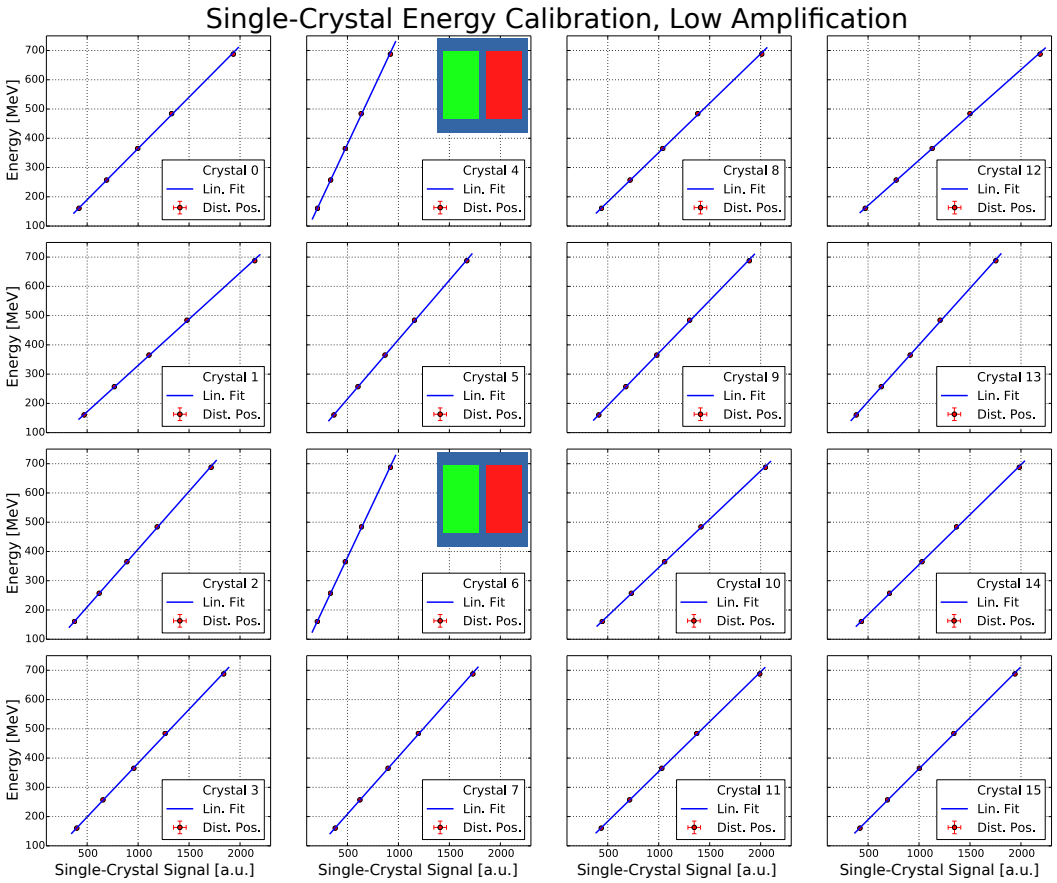

Figure C.1: The plot shows the single-crystal energy calibration in the low amplification for the APFEL preamplifier. The pictograms at crystal 4 and 6 indicate the absence of one APD channel, respectively.

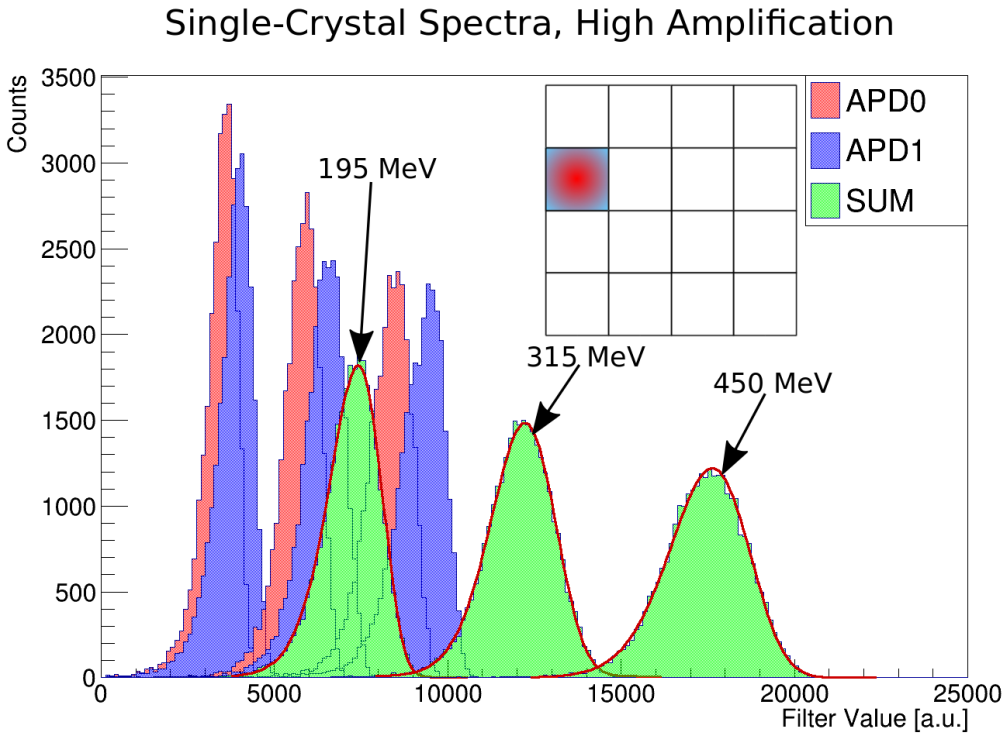

Figure C.2: The plot shows examples of single-crystal spectra in the high amplification of the APFEL preamplifier. In contrast to the spectra recorded in the low amplification, only the lowest three energies can be analysed since higher energies lead to a saturation of the high gain amplifier.

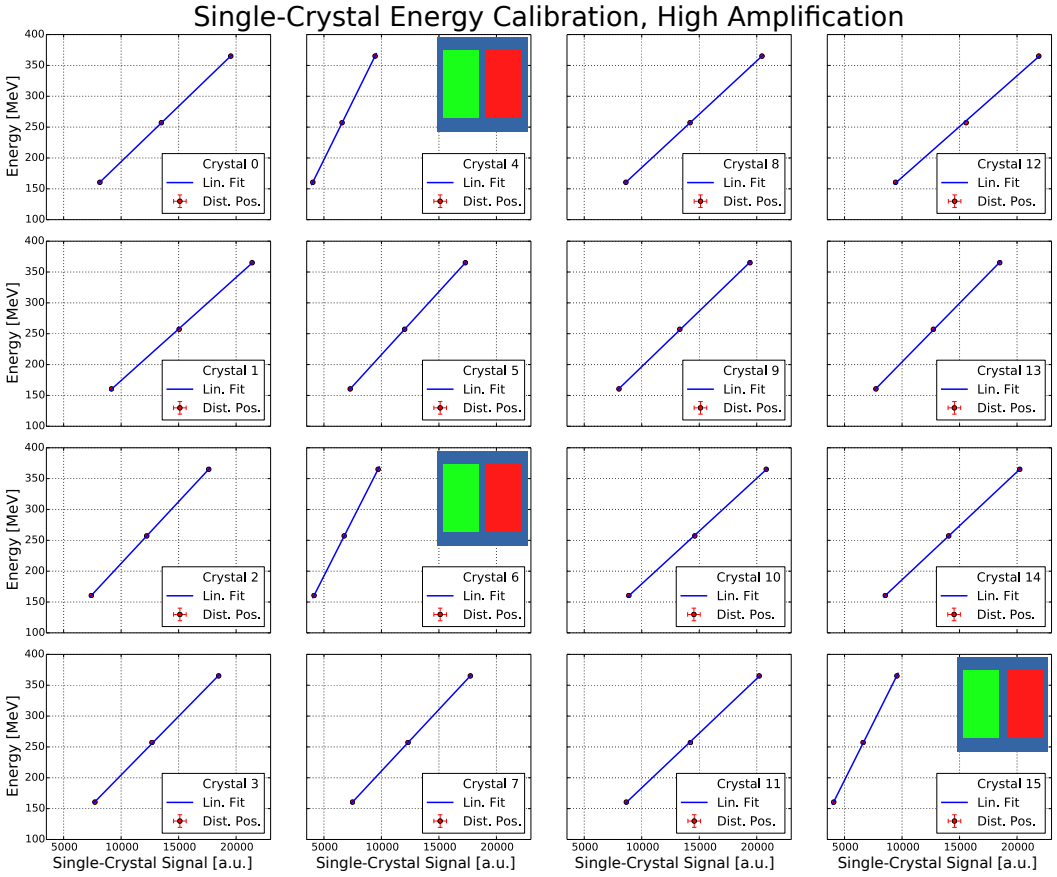

Figure C.3: The plot shows the single-crystal energy calibration in the high amplification of the APFEL preamplifier. The pictograms for crystal 4,6 and 15 indicate the absence of one APD channel, respectively. By comparing the energy calibrations of high and low amplification, the ratio between the amplification modes can be determined.

C.2 Relative Energy Resolution

The relative energy resolution of the EMC prototype was discussed for one example 3×3 matrix in the main text. In the following, the relative energy resolutions recorded with the other three 3×3 crystals matrices are given.

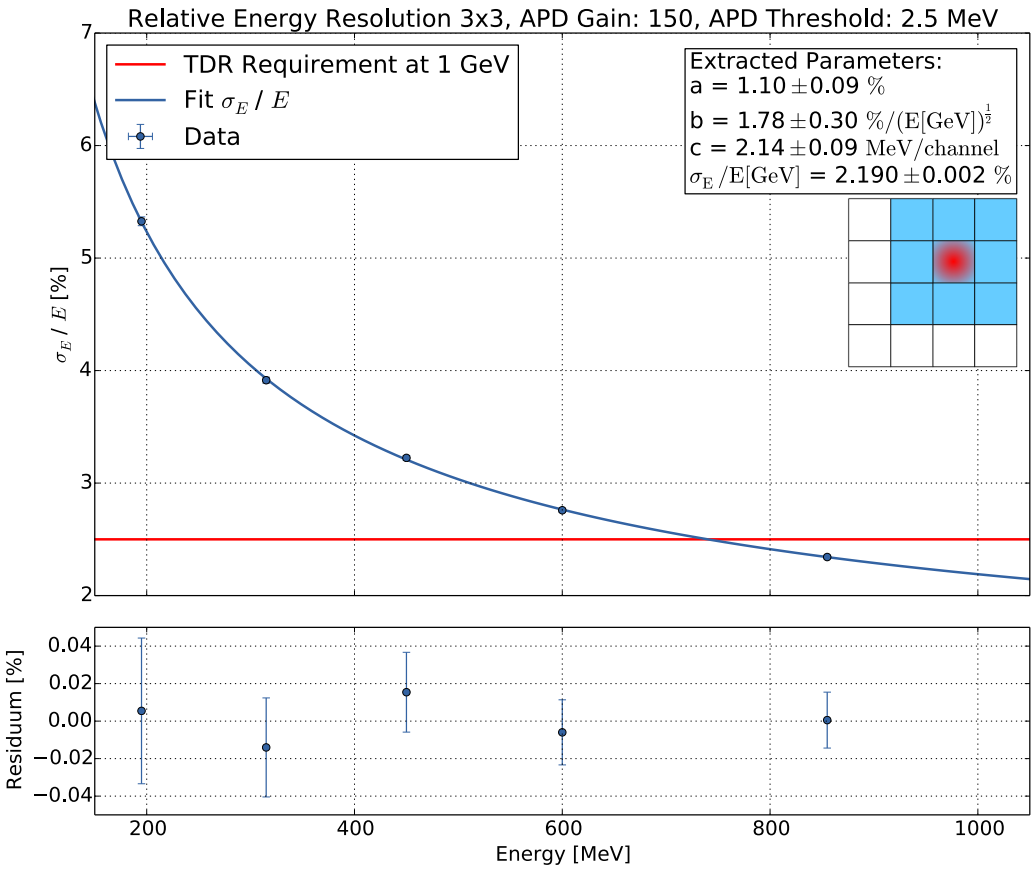

Figure C.4: APD gain: 150, APD threshold: 2.5 MeV

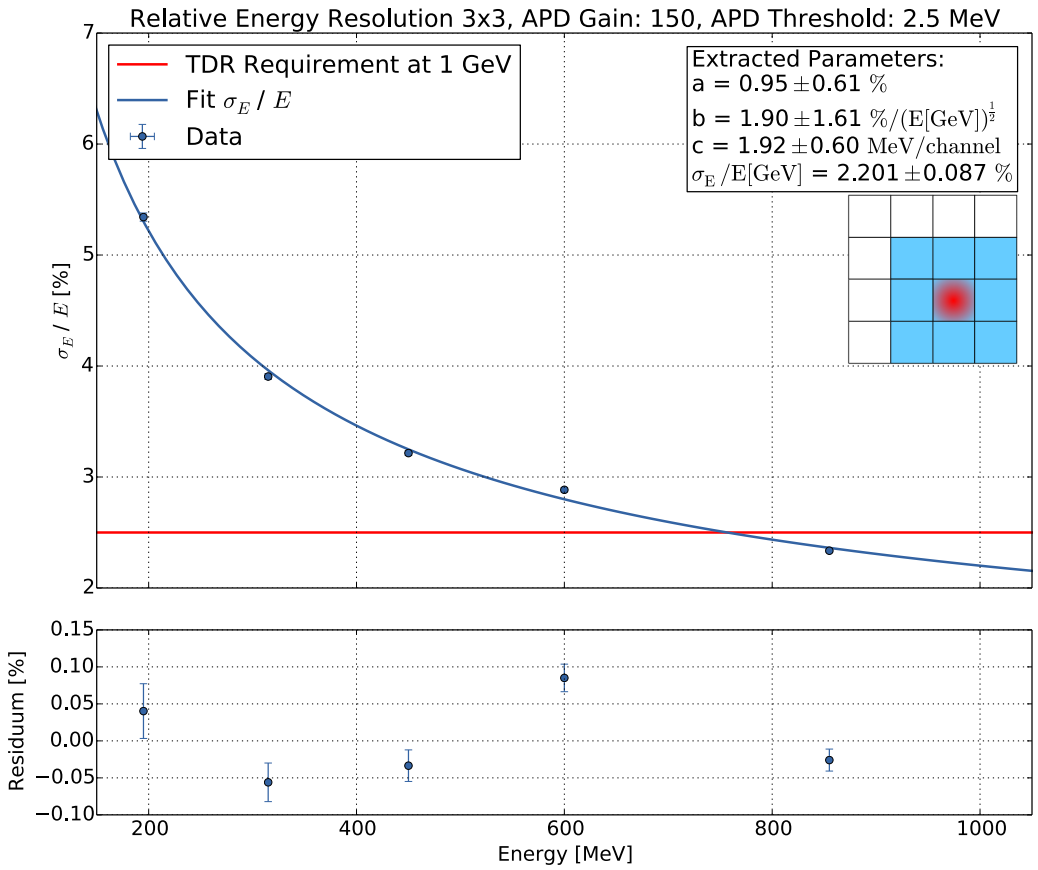

Figure C.5: APD gain: 150, APD threshold: 2.5 MeV

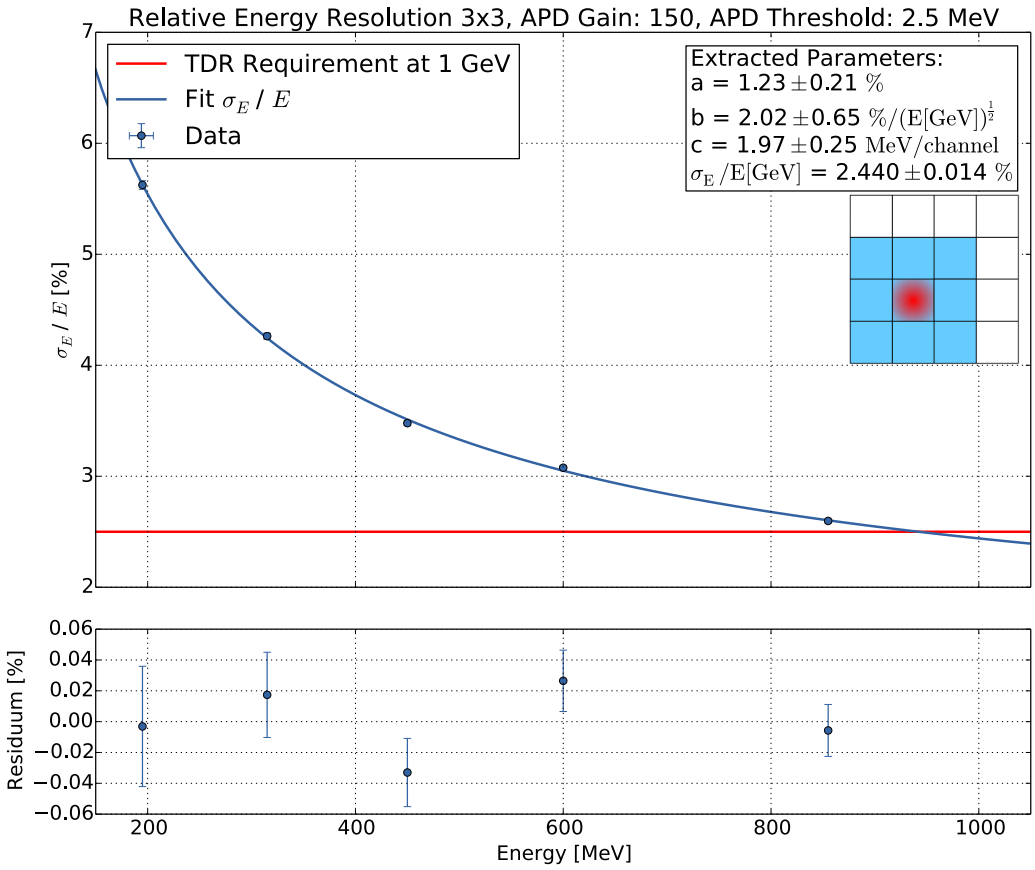

Figure C.6: APD gain: 150, APD threshold: 2.5 MeV. Due to a malfunction of one of the two APDs of the central crystal, the relative energy resolution is worse compared with the neighbouring clusters.

C.3 Relative Energy Resolution: Threshold Dependency

The threshold dependency of the relative energy resolution was discussed for one example 3×3 matrix in the main text. In the following, the results recorded with the other three 3×3 crystals matrices are given.

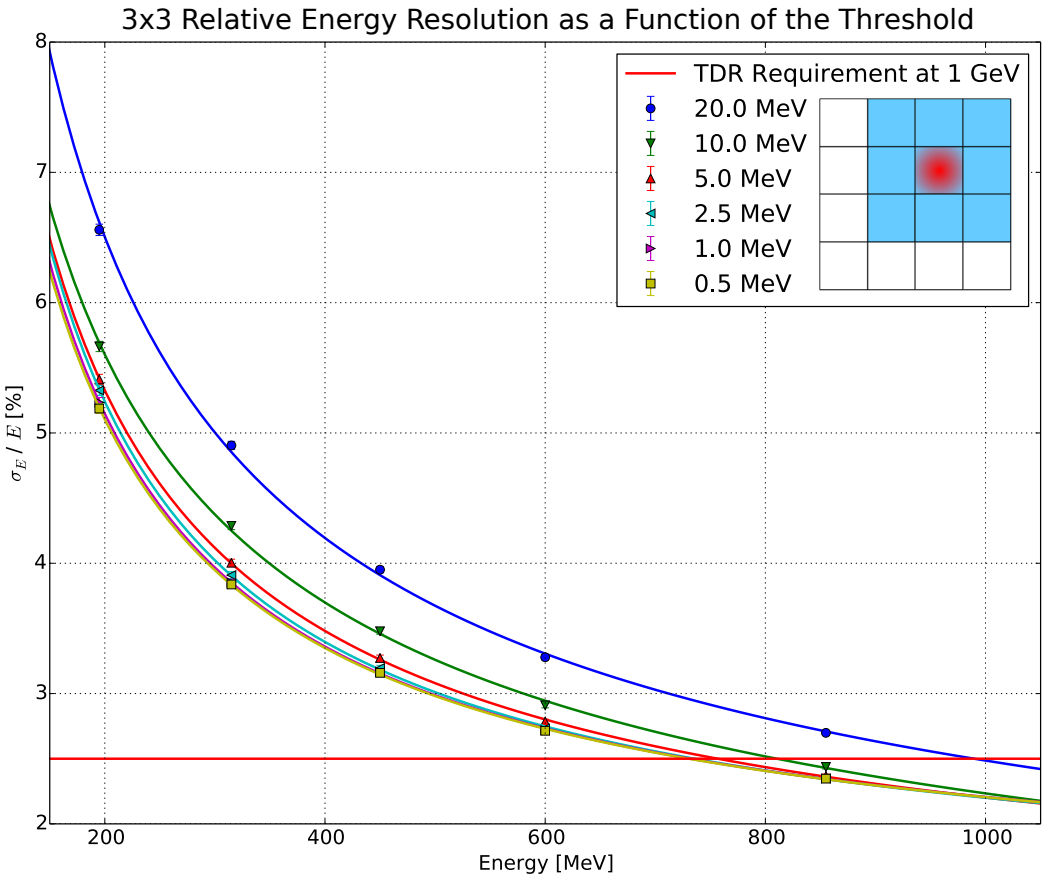

Figure C.7: APD gain: 150, threshold scan.

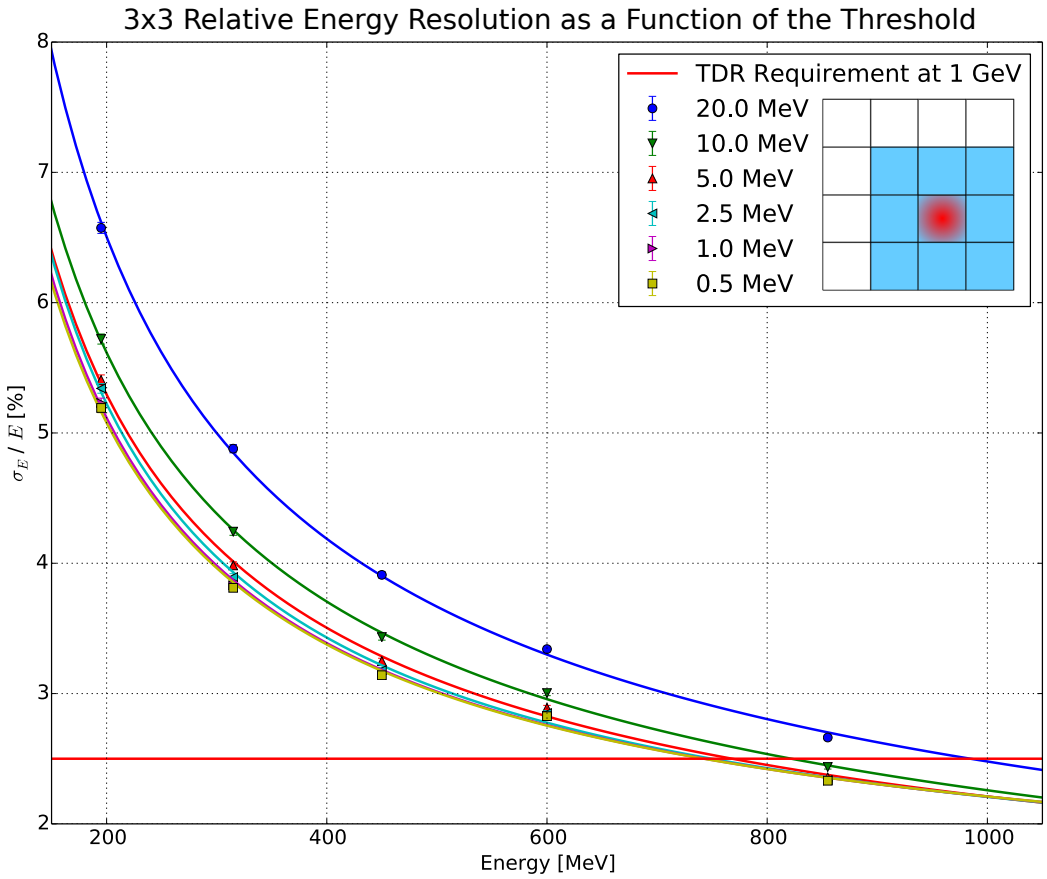

Figure C.8: APD gain: 150, threshold scan.

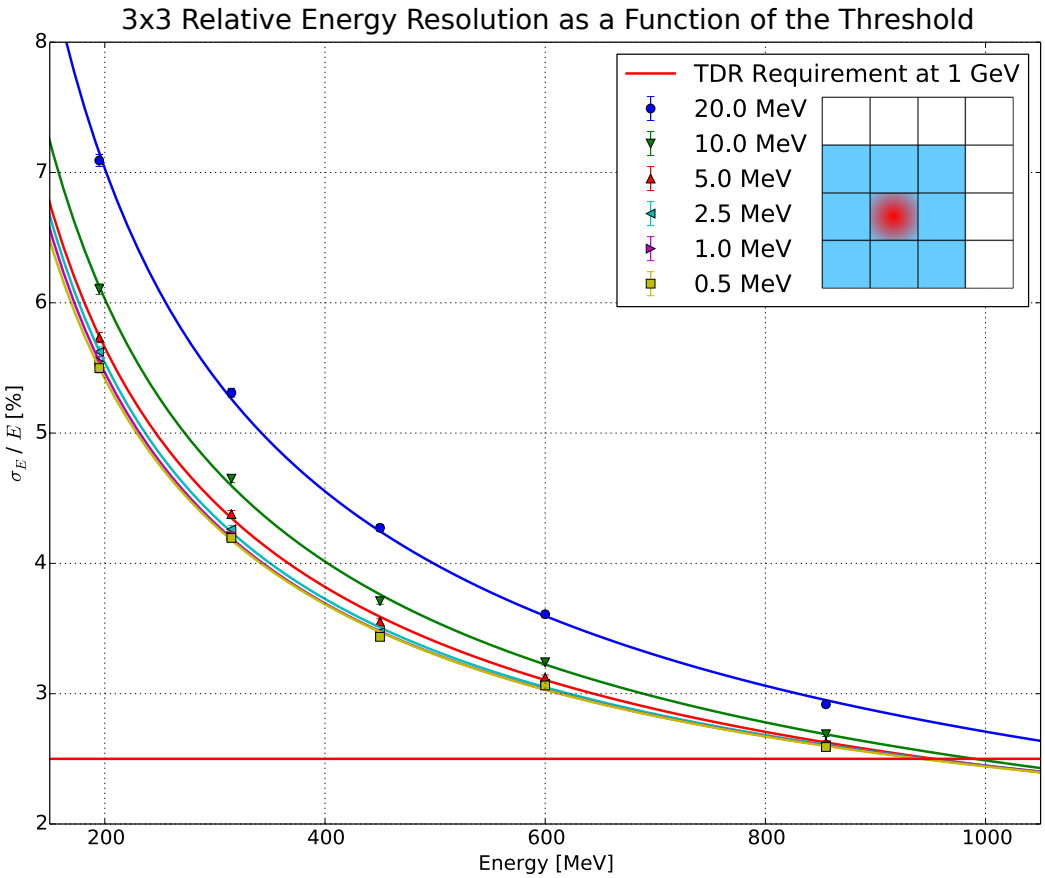

Figure C.9: APD gain: 150, threshold scan. Due to a malfunction of one of the two APDs of the central crystal, the relative energy resolution is worse compared with the neighbouring clusters.

C.4 Linearity of the EMC Prototype Response

The linearity of the EMC prototype response was discussed for one example 3×3 matrix in the main text. In the following, the results recorded with the other three 3×3 crystals matrices are given.

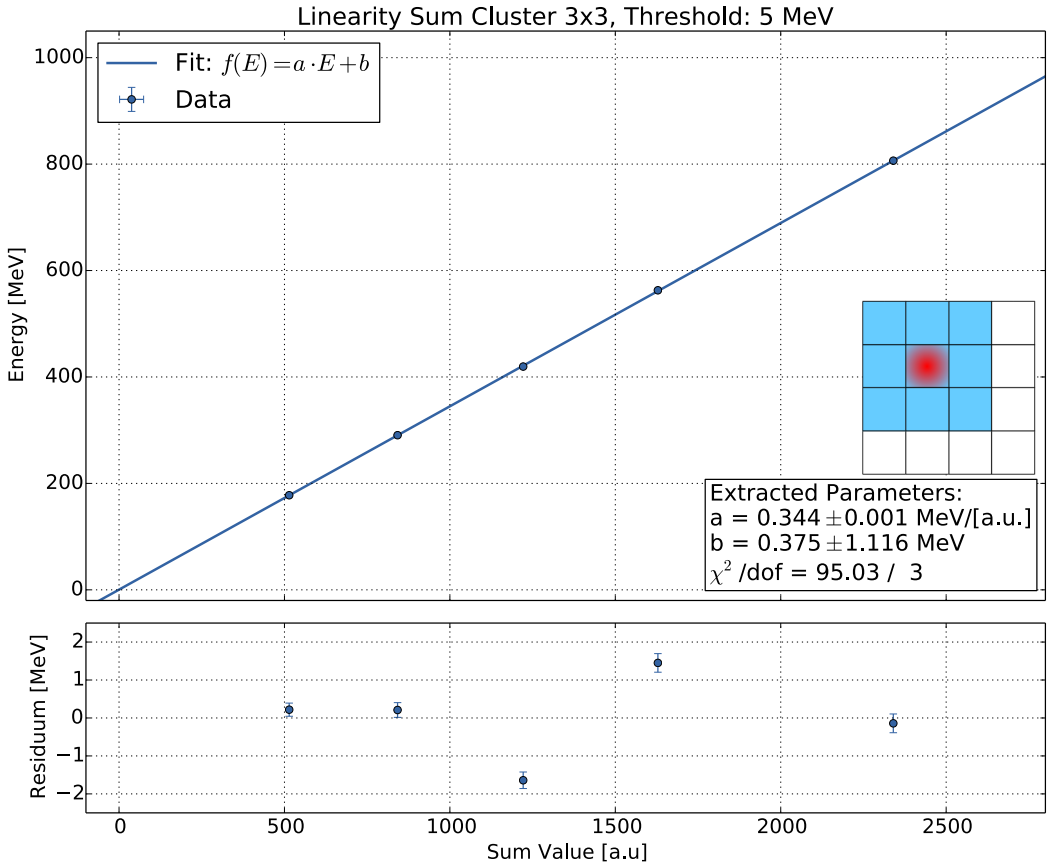

Figure C.10: APD gain: 150, Threshold: 5 MeV.

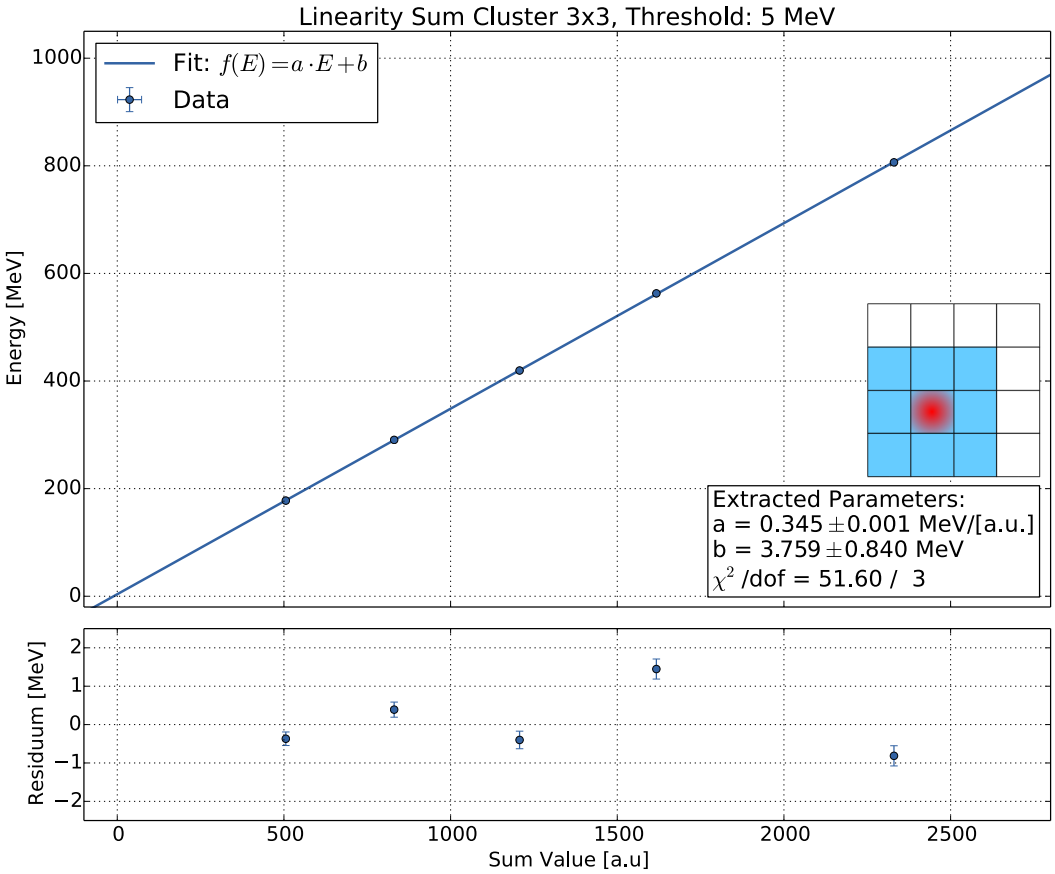

Figure C.11: APD gain: 150, Threshold: 5 MeV.

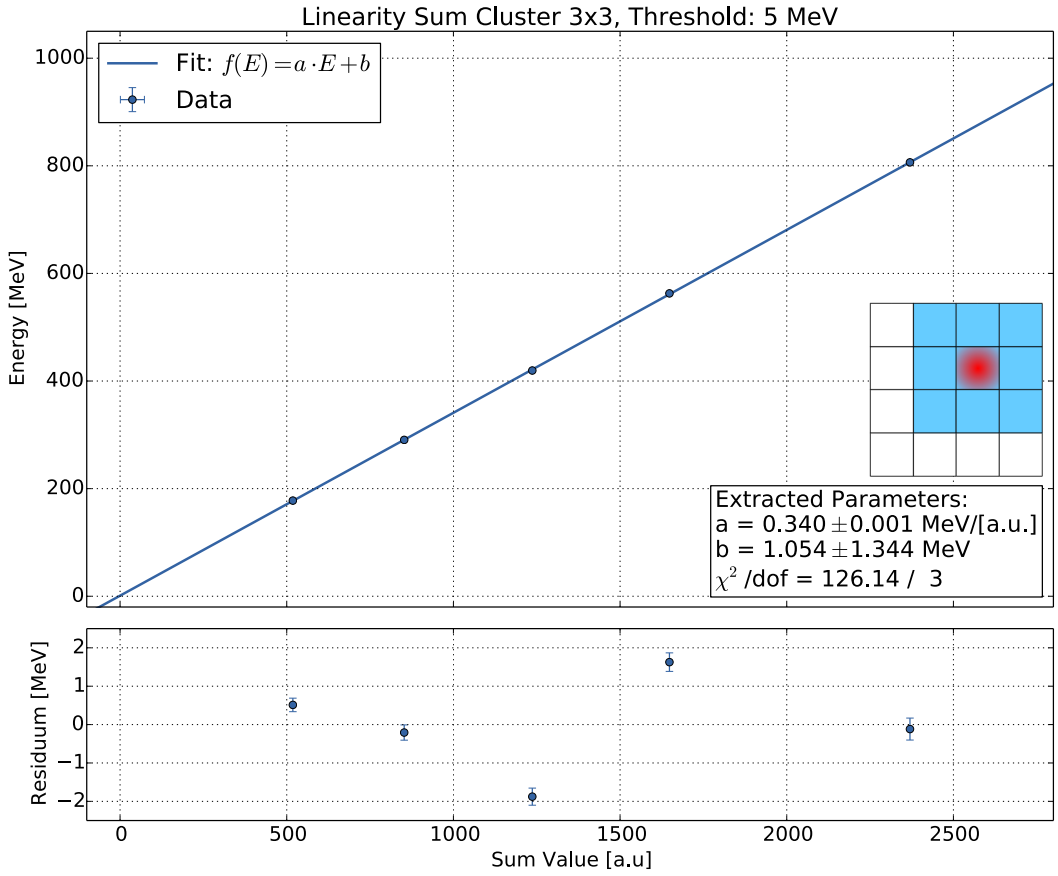

Figure C.12: APD gain: 150, Threshold: 5 MeV.

Appendix D

In-Situ Characterisation of Avalanche Photodiodes

Avalanche photodiodes (APDs) have individual characteristics. The $\bar{\text{P}}$ANDA calorimeter has thousands of APDs. Thus, a characterisation is needed to have a uniform response. The $\bar{\text{P}}$ANDA collaboration initiates an APD screening programme to determine the APD characteristics ([TDR08], 78). Besides others, its primary purpose is to specify the gain as a function of the bias voltage. The measurement is performed by illuminating the APD with a continuous light source. The APD gain characteristic is subsequently determined as the APD output current as a function of the bias voltage. The following function describes the output of such a measurement:

$$f_{\text{con.}}(U, A, U_b, \alpha, C) = \frac{A}{1 - (\frac{U}{U_b})^{\alpha}} + C \tag{D.1}$$

Here U is the bias voltage, U_b is the breakdown voltage and A, C and α are coefficients. The reference for the APD gain is the value of $f_{\text{con.}}$ at $U = 0$:

$$f_{\text{con.}}(U, A, U_b, \alpha, C)\big|_{U=0} = A + C \tag{D.2}$$

By using Equation D.1 and Equation D.2 it follows for the APD gain M:

$$M(U, A, U_b, \alpha, C) = \frac{f_{\text{con.}}(U, A, U_b, \alpha, C)}{A + C} \tag{D.3}$$

In Figure D.1 the gain as a function of the bias voltage for a typical EMC APD is shown.

D.1 Motivation of In-Situ Characterisation

The need for an in-situ APD characterisation was motivated by the lack of data from the $\bar{\text{P}}$ANDA screening programme during the EMC prototype phase. As a consequence, a procedure was developed to determine the APD characteristics by using already

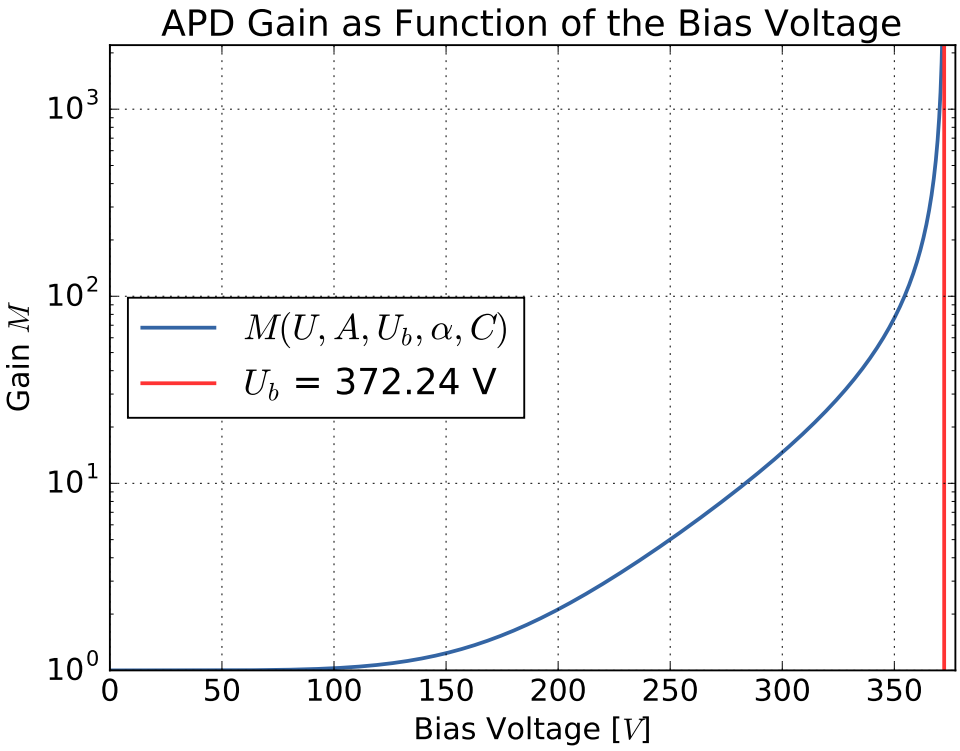

Figure D.1: The plot shows the gain characteristics of a typical APD by plotting Equation D.3. The shown curve only applies to continuous light data.

installed APDs inside the calorimeter. Furthermore, the procedure can help to monitor the ageing of APDs within a long-term experiment like $\bar{\text{P}}$ANDA . In contrast to the continuous light measurement at the $\bar{\text{P}}$ANDA screening programme, the in-situ gain determination has to be a pulsed measurement. The reason is the charge sensitive preamplifier (APFEL), which has a finite entrance capacitance and thus it is not capable of handling continuous signals.

D.2 Light Pulse Intensity Intervals

Limitations of the detector electronics entrance area demands a piecewise measurement. The light intensity from the detector light pulse system has to be reduced when the bias voltage increases. As a result, the measurement is divided into intervals, each with fixed light intensity. The different ranges need to overlap to merge the data in the next step (Figure D.2).
By the evaluation of the amplitude ratios and the derivatives of the amplitude course in the overlap regions, the proper scaling factors are determined. Figure D.3 shows

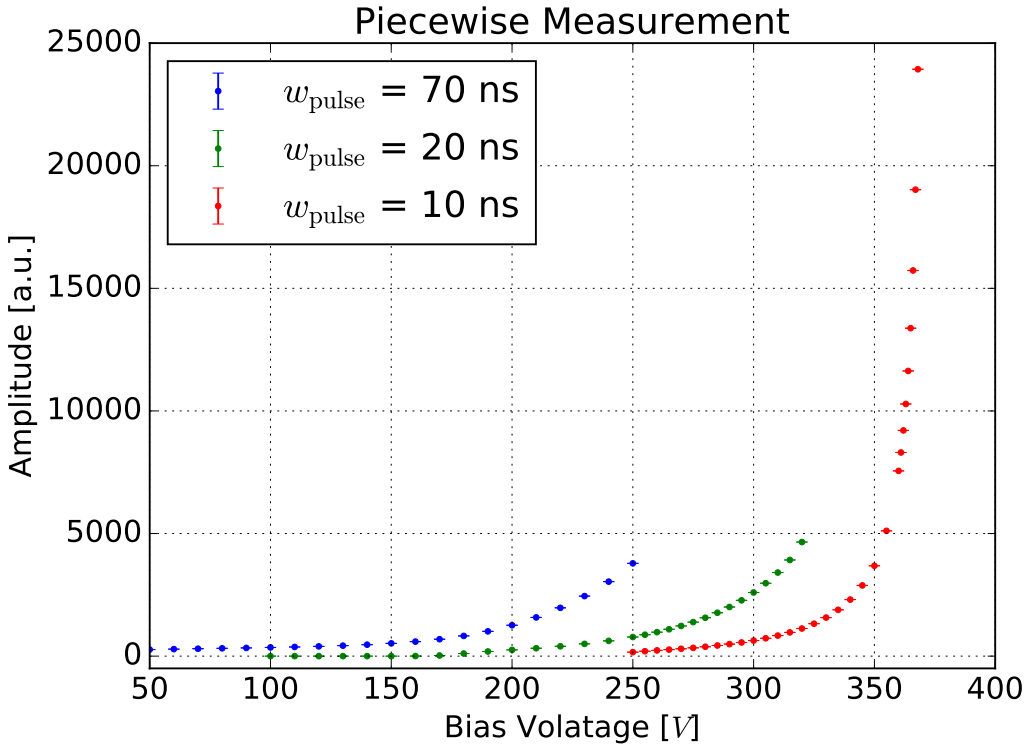

Figure D.2: The plot shows different measurement intervals. By increasing the bias voltage at a fixed light intensity, the electronics reaches more and more its full level. As a result, the light intensity has to be decreased (pulse width, w_{pulse}). As a consequence, the different intervals need to be merged. The overlapping regions help to find the proper scaling factor.

the data points after the merging process. The figure reveals a discrepancy between the measured data and the theory function described by Equation D.1 and depicted in Figure D.1. Instead of a flat course at low bias voltages, the measured data have a slope at this region. Only at higher bias voltages, the data points behave more and more like the continues light theory function. Especially the course at low bias voltages and in particular the amplitude value at 0 V is necessary to determine the gain characteristic of the APD. Thus, the pulsed light measured data need to be transformed into continuous light data.

D.3 Fit Function for Pulsed Measurements

Due to the interaction between the APD detector capacitance C_d with the preamplifier entrance capacitance C_i, there is a discrepancy between data measured with

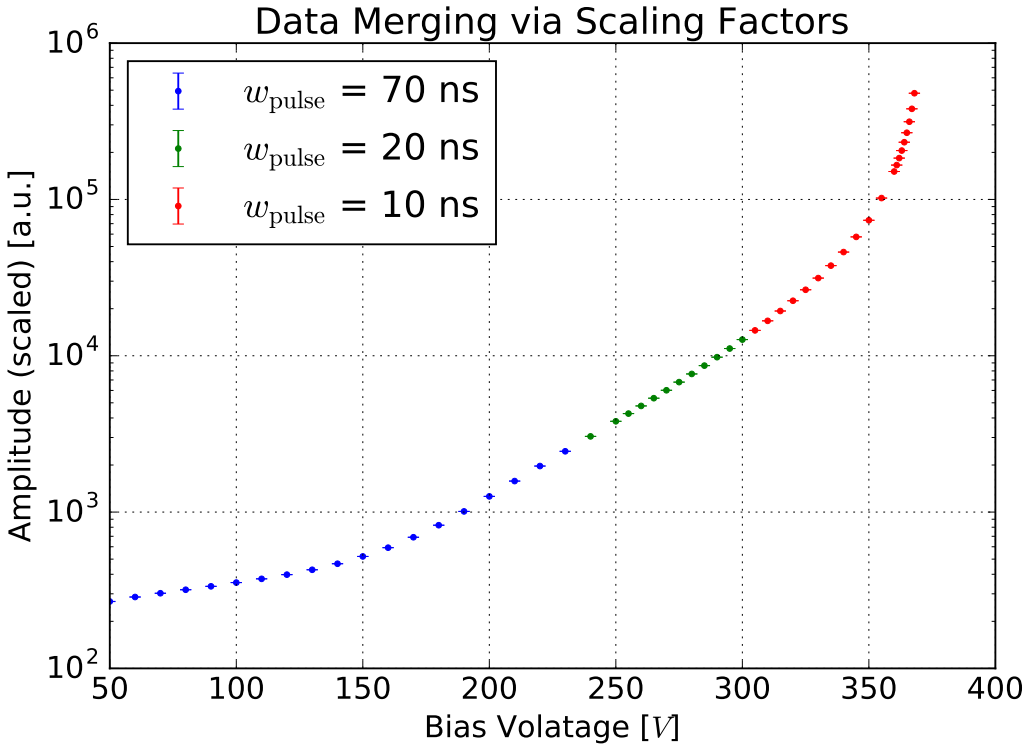

Figure D.3: The plot shows the data points of the different measuring intervals after the merging process. The scaling factors are determined by the evaluation of the ratios and the derivatives of the overlapping regions. By comparing the measured data with the theory function depicted in Figure D.1, a discrepancy is apparent. In particular, the data points at low bias voltages do not fit with the continuous light function course. Thus an pulsed data to continuous data mapping is needed.

a pulsed light source, and data measured with a continuous light source. In the book *Semiconductor Detector Systems* by Helmuth Spieler ([Spi05] ,91 ff.), the impact of the interaction among the capacitances on the measured charge Q_s for a theory preamplifier is derived. Spieler found the following approximation for the charge, which is transferred to the amplifier:

$$Q(t) \approx \frac{Q_s}{1 + \frac{C_d}{C_i}}\left(1 - e^{-t/\tau_u}\right), \tag{D.4}$$

whereby $\tau_u = R_i C_d$ being the input time constant. Since the APFEL preamplifier is a charge sensitive preamplifier, its output has to be proportional to the measured charge Q_s. Under the assumption that $Q_s\left(1 - e^{-t/\tau_u}\right)$ is proportional to the undistorted

signal, the measurement behaviour can be described with:

$$f_{\text{pulsed}} \approx \frac{f_{\text{con.}}}{1 + \frac{C_d}{C_i}} \tag{D.5}$$

The APFEL input capacitance C_i is a constant and is in the order of 10 pF [Wie09]. The approach is to find a model function, which describes the APD capacitance as a function of the bias voltage $C_d(U)$. In Figure D.4 data[1] from an APD capacitance measurement is shown. The APD capacitance falls with increasing bias voltage in accordance with $\frac{1}{\sqrt{1+U}}$. Beginning at around 170 V a kink appears. Thus, an additional term is needed to describe the course of the capacitance. The detector capacitance model function is found to be

$$C_d(U, a, b, c, d, e) = e \cdot \left(\frac{a}{\sqrt{1 + b \cdot U}} - \frac{1}{1 + e^{-c \cdot (U-d)}} \right) \tag{D.6}$$

Consequently, the aim is to fit the data from the pulsed measurement (Figure D.3) with Equation D.5. In order to derive a fit function, some substitutions have to be made. Firstly, the C parameter in Equation D.1 can be eliminated by using the condition $f_{\text{con.}}\big|_{U=0} = 1$. C is then substituted by $1 - A$ and Equation D.1 becomes

$$\widetilde{f}_{\text{con.}}(U, A, U_b, \alpha) = \frac{A}{1 - (\frac{U}{U_b})^{\alpha}} + 1 - A \tag{D.7}$$

Since the measured data are in arbitrary units, Equation D.7 has to be scaled with a factor R. Moreover, the entrance capacitance of the preamplifier can be absorbed in the e parameter of Equation D.6. Thus, the denominator of Equation D.5 becomes $1 + C_d$. The final fit function is:

$$F_{\text{fit}}(U, A, U_b, \alpha, a, b, c, d, e, R) = \frac{R \cdot \widetilde{f}_{\text{con.}}(U, A, U_b, \alpha)}{1 + C_d(U, a, b, c, d, e)} \tag{D.8}$$

In Figure D.5 the result of the fit is presented. The residuum plot reveals a good agreement with the data. The residua have a relative deviation of less than 1.2 %. However, the fluctuations are not statistically distributed and have a structure. Nevertheless, the fit function describes the data with sufficient accuracy.

D.4 Mapping from Pulsed Light Data into Continuous Light Data

By rearranging Equation D.8, the mapping between pulsed light data and continuous light data is defined by

$$T(U, a, b, c, d, e, R) = \frac{1 + C_d(U, a, b, c, d, e)}{R} \tag{D.9}$$

[1] The data stem from the $\bar{\text{P}}$ANDA APD screening programme. [Wil16]

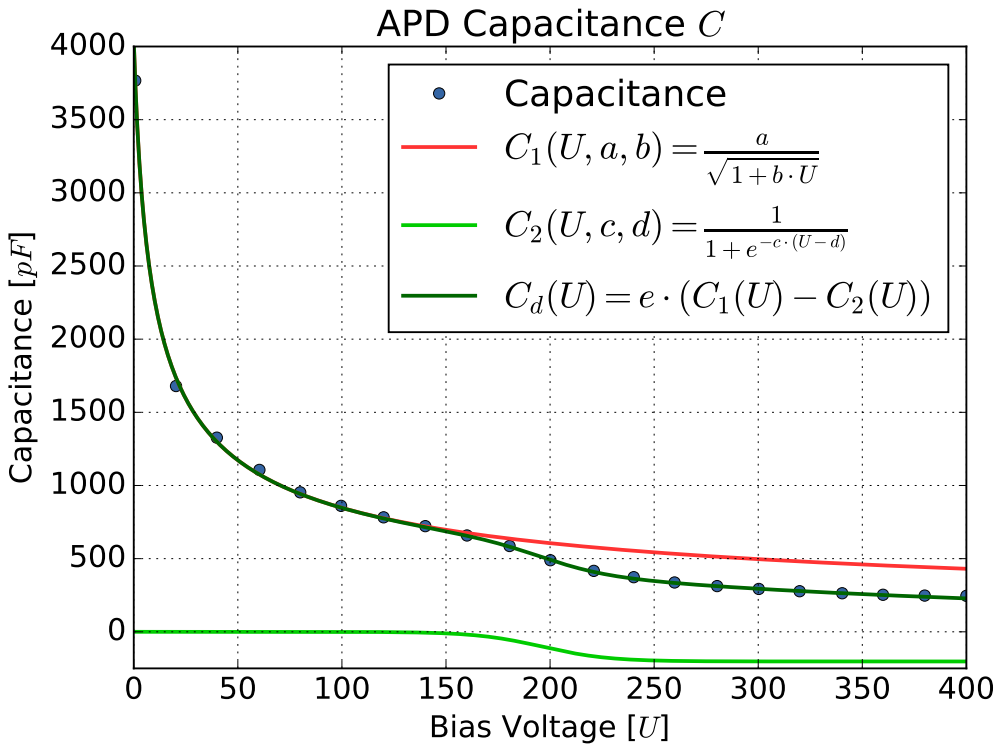

Figure D.4: The plot shows the APD capacitance as a function of the bias voltage. For lower voltages, the course can be described by $\frac{1}{\sqrt{1+U}}$. At a certain point ($\sim 170\,\mathrm{V}$) a kink appears, which needs to be described with a second term. The sum of both terms describes the course of the APD capacitance sufficiently. Since the data were only used to construct a model function, the error bars are not drawn.

In Figure D.6 the final result of the transformation is shown. In contrast to Figure D.3, both the data and the fit function have a well-defined normalisation. Thus, the APD gain as a function of the bias voltage is disclosed. Furthermore, the breakdown voltage can be extracted from the fit parameters. For the particular example the breakdown voltage is $U_b = 372.24(3)\,\mathrm{V}$. Finally, as a by-product, the bias voltage-capacitance dependency of the APD can be extracted.

D.5 Dependence of the Avalanche Phododiode Capacitance on the Bias Voltage

Since the APD bias voltage-capacitance dependency is an explicit part of the fit function, it can easily be extracted. However, there is uncertainty in the scaling. The

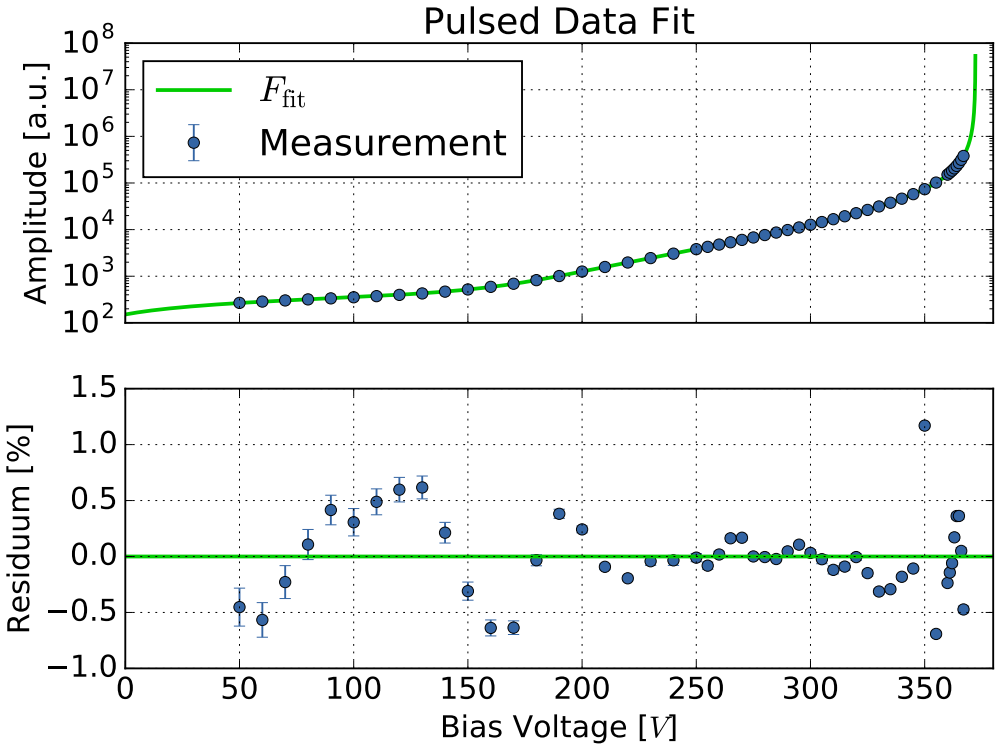

Figure D.5: The plot shows the pulsed data fit using the developed fit function. The relative deviation of the residua is less than 1.2 %. However, the residua do not fluctuate erratically and have a structure. Nevertheless, the fit function describes the data within a sufficient accuracy.

APD data sheet [HAM09] gives a value for the terminal capacitance of 270 pF for gain $M = 50$. The number refers to an event rate of 100 kHz. By using the datasheet value, a scaling factor can be determined. In Figure D.7 the scaled bias voltage-capacitance dependency is depicted. The shown values should not be overestimated due to the uncertainty in the scaling factor determination. Nonetheless, the extracted dependency describes the course similar to the bias voltage dependency of a measured APD capacitance (Figure D.4).

D.6 Correction of Beam Test Data

In the following, the in-situ method is used to correct beam test data. The detector APDs were adjusted by using data from the $\bar{\text{P}}$ANDA screening programme. Back then, the screening process was not fully developed, which led to incorrect calibration data. As a result, the beam test had to be performed with an inhomogeneous APD

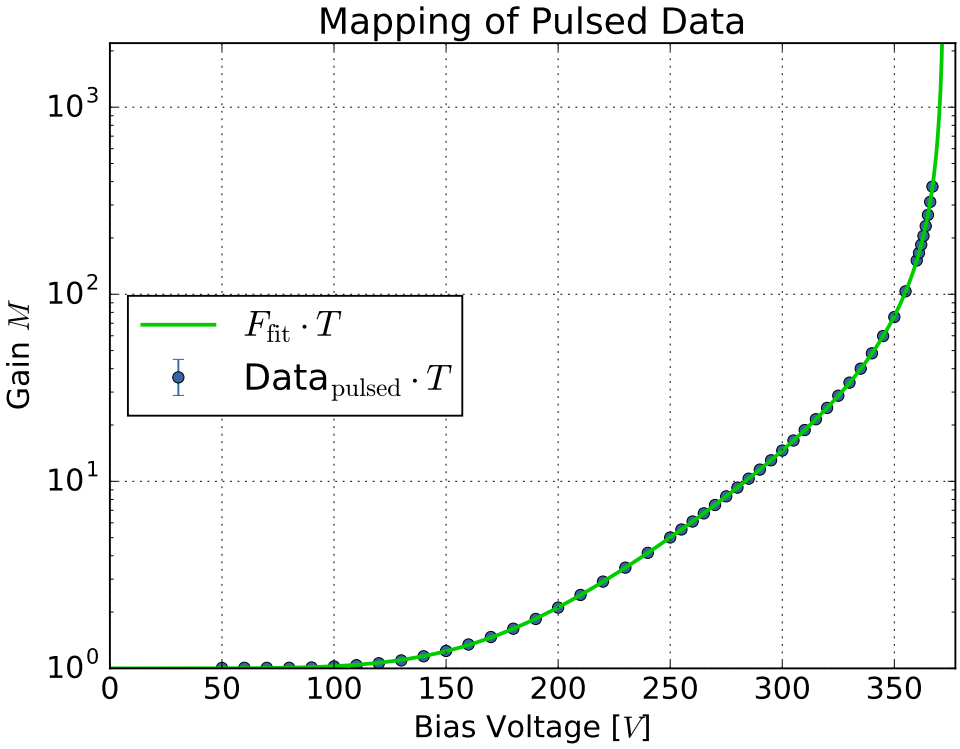

Figure D.6: The plot shows the impact of the mapping on both the fit function (F_{fit}) and the data. The result is a well-defined normalisation. All relevant quantities such as the APD gain as a function of the bias voltage or the breakdown voltage can be extracted.

gain distribution. In Figure D.8 the single APD channel spectra for the energies 195 MeV, 450 MeV and 855 MeV of one crystal are given. In the example, the APD gains were adjusted to a nominal gain of $M = 400$. Under the assumption of a sufficient optical coupling between APDs and crystal, the spectra are expected to be congruent. However, the APD spectra mean positions at given energy do differ significantly.
By utilising the in-situ characterisation method, the actual APD gains were determined. Instead of gain 400, APD0 had a gain of $M_0 = 189$ and APD1 had a gain of $M_1 = 128$. In Figure D.9 the corrected spectra according to the in-situ characterisation data are shown. The spectra data were divided by the actual APD gain and scaled by an arbitrary value of 200 to move them back in their original regions. After the procedure, the spectra are nearly congruent.

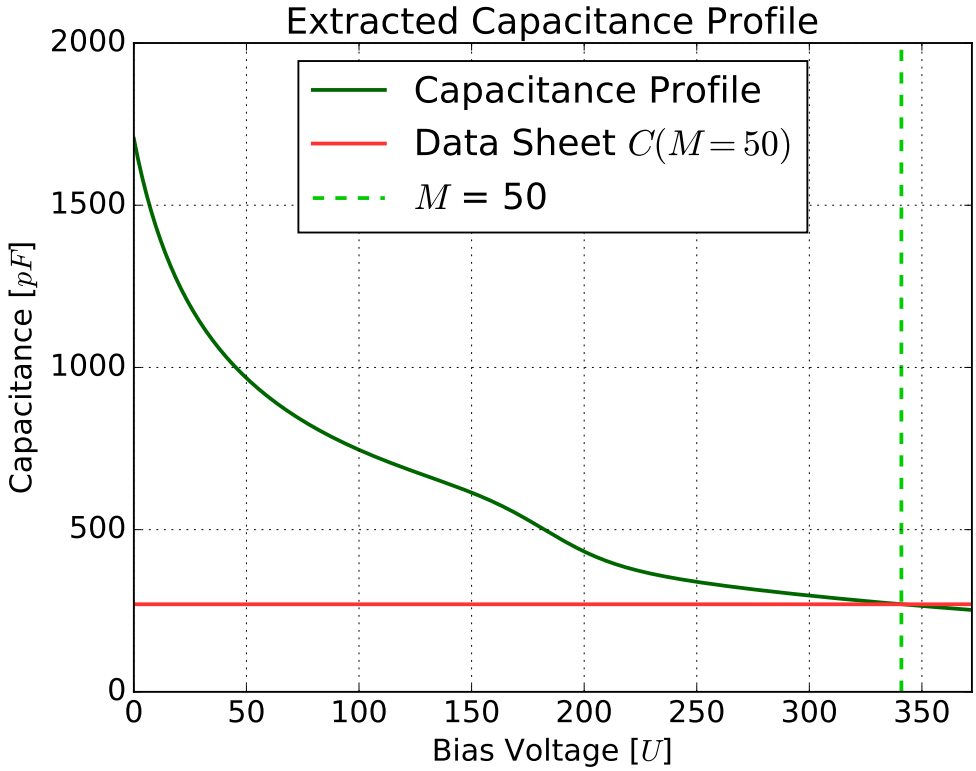

Figure D.7: The plot shows the extracted capacitance profile from the fit function (F_{fit}). The scaling was performed by using the datasheet value for the APD capacitance at $M = 50$, which is 270 pF. The course is similar to a measured APD capacitance profile (Figure D.4). The particular values from the extracted profile should not be overrated because of uncertainties in the model function and the datasheet value.

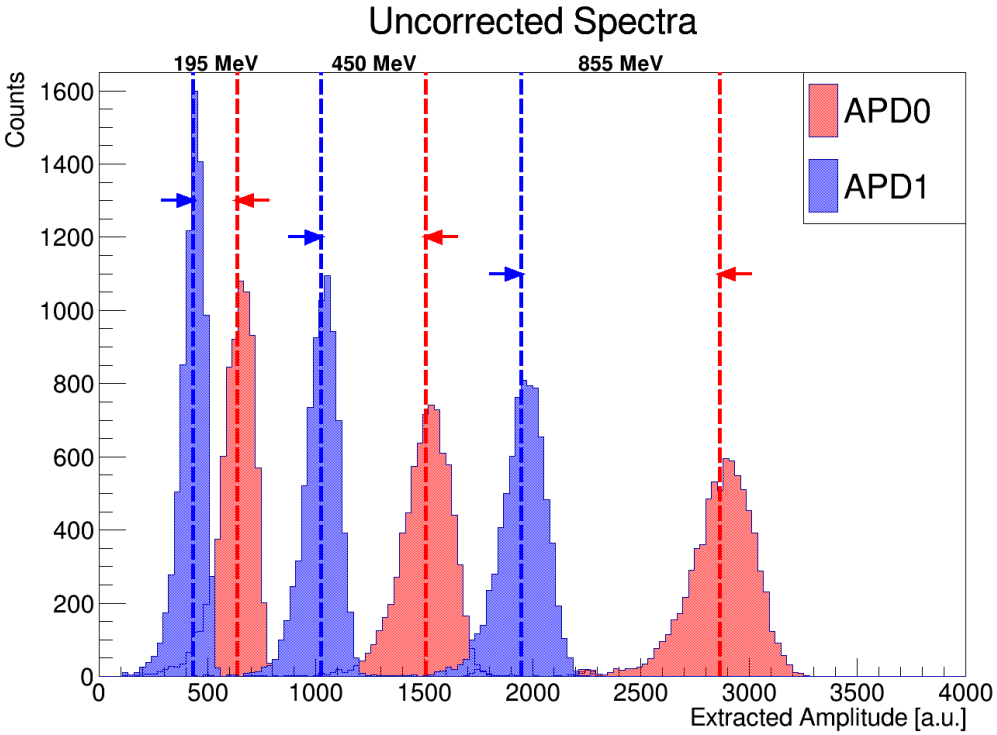

Figure D.8: The plot shows single APD spectra of one crystal for the energies 195 MeV, 450 MeV and 855 MeV. The APD gain was adjusted to a nominal gain of $M = 400$. Under the assumption, that the APD see the same light intensity (optical coupling), the spectra are expected to be congruent. The dashed lines are marking the mean positions of the individual histograms. There is a significant discrepancy between the APD spectra at given energies.

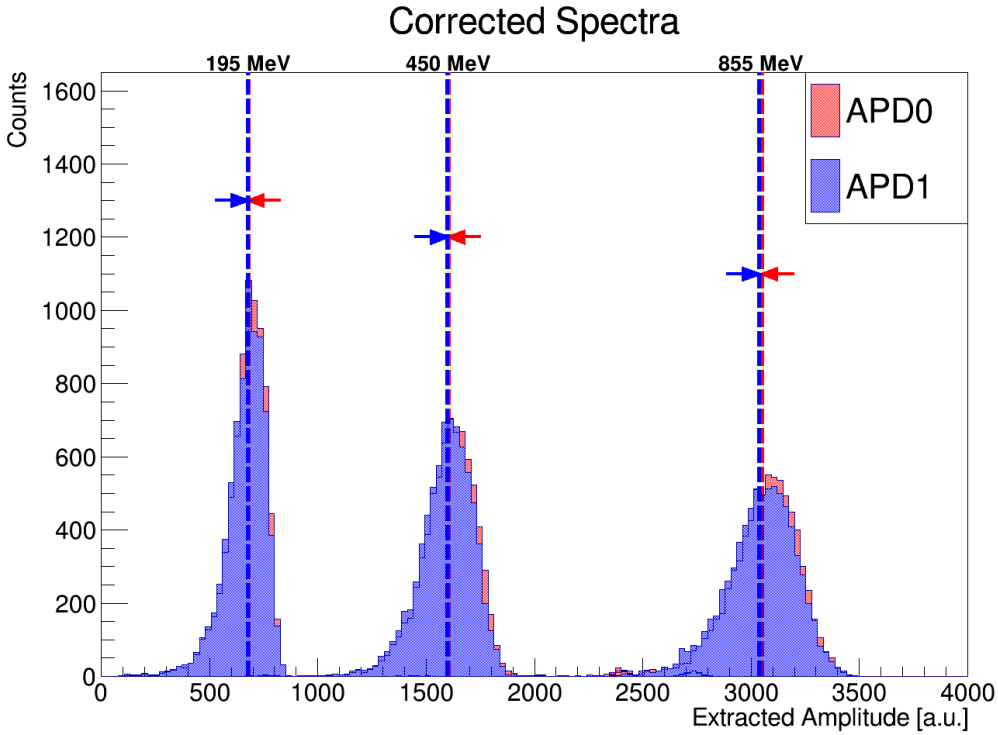

Figure D.9: The plot shows the corrected spectra by using the in-situ method. The measured spectra are divided by their actual gain and then scaled to move them in their original region. The dashed lines indicate the mean values of the different spectra. The spectra are nearly congruent for given energies.

Bibliography

[A+08] R. Achenbach et al. The ATLAS level-1 calorimeter trigger. *JINST*, 3:P03001, 2008.

[A+17] Roel Aaij et al. Measurement of matter-antimatter differences in beauty baryon decays. *Nature Phys.*, 13:391–396, 2017.

[A+19] M. Ablikim et al. Study of the process $e^+e^- \to p\bar{p}$ via initial state radiation at BESIII. *Phys. Rev.*, D99(9):092002, 2019.

[A+20] Medina Ablikim et al. Measurement of proton electromagnetic form factors in $e^+e^- \to p\bar{p}$ in the energy region 2.00 - 3.08 GeV. *Phys. Rev. Lett.*, 124(4):042001, 2020.

[AHKN12] Tatsumi Aoyama, Masashi Hayakawa, Toichiro Kinoshita, and Makiko Nio. Complete Tenth-Order QED Contribution to the Muon g-2. *Phys. Rev. Lett.*, 109:111808, 2012.

[Aul11] K. Aulenbacher. Polarized beams for electron accelerators. *Eur. Phys. J. ST*, 198:361–380, 2011.

[B+06] G. W. Bennett et al. Final Report of the Muon E821 Anomalous Magnetic Moment Measurement at BNL. *Phys. Rev.*, D73:072003, 2006.

[B+20] Sz. Borsanyi et al. Leading-order hadronic vacuum polarization contribution to the muon magnetic momentfrom lattice QCD. 2020.

[Ber13] Jan C. Bernauer. The Mainz high-precision proton form factor measurement. *AIP Conf.Proc.*, 1560:549–553, 2013.

[Bii15] Cristina Biino. The CMS Electromagnetic Calorimeter: overview, lessons learned during Run 1 and future projections. *J. Phys. Conf. Ser.*, 587(1):012001, 2015.

[Bir64] John B. Birks. *The Theory and practice of scintillation counting.* Nuclear Scinece Abstracts, 1964.

[BZD+20] Yu M. Bystritskiy, V.A. Zykunov, A. Dbeyssi, M. Zambrana, F. Maas, and E. Tomasi-Gustafsson. Radiative corrections in proton–antiproton annihilation to electron-positron and their application to the PANDA experiment. *Eur. Phys. J. A*, 56(2):58, 2020.

[Cap19] Luigi Capozza. Data from the Background Energy Distribution Analysis. *Private Communication*, 2019.

[CER19] CERN. Geant4, toolkit for the simulation of the passage of particles through matter. `https://geant4.web.cern.ch/`, 2019.

[CGM+20] L. Capozza, M. Gorshteyn, F. Maas, O. Noll, and S. Wolff. Measurement of the Electromagnetic Transition Form Factor of the π^0 in the space-like region via Primakoff Electroproduction. *Letter of Intent, Submitted to the MAMI Program Advisory Committee*, March 2020.

[CHK+14] Gilberto Colangelo, Martin Hoferichter, Bastian Kubis, Massimiliano Procura, and Peter Stoffer. Towards a data-driven analysis of hadronic light-by-light scattering. *Phys. Lett.*, B738:6–12, 2014.

[Com19] The SciPy Community. Scipy signal remez. `https://docs.scipy.org/doc/scipy/reference/generated/scipy.signal.remez.html`, 2019.

[Cor18] Linear Technology Corporation. Electrical specifications ltm9011-14/ltm9010-14/ltm9009-14 14-bit, 125msps/ 105msps/ 80msps low power octal adcs. `https://www.analog.com/media/en/technical-documentation/data-sheets/ltm9011-14-9010-14-9009-14.pdf`, 2018.

[Des14] M. Destefanis. Spin studies via Drell-Yan processes at PANDA. *EPJ Web Conf.*, 73:02012, 2014.

[Dir28] Paul A. M. Dirac. The quantum theory of the electron. *Proc. Roy. Soc. Lond.*, A117:610–624, 1928.

[E+13] W. Erni et al. Technical design report for the PANDA (AntiProton Annihilations at Darmstadt) Straw Tube Tracker. *Eur. Phys. J.*, A49:25, 2013.

[FAI20] FAIR. Der fair-komplex. `http://www.fair-center.de/de/oeffentlichkeit/was-ist-fair.html`, January 2020.

[Fel14] F. Feldbauer. The Detector Control of the PANDA Experiment. *JINST*, 9:C08025, 2014.

[FHH+19] Manami Fujita, Ryotaro Honda, Kenji Hosomi, Yuji Ishikawa, Honoka Kanauchi, Takeshi Koike, Hirokazu Tamura, Mifuyu Ukai, and Takeshi O. Yamamoto. The Ξ- Atom X-ray Spectroscopy at J-PARC. *JPS Conf. Proc.*, 26:031016, 2019.

[FW11] H. Flemming and P. Wieczorek. Low noise preamplifier ASIC for the PANDA experiment. *JINST*, 6:C12055, 2011.

[GKPN19] K. Götzen, R. Kliemt, K. Peters, and Frank Nerling. Precision spectroscopy of charmonium-like (exotic) XYZ states at PANDA/FAIR. *PoS*, Confinement2018:120, 2019.

[GM73] D. N. Goswami and D. P. Majumdar. Electroproduction of pi0 mesons via the primakoff effect. *Phys. Rev.*, D8:2086–2096, 1973.

[Gra18] Phillip Grasemann. Characterisation of a Self Triggering ASIC Digitiser and Development of an Electron Tagger Prototype. *Master Thesis*, 2018.

[GSSK13] C. Gnendiger, D. Stöckinger, and H. Stöckinger-Kim. The electroweak contributions to $(g-2)_\mu$ after the Higgs boson mass measurement. *Phys. Rev.*, D88:053005, 2013.

[HAM09] HAMAMATSU. Datasheet of apd type s11048(x2) (extract from k03-0012-2 g). `https://jazz.physik.unibas.ch/panda/uploads/2012-11-13--12-43-06_Specification_Sheet_S11048_X2_20101.pdf`, November 2009.

[HG13] Y. K. Hsiao and C. Q. Geng. Identifying Glueball at 3.02 GeV in Baryonic B Decays. *Phys. Lett.*, B727:168–171, 2013.

[HHK+18] Martin Hoferichter, Bai-Long Hoid, Bastian Kubis, Stefan Leupold, and Sebastian P. Schneider. Dispersion relation for hadronic light-by-light scattering: pion pole. *JHEP*, 10:141, 2018.

[HM55] R. Hofstadter and R. W. McAllister. Electron Scattering From the Proton. *Phys. Rev.*, 98:217–218, 1955.

[IKP09] A. Mann1 I. Konorov, H. Angerer1 and S. Paul1. Soda: Time distribution system for the pandaexperiment. `https://panda-wiki.gsi.de/foswiki/pub/Daq/SoDA/nssmic_pdf_2009.pdf`, 2009.

[JAM17] Sergei Linev Jörn Adamczewski-Musch, Nikolaus Kurz. Gsi data acquisition system mbs, release notes v6.3. `https://www.gsi.de/fileadmin/EE/MBS/gm_mbs_rel_63.pdf`, November 2017.

[Jan06] Andreas Jankowiak. *The Mainz microtron MAMI - Past and future*, volume 28, pages 149–160. 01 2006.

[Jeg19] Fred Jegerlehner. Variations on Photon Vacuum Polarization. *EPJ Web Conf.*, 218:01003, 2019.

[Kha17] Dmitry A. Khaneft. *An investigation of the proton structure in the space-like domain and feasibility studies of the proton electromagnetic form factor measurement in the time-like region.* PhD thesis, Mainz U., 2017.

[Kho11] Alfons Khoukaz. Internal targets for the PANDA experiment. *PoS*, STORI11:036, 2011.

[Kop12] Bertram Kopf. Exotics at PANDA. *Hyperfine Interact.*, 213(1-3):13–21, 2012.

[KW16] Hermann Kolanoski and Norbert Wermes. *Teilchendetektoren*. Springer, 2016.

[KZ07] Eberhard Klempt and Alexander Zaitsev. Glueballs, Hybrids, Multiquarks. Experimental facts versus QCD inspired concepts. *Phys. Rept.*, 454:1–202, 2007.

[L+95] P. Lecoq et al. Lead tungstate (PbWO-4) scintillators for LHC EM calorimetry. *Nucl. Instrum. Meth.*, A365:291–298, 1995.

[L+09] M. F. M. Lutz et al. Physics Performance Report for PANDA: Strong Interaction Studies with Antiprotons. 2009.

[L+13a] J. P. Lees et al. Production of charged pions, kaons, and protons in e^+e^- annihilations into hadrons at $\sqrt{s}$=10.54 GeV. *Phys. Rev.*, D88:032011, 2013.

[L+13b] J. P. Lees et al. Study of $e^+e^- \to p\bar{p}$ via initial-state radiation at BABAR. *Phys. Rev.*, D87(9):092005, 2013.

[M+17] P Marciniewski et al. A compact size, 64-channel, 80 msps, 14-bit dynamic range adc module for the panda electromagnetic calorimeter. `https://indico.cern.ch/event/608587/contributions/2614165/contribution.pdf`, September 2017.

[MAM19] MAMI. Der mainzer mikrotron. `https://www.kernphysik.uni-mainz.de/beschleuniger/mainzer-mikrotron/`, August 2019.

[MIP01] Inc. Maxim Integrated Products. Inl/dnl measurements for high-speed analog-to-digital converters (adcs),tutorial 283. `https://www.maximintegrated.com/en/app-notes/index.mvp/id/283`, November 2001.

[MMR+00] J. Marler, T. McCauley, S. Reucroft, J. Swain, D. Budil, and S. Kolaczkowski. Studies of avalanche photodiode performance in a high magnetic field. *Nucl. Instrum. Meth.*, A449:311–313, 2000.

[Mor19] S. Morgenstern. ATLAS LAr calorimeter performance in LHC Run-2. *Nucl. Instrum. Meth.*, A936:86–89, 2019.

[MP05] J. H. McClellan and T. W. Parks. A personal history of the parks-mcclellan algorithm. *IEEE Signal Processing Magazine*, 22(2):82–86, March 2005.

[Mü19] Johannes Sebastian Müllers. An FPGA-based Sampling ADC for the Crystal Barrel Calorimeter. *Dissertation*, 2019.

[N+18] K. Nakamura et al. Review of particle physics. *Phys. Rev. D*, 98:030001, Aug 2018.

[Nay19] Gouranga C. Nayak. Matter-Antimatter Asymmetry of the Universe and Baryon Formation from Non-Equilibrium Quarks and Gluons. 2019.

[NK05] Newnes and Walt Kester. *The Data Conversion Handbook*. https://www.analog.com, 2005. ISBN:0-7506-7841-0.

[Nol14] Oliver Noll. Prototypentwicklung für die rückwärtige Endkappe des PANDA-Kalorimeters. *Masterarbeit*, 2014.

[Nol19] Oliver Noll. Time Measurement and Amplitude Extraction (TMAX), Feature Extraction for APFEL Preamplifier Signals. *Techniques and Software Guide*, 2019.

[NT19a] National Institute of Standards NIST and Technology. Elementary charge *e*. `https://physics.nist.gov/cgi-bin/cuu/Value?e`, October 2019.

[NT19b] National Institute of Standards NIST and Technology. Estar : Stopping power and range tables for electrons. `https://physics.nist.gov/PhysRefData/Star/Text/ESTAR.html`, 2019.

[Och13] Wolfgang Ochs. The Status of Glueballs. *J. Phys.*, G40:043001, 2013.

[Oss16] Martin Ossmann. Filter auf dem red pitaya. *Elektor Magazin*, 47. Jahrgang(547/548):67–71, Juli/August 2016.

[PAN18] PANDA. Scientific strategy for day-1 of panda. Panda Collaboration Meeting, November 2018, Talk: PubCom/PhysCom by Johan Messchendorp, October 2018.

[PAN19] PANDA. The panda detector. `https://panda.gsi.de/panda`, November 2019.

[Pap16] Michael Papenbrock. Antihyperon-Hyperon production in antiproton-proton annihilations with PANDA at FAIR. *EPJ Web Conf.*, 113:05005, 2016.

[Pau27] W. Pauli. Zur Quantenmechanik des magnetischen Elektrons. *Zeitschrift für Physik*, 43(9-10):601–623, 1927.

[Pau14] Vladyslav Pauk. *Light-by-light scattering and muon- anomalous magnetic moment*. PhD thesis, Mainz U., 2014.

[PPV07] C.F. Perdrisat, V. Punjabi, and M. Vanderhaeghen. Nucleon Electromagnetic Form Factors. *Prog.Part.Nucl.Phys.*, 59:694–764, 2007.

[PSRZ14] B. Povh, C. Scholz, K. Rith, and F. Zetsche. *Particles and nuclei: An introduction to the physical conceptions. (In German).* Springer Science, 2014.

[PV14] Vladyslav Pauk and Marc Vanderhaeghen. Anomalous magnetic moment of the muon in a dispersive approach. *Phys. Rev.*, D90(11):113012, 2014.

[Ros50] M. N. Rosenbluth. High Energy Elastic Scattering of Electrons on Protons. *Phys. Rev.*, 79:615–619, 1950.

[S+13] B. S. Schlimme et al. Measurement of the neutron electric to magnetic form factor ratio at $Q^2 = 1\ 58GeV^2$ using the reaction ${}^3\vec{H}e(\vec{e}, e'n)pp$. *Phys. Rev. Lett.*, 111(13):132504, 2013.

[S+15] B. P. Singh et al. Experimental access to Transition Distribution Amplitudes with the PANDA experiment at FAIR. *Eur. Phys. J.*, A51(8):107, 2015.

[S+16] B. Singh et al. Feasibility studies of time-like proton electromagnetic form factors at $\overline{\text{P}}$ANDA at FAIR. *Eur. Phys. J.*, A52(10):325, 2016.

[S+17] B. Singh et al. Feasibility study for the measurement of πN transition distribution amplitudes at $\overline{P}$ANDA in $\bar{p}p \to J/\psi\pi^0$. *Phys. Rev.*, D95(3):032003, 2017.

[Sch48] Julian S. Schwinger. On Quantum electrodynamics and the magnetic moment of the electron. *Phys. Rev.*, 73:416–417, 1948.

[Sch16] Stefan Scholl. Exact signal measurements using fft analysis, 2016.

[Sel] I. Selesnick. Linear-phase fir filters, el 713 lecture notes. `http://eeweb.poly.edu/iselesni/EL713/zoom/linphase.pdf`.

[SH99] Samuel D. Stearns and Don R. Hush. *Digitale Verarbeitung analoger Signale (german).* R. Oldenbourg Verlag München Wien, 1999.

[SLBSP15] Alicia Sanchez Lorente, Sebastian Bleser, Marcell Steinen, and Josef Pochodzalla. Antihyperon potentials in nuclei via exclusive antiproton–nucleus reactions. *Phys. Lett.*, B749:421–424, 2015.

[Spi05] Helmuth Spieler. *Semiconductor Detector Systems*, volume v.12 of *Semiconductor Science and Technology.* Oxford University Press, Oxford, 2005.

[TDR08] Technical Design Report for PANDA Electromagnetic Calorimeter (EMC). *arXiv-Instrumentation and Detectors*, 2008.

[Tho12] Erik Thomé. *Multi-Strange and Charmed Antihyperon-Hyperon Physics for $\bar{P}ANDA$.* PhD thesis, Uppsala U., 2012.

[VDR09] O.Missevitch V. Dormenev, M.Korjik and R.W.Novotny. Basic principles of the stimulated recovery of the radiation induceddamage in pwo scintillator. https://indico.gsi.de/event/678/session/1/contribution/2/material/slides/0.pdf, September 2009.

[VdWO13] Jacques Van de Wiele and Saro Ong. Radiative corrections in nucleon time-like form factors measurements. *Eur. Phys. J.*, A49:18, 2013.

[W+09] Shu-Jun Wei et al. Introduction to BESIII EMC sub-trigger system. *Nucl. Instrum. Meth.*, A598:323–327, 2009.

[Whi89] S. A. White. Applications of distributed arithmetic to digital signal processing: a tutorial review. *IEEE ASSP Magazine*, 6(3):4–19, July 1989.

[Wie09] Peter Wieczorek. *Entwicklung eines ladungsempfindlichen Vorverstärkers zur Auslese von Lawinenfotodioden*. PhD thesis, Ruhr-Universität Bochum, 2009.

[Wie19] Peter Wieczorek. Private communication: Amplification factor of apfel preamplifier v. 1.5, 2019.

[Wil16] Andrea Wilms. News from apd screening @ p/l. https://slideplayer.com/slide/13571560/, June 2016.

[Wol18] Sahra A. Wolff. Feasibility Studies for a FAIR Phase-0 Project at MAMI. *Master Thesis*, 2018.

[WolXX] Sahra A. Wolff. PhD Thesis, currently in preparation (2019). *Dissertation*, 20XX.

[Xil16] Inc. Xilinx. 7 series fpgas configurable logic block, ug474 (v1.8). https://www.xilinx.com/support/documentation/user_guides/ug474_7Series_CLB.pdf, September 2016.

[Xil17] Inc. Xilinx. Vivado design suite user guide, implementation, ug904 (v2017.3). https://www.xilinx.com/support/documentation/sw_manuals/xilinx2017_3/ug904-vivado-implementation.pdf, October 2017.

[Xil18a] Inc. Xilinx. 7 series dsp48e1 slice, ug479 (v1.10). https://www.xilinx.com/support/documentation/user_guides/ug479_7Series_DSP48E1.pdf, March 2018.

[Xil18b] Inc. Xilinx. 7 series fpgas data sheet: Overview, ds180 (v2.6). https://www.xilinx.com/support/documentation/data_sheets/ds180_7Series_Overview.pdf, February 2018.

[Xil18c] Inc. Xilinx. Vivado design suite user guide, synthesis, ug901 (v2018.2). https://www.xilinx.com/support/documentation/sw_manuals/xilinx2018_2/ug901-vivado-synthesis.pdf, June 2018.

[Zim18] Iris Zimmermann. *Feasibility studies for the measurement of the time-like electromagnetic proton form factors at the PANDA experiment.* PhD thesis, Mainz U., 2018.

Curriculum Vitae

Personal Data

Name:	Ernst Johannes Oliver Noll
Date of Birth:	28^{th} of April 1988
Nationality:	German

Education

2015 – 2020	PhD study at Johannes Gutenberg University (JGU), Helmholtz Institute Mainz
2012 – 2014	Master of Science in Physics, JGU Mainz
2009 – 2012	Bachelor of Science in Physics, JGU Mainz
2008 – 2009	General Matriculation Standard, Carl-Benz-Schule Koblenz
2007 – 2008	Advanced Technical Collage Certificate, Carl-Benz-Schule Koblenz
2003 – 2007	Vocational Training as Precision Engineering Technician, Reuth GmbH Großmaischeid